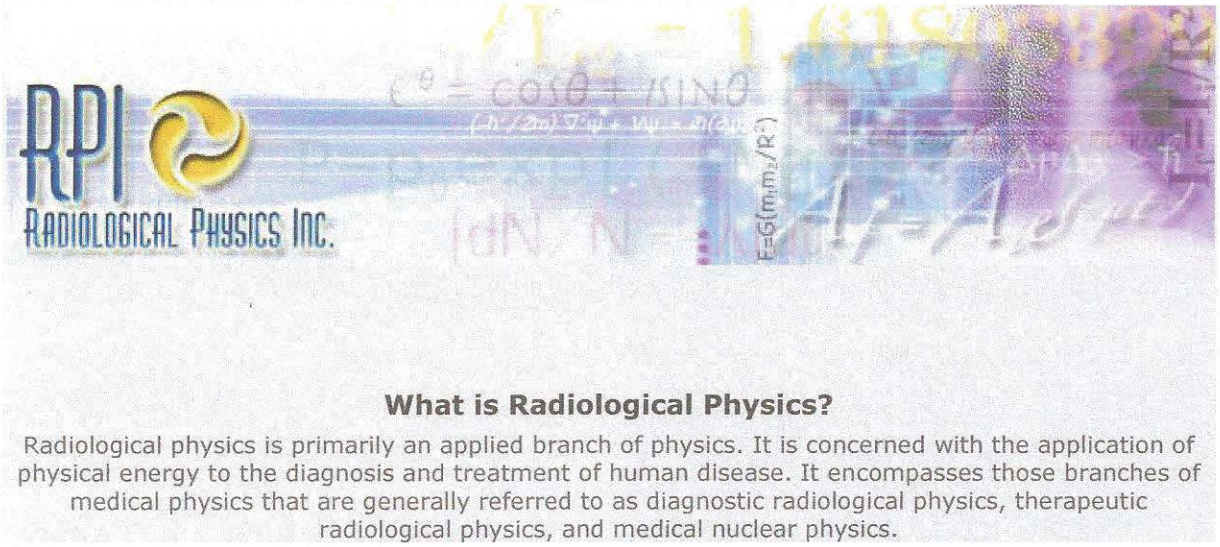
Introduction to Radiological Sciences

↓
Radiation Dosimetry

website: www.umich.edu/~ners590

Class Policy: see web

Class Schedule: see web



... alternatively ...

Radiological Physics is a scientific effort that involves the use of Radiation Physics (how radiation interacts with matter) and Engineering (design of radiation sources/design of physical systems and software systems) to impact life.

Generally, these efforts are beneficial to life: therapeutic medical physics, radiology (imaging and therapy).

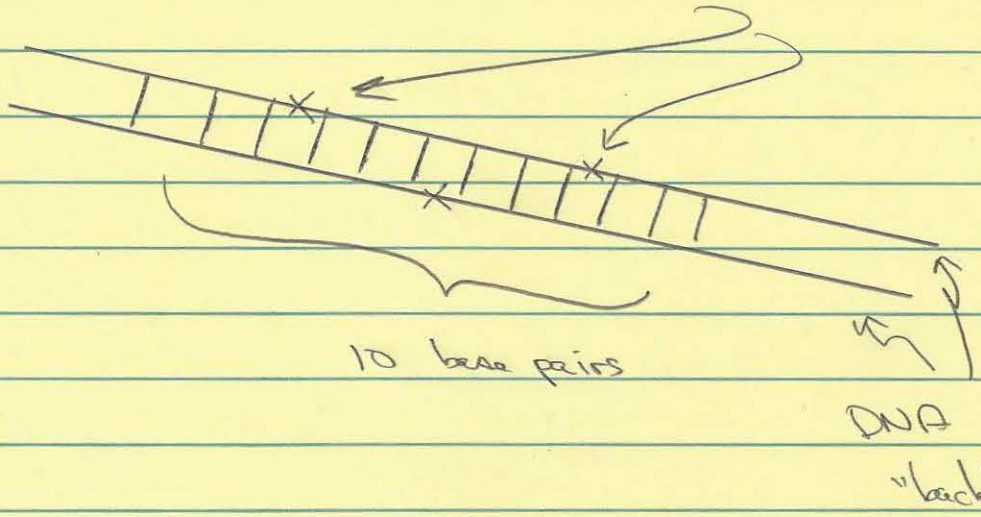
Sometimes (unfortunately) these efforts are harmful: radiological bombs, atomic and thermonuclear weapons.

Google: "Radiological Physics"
"What is Radiological Physics?"

How does radiation impact life?

Google: "How does radiation affect human cells?"

Radiation causes "lesions"



Generally, 3 lesions within 10 base pairs is lethal (DNA can not replicate), and the cell dies.

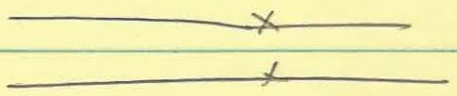
How are lesions formed?

About equal
- Direct impact (chemical transformation, ionization, excitation)
- Indirect, radical formation OH^- H^+ which diffuse and cause damage

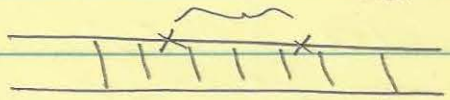
The DNA in every cell in our bodies is disrupted (one lesion) every second in <u>each</u> cell.

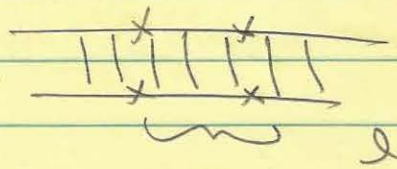
Our natural evolution has developed very robust repair mechanisms, that repair these lesion faithfully within a timespan of about 5 minutes.

DNA misrepairs happen



breaks off, flips and reattaches





loss, reattachment
re-orientation & attachment

Rarely, one of these bad repairs leads to a cell that is viable (lives, can reproduce), but is not functionally useful to the collective.

Reproducing, without check, leads to <u>cancer</u>. (oncogenesis)

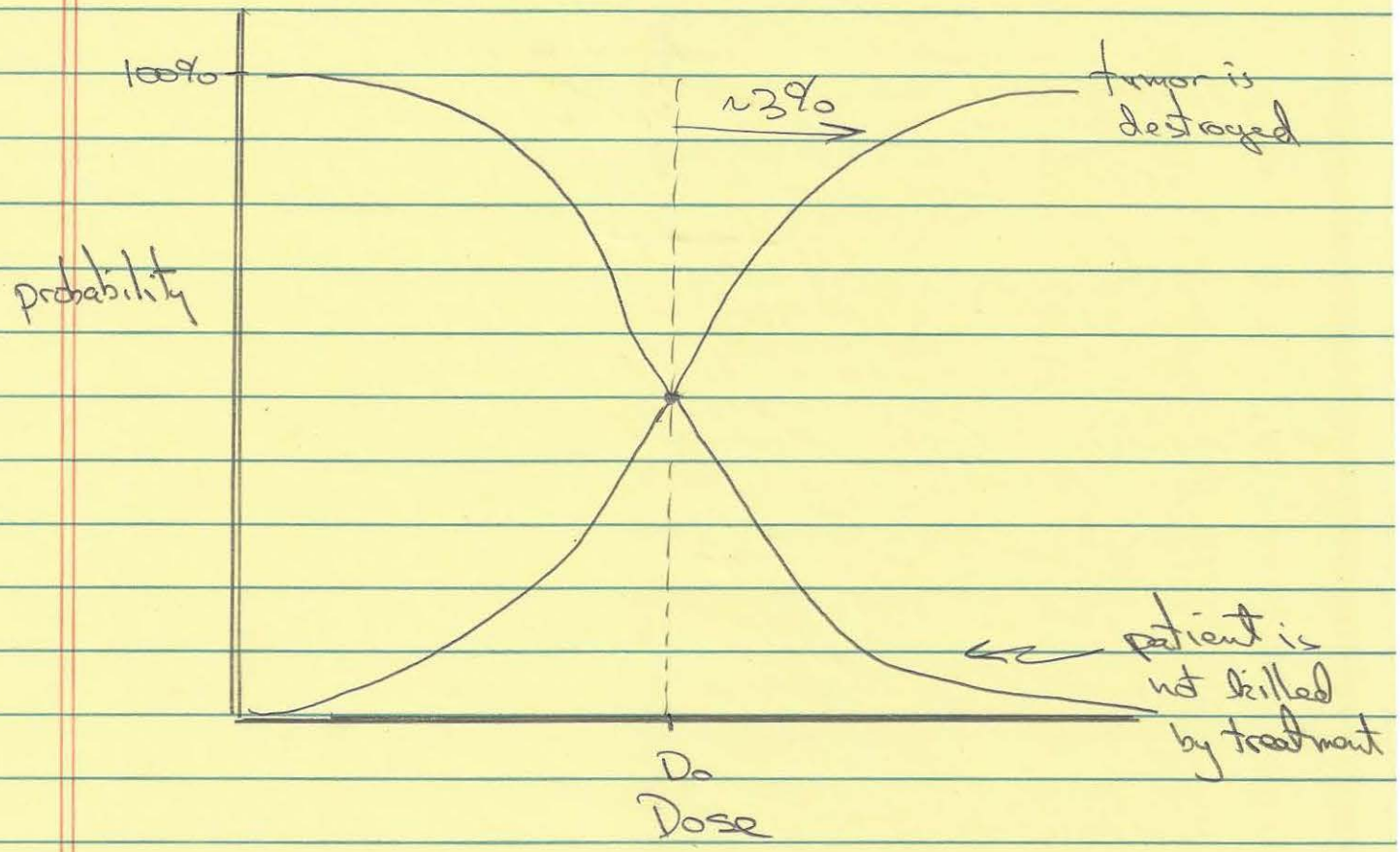
Radiotherapy, an important branch of medical physics, aims to use radiation to kill cancer cells, using beams of particles (usually photons, but, e^-, p, α's are used as well) directed at cancerous tumors.

Healthy cells are killed as well.

It is a "very delicate" balance.

A 3% wrong dose, has therapeutic outcomes.

3% too high, normal tissue complication
3% too low, cancer is not eradicated



Hence, dosimetry (measurement of radiation) is <u>critical</u>, and

that is what this course is about

What this course is about...

1) Dosimetry
2) Definition & applications of fluence, as well as other radiometric quantities
   e.g. kerma, exposure, dose
3) The definition, application & implications of radiation equilibrium

4) How to think about radiation microscopically (radiation interactions)

5) How dose is defined & measured

6) How hospitals guarantee accuracy of dose (the dosimetry chain)
   - i.e. How the international community has agreed on a standard
   - how it is measured absolutely in national standards' labs
   - how that measurement (absolute) gets transmitted to hospitals

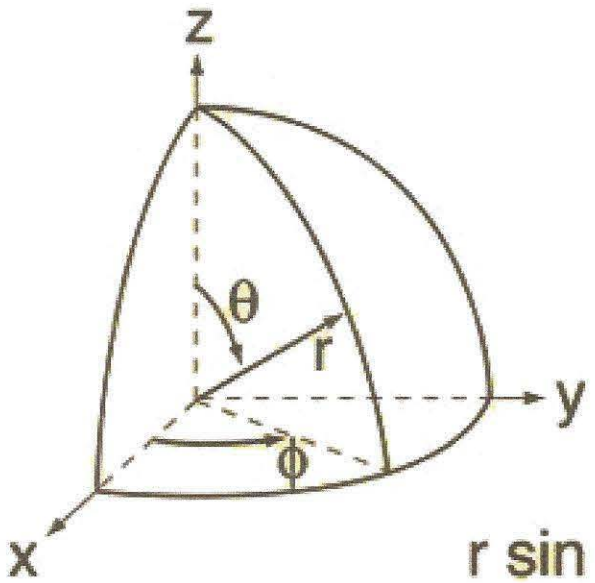
Radiation Quality

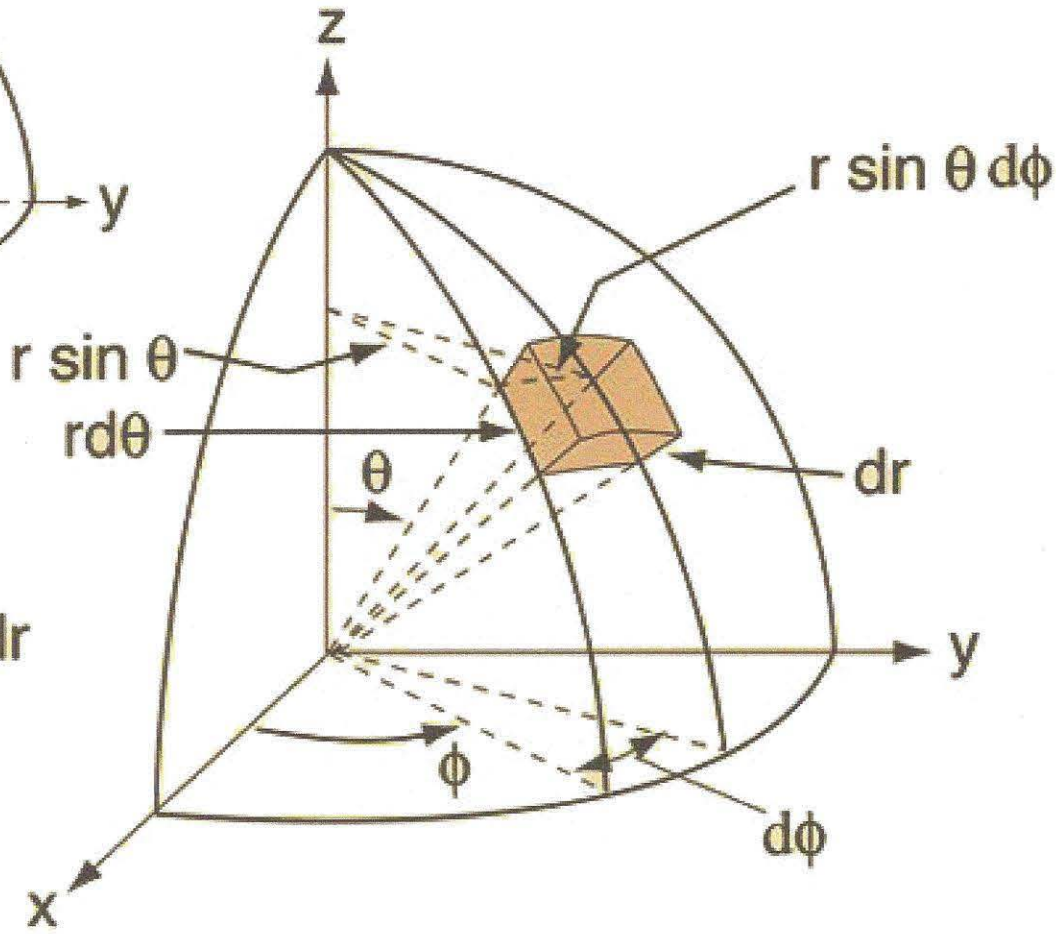
Radiation quality refers to:
- the particle species ($n, \gamma, \beta, p \ldots$) in a radiation field
  jargon: "field" means that there are so many particles, that the distributions are assumed to be continuous (allowing us to use calculus) (it is an approximation)
- their distribution(s) in energy
- spatial distribution (collimation perhaps)
- angular distributions
- temporal distributions (if any)

Radiation quality can be represented as a macroscopic, continuous function:

$$n_i(\vec{x}, \vec{\Omega}, E)$$ (we will ignore time, since fields are constant in time in all our applications)

i: particle type index indicating species ($e^-, \gamma, n, p \ldots$)
$\vec{x}$: space vector, position in space
$\vec{\Omega}$: direction vector $\vec{\Omega} := (u, v, w) = (\sin\theta\cos\phi, \sin\theta\sin\phi, \cos\theta)$
θ: polar angle $0 \le \theta \le \pi$ $\hat{z} \cdot \vec{x} = r\cos\theta$
ϕ: azimuthal angle $0 \le \phi \le 2\pi$





Volume element

$dV = r^2 \sin\theta \, d\theta \, d\phi \, dr$

Dosimetry

is the science of measuring "dose" in a radiation field because dose is an excellent predictor of radiological change.

There are two branches of dosimetry

"absolute" dosimetry is measured dose directly and absolutely

Given a detector with a dose response function $r_i(\vec{x}, \vec{\Omega}, E)$, we can write

dose $D = \sum_i \int d\vec{x}\, d\vec{\Omega}\, dE\; r_i(\vec{x}, \vec{\Omega}, E)\, d_i(\vec{x}, \vec{\Omega}, E)$

We'll employ the shorthand

$D = r \circledast d$ to represent this

Absolute dosimetry is only done in National Radiation Standards' Laboratories, national government institutions that maintain the radiation "standard". The "standard" really refers to the device (an ionization chamber, typically) that is typically extremely well characterized.

The radiation beams at national standards labs are not all that well characterized. (They do have a good idea though.) So, by understanding "d" and measuring, they determine D to an absolute accuracy of about 0.5%. The cost of maintaining an absolute standard is quite high, hence the governmental control.

"reference" dosimetry is a less expensive way of determining the dose from, for example, a linear accelerator in a hospital setting. Neither the hospital's chamber nor the radiation field is all that well characterized. With the assistance of the National Standard Lab, absolute dose in the hospital can be determined.

The itinerant standard model.

The "standard" travels from hospital to hospital. The standard dector d_S, and the hospital's detector d_H are both exposed to identical radiation fields. The standard chamber's measurement gives absolute dose, and the ratio of the two gives a calibration factor, that can be used to infer dose

$$D_S = n_H \otimes d_S$$
$$D_H = n_H \otimes d_H$$

$n_H \equiv$ hospital's beam calibration step

$$C = \frac{n_H \otimes d_S}{n_H \otimes d_H}$$

} calibration constant

$$n'_H \otimes d_H = \underbrace{[n'_H \otimes d_S]}_{D'} \underbrace{\left[\frac{n'_H \otimes d_H}{n'_H \otimes d_S}\right]}_{= 1/C}$$

$$\boxed{D' = [n'_H \otimes d_H]\, C}$$

reference (absolute) dose

Advantages

- "best" reference system

Disadvantages

- cost
- risk of damaging the standard

New Zealand does it this way.

The itinerant secondary standard model

The hospital's instrument travels to the Standards' lab.

In this case



$$C_s = \frac{n_s \otimes d_s}{n_s \otimes d_H}$$

calibration factor provided by the Stds lab

$$n_H \otimes d_H = \underbrace{n_H \otimes d_s}_{D} \frac{n_H \otimes d_H}{n_H \otimes d_s}$$

$$= D \; \underbrace{\frac{n_S \otimes d_H}{n_S \otimes d_S}}_{\frac{1}{C_S}} \; \underbrace{\frac{\left[\frac{n_H \otimes d_H}{n_S \otimes d_H}\right]}{\left[\frac{n_H \otimes d_S}{n_S \otimes d_S}\right]}}_{\frac{1}{A}}$$

$$D = \underbrace{[n_H \otimes d_H]}_{\text{measurement in hospital's beam using hospital's detector}} \; C_S \; A$$

↑ dose

↑ calibration factor in the standard lab's beam

A: a "theoretical" correction factor
usually $0.95 - 1.05$
It hinges on the insensitivity of the detector to radiation qualities. For well designed chambers, this is true

The rest of the world does their reference dosimetry this way

The rest of the course is devoted to understanding radiation beams & their detectors.

1 Species of radiation types and how they are produced

n, p, e^- (e^+ is a byproduct), γ, α, $^A X$, π

have been used for R_x

γ's account for about $\approx 85\%$ of radiation treatments

e^- for about $\gtrsim 10\%$

the rest $\lesssim 5\%$

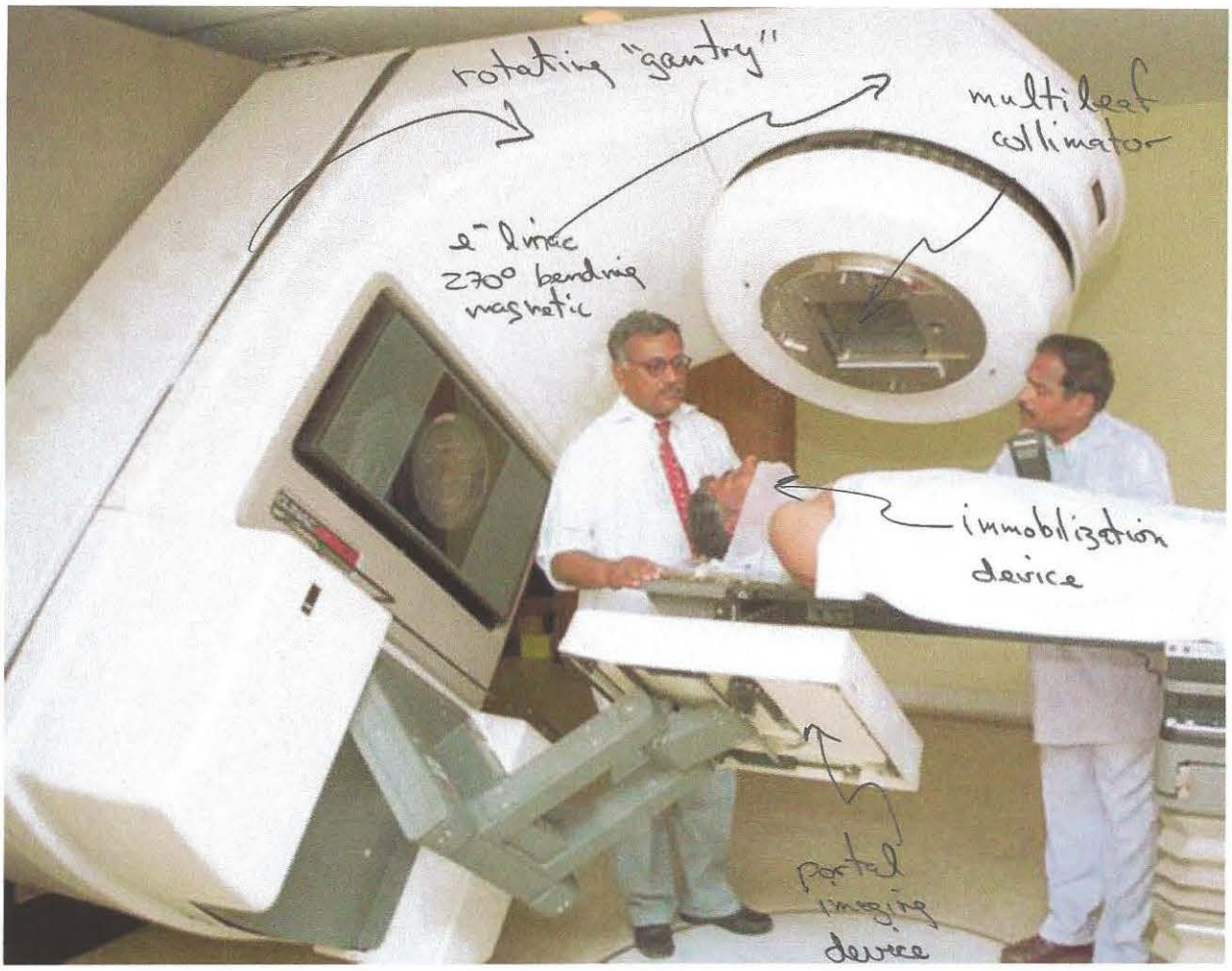
High-energy X-Rays (γ's), in the range

rarer, but exist ← 2 → 6 → 21 → 50 MeV

(6 → 21: most common in medical physics)

are produced by the bremsstrahlung process

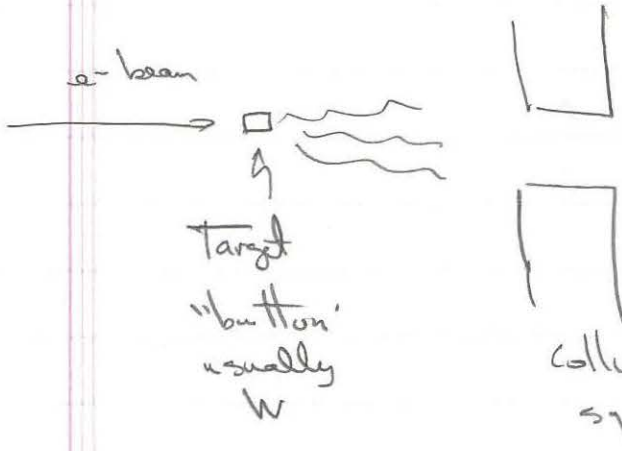
Radiotherapy set up.



From "The Hindu" London, May 11, 2010.

"New study offers hope to colon cancer patients"

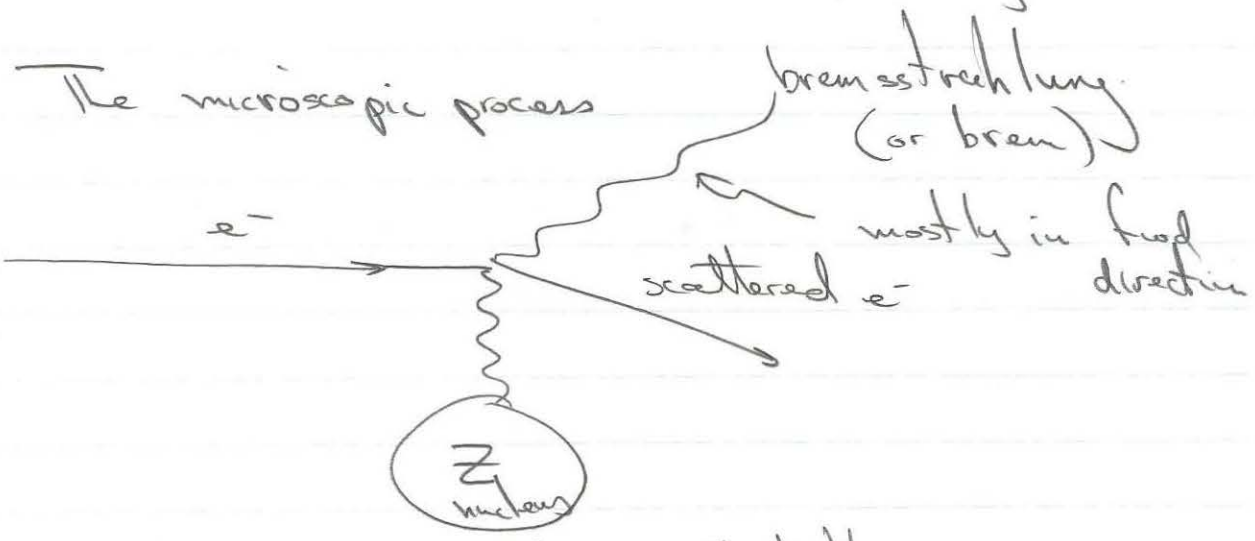
?



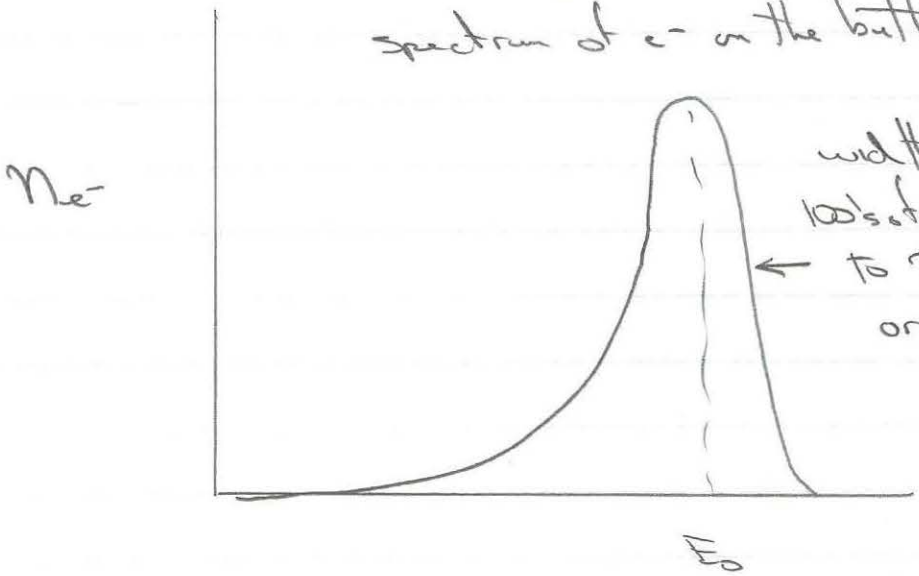
The energy quality is denoted MV (eg. 6MV) which is the end-point energy

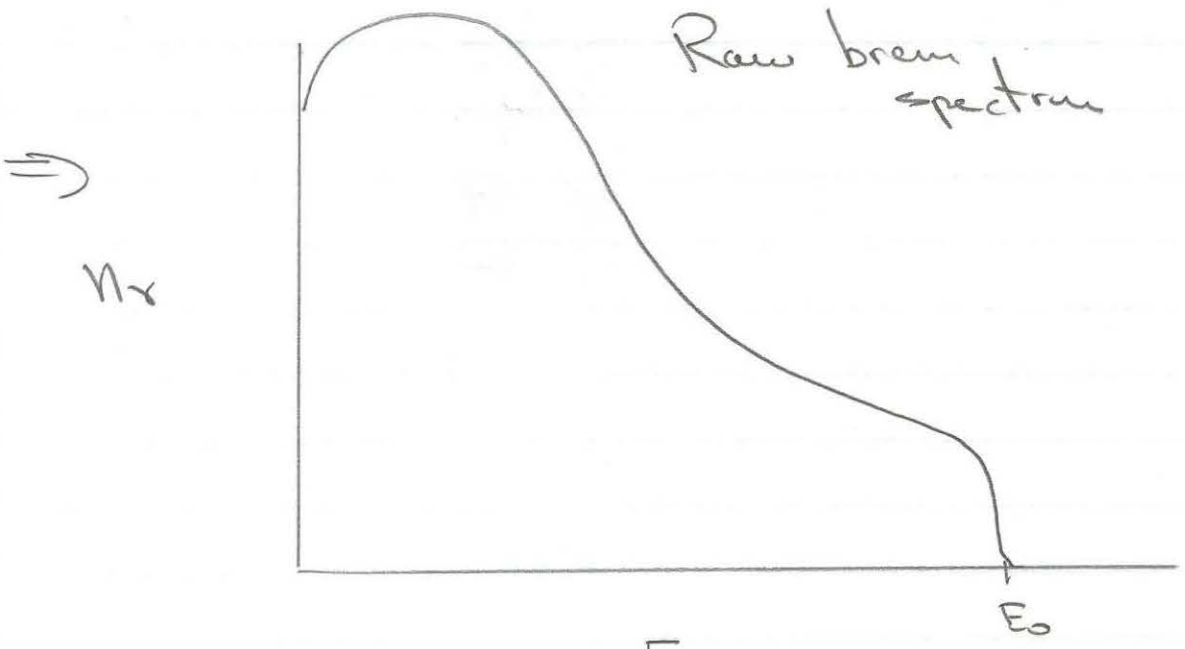
The microscopic process

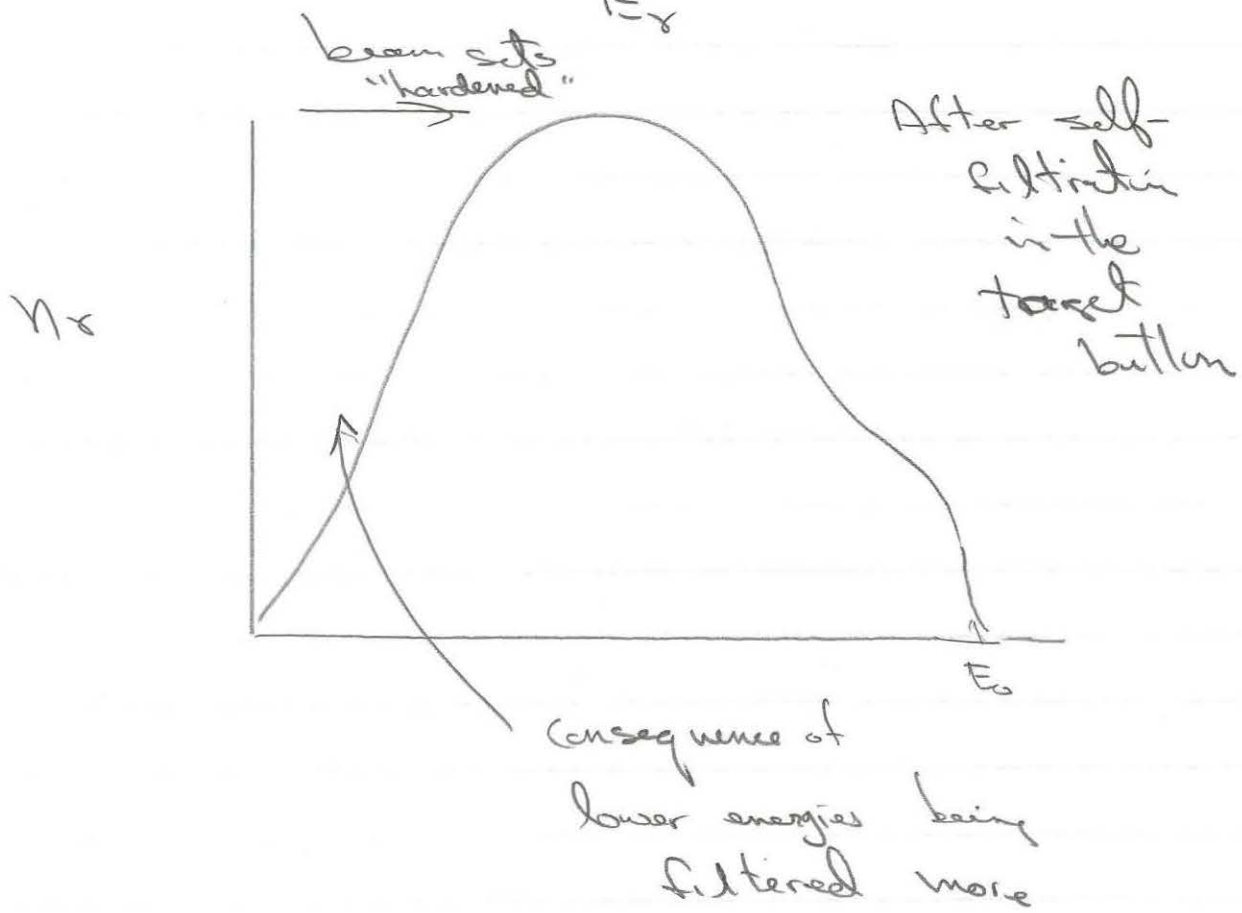
(German for (braking radiation))



spectrum of e⁻ on the button




Raw brem spectrum
n_γ
E_0
E_γ


beam gets "hardened"
After self-filtration in the target button
n_γ
E_0
Consequence of lower energies being filtered more

The energy quality of determines its penetrating power. HE ↑ for deeper seated tumors.

monoenergetic γ energy	mean free path in water (cm)
1	14
6	36
10	45

$$I = I_0 e^{-\mu x} \qquad mfp = \frac{1}{\mu}$$

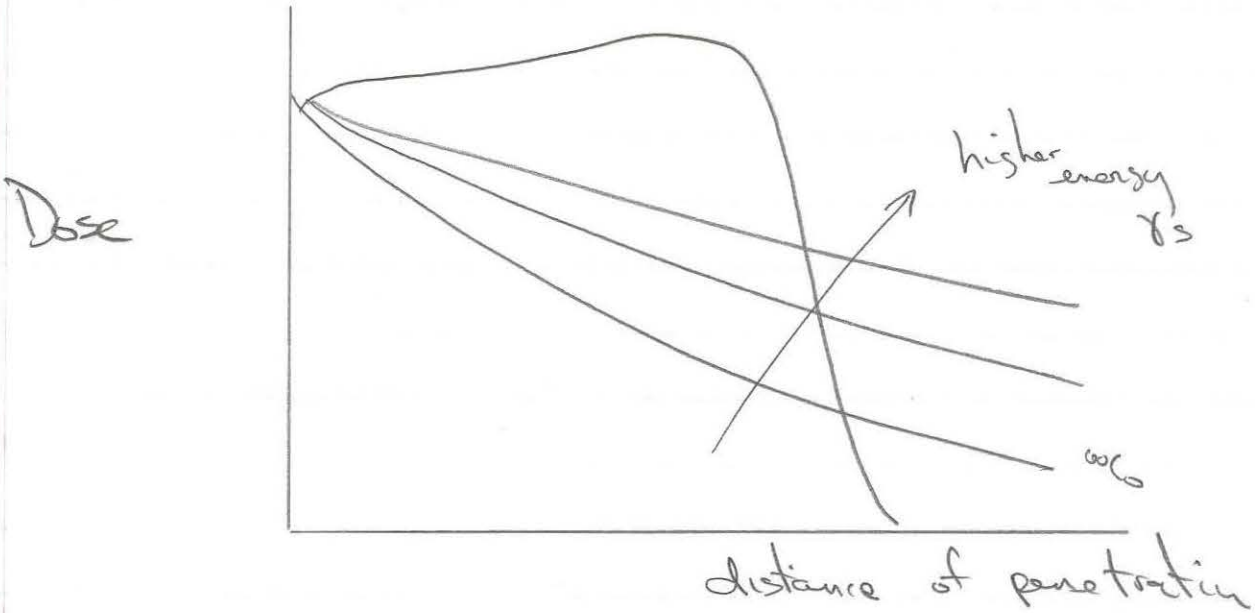
Sometimes the electron beams are used directly, or more commonly to "boost" photon treatments.

However, a 20MeV e⁻ beam only penetrates about 10 cm. It is more useful for surface treatments. However, it does have the advantage that tissue beyond its range does not get irradiated (much)

Low energy sources

$^{60}Co \rightarrow {}^{60}Ni^{*} + e^{-} + \bar{\nu}_e$

${}^{60}Ni^{*} \rightarrow {}^{60}Ni + 2\gamma's$ [1.17 ; 1.33 MeV]
almost 50/50



^{60}Co is a radioactive substance
Most of the cost is acquiring the source.
(5.26 year half-life) Used mostly in the non-industrialized world.
^{137}Cs 30.0 year half life $\gamma = 0.662$ MeV
has also been used. Larger source, though

Chapter 4 : Macroscopic Radiation Physics

4.1 Fluence

Fluence is the most useful of all the radiometric quantities for dosimetry, because it is (by construction) the most closely aligned with radiological outcomes. (More on this in a few moments.)

The definition of fluence is very precise, and often found to be incorrect (google has it wrong).

It is often confused with "flux", particles hitting some surface.

We will be very exact about this ...

The symbol for fluence is

(4.1) $\varphi_i(\vec{x}, E, t)$

$\vec{x}$: space vector
E : energy (kinetic)
t : time
i : species type $e^-, n, p, \ldots$

(We generally integrate over all time to measure the total radiological effect,

most common

(4.2) $$\bar{\Phi}_i(\vec{x},E) = \int_{-\infty}^{\infty} dt\ \phi_i(\vec{x},E,t)$$

or, if time intervals are required (rare)

(4.3) $$\bar{\Phi}_i(\vec{x},E,t_i,t_f) = \int_{t_i}^{t_f} dt\ \phi_i(\vec{x},E,t)$$

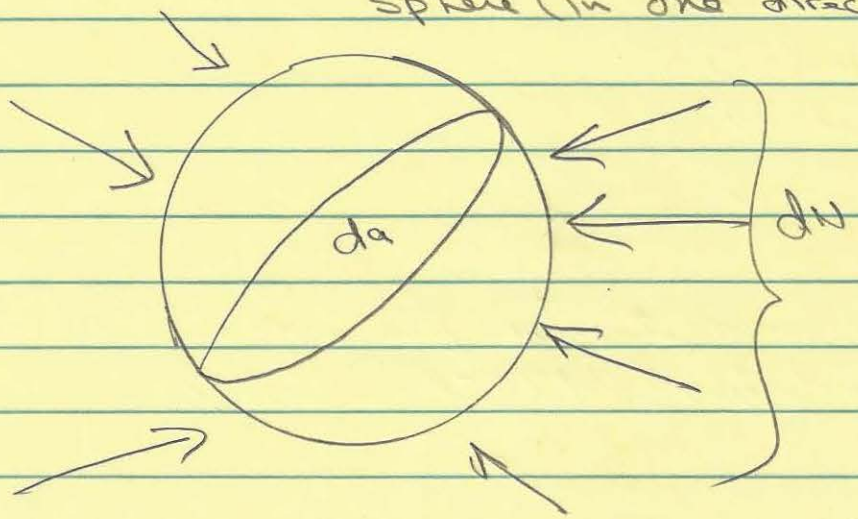
For economy, ...

$\bar{\Phi}$ means $\bar{\Phi}_i(\vec{x},E)$
unless someone says otherwise

Finally, the precise definition

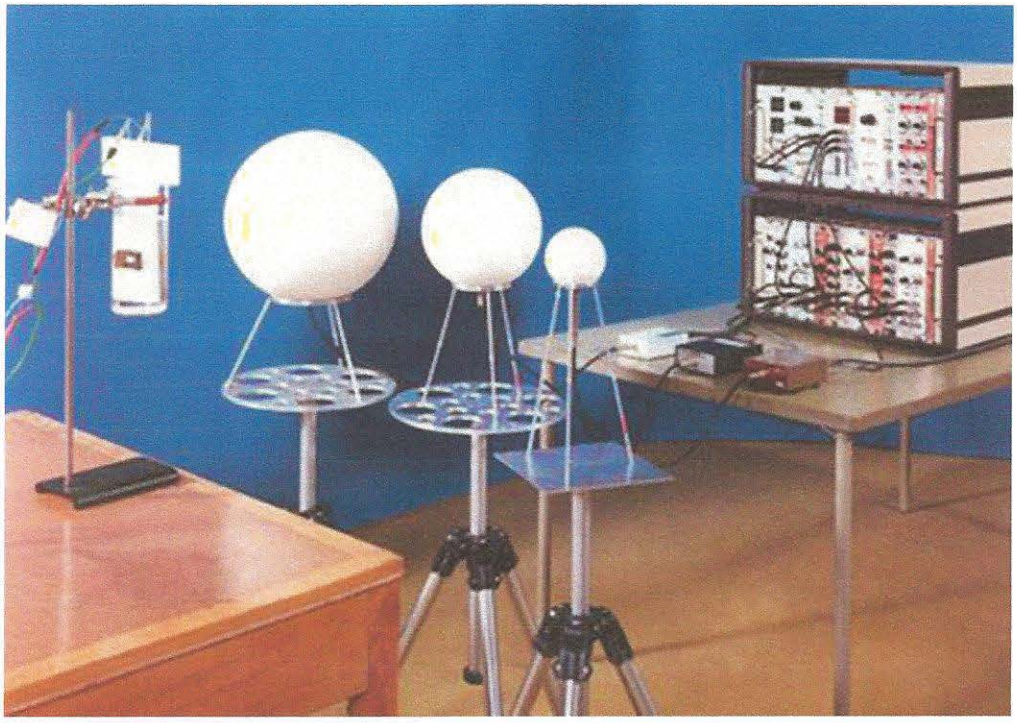
(4.4) $$\bar{\Phi} = \lim_{da \to 0} \frac{dN}{da}$$

$da \equiv$ cross sectional area of a small sphere
$dN \equiv$ number of particles crossing that sphere (in one direction only)



Bonner spheres in a measurements laboratory:

These measurement devices are the closest approximation to an instrument that measures fluence according to its definition.



From Wikipedia (google "Bonner Sphere"):

Bonner spheres are used to determine the energy spectrum of a neutron beam. The methodology, which was first described in 1960 by Rice University's Bramblett, Ewing and Bonner, employs thermal neutron detectors embedded in moderating spheres of different sizes. Comparison of the neutrons detected by each sphere allows accurate determination of the neutron energy.

See the discussion in the book regarding treating a discrete quantity, N, as a continuous variable.

Upshot:

$$(4.5) \quad \bar{\Phi} \approx \frac{\langle \Delta N \rangle}{\Delta a} = \frac{\int dn}{S} \quad (4.10)$$

Works very well when ΔN is large enough and the radiation fields being measured are constant in time (the usual case) and the radiation fields are uniform over the 4π finite sphere.

Why is this definition of $\bar{\Phi}$ contrived in such an awkward way?

The important thing is that the direction of the radiation does not matter because a sphere is uniform in all directions.

As practical measurement devices, spheres are hard to make.

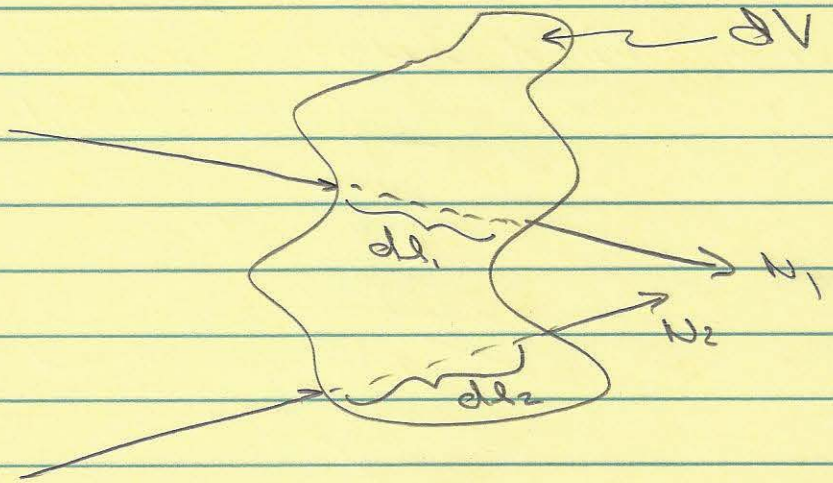
Commonly, one wants to use an object of arbitrary shape to measure (or calculate) fluence.

N.B. Chilton provided an elegant proof (1970) that the shape is irrelevant.

His version of fluence is

$$\bar{\Phi} = \lim_{dV \to 0} \frac{\sum_{i=1}^{dN} dl}{dV} \quad (4.8) \quad = \quad \frac{\bar{l}}{V} \quad (4.10)$$

where dV is an infinitessimal (but arbitrarily-shaped) volume, and Σl is the sum of the "tracklengths" of those dN particles through it



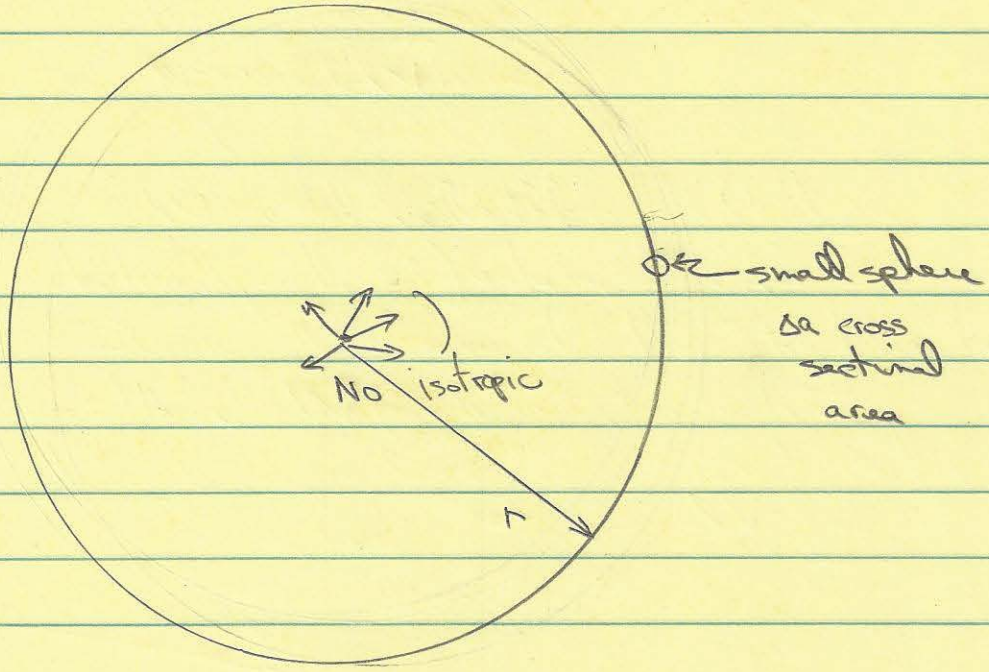
This is a truly remarkable result!

Some illustrations are in order.

Example 1

monoenergetic

Q. An isotropically radiating point source, sizes off No particles. What is the fluence measured at any point in space?



A. Since the source radiates isotropically, put the da spherical detector at any point on that sphere

So N_0 particles go through the big sphere, that has surface area $4\pi r^2$.

The fraction that go through the detector is

$$dN = \frac{N_0\, da}{4\pi r^2}$$

So $$\overline{\Phi} = \lim_{da \to 0} \frac{dN}{da} = \lim_{da \to 0} \left(\frac{1}{da}\right)\left(\frac{N_0\, da}{4\pi r^2}\right)$$

$$= \frac{N_0}{4\pi r^2}$$

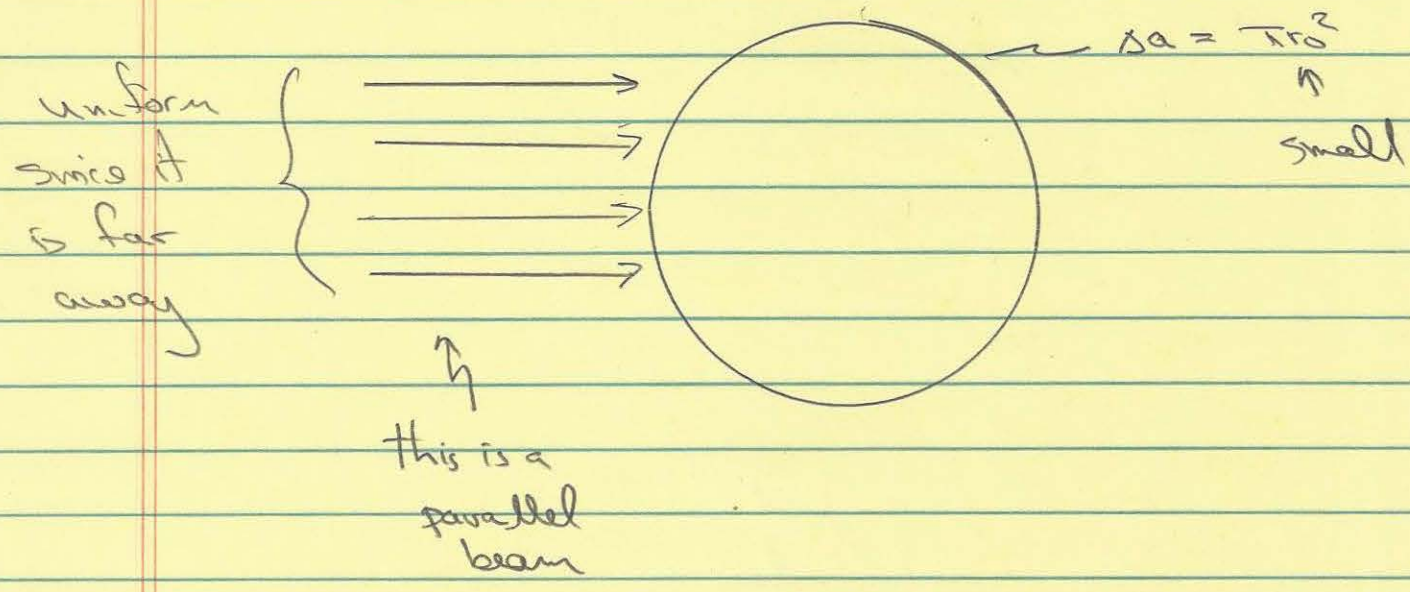
$$\boxed{\overline{\Phi} = \frac{N_0}{4\pi r^2}}$$

Doing the hard way!
Use Chilton's theorem

Note: Both methods, ICRU & Chilton give the same answer. In general, use the easiest (unless you're a teacher and a pedant)

Chilton: $\bar{\Phi} = \frac{\int dl}{V}$ when V is very far from the point source

A. When the sphere Δa is very far from the test source, the radiation cross the sphere looks like



$$\Phi = \left(\frac{\pi r_0^2}{4\pi r^2}\right) N_0 \qquad \frac{\int dl}{V}$$

$\left(\frac{\pi r_0^2}{4\pi r^2}\right) N_0$: number of particles that reach the detector

$\frac{\int dl}{V}$: average chord length from a monodirectional source on a sphere

Since the source is monodirectional but the detector is isotropically symmetric, we would get the same result if we had an isotropic source.

In this case we can use

$$\int dl = \frac{4V}{S}$$ for "concave" volumes

↑ one in which a ray touches the surface at only two points unless it's tangent

$$\Phi = \frac{\int dl}{V} = \frac{4V}{S}\left(\frac{1}{V}\right) = \frac{4}{S} = \frac{1}{\pi r_0^2}$$

$$\therefore \boxed{\Phi = \frac{N_0}{4\pi r^2}}$$



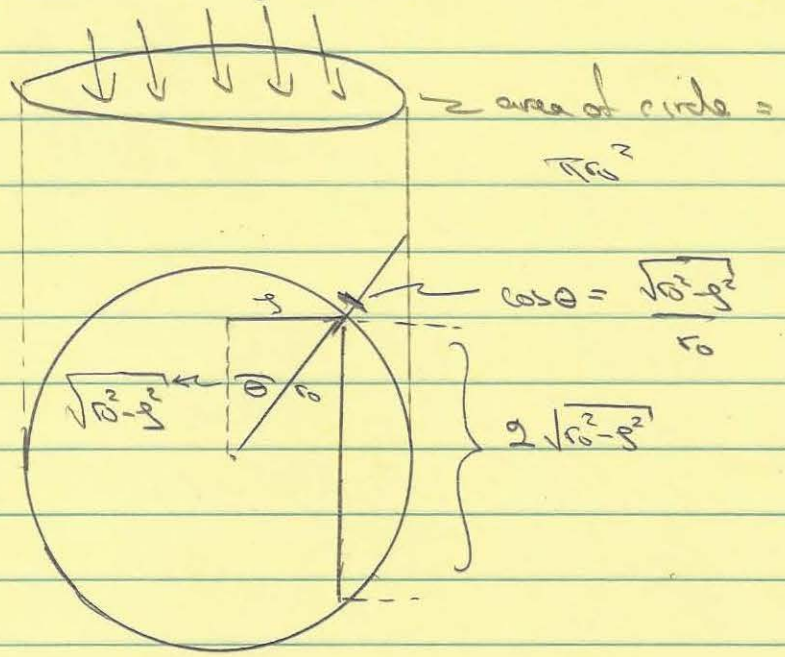
You want proof? I'll give you proof!

of Sdl = $\frac{4V}{S}$ for a sphere

$$\frac{4V}{S} = \frac{4 \cdot \frac{4}{3}\pi r_0^3}{4\pi r_0^2} = \frac{4}{3} r_0$$

See next page.

Here's your proof! (The right one, this time.)



$$\langle \ell \rangle = \underbrace{\frac{1}{\pi r_0^2}}_{\text{over the incident circle}} \int_0^{2\pi} d\phi \int_0^{r_0} \rho\, d\rho \; \underbrace{2\sqrt{r_0^2-\rho^2}}_{\text{length of the ray}} \; \frac{\sqrt{r_0^2-\rho^2}}{r_0}$$

$\int_0^{2\pi} d\phi \int_0^{r_0}$: integral over the circle

$$= \left(\frac{1}{\pi r_0^2}\right)\underbrace{(2\pi)}_{\text{did int over } d\phi} r_0^3 \underbrace{\int dz\,(1-z^2)}_{z=\rho^2}$$

$$= 2r_0\left(\frac{2}{3}\right) \leftarrow \text{integral over } z$$

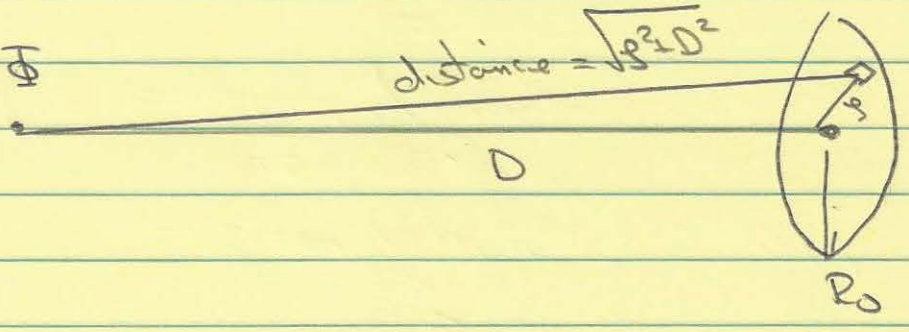
$$\langle \ell \rangle = \frac{4}{3} r_0 \quad \text{!! QED (Yippee!)}$$

Q. An infinitely thin disk source, radius R_0, gives off monoenergetic radiation isotropically, with an areal density of S_0.
[Note: this is very close to problem 2 in the assignment]

What is the fluence at a point D away. Assume the fluence detector is at $\vec{x} = (0,0,0)$ and the disk at $\vec{x} = (0,0,D)$ with its normal aligned with the z-axis.

A.

$$d\Phi = \overbrace{\rho d\rho d\phi S_0}^{\text{amount of radiation from } dA \text{ on the sphere}} * \frac{1}{4\pi(D^2+\rho^2)}$$



$$\therefore \Phi = \frac{S_0}{4\pi} \underbrace{\int_0^{2\pi} d\phi}_{2\pi} \int_0^{R_0} \rho d\rho \frac{1}{D^2+\rho^2} \quad \text{let } \rho^2 = z$$

$$= S_0 \int_0^{R_0^2} dz \frac{1}{D^2+z}$$

$$\bar{\Phi} = \frac{S_0}{4} \log\left(\frac{D^2+R_0^2}{D^2}\right)$$

The total # of particles emitted by the source is

$$N_0 = S_0 \pi R_0^2$$

So, we can also write

$$\boxed{\bar{\Phi} = \frac{N_0}{4\pi R_0^2} \log\left(1 + \frac{R_0^2}{D^2}\right)}$$

Note: If we shrink the disk to a point hold N_0 constant

$$\bar{\Phi} \underset{R_0 \to 0}{\rightarrow} \frac{N_0}{4\pi R_0^2}\left\{\frac{R_0^2}{D^2} + O\left(\left(\frac{R_0}{D}\right)^4\right)\right\}$$

$$= \frac{N_0}{4\pi D^2}$$

Expected! Looks like fluence from a point!

Fluence 4.1 (cont.)

(note: The remainder of 4.1 discussed here, is not in the book

Integrated fluence

In this section we consider measurements of fluence, using fluence detectors of finite size.

Consider a volume of space V_D, representing the sensitive volume of a fluence detector.

Consider, as well, a volume of space V_S, that represents the source.
Ignoring attenuation and scatter, the integrate fluence is

The differential fluence at point $\vec{x}_D$ in the detector due to a particle emerging from $\vec{x}_S$ is:

$$d\bar{\Phi}_M^{D,S} = \frac{1}{V_D} dV_D \frac{1}{V_S} \frac{dV_S \, \phi(\vec{x}_S)}{4\pi |\vec{x}_S - \vec{x}_D|^2}$$

($\phi(\vec{x}_S)$: # of particles emanating from $\vec{x}_S$; $\frac{1}{4\pi |\vec{x}_S - \vec{x}_D|^2}$: elemental fluence at $\vec{x}_S$ from the source at $\vec{x}_D$)

Thus the integrated fluence is

$$\bar{\Phi}_M^{D,S} = \frac{1}{V_D}\frac{1}{V_S}\int d\vec{x}_D \int d\vec{x}_S \frac{\varphi(\vec{x}_S)}{4\pi|\vec{x}_S - \vec{x}_D|} \quad (1)$$

Now, consider the special case, where $\varphi(\vec{x}_S)$ is a constant, and $\int dV_S \varphi(\vec{x}_S) = N_0$

Then

$$\bar{\Phi}_M^{D,S} = \frac{N_0}{V_D V_S}\int d\vec{x}_D \int d\vec{x}_S \frac{1}{|\vec{x}_S - \vec{x}_D|^2} \quad (2)$$

Note the symmetry in this equation (2)!

$$\bar{\Phi}_M^{D,S} = \bar{\Phi}_M^{S,D}$$

i.e. The integrated fluence in M from the source in S, is the same as a measurement of fluence in S, from a source spread out uniformly (No being the same) in D!

So, all the work in A1 ... we can use this to set integrated fluences in line, shell and spherical detectors.

Let's take this even further!

Most measurement scenarios involve small detectors and small sources, and long distances between them.

To be concise, the span of $d\vec{x}_S$ or $d\vec{x}_D$ is $\gg |\vec{x}_S - \vec{x}_O|$

Now, do the following:

Let $\vec{x}_S = \vec{x}_{O,S} + \vec{\varepsilon}_S$

$\vec{x}_D = \vec{x}_{O,D} + \vec{\varepsilon}_D$

and locate $\vec{x}_{OS}, \vec{x}_{O,D}$ at the "geometrical center" of each

In other words

$$\int_{\text{source}} d\vec{\varepsilon}_S \, \vec{\varepsilon}_S = 0 = \int_{\text{detector}} d\vec{\varepsilon}_D \, \vec{\varepsilon}_D$$

Then

$$|\vec{x}_D - \vec{x}_S|^2 = \underbrace{|\vec{x}_{OS} - \vec{x}_{OD}}_{\text{d, the distance between the centers}} + \vec{\varepsilon}_S - \vec{\varepsilon}_D|^2$$

this is just a constant

This page is intentionally blank.

$$d^2 + 2\vec{d}\cdot(\vec{\varepsilon}_s - \vec{\varepsilon}_0) + |\vec{\varepsilon}_s - \vec{\varepsilon}_0|^2$$

$$= d^2\left[1 + 2\frac{\vec{d}}{d^2}\cdot(\vec{\varepsilon}_s - \vec{\varepsilon}_0) + \frac{1}{d^2}|\vec{\varepsilon}_s - \vec{\varepsilon}_0|^2\right]$$

$$\frac{1}{|\vec{x}_0 - \vec{x}_{s1}|^2} = \frac{1}{d^2}\left[1 + 2\frac{\vec{d}}{d^2}\cdot(\vec{\varepsilon}_s - \vec{\varepsilon}_0) + \frac{1}{d^2}|\vec{\varepsilon}_0 - \vec{\varepsilon}_s|^2\right]^{-1}$$

$\frac{1}{1+x} \approx 1 - x + x^2 \cdots$

$$= \frac{1}{d^2}\left[1 - 2\frac{\vec{d}}{d^2}\cdot(\vec{\varepsilon}_s - \vec{\varepsilon}_0) - \frac{1}{d^2}|\vec{\varepsilon}_s - \vec{\varepsilon}_0|^2 + \frac{4}{d^4}\left[\vec{d}\cdot(\vec{\varepsilon}_s - \vec{\varepsilon}_0)\right]^2\right]$$

$$= \frac{1}{d^2}\left[1 - 2\frac{\vec{d}}{d^2}\cdot(\vec{\varepsilon}_s - \vec{\varepsilon}_0) + \frac{4}{d^2}\left[(\hat{d}\cdot\vec{\varepsilon}_s)^2 - 2(\hat{d}\cdot\vec{\varepsilon}_s)(\hat{d}\cdot\vec{\varepsilon}_0) + (\hat{d}\cdot\vec{\varepsilon}_0)^2\right]\right.$$
$$\left. - \frac{1}{d^2}\left(\vec{\varepsilon}_s^2 - 2\vec{\varepsilon}_s\cdot\vec{\varepsilon}_0 + \vec{\varepsilon}_0^2\right)\right]$$

$$= \frac{1}{d^2}\left[1 + \frac{1}{d^2}\left\{\left[4(\hat{d}\cdot\vec{\varepsilon}_s)^2 - \vec{\varepsilon}_s^2\right] + \left[4(\hat{d}\cdot\vec{\varepsilon}_0)^2 - \vec{\varepsilon}_0^2\right]\right\}\right]$$

So, $\Phi_{rs} = \frac{N_0}{4\pi d^2}\left[1 + \frac{1}{d^2}\left\{4\langle(\hat{d}\cdot\vec{\varepsilon}_s)^2\rangle - \langle\vec{\varepsilon}_s^2\rangle\right\}\right.$
$\left. + \frac{1}{d^2}\left\{4\langle(\hat{d}\cdot\vec{\varepsilon}_0)^2\rangle - \langle\vec{\varepsilon}_0^2\rangle\right\}\right]$

meaning, if you are careful to use a $\vec{d}$ that is measured between the gravitational source centers, the flavor variation are 2nd order!

Illustration, the 3 examples from the assignment

1.3 The line source $\hat{\alpha} \cdot \vec{E}_0 = 0$ orthogonal

$$\langle \varepsilon_0^2 \rangle = \frac{1}{a} \int_{-\frac{a}{2}}^{\frac{a}{2}} dz\, z^2$$

$$= \frac{1}{a} \frac{2}{3} \left(\frac{a}{2}\right)^3 = \frac{a^2}{12} \checkmark$$

$\therefore$

$$\overline{\Phi}(z) \rightsquigarrow \frac{N_0}{4\pi z^2} \left\{ 1 - \frac{a^2}{12 z^2} \right\}$$

$$\text{or } \frac{1}{\pi} \left(\frac{a}{2z}\right)^2 \checkmark$$

1.1 The sphere

$$\langle \varepsilon_0^2 \rangle = \frac{\int_0^a r^2 dr\, r^2}{\int_0^a r^2 dr} = \frac{\frac{a^5}{5}}{\frac{a^3}{3}} = \frac{3}{5} a^2$$

$$\langle (\hat{z} \cdot \vec{\varepsilon}_0)^2 \rangle = \frac{\int_{-1}^{1} d\mu \int_0^a r^2 dr\, \mu^2 r^2}{\int_{-1}^{1} d\mu \int_0^a r^2 dr} = \frac{\frac{3}{5} a^2 \cdot \frac{2}{3}}{2} = \frac{1}{5} a^2$$

$$4 \langle (\hat{z} \cdot \vec{\varepsilon}_0)^2 \rangle - \langle \varepsilon_0^2 \rangle = \left(\frac{4}{5} - \frac{3}{5}\right) a^2 \checkmark$$

$$= \frac{1}{5} a^2 \checkmark$$

1.2 The spherical shell

$$\langle (\vec{\varepsilon}_D \cdot \vec{d})^2 \rangle \quad a^2 \frac{\int d\mu\, \mu^2}{\int d\mu} = \frac{2/3}{2} = \frac{1}{3} a^2$$

$$\langle \vec{\varepsilon}_D^{\,2} \rangle = a^2$$

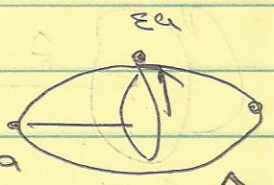
$$4 \langle (\vec{\varepsilon}_D \cdot \vec{d})^2 \rangle - \langle \vec{\varepsilon}_D^{\,2} \rangle = \left(\frac{4}{3} - \frac{1}{3}\right) a^2 = \frac{1}{2} a^2 \checkmark$$

And now! The ellipsoid!

Let's make it an ellipsoid of revolution

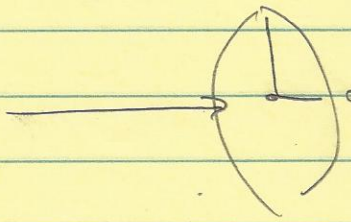
$$z^2 + \frac{x^2+y^2}{\varepsilon^2} = a^2$$

ε = eccentricity factor $\quad \varepsilon^2 < 1$



prolate

$\varepsilon^2 > 1$



oblate

$$\langle \vec{\varepsilon}_D^2 \rangle = \frac{1}{\frac{4\pi}{3}\pi\varepsilon a^3} \int_{\text{ellipsoid}} d\vec{x}\,(x^2+y^2+z^2)$$

Let $\quad x = \varepsilon u_1 \,;\; y = \varepsilon u_2 \,;\; z = u_3$

$$\langle \vec{\varepsilon}_D^2 \rangle = \frac{3\varepsilon^2}{\pi 4\varepsilon^2 a^3} \int_{\text{sphere}} d\vec{u}\;\; \varepsilon^2 u_1^2 + \varepsilon^2 u_2^2 + u_3^2$$

$$= \frac{3}{4\pi a^3} \int_{\text{sphere}} d\vec{u}\;\; \varepsilon^2 u^2 (1-\mu^2) + u^2\mu^2$$

$$= \frac{3}{4\pi a^3} \int_{\text{sphere}} d\vec{u}\;\; u^2\varepsilon^2 + u^2\mu^2(1-\varepsilon^2)$$

$$\frac{3}{4\pi a^3} \left\{ \frac{a^5}{5}\varepsilon^2 + \frac{a^5}{5}\frac{1}{3}(1-\varepsilon^2) \right\} 4\pi$$

$$= -Q^2\left(\frac{1}{5} + \frac{2}{5}\epsilon^2\right)$$

$$= \frac{Q^2}{5}\left(1 + 2\epsilon^2\right)$$

$$\langle(\hat{z}\cdot\vec{E}_D)^2\rangle = \frac{3}{4\pi\epsilon^2 a^3}\int_{\text{ellipsoid}} d\vec{x}\; z^2$$

$$= \frac{3}{4\pi\epsilon^2 Q^2}\,\epsilon^2 \int_{\text{sphere}} d\vec{u}\; a^2 u^2$$

$$= \frac{3}{4\pi Q^2}\left\{\frac{a^5}{5}\,\frac{1}{3}\right\}4\pi$$

$$= \frac{a^3}{5} \qquad \text{expect } \frac{1}{5}a^2 -$$

$$4\left\{\langle(\hat{d}\cdot\vec{E}_D)^2\rangle - \langle\vec{E}_D^2\rangle\right\}$$

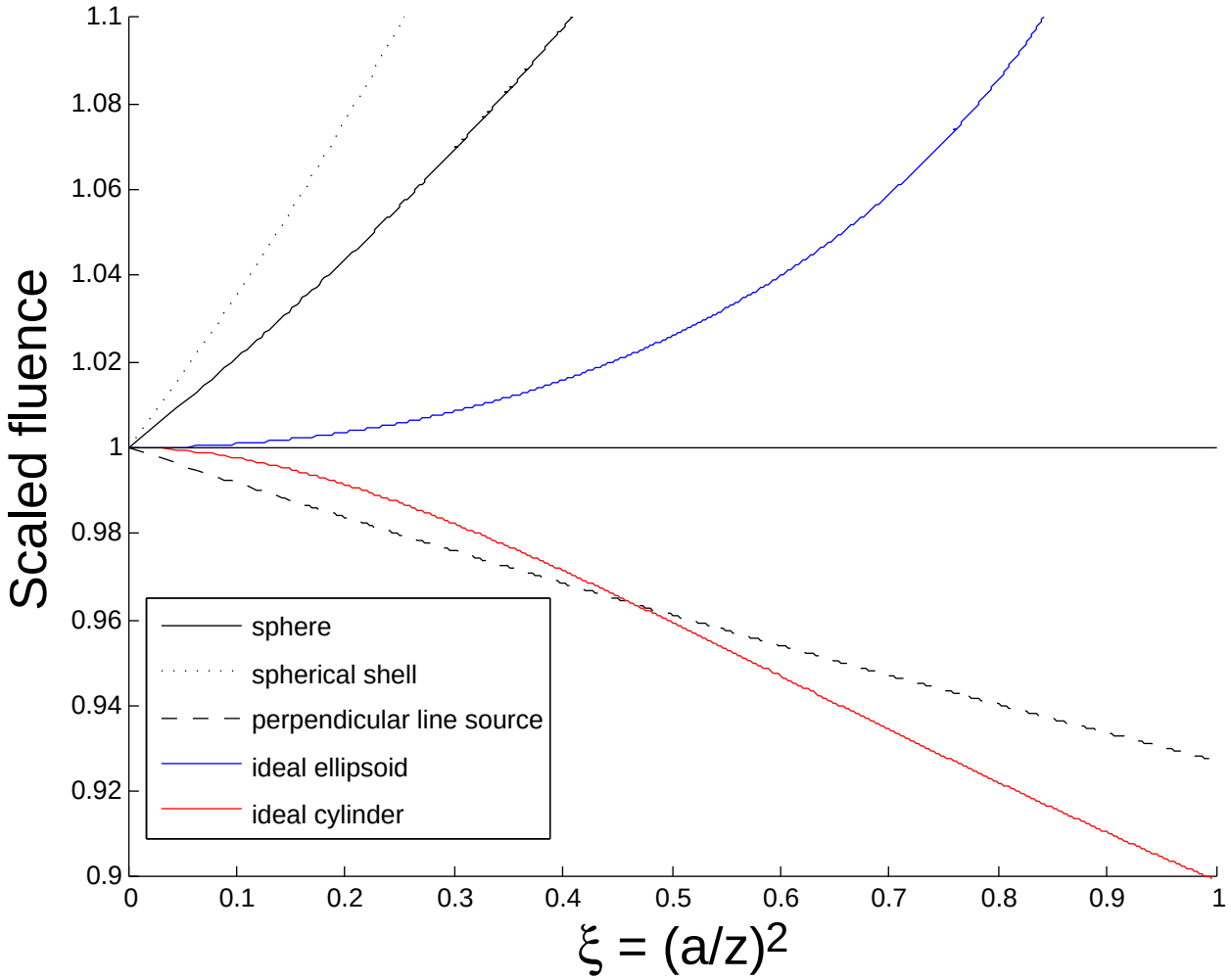
$$\frac{a^3}{5}\left\{4 - (1+2\epsilon^2)\right\}$$

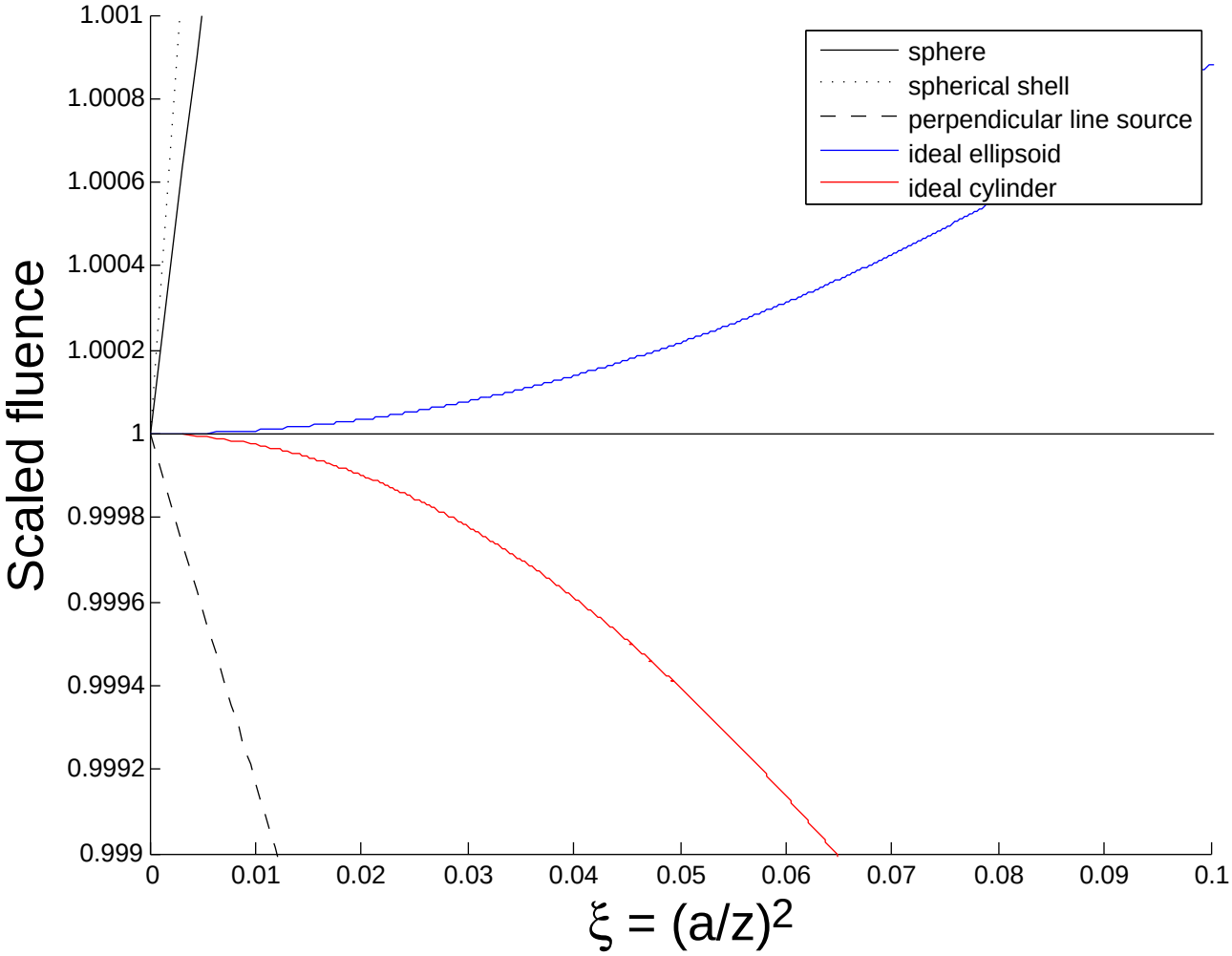
$$= \frac{Q^2}{5}\left\{3 - 2\epsilon^2\right\}$$

So, if $3 - 2\epsilon^2 = 0$

$$\epsilon^2 = \frac{3}{2}$$

There should be no second order term.


Scaled fluence
1.1
1.08
1.06
1.04
1.02
1
0.98
0.96
0.94
0.92
0.9
0
0.1
0.2
0.3
0.4
0.5
0.6
0.7
0.8
0.9
1
ξ = (a/z)2
sphere
spherical shell
perpendicular line source
ideal ellipsoid
ideal cylinder


Scaled fluence
1.001
1.0008
1.0006
1.0004
1.0002
1
0.9998
0.9996
0.9994
0.9992
0.999
0
0.01
0.02
0.03
0.04
0.05
0.06
0.07
0.08
0.09
0.1
ξ = (a/z)2
sphere
spherical shell
perpendicular line source
ideal ellipsoid
ideal cylinder

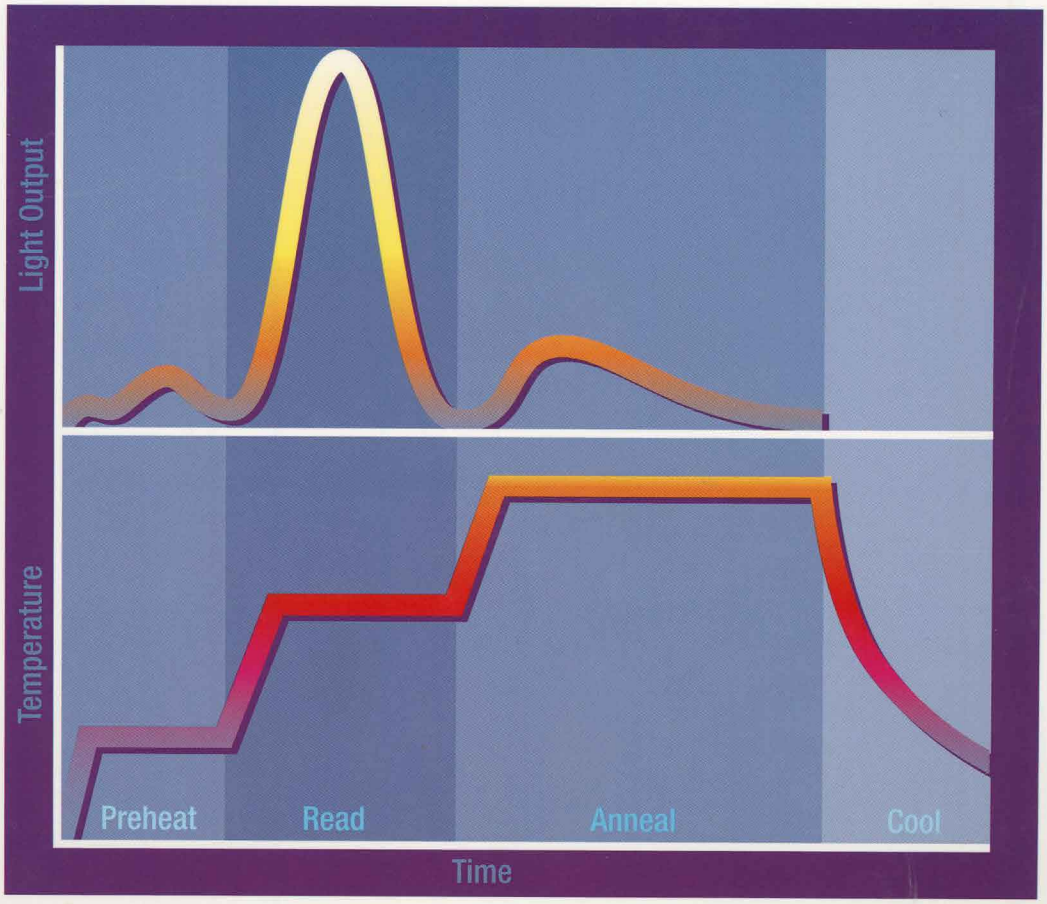
PHYSICS TEXTBOOK

P52

WILEY-VCH

Frank Herbert Attix

Introduction to Radiological Physics and Radiation Dosimetry



D. An Alternative Definition of Fluence

Chilton (1978, 1979) has proven the validity of an alternative definition of fluence, namely:

> The fluence at a point P is numerically equal to the expectation value of the sum of the particle track lengths (assumed to be straight) that occur in an infinitesimal volume dV at P, divided by dV.

This statement was shown to be true for nonisotropic as well as isotropic fields, irrespective of the shape of the volume. Thus one need not require a spherical volume to define fluence in this way. Moreover this definition lends itself to dosimetry calculations by the Monte Carlo method.

E. Planar Fluence

Planar fluence is the number of particles crossing a fixed plane in either direction (i.e., summed by scalar addition) per unit area of the plane. The name "planar fluence" was given to it by Roesch and Attix (1968), who also defined a vector-sum quantity corresponding to the planar flux density that they called the *net flow*, that is, the number of particles per unit time passing through unit area of the plane in one sense (say side A to side B) *minus* those going the other way ($B \rightarrow A$). This quantity is of little dosimetric relevance, however. Although vectorial methods are convenient for field calculations, as shown by Rossi and Roesch (1962) and Brahme (1981), radiation dosimetry finally requires scalar, not vector, addition of the effects of individual particles.

The concept of net flow was first put forward in the context of radiological physics by Whyte (1959). He dealt with the flow of energy carried by particles, and applied the name "plane intensity" to the vector sum of the energy flowing through a fixed plane. Whyte's illustrative diagram is reproduced in Fig. 1.5, which will be used here to discuss fluence vs. planar fluence.

A plane homogeneous beam of radiation is shown perpendicularly incident upon a flat scattering (but not absorbing) foil. All particles are shown for simplicity being scattered through the same angle θ, at any azimuthal angle β. A spherical and a flat detector of equal cross-sectional area are shown positioned above and below the foil. The flat detector is oriented parallel to the foil, and thus is perpendicular to the beam of incident radiation. The number of incident particles striking each detector above the foil is clearly the same, and the planar fluence with respect to the plane of the flat detector is identical to the fluence in the same field. This can only be true in a plane-parallel beam, orthogonal to the flat detector, as shown.

The number of scattered particles striking the spherical detector below the foil is $|1/\cos\theta|$ times the number striking the flat detector, which in turn is the same as the number it received above the foil. Thus the fluence is $|1/\cos\theta|$ times the planar fluence. This increase in fluence contributes to an effect sometimes seen in broad-beam geometry, in which the fluence behind an attenuating layer can be greater than that incident (see Chapter 3, Section V).

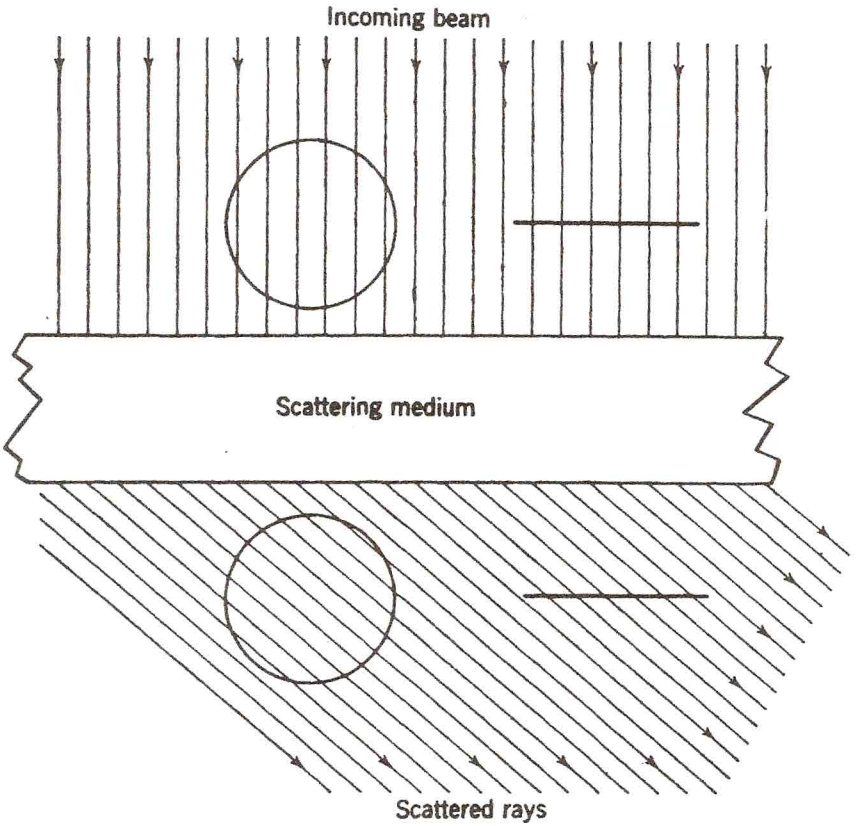


FIGURE 1.5. Particles scattered through an angle θ in a nonabsorbing foil, illustrating effect on fluence vs. planar fluence. (After Whyte, 1959.)

The effect of radiation striking a detector depends on the penetrating power of the radiation. Consider the two limiting cases in which: (a) the radiation penetrates straight through both detectors shown in Fig. 1.5, and (b) the radiation is stopped and absorbed in both detectors. For both cases we will take the response of the detector to be proportional to the energy imparted in it.

For case (a) we will also assume that the energy imparted is approximately proportional to the total track length of the rays crossing the detector, or to the fluence according to the Chilton definition. This assumption is by no means proven at this point, but it is reasonably good for homogeneous radiation crossing a small, easily penetrated detector. The spherical detector in Fig. 1.5 will read more below the foil in proportion to the number of rays striking it, which is $|1/\cos\theta|$ times the number striking it above the foil. The average length of the paths in the sphere is obviously the same above and below. The number of rays striking the flat detector is the same above and below the foil, but the length of each track within the detector is $|1/\cos$

$\theta|$ times as long below as it is above the foil. Thus the total track length in the flat detector is also $|1/\cos\theta|$ times as great below the foil as above. Evidently, then, both of the detectors read more by the factor $|1/\cos\theta|$ below the foil for the case of penetrating radiation.

Now consider the easily stopped radiation in case (b). The sphere again reads more below the foil than above by the factor $|1/\cos\theta|$, since that is the factor by which the number of striking rays increases, and each ray deposits all its energy. The flat detector, however, responds *the same* below as above the foil, since the number of rays striking it does not change, and track length is now irrelevant.

In other words, for the case of *nonpenetrating* rays striking a flat detector or other absorber, the energy deposited is related to the planar fluence with respect to the detector plane, instead of the fluence. Only in this case does planar fluence arise as a practical concept in dosimetry.

To quantify planar fluence for multidirectional radiation fields, we consider a particular great circle of the small sphere at P in Fig. 1.2: the one that is fixed in the x–y plane. The number of particles per unit time, having energies between E and $E + dE$, that pass through the element of solid angle $d\Omega = \sin\theta\, d\beta\, d\theta$ at the given angles θ and β before passing through the fixed great circle, per unit area of the circle, can be expressed [from Eq. (1.15)] as

$$\varphi'(\theta, \beta, E)|\cos\theta|\, d\Omega\, dE \tag{1.27}$$

The absolute value of $\cos\theta$ means that the particles are counted positively, regardless of the direction from which they come.

Inserting the factor $|\cos\theta|$ into Eq. (1.16) gives an equation for the planar flux density φ_p with respect to the x–y plane in Fig. 1.2:

$$\varphi_p = \int_{\theta=0}^{\pi}\int_{\beta=0}^{2\pi}\int_{E=0}^{E_{\max}} \varphi'(\theta, \beta, E)|\cos\theta|\, \sin\theta\, d\theta\, d\beta\, dE \tag{1.28}$$

and the planar fluence Φ_p is simply the time integral of φ_p over any desired time interval, as in Eq. (1.7).

In an isotropic field of radiation we have $\varphi_p = \frac{1}{2}\varphi$; hence $\Phi_p = \frac{1}{2}\Phi$ for a given time interval. The factor $\frac{1}{2}$ is obtained as the ratio of Eq. (1.28) to Eq. (1.16), which can be simplified in steps, as in Eqs. (1.23)–(1.25) to give

$$\frac{\varphi_p}{\varphi} = \frac{\displaystyle\int_{\theta=0}^{\pi} |\cos\theta|\sin\theta\, d\theta}{\displaystyle\int_{\theta=0}^{\pi} \sin\theta\, d\theta} = \frac{\sin^2\theta\,|_0^{\pi/2}}{-\cos\theta\,|_0^{\pi}} = \frac{1}{2} \tag{1.29}$$

For the same case the net flow through the x–y plane is zero, since

$$\int_{\theta=0}^{\pi} \cos\theta\, \sin\theta\, d\theta = 0 \tag{1.30}$$

4.2.1 Planar fluence

Planar fluence is often confused with fluence. Therefore it is important to clarify that point now. Planar fluence is the number of particles that strike a surface irrespective of direction. It may be calculated using the fluence from the relation,

$$\varphi_i(\vec{x}, E, t) = \frac{1}{4\pi} \int \mathrm{d}\Omega \left(\frac{\mathrm{d}n_i(\vec{x}, \vec{\Omega}, E, t)}{|\vec{\Omega} \cdot \vec{n}_S|} \right) , \tag{4.14}$$

where $\vec{n}_S$ is the inward normal to the surface. Often, one is interested in separating the planar fluence based on its orientation with respect to the surface. In this case, we write,

$$\mathrm{d}n_i(\vec{x}, \vec{\Omega}, E, t) = \mathrm{d}n_i^+(\vec{x}, \vec{\Omega}, E, t) + \mathrm{d}n_i^-(\vec{x}, \vec{\Omega}, E, t) , \tag{4.15}$$

for the ingoing and outgoing parts.

This planar fluence is also sometimes called the *total scalar flux*. It is also possible to define the *net scalar flux* as,

$$\mathrm{d}n_i(\vec{x}, \vec{\Omega}, E, t) = \mathrm{d}n_i^+(\vec{x}, \vec{\Omega}, E, t) - \mathrm{d}n_i^-(\vec{x}, \vec{\Omega}, E, t) . \tag{4.16}$$

It is important to note that planar fluence and fluence are fundamentally different. Fluence is a point function defined as a volumetric quantity, even in the limit that this volume is made vanishingly small. The ICRU definition obscures this fact, which is probably the source of confusion, but Chilton's definition makes it clear. Planar fluence is a surface-related quantity, and embeds within it, information about the source. This is best illustrated by an example.

Consider a uniform, monodirectional fluence, Φ and a right cylindrical detector with radius a and depth d. The integrated inward flux of the detector and the fluence are related by,

$$\Phi = \frac{n(\theta)}{\pi a(a\cos\theta + d|\sin\theta|)} , \tag{4.17}$$

where $n(\theta)$ is the number of particles measured with orientation θ, θ is the angle the normal the flat face of the detector with respect to the incident fluence direction. Thus, a measurement of planar fluence can yield the value of the fluence. Equation (4.17) appears to be singular in the limit $d \to 0, \theta \to \pi/2$. However, in this limit, $n \to 0$ as well. Φ really is a well-defined number in this context, and it is a constant in this example, independent of orientation.

4.2 Radiation equilibrium

All radiometric quantities measure particle fluence in some fashion, as fluence is the most fundamental quantity describing a radiation field, from which all others may be derived. The statement of radiation equilibrium is as follows, assuming we have a fluence measuring device that may or may not have a directional dependence in a monodirectional field, is sensitive to only one of the particle species in the radiation field, and is sensitive to only one energy component, E, of the radiation field . We shall call this detector $D_i(E, \vec{\Omega}_D)$. We may also consider that there may be an externally defined constant vector (gravity, magnetic field, electric field, some aspect of the source) that provides a coordinate system orientation for the detector's $\vec{\Omega}_D$.

A region of space, V, is considered to be in a state of radiation equilibrium with respect to particle species i, if that radiation field is constant in time, and any measurement of $\Phi(\vec{x}, E)$ is invariant with respect to translations of the detector from $\vec{x}$ to $\vec{x}'$ within V. In this case we conclude that $\Phi(\vec{x}, E) = \Phi(E)$ within V.

A second statement is required for isotropic radiation.

A region of space, V, is considered to be in a state of isotropic radiation equilibrium with respect to particle species i, if that radiation field is constant in time, and any measurement of $\Phi(\vec{x}, E)$ is invariant with respect to translations of the detector from $\vec{x}$ to $\vec{x}'$ within V and invariant with respect to rotations of the detector, $\vec{\Omega}_D \rightarrow \vec{\Omega}'_D$ in V, providing that the detector response is uniform with respect to externally defined directions (gravity, electric and magnetic fields). In this case we conclude that $\Phi(\vec{x}, E) = \Phi(E)$ within V, and that the source is isotropic.

The consequences of radiation equilibrium are central to radiation dosimetry. Consider the first case, where the radiation field has a direction associated with it, but the detector is insensitive to it's orientation within this fields. This idealization is closely approximated by good radiation detectors. Let us imagine that we have such an ideal detector, and it is spherical in shape, clearly insensitive to direction. Moreover, the size of this detector, so long that is fits in V always measures the same fluence. Now, take an arbitrarily-shaped detector, still that fits in V. Form this arbitrary shape from spherical detectors of smaller and smaller size, so that in the limit, the volume of this aggregation of spheres equals the volume of the arbitrarily-shaped detector and the shape is the same in the limit of small spheres. (See Figure 4.1.) Each one of these spheres measures the same fluence, and hence, so the the arbitrarily shaped one. The conclusion is that an ideal detector is independent of its shape and orientation in a radiation field that is in equilibrium.

Remarkably, conditions of near particle equilibrium and near ideal detectors do exist in radiation physics and enable accurate dosimetry to be done without excessive concern about exact detector positioning and orientation. (They still are, however, important.) Real detectors are prone to positioning and orientation differences. Thankfully, they are minimized so long as the radiation fields are near equilibrium.

Finally, sources that produce uniform fields maybe be realized by several means, first as mathematical ideals, and nearly, as physical constructs. An isotropic source may be produced at the center of a very large sphere with a uniform surface source, or uniform volume source ($R \gg \Delta a$). A monodirectional source may be produced by a point source moved a very long distance away from the detector ($D \gg \Delta a$). A uniform source with angular dependence may be produced by a very large plane source ($D \gg \Delta a$), of some uniform thickness with a source distributed through its volume. Self-shielding will cause an angular dependence in

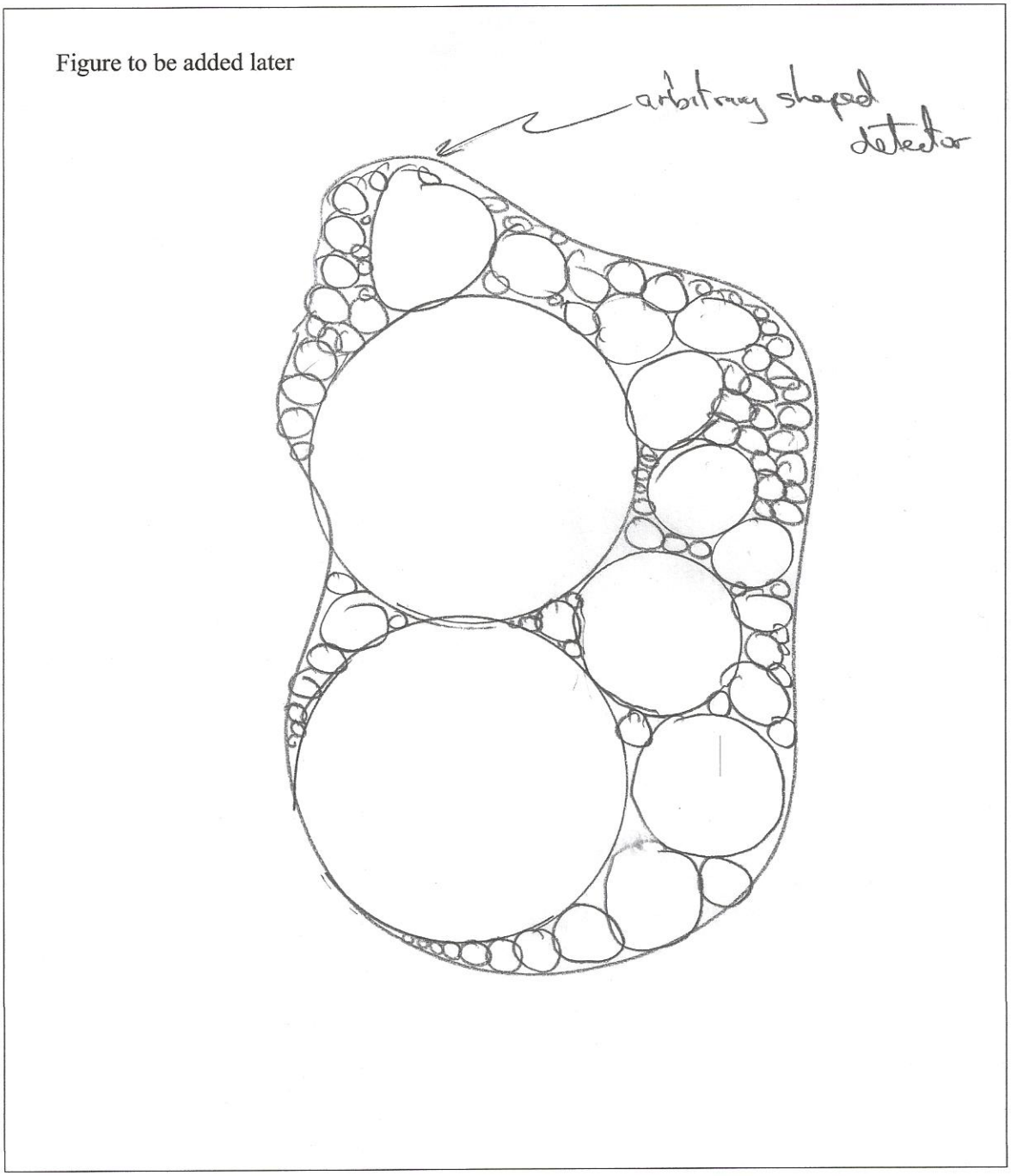


Figure 4.1: An ideal detector of arbitrary shape may be made of up small spherical ideal detectors.

4.5 Fano's theorem

Consider the time-independent transport equation in a uniform medium,

$$\vec{\Omega}\cdot\vec{\nabla}n(\vec{x},\vec{\Omega},E)+\Sigma(\vec{x},E)n(\vec{x},\vec{\Omega},E) = S(\vec{x},\vec{\Omega},E)+\int_0^\infty \mathrm{d}E' \int_{4\pi} \mathrm{d}\Omega'\, \Sigma_s(\vec{x},E'\rightarrow E,\vec{\Omega}\cdot\vec{\Omega}')n(\vec{x},\vec{\Omega}',E') \;, \tag{4.40}$$

where $n(\vec{x},\vec{\Omega},E)$ is the total scalar flux, $\Sigma(\vec{x},E)$ is the "out-scattering" macroscopic cross section ("out in the sense of out from $(E,\vec{\Omega})$ to a different energy and/or direction, $\Sigma_s(\vec{x},E'\rightarrow E,\vec{\Omega}\cdot)$ is the "in-scattering" macroscopic cross section ("in" in the sense of from $(E',\vec{\Omega}')$ to $(E,\vec{\Omega})$, and $S(\vec{x},\vec{\Omega},E)$ is the source. Assume that the local density, $\rho(\vec{x})$ is everywhere non-zero, and that Σ, Σ_s, and S are proportional to the local ρ. That is,

$$\begin{aligned} \Sigma(\vec{x},\vec{\Omega},E) &= \rho(\vec{x})\mu(\vec{\Omega},E) \\ \Sigma_s(\vec{x},E'\rightarrow E,\vec{\Omega}\cdot\vec{\Omega}') &= \rho(\vec{x})\mu_s(E'\rightarrow E,\vec{\Omega}\cdot\vec{\Omega}') \\ S(\vec{x},\vec{\Omega},E) &= \rho(\vec{x})s(\vec{\Omega},E) \end{aligned} \tag{4.41}$$

(The macroscopic usually are unless the atomic composition changes. We are making an assumption about the source, in this case.) Divide by the local density to give,

$$\frac{\vec{\Omega}\cdot\vec{\nabla}n(\vec{x},\vec{\Omega},E)}{\rho(\vec{x})}+\mu(E)n(\vec{x},\vec{\Omega},E) = s(\vec{\Omega},E)+\int_0^\infty \mathrm{d}E' \int_{4\pi} \mathrm{d}\Omega'\, \mu_s(E'\rightarrow E,\vec{\Omega}\cdot\vec{\Omega}')n(\vec{x},\vec{\Omega}',E') \;. \tag{4.42}$$

Now consider the tentative solution for the total scalar flux,

$$\mu(E)n_0(\vec{\Omega},E) = s(\vec{\Omega},E)+\int_0^\infty \mathrm{d}E' \int_{4\pi} \mathrm{d}\Omega'\, \mu_s(E'\rightarrow E,\vec{\Omega}\cdot\vec{\Omega}')n_0(\vec{\Omega}',E') \;, \tag{4.43}$$

with the same $\mu(E)$, $\mu_s(E'\rightarrow E,\vec{\Omega}\cdot\vec{\Omega}')$, and $s(\vec{\Omega},E)$.

Since there should be a unique solution to the transport equation, this solution, independent of $\vec{x}$ is also a solution to the space-dependent equation 4.42. Therefore, invoking this property of uniqueness, we may identify $n(\vec{x}, \vec{\Omega}, E)$ in equation 4.42 with $n_0(\vec{\Omega}, E)$ in equation 4.43.

Therefore, under the conditions specified by expressions 4.41,

$$\vec{\nabla} n(\vec{x}, \vec{\Omega}, E) = 0 \ . \tag{4.44}$$

In other words, if the macroscopic cross sections and the source are proportional to density, the total scalar flux is independent of $\vec{x}$, irrespective of how the density changes. In addition, since fluence may be derived from total scalar flux via equation 4.14.

This is a powerful result and, along with the concept of radiation equilibrium has far-reaching consequences for radiation dosimetry. It has already been argued that if radiation equilibrium exists in some volume of space, measurements become insensitive to position of the detector. Now, we find that under these conditions, the density of the medium may change arbitrarily, so long as the source and scattering physics are proportional to density. Again, we shall find that conditions of radiation equilibrium are not uncommon in our applications. Therefore, as we shall see shortly, we we wish to determine the dose to water (for example) in a region of near equilibrium, we may use a detector of any density, so long as the atomic composition is the same. Air-filled ionization chambers are such a device. It is truly remarkable that we may take an ionization chamber measurement in water and measure the dose to within an accuracy of a few percent. The few-percent departures account for departures from equilibrium and atomic composition, and may be calculated or measured to within an accuracy of a percent or so with good confidence. (We shall discuss this topic in detail later.) Were this not the case, the entire field of radiation dosimetry, that requires accuracy to within a percent or so for medical physics purposes, would be on very shaky ground. Fortunately, dosimetry methods are very robust, and obtaining sufficient accuracy is always possible in the field with enough care and practice.

4.3 Fluence-related radiometric quantities

Recall, from Section 4.1

Fluence $\varphi_i(\vec{x}, E, t)$
↑ l.c. "phi"

i: particle-type index
$\vec{x}$: position
E: Energy (kinetic)
t: time

new definition

(4.3.1) energy fluence $\Psi_i(\vec{x}, E, t) \equiv E\varphi_i(\vec{x}, E, t)$ (4.18)
↑
l.c. "psi"

why? Ψ_i is a measure of the ability to effect radiological change.
φ_i gives the "amount" of radiation
Ψ_i takes φ_i and applies the action E

common integrated energy fluence expressions

(4.19) $\Psi(E, t_i, t_f) = \int_{t_i}^{t_f} dt\, E\varphi(E,t)$
↑ u.c. psi

(4.20) $\Psi(\epsilon) = \int_{-\infty}^{\infty} dt\, E\varphi(E,t)$

(4.21) $\Psi(E_i, E_f) = \int_{E_i}^{E_f} dE\, E\dot{\varphi}(E,t)$

} note $i, \vec{x}$ suppressed, but understood to be there

(4.22) $\Psi = \int_{-\infty}^{\infty} dE \, F\Phi(E)$

If the fluence is monoenergetic, then

(4.23) $\Psi = E_0 \bar{\Phi}(E_0)$

Next

γ's { Chapter 1.1 Basic photon interaction processes

applies to γ's { 4.4 Attenuation, radiological pathlength

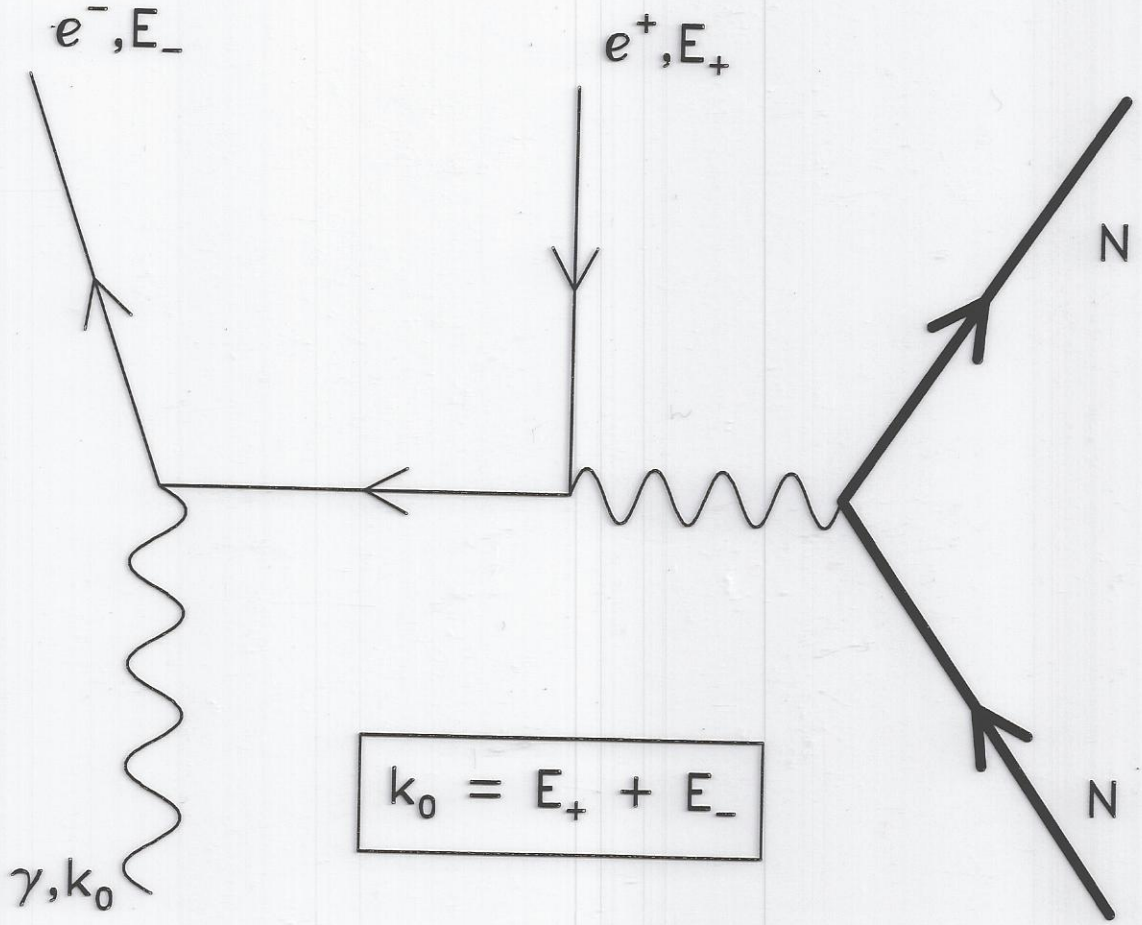
e^- { 2.1 Catastrophic e^- interaction (hard scattering)
2.2 Statistically grouped e^- interactions (soft scattering)



Dose models

1.1 Basic Photon Interaction Process

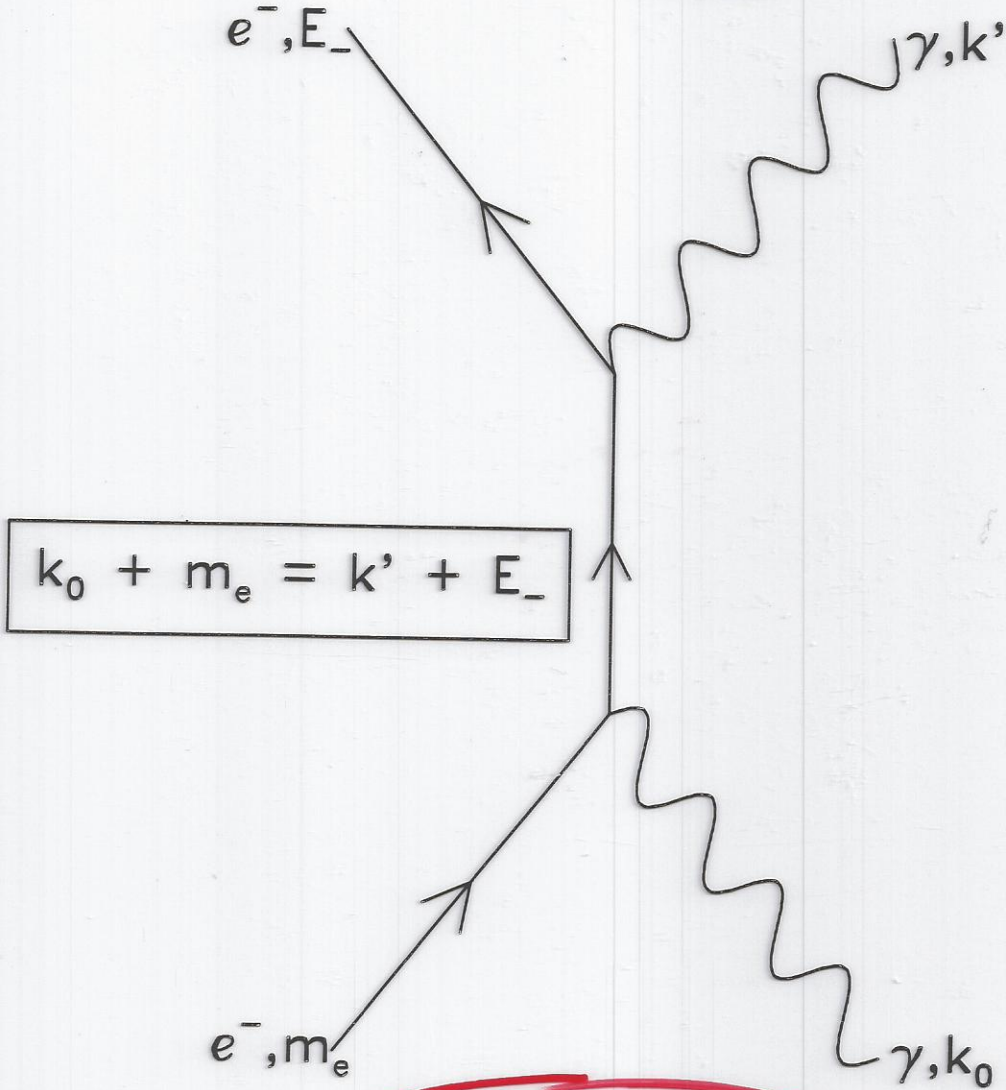
- scales like Z^2
- triplet distributions ignored, incl. in total σ_{pair}
- < 50 MeV Storm + Israel
  > 50 MeV ERL
- default $\Phi = m_0c^2/R_0$



pair production

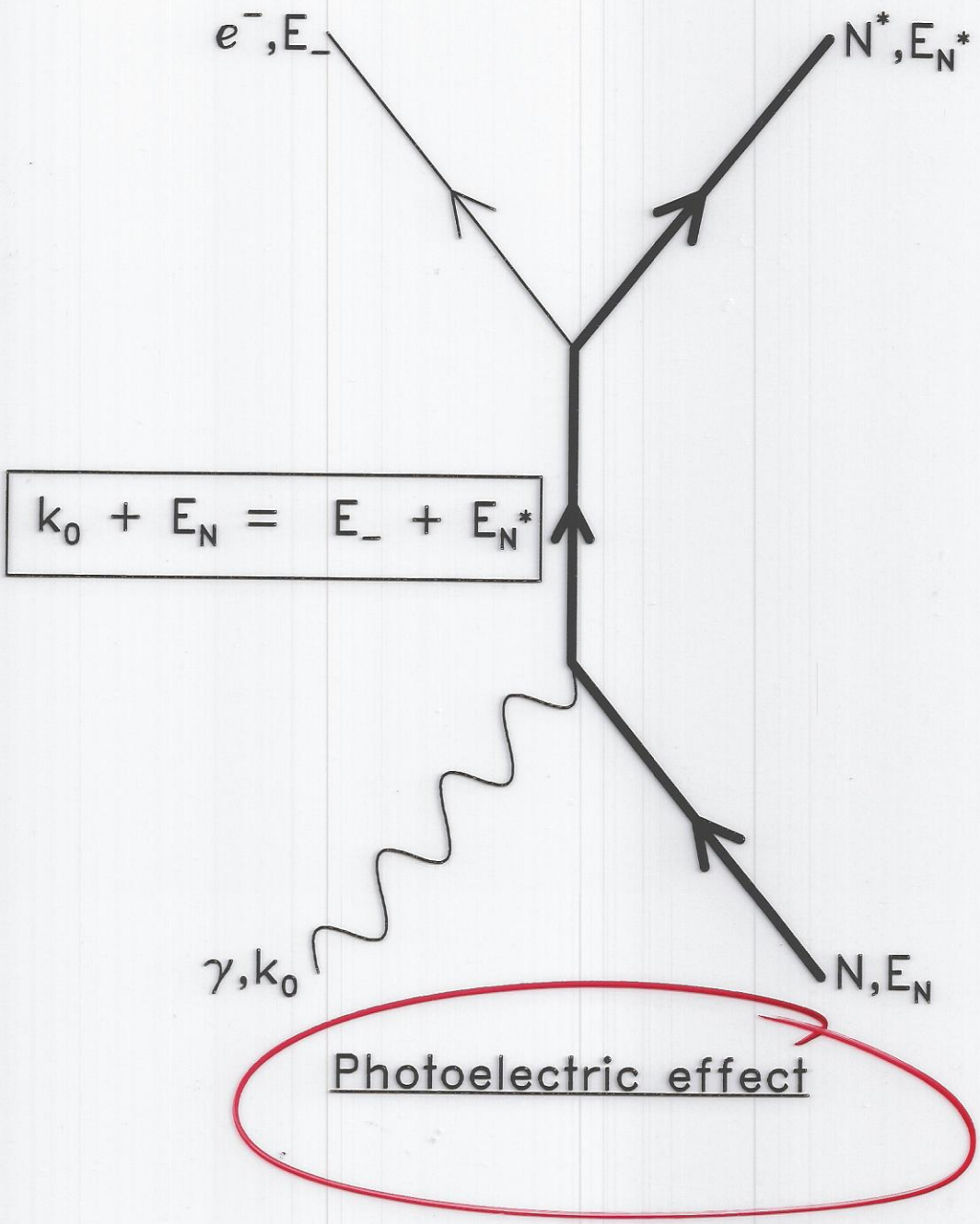
- threshold $\geq 2m_0c^2$
- $\sigma \sim \log k$
  $k \to \infty$

- Klein-Nishina $d\sigma$
- e^- is "free" good to $E \gg E_K$
- scales like Z
- $\sim 1/k$ for $k \to \infty$, const for $k \to 0$

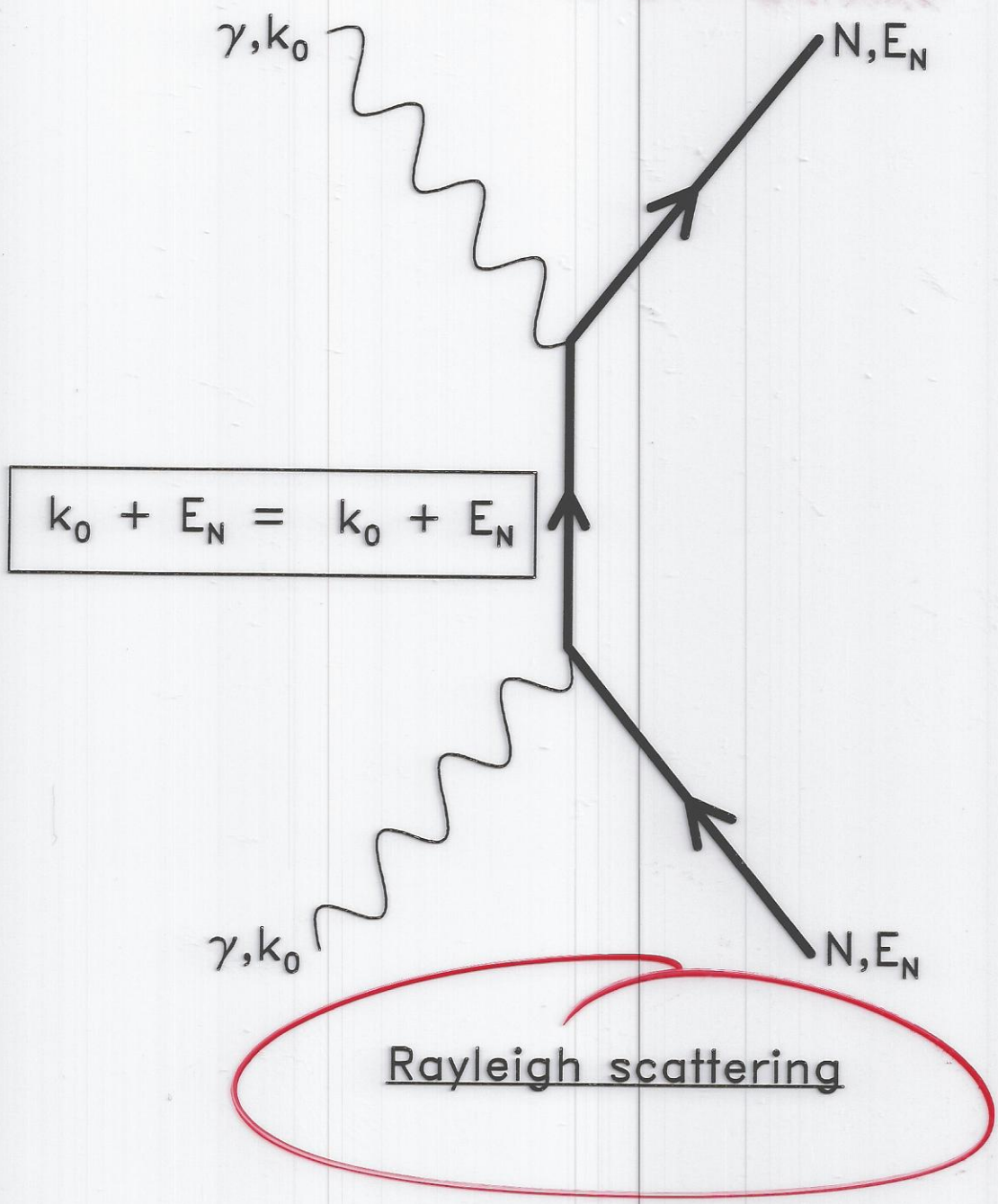


Compton scattering

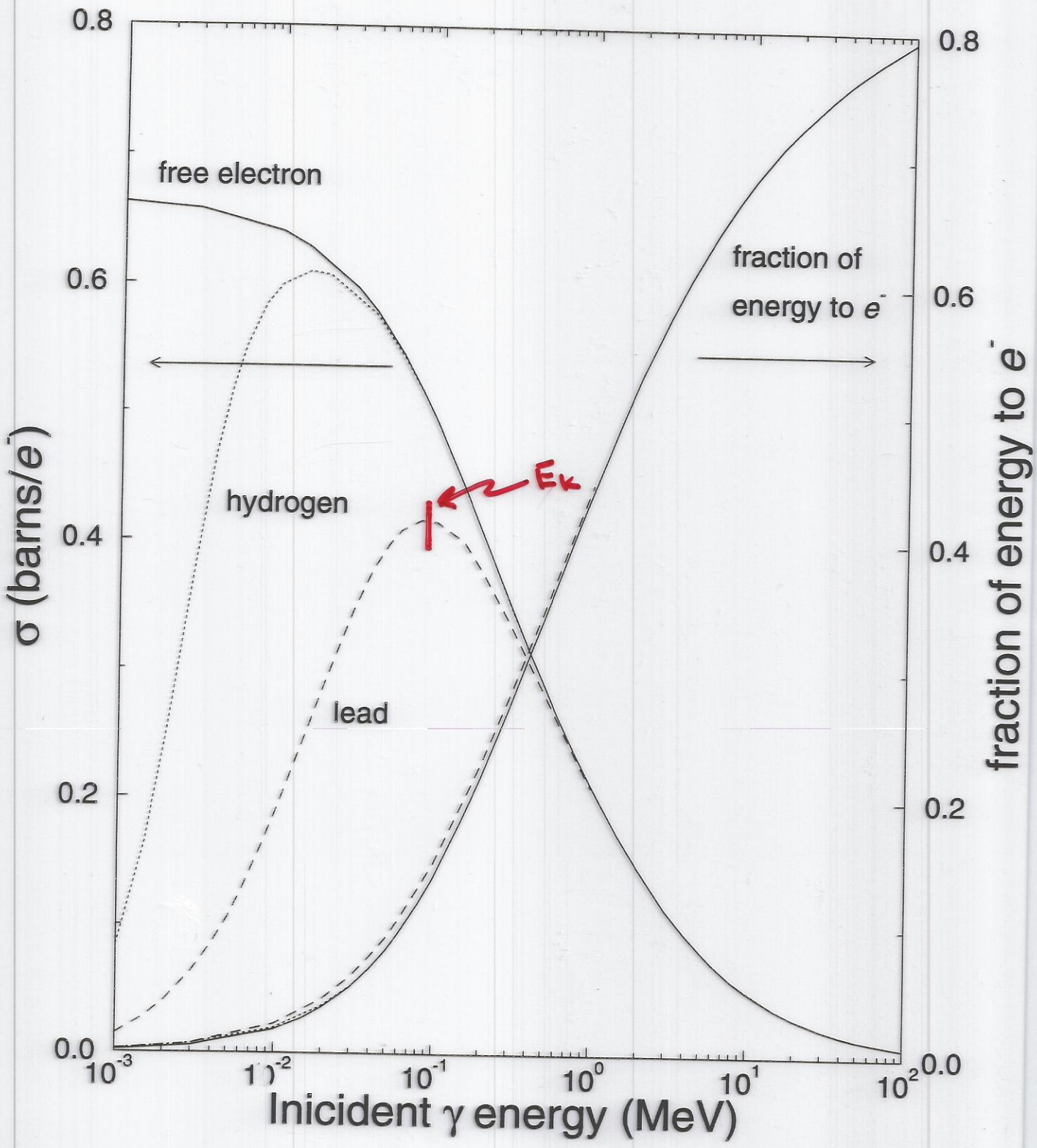
- scales like $Z^4 \rightarrow Z^{4.6}$, depending on k_0
- $\Theta = 0$!
- K_α & K_β fluorescent γ's possible
- $\sigma \propto \frac{Z^4}{E^3}$ good for many applications

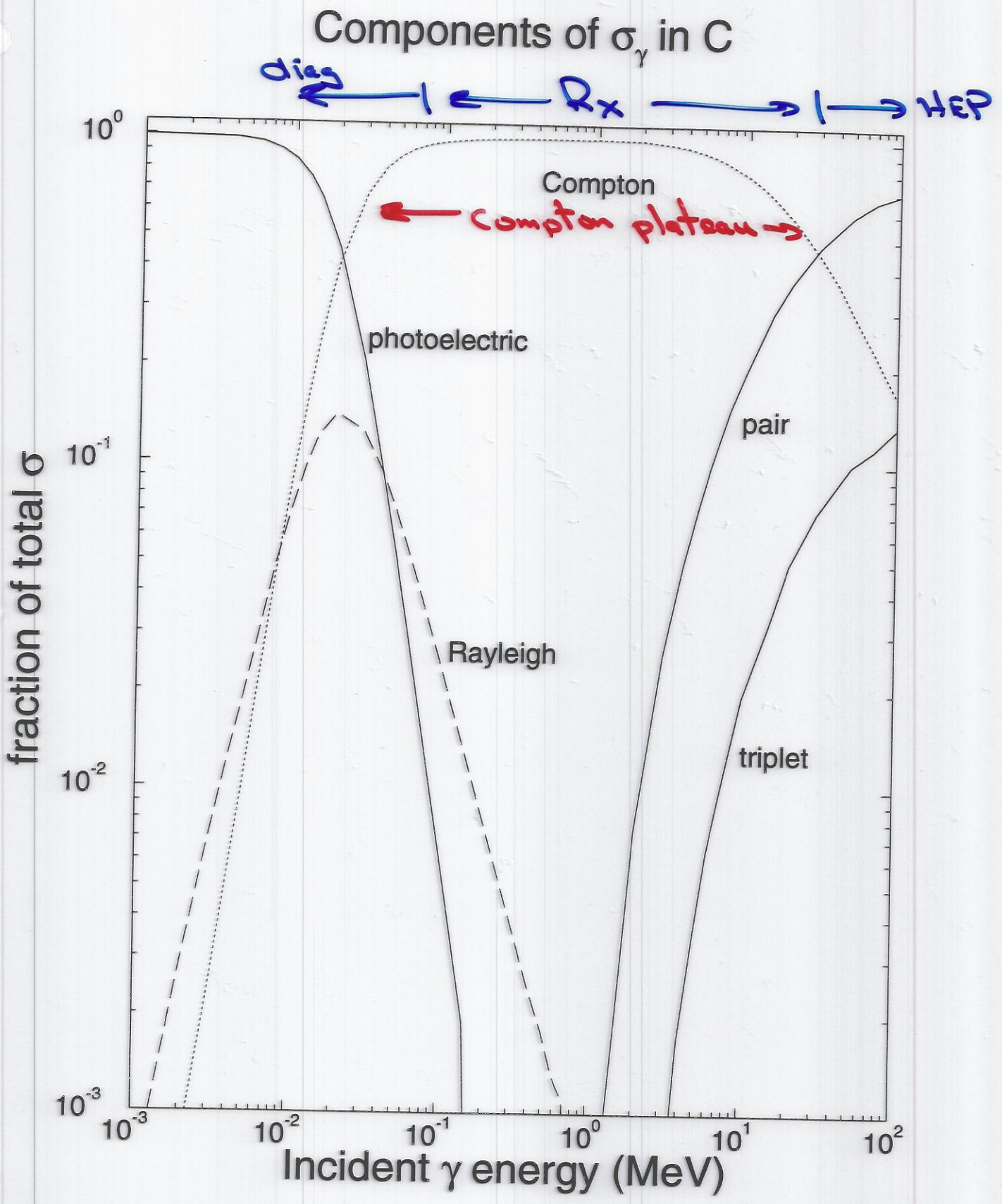


- elastic process
- independent atom approx.
- Z^2 (small θ) $\rightarrow$ Z^3 (large θ)

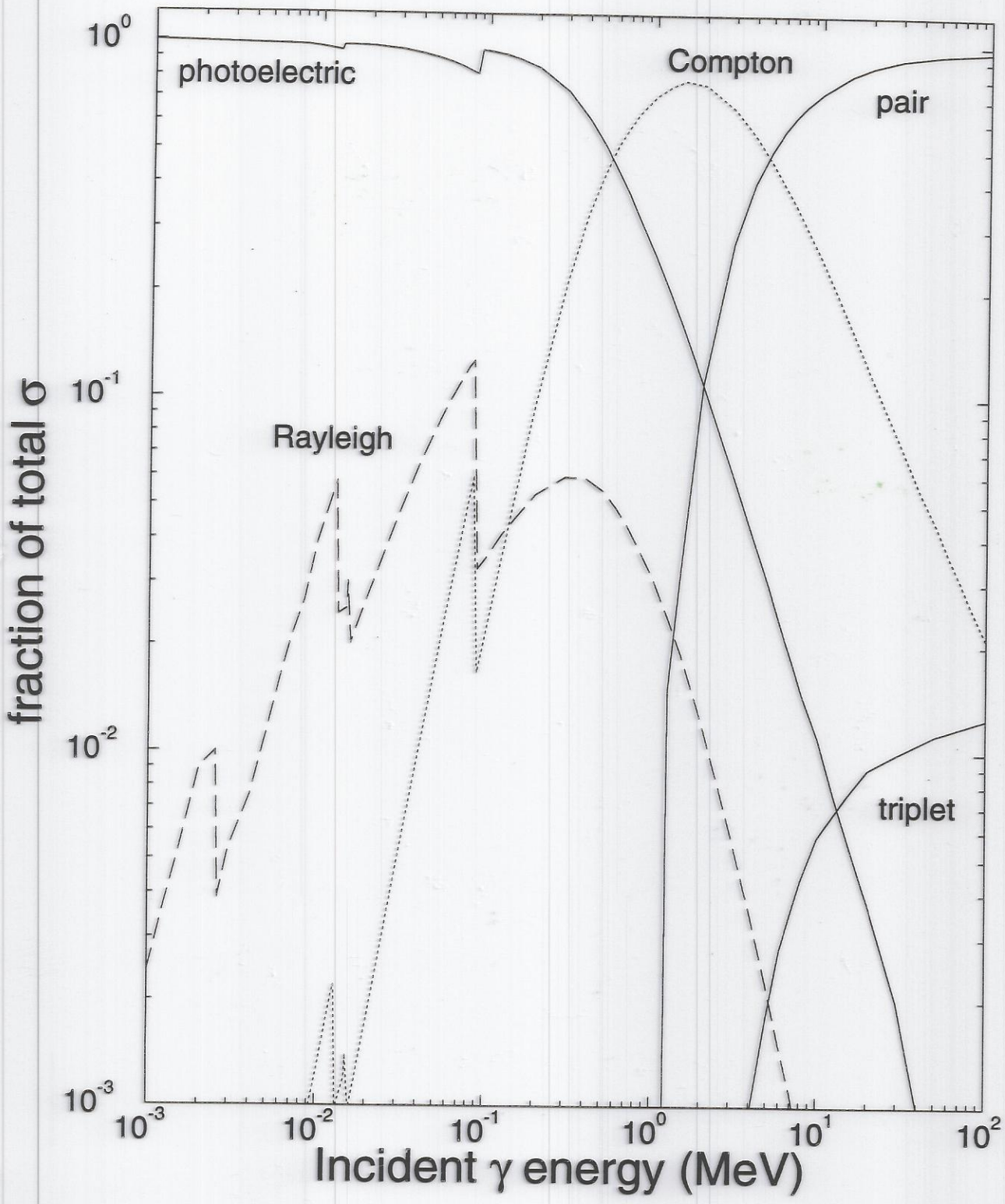


Effect of binding on Compton cross section

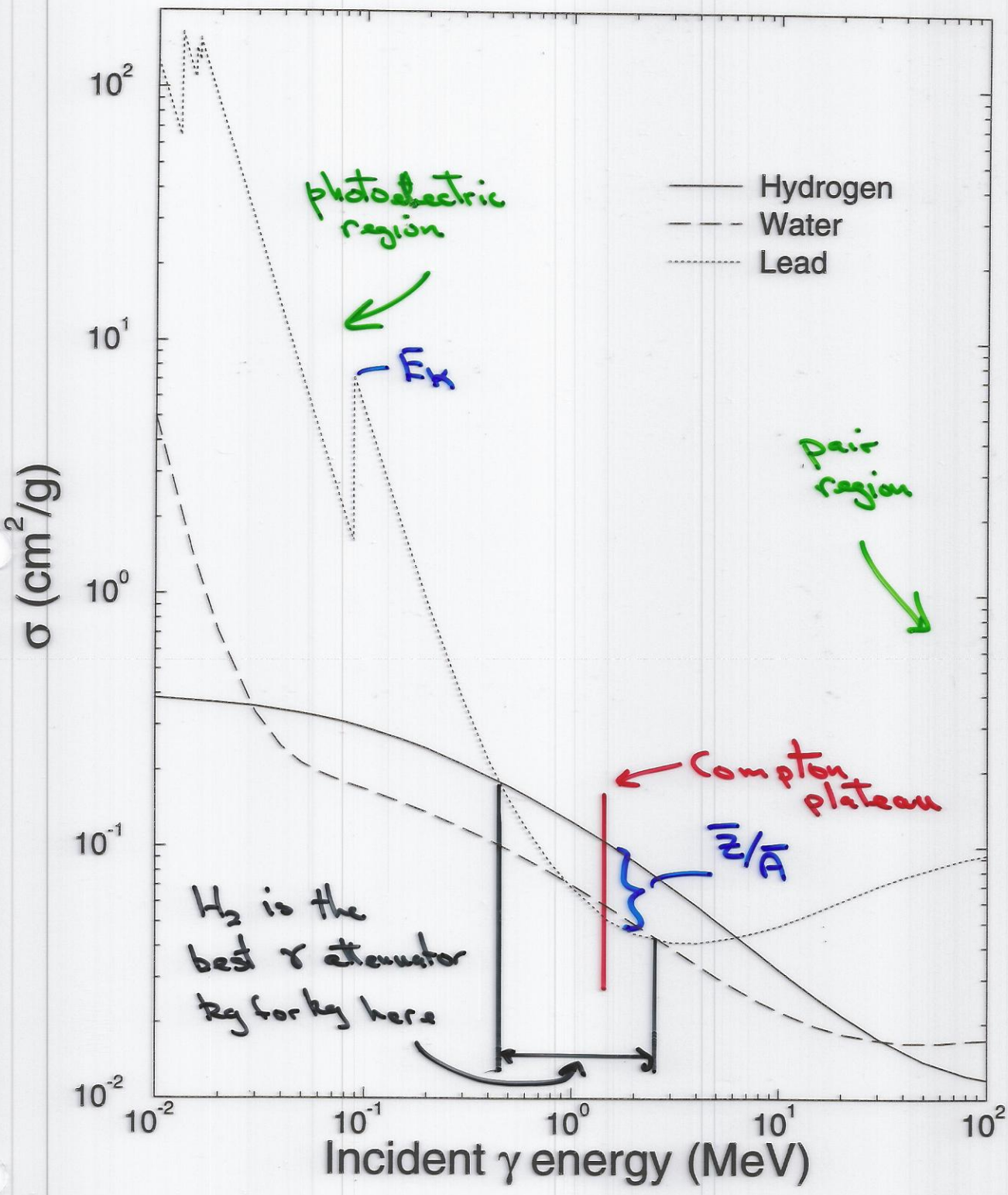



Components of σ_γ in C
diag
Rx
HEP
Compton
Compton plateau
photoelectric
pair
Rayleigh
triplet
fraction of total σ
Incident γ energy (MeV)
10^0
10^{-1}
10^{-2}
10^{-3}
10^{-3}
10^{-2}
10^{-1}
10^0
10^1
10^2

Components of σ_γ in Pb



Total photon σ *vs* γ-energy



4.4 Attenuation, radiological pathlength

We start by considering the classical derivation of the attenuation law.

Imagine a monoenergetic, monodirectional beam of particles aligned with the $\hat{z}$-axis, with energy E, with infinitesimal cross sectional area $\mathrm{d}B$ impinging normally on a semi-infinite plane of matter. The matter is composed homogeneously of identical "scattering centers" with cross sectional area $\sigma(E)$. At some depth x, the probability of a single particle in the beam interacting with one of the scattering centers is:

$$\mathrm{d}p = n_s(\vec{x})(\mathrm{d}B\mathrm{d}z)\left(\frac{\sigma}{\mathrm{d}B}\right) \ , \tag{4.24}$$

where $n_s(x)$ is the density of scatterers (units: L^{-3}), $n_s(x)\mathrm{d}B\mathrm{d}x$ is the number of scatterers in $\mathrm{d}B\mathrm{d}x$, and σ/B is the fractional area covered by the scatterers. Assuming, for the time being, that the scatterers are atomic centers, we may write,

$$\mathrm{d}p = \rho(\vec{x})\frac{N_\mathrm{A}}{A}\sigma\mathrm{d}z \ , \tag{4.25}$$

where $\rho(\vec{x})$ is the mass density (units: ML^{-3}), N_A is Avogadro's number ($6.023\times10^{23}(\mathrm{mole}^{-1})$ and A is the atomic mass (units: M-mole^{-1}). Therefore, the change in primary fluence is described by,

$$\mathrm{d}\Phi_0(\vec{x}) = -\Phi_0(\vec{x})\mu\rho(\vec{x})\mathrm{d}z \ , \tag{4.26}$$

where

$$\mu = \frac{N_\mathrm{A}}{A}\sigma \ , \tag{4.27}$$

μ is the *mass linear attenuation coefficient* (units: L^2/M). It is a function of the particle energy. It is usually a constant in space unless the atomic composition of the medium changes. The *mass linear attenuation coefficient* or *macroscopic cross section* is

$$\Sigma(\vec{x}) = \rho(\vec{x})\mu \ , \tag{4.28}$$

is sometimes used, but is proportional to the density. We mention it here for convenience, but shall rarely use it.

The integral in expression 4.27 is elementary, yielding,

$$\Phi_0(\vec{x}, E) = \Phi_0(\vec{x}; z = 0, E)\exp\left(-\int_0^z \mathrm{d}z\,\mu(E)\rho(x, y, z')\right) \ . \tag{4.29}$$

The factor,

$$\int_0^z \mathrm{d}z\, \mu(E)\rho(x,y,z') \ , \tag{4.30}$$

is called the *radiological path*.

We often consider the case where the density of the material is a constant. In this case, the above simplifies to:

$$\Phi_0(\vec{x},E) = \Phi_0(\vec{x};z=0,E)e^{-\mu(E)\rho z} \ , \tag{4.31}$$

the most familiar form of the exponential attenuation "law".

4.4.1 Solid angle subtended by a surface

We shall have need for this type of calculation shortly, and establish the notation now.

Consider a surface S, a surface element $\mathrm{d}S$ at $\vec{x}_S$, and its unit normal $\hat{n}(\vec{x}_S)$. The solid angle element of that surface element

$$\mathrm{d}\Omega = \mathrm{d}S\frac{|\hat{n}(\vec{x}_S)\cdot(\vec{x}-\vec{x}_S)|}{|\vec{x}-\vec{x}_S|^3} \ , \tag{4.32}$$

which is just the surface element, divided by the r^{-2} term, times the magnitude of the cosine of the angle between $\hat{n}$ and the vector $\vec{x}-\vec{x}_S$.

The total solid angle of the surface with respect to the point $\vec{x}$ is:

$$\Omega_S = \int_{S_v} \mathrm{d}S\frac{|\hat{n}(\vec{x}_S)\cdot(\vec{x}-\vec{x}_S)|}{|\vec{x}-\vec{x}_S|^3} \ , \tag{4.33}$$

where the integral only includes surface elements that are visible to point $\vec{x}$.

Clearly, the solid angle of any closed surface enclosing $\vec{x}$ is 4π. Also, for closed surfaces, whether or not $\vec{x}$ is located inside the surface, we can relax the visibility criterion, and integrate over the entire surface, as follows.

$$\Omega_S = \left|\int_S \mathrm{d}S\frac{\hat{n}(\vec{x}_S)\cdot(\vec{x}-\vec{x}_S)}{|\vec{x}-\vec{x}_S|^3}\right| \ . \tag{4.34}$$

The absolute value is required because the direction of $\hat{n}$ is arbitrary.

4.4.2 Primary fluence determinations

Distributed volumetric source

Consider an elemental volumetric source, in vacuum, of radiation emitting particles with energy E at a rate $\dot{n}(\vec{x}', \vec{\Omega}, E, t)\mathrm{d}\vec{x}'$. A measurement of fluence at $\vec{x}$ is,

$$\mathrm{d}\varphi_i(\vec{x}, E, t) = \frac{1}{4\pi} \frac{\dot{n}(\vec{x}', \vec{\Omega}_{\vec{x}-\vec{x}'}, E, t)\mathrm{d}\vec{x}'}{(\vec{x}-\vec{x}')^2} \exp\left(- \int_{\vec{x}'}^{\vec{x}} \mathrm{d}l\, \mu(E, l)\rho(l) \right) , \tag{4.35}$$

where the integral over l is the straight-line path from the source element to the point of fluence measurement, and accounts for attenuation. Note that both the material composition and the density of the medium can vary along this path.

Integrating over the source gives

$$\varphi_i(\vec{x}, E, t) = \frac{1}{4\pi} \int_V \frac{\dot{n}(\vec{x}', \vec{\Omega}_{\vec{x}-\vec{x}'}, E, t)\mathrm{d}\vec{x}'}{(\vec{x}-\vec{x}')^2} \exp\left(- \int_{\vec{x}'}^{\vec{x}} \mathrm{d}l\, \mu(E, l)\rho(l) \right) . \tag{4.36}$$

A common example is for a fluence measurement at $\vec{x} = 0$, due to a point, isotropic, monoenergetic source, constant in time, with uniform intervening medium, for which the result is:

$$\Phi(E) = n_0 \frac{e^{-\mu(E)\rho r}}{4\pi r^2} . \tag{4.37}$$

4.4.3 Volumetric symmetry

The result of the previous section may be used to illustrate an interesting symmetry. Imagine that a measurement, M, involves an integral over the volume of a detector, and the response function of the detector $R(E)$. The measurement is expressed as follows,

$$M_{D\leftarrow S}(E) = \int_D \mathrm{d}\vec{x}\, \Phi_i(\vec{x}, E) R(E) = \frac{1}{4\pi} \int_D \mathrm{d}\vec{x} \int_S \frac{n(\vec{\Omega}_{|\vec{x}-\vec{x}'|}, E)\mathrm{d}\vec{x}'}{(\vec{x}-\vec{x}')^2} \exp\left(- \int_{\vec{x}'}^{\vec{x}} \mathrm{d}l\, \mu(E, l)\rho(l) \right) , \tag{4.38}$$

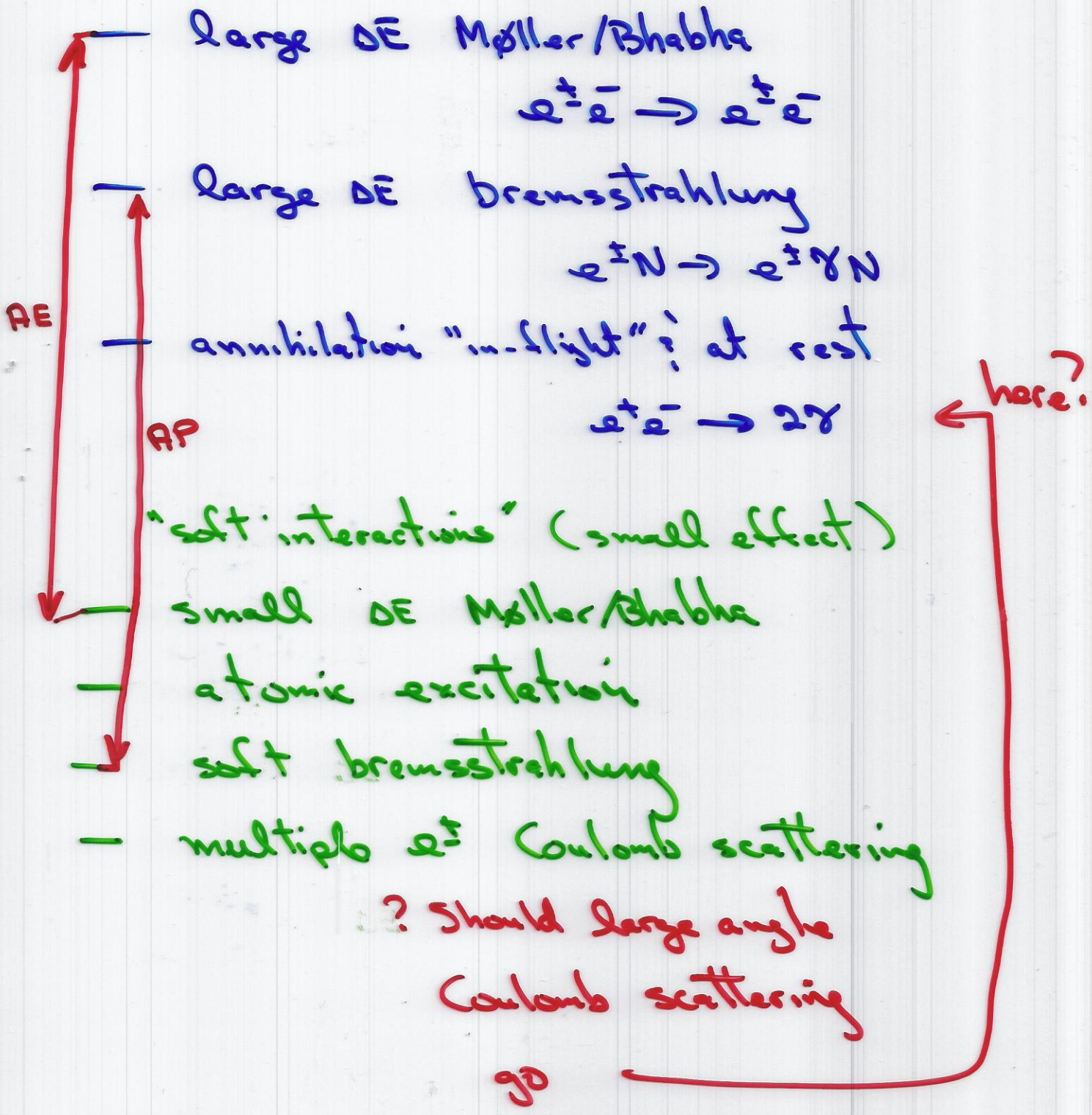
where the subscripts D and S refer to the detector and source regions respectfully, and the source is homogeneous and has the symmetry, $n(\vec{\Omega}_{\vec{x}-\vec{x}'}, E) = n(\vec{\Omega}_{|\vec{x}-\vec{x}'|}, E)$. This is the case for isotropic sources, and can be arranged for directional sources.

Note that

$$M_{D\leftarrow S}(E) = M_{S\leftarrow D}(E) , \tag{4.39}$$

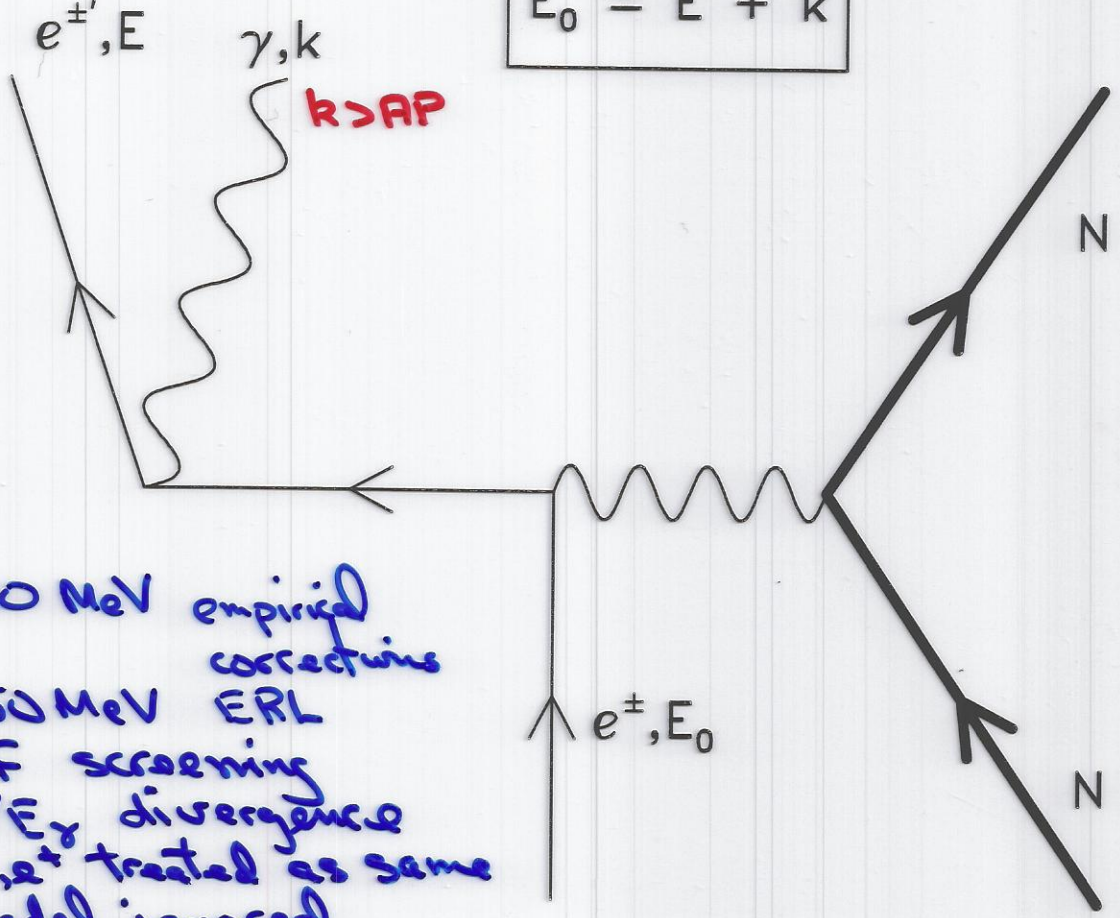
"catastrophic" interactions (big effect)

Discrete sampling:



- Z^2 scaling
- 3 body angular distn ignored
  $e^{\pm}N \Rightarrow e^{\pm}e^{-}\gamma N^*$
  $Z^2 \Rightarrow Z(Z+\xi(Z))$

$$E_0 = E + k$$

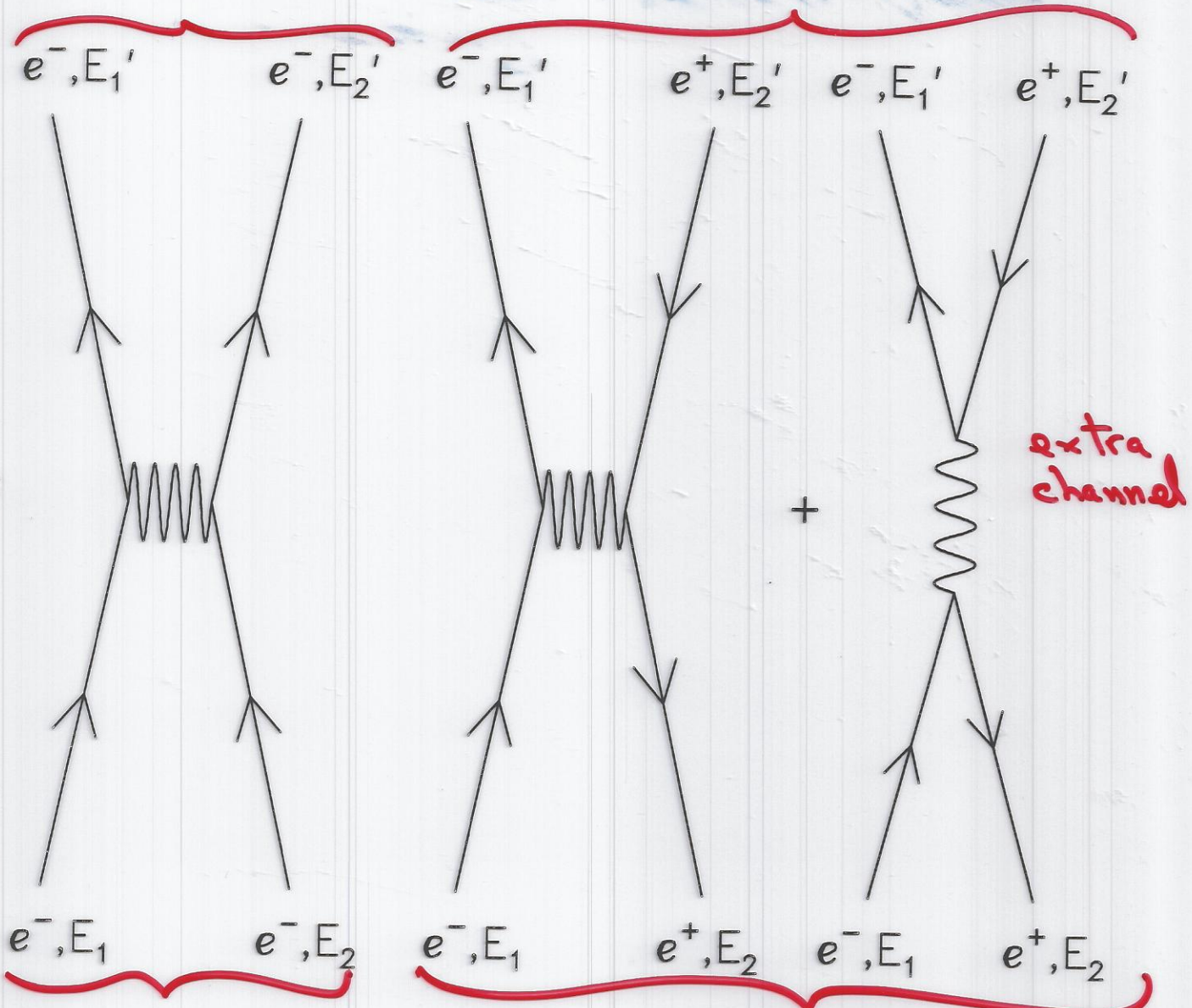


- <50 MeV empirical corrections
- >50 MeV ERL
- TF screening
- $1/E_\gamma$ divergence
- e^-, e^+ treated as same
- Migdal ignored
  > 1 TeV
- p_t not deflected
- $\theta_\gamma = m_e/E_0$
- "t·p" → 0

bremsstrahlung

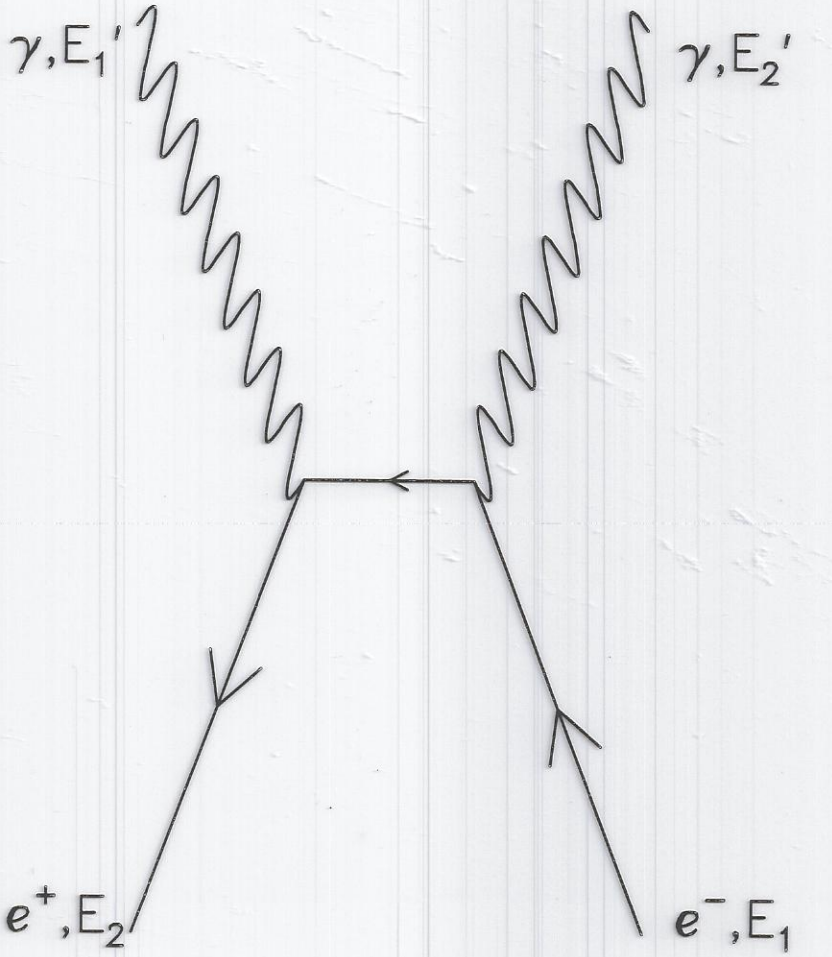
identical particles
- threshold $2(\Delta E - RM)$

different particles
- threshold $\Delta E - RM$



- goes like $1/v^2$
- scales like Z
- Target e^- is "free"

- in flight
- e^+e^- → $n\gamma$ and at rest
- e^+e^-N → γN^* ($n>2$) ignored
- at ECUT e^+ annihilates. Residual drift is ignored
- no binding



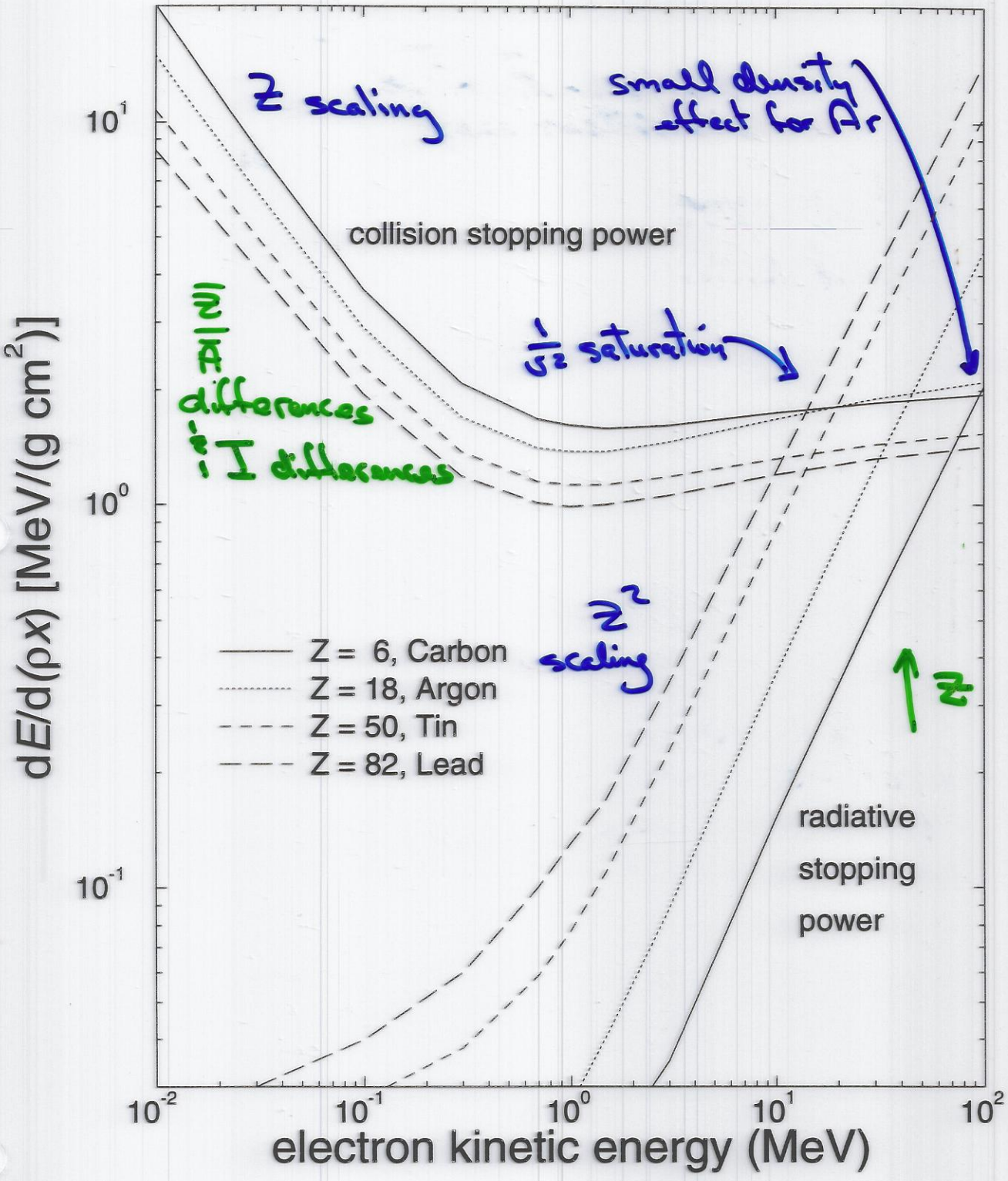
Annihilation

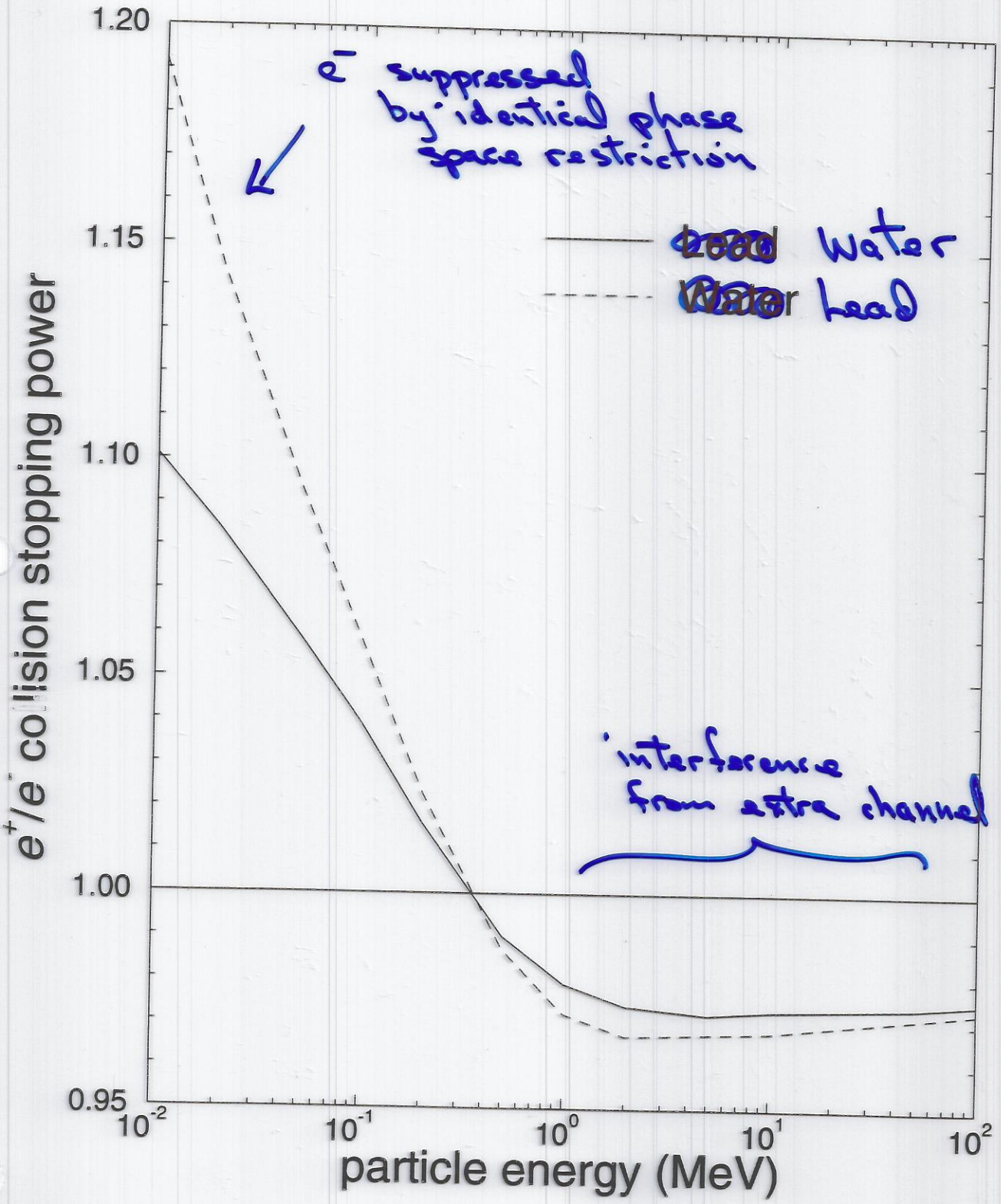
Statistically grouped interactions

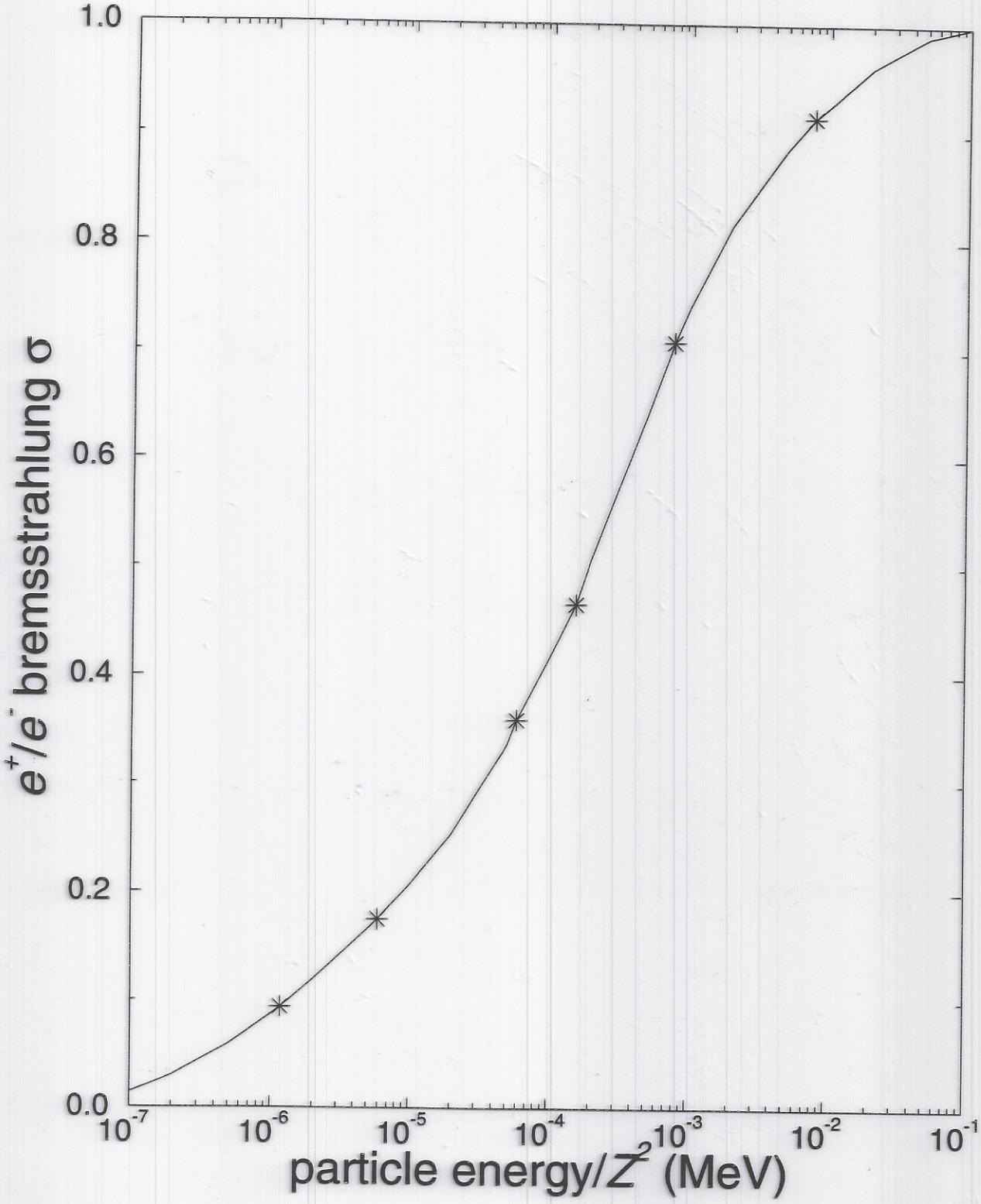
1) collisional energy loss (e^+ different)
   - Bethe-Bloch theory + density effect
     - well-above K shell energy
     - many electron atoms

     $\propto \frac{Z}{A}$

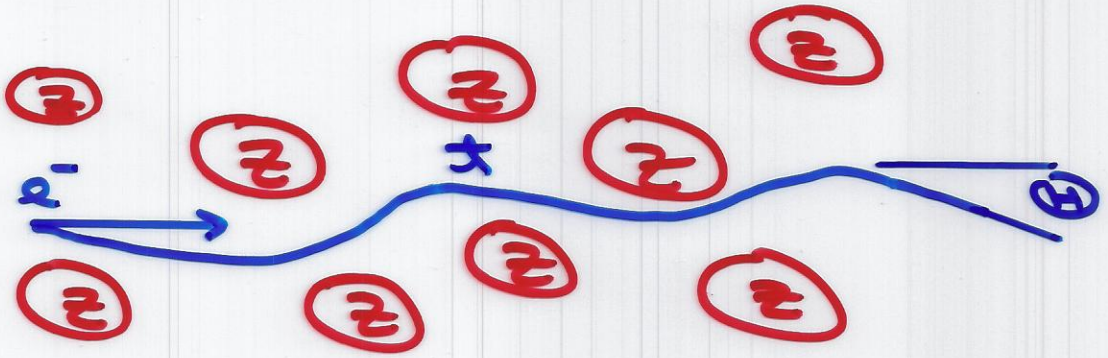
2) radiative energy loss (e^+ treated same)
   - integration of Bremsstrahlung cross sections
   - same approximations
   - e^+, e^- treated as identical


Z scaling
small density effect for Ar
collision stopping power
1/√2 saturation
Z differences
I differences
Z = 6, Carbon
Z = 18, Argon
Z = 50, Tin
Z = 82, Lead
Z² scaling
Z
radiative stopping power
dE/d(ρx) [MeV/(g cm²)]
electron kinetic energy (MeV)
10¹
10⁰
10⁻¹
10⁻²
10⁻¹
10⁰
10¹
10²


1.20
1.15
1.10
1.05
1.00
0.95
e^+/e^- collision stopping power
10^{-2}
10^{-1}
10^{0}
10^{1}
10^{2}
particle energy (MeV)
e^- suppressed by identical phase space restriction
Water
Lead
interference from extra channel


1.0
0.8
0.6
0.4
0.2
0.0
e^+/e^- bremsstrahlung σ
10^{-7}
10^{-6}
10^{-5}
10^{-4}
10^{-3}
10^{-2}
10^{-1}
particle energy/Z^2 (MeV)

Multiple Scattering



$f(\Theta) = ?$ after pathlength x

Fermi-Eyges Theory

$$f(\Theta) = N e^{-\Theta^2/\bar{\Theta}^2(x)}$$

- good for forward angles
- moments do not make sense
- can include energy loss

Multiple Scattering

Fermi-Eyges theory:

$$F(x, y, \theta_y) = \frac{1}{4\pi\sqrt{B}} \exp\left[-\frac{\theta_y^2 A_2 - 2y\theta_y A_1 + y^2 A_0}{4B}\right]$$

$$A_n = \int_0^x \frac{(x-\eta)^n}{W^2(\eta)}\, d\eta$$

$$W = 2p\beta/E_s \; ; \quad B = A_0 A_2 - A_1^2$$

- Small angles only
- need to put large angles in seperately

Goudsmit-Saunderson Theory

$$F_{GS}(\theta, t) = \sum_{l=0}^{\infty} (l+\tfrac{1}{2}) e^{-t G_l} P_l(\cos\theta)$$

$$G_l = 2\pi \frac{N_a}{A} \int_0^{\pi} [1 - P_l(\cos\theta)] \sigma(\theta) \sin\theta \, d\theta$$

- Regarded as "the best"
- any angle, any σ
- no energy loss
- Very difficult for variable t
  Monte Carlo's like EGS
- Used by ETRAN because of a fixed set of t's

Moliere's small angle large pathlength theory

$$\sigma(\chi) \propto \frac{1}{(\theta^2 + \chi_a^2)^2}$$

Screened Rutherford x-sect

χ_a ← screening angle

$$F_1(\theta, t) = 2e^{-\varphi^2} + \frac{f^{(1)}(\varphi)}{B} + \frac{f^{(2)}(\varphi)}{B^2} + \dots$$

↑ FLUKA stops here

$$\varphi = \frac{\theta}{\chi_c \sqrt{\lambda B}}$$

$$B - \ln B = 1 - 2\alpha + \ln \lambda$$

λ ← # of mfp's

α ← Euler's constant 0.577216...

Good for $\lambda > 20$ (6% error in peak)

FLUKA uses $\lambda \geq 3$!

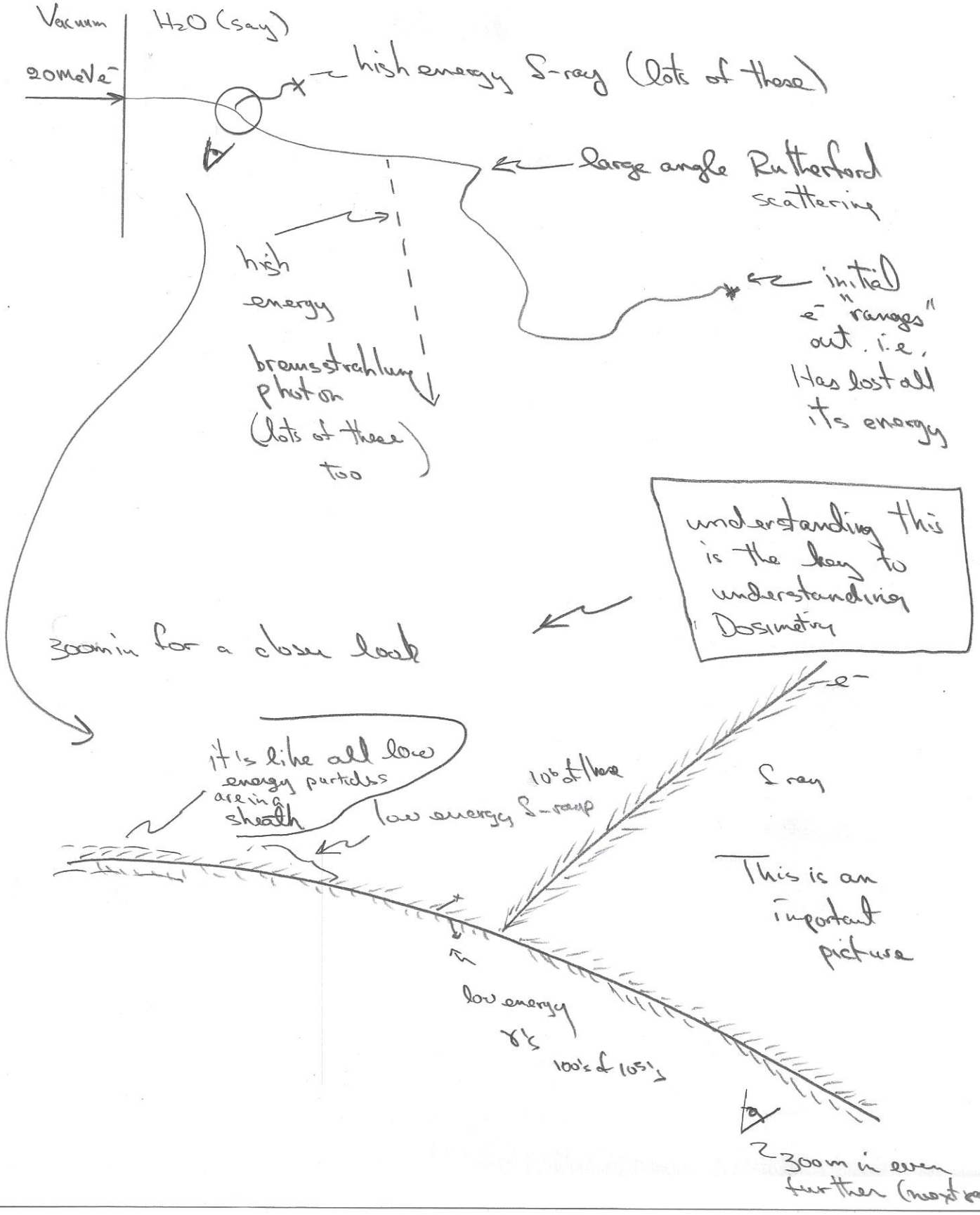
Small angle MS theories

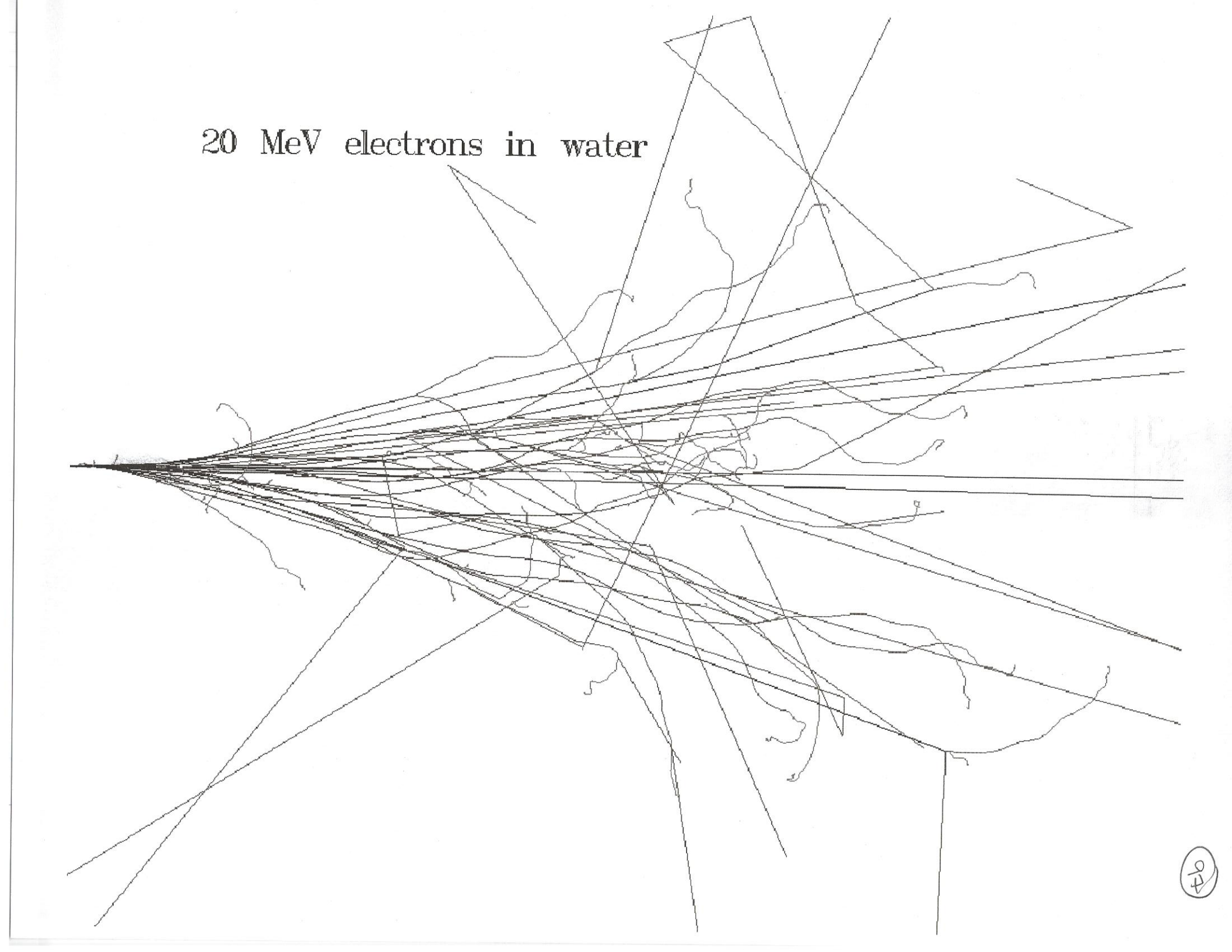
$$F_{SA}(\theta, t) = \int_0^\infty d\eta\, \eta J_0(\eta\theta) e^{-t g(\eta)}$$

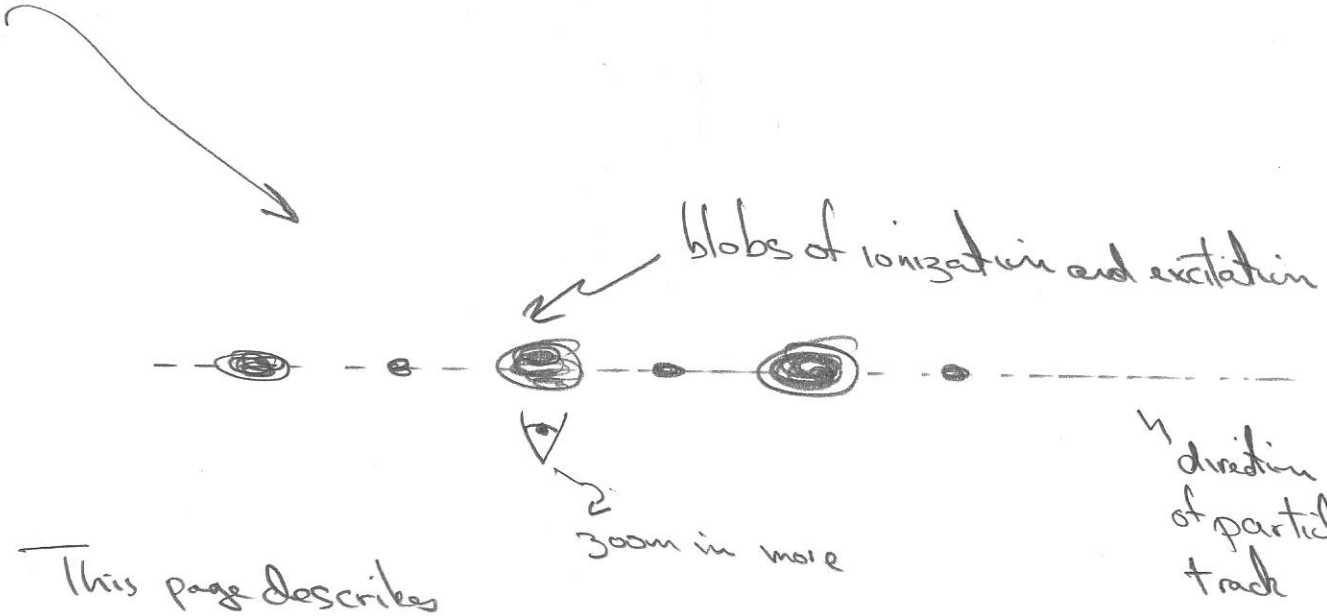
$$g(\eta) = \frac{2\pi N_a}{A} \int_0^\infty dx\, x \sigma(x) [1 - J_0(\eta x)]$$

- same as GS except small angle
- Bethe (1953) showed how to make large angle work

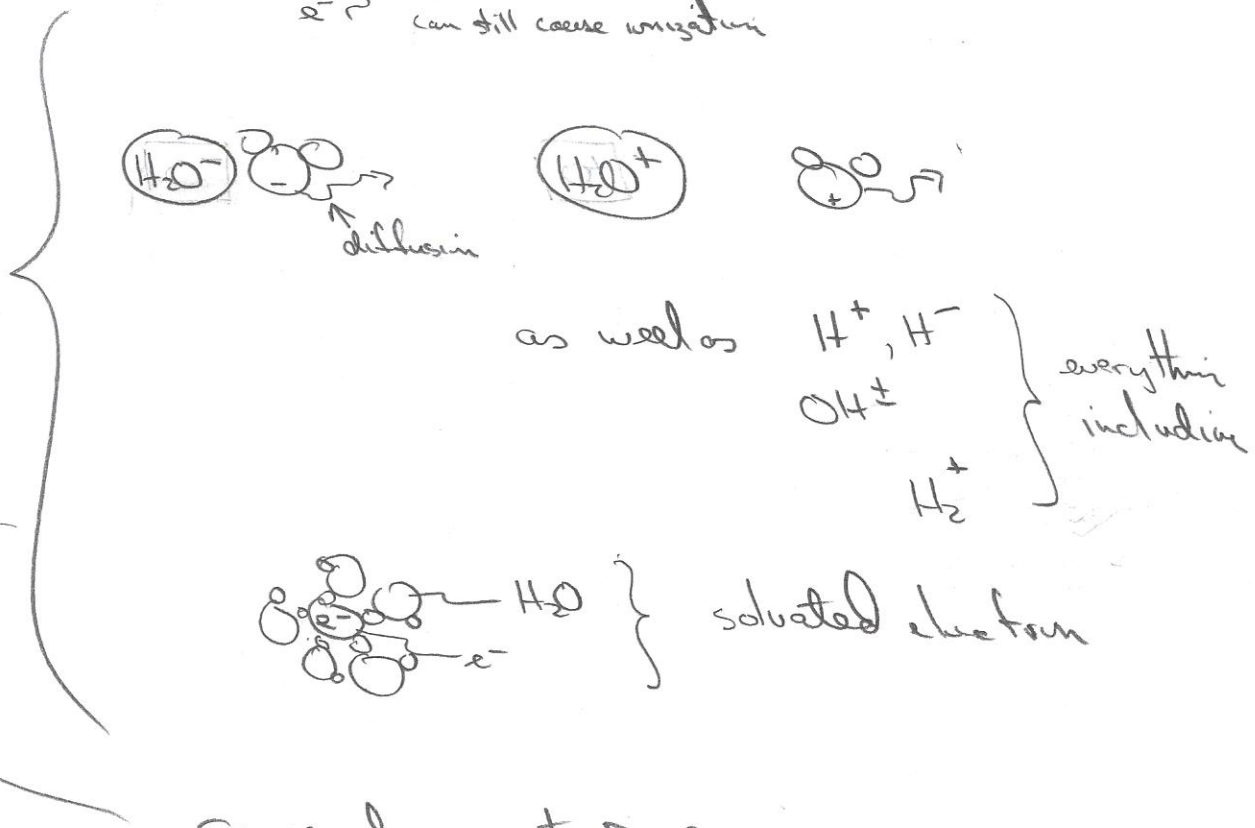
Typical electron tracks in media



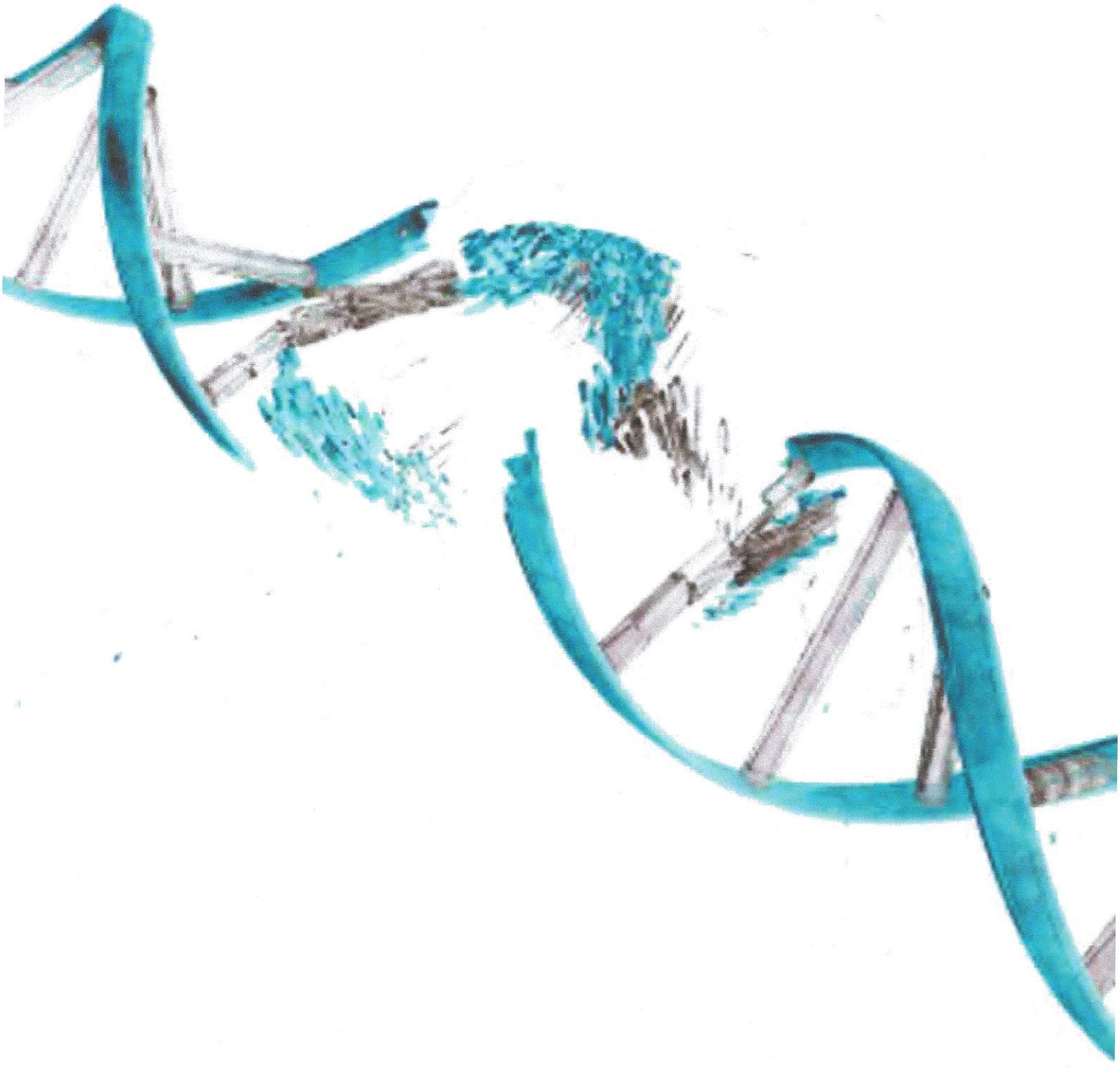

20 MeV electrons in water

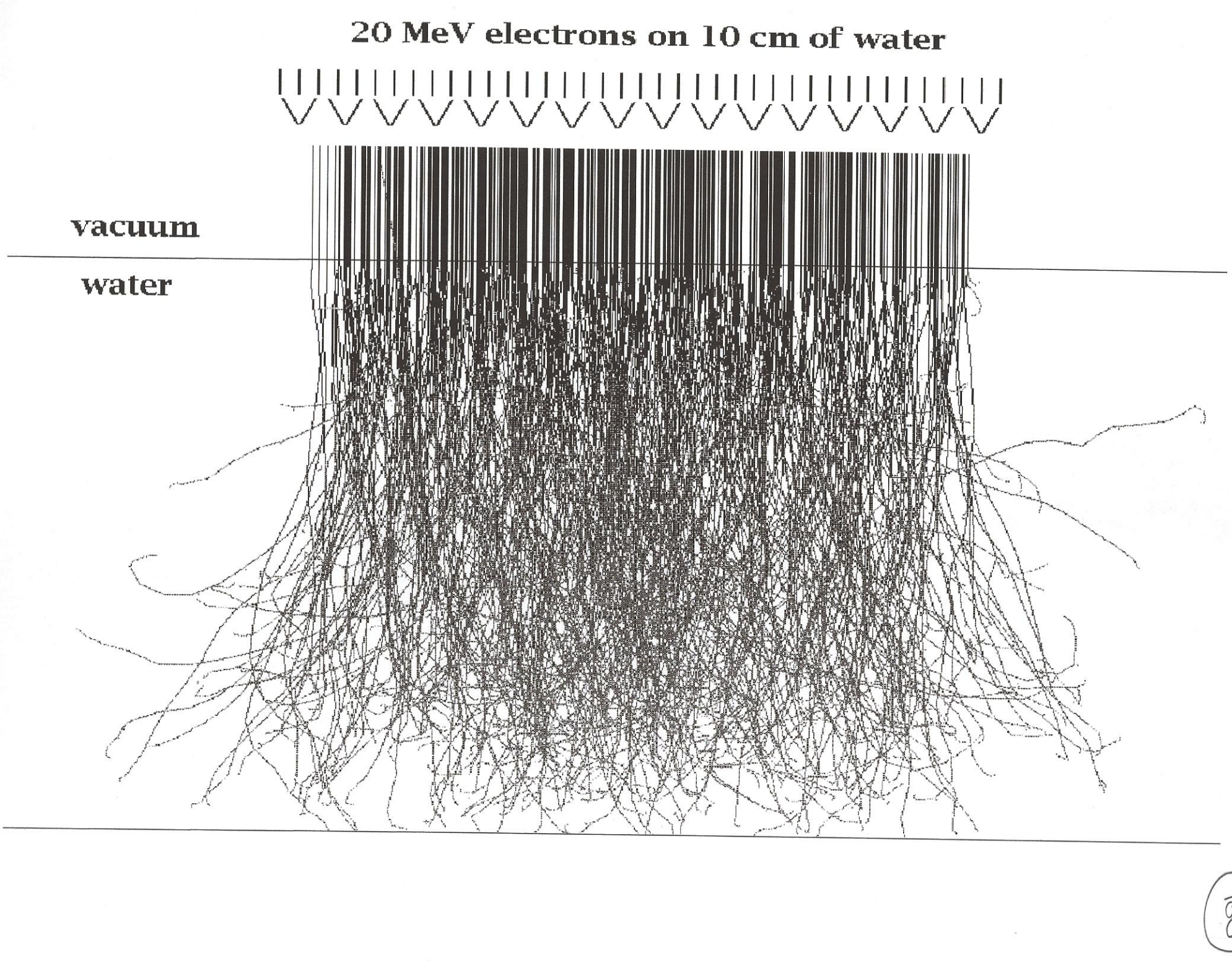


This page describes the field of microdosimetry
Great topic - not this course



cause damage to DNA




20 MeV electrons on 10 cm of water
vacuum
water

Chapter 5 Photon Dose Calculation Models

5.1.1 Kerma

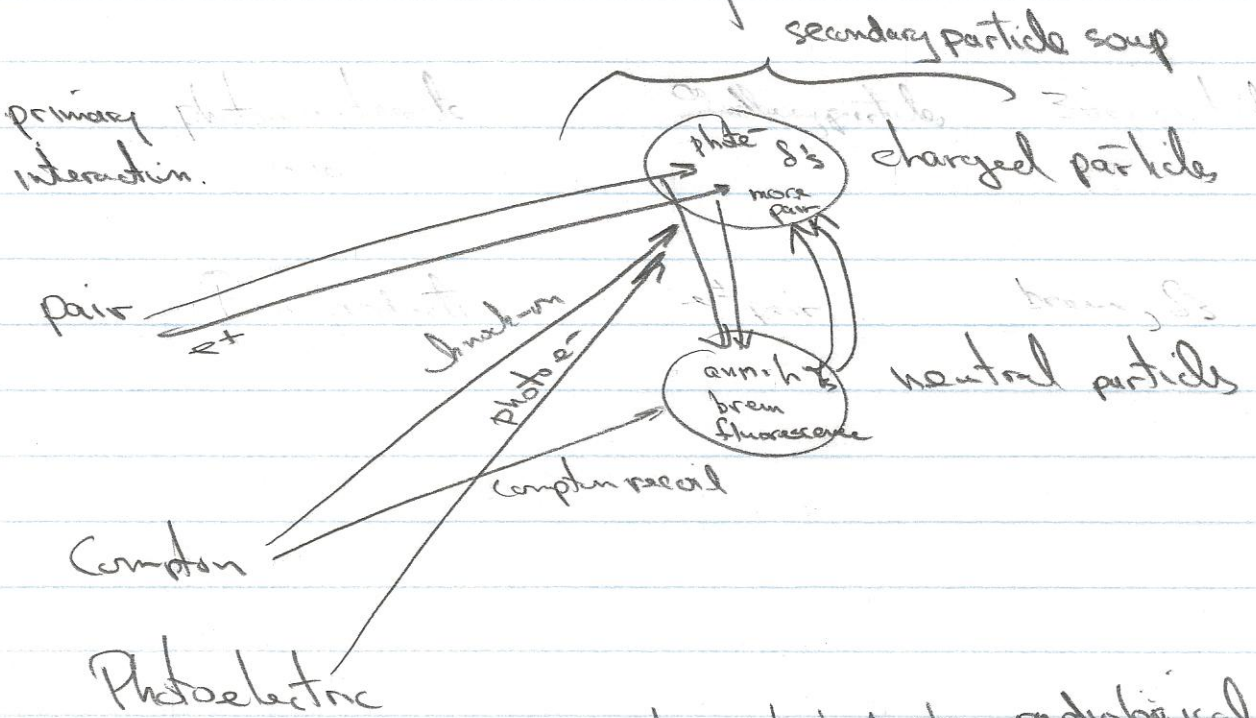
Now we adapt what we have learned from the μ-world, to find practical ways of of calculating radiological effect.

Kerma is an acronym for

Kinetic Energy Released per unit MAss

It only truly applied to photons

We know that, when a photon interacts, it can do the following



Rayleigh → does not contribute to radiological effect

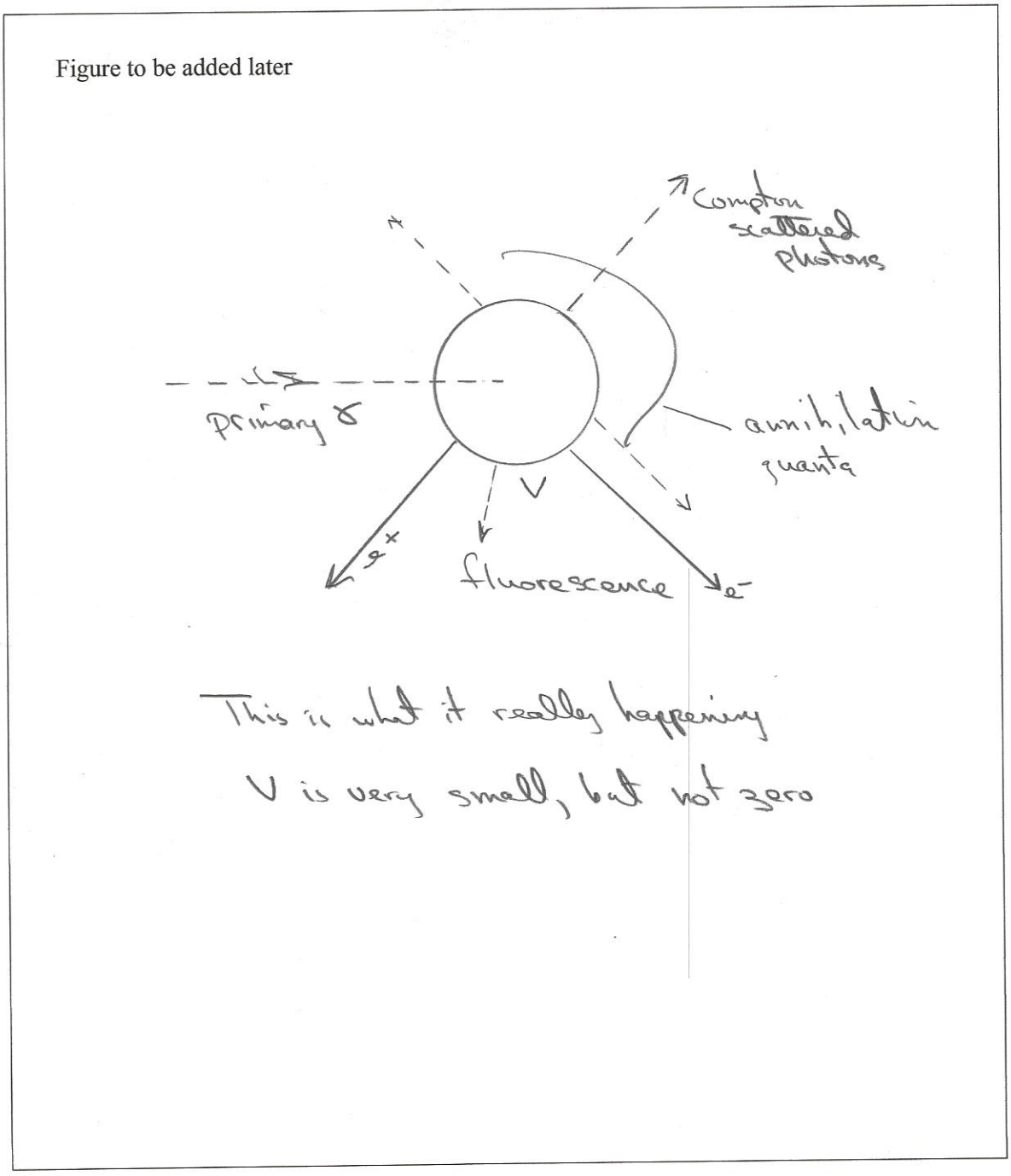


Figure 5.1: Idealizations of photons interacting in matter, employed to construct the Kerma.

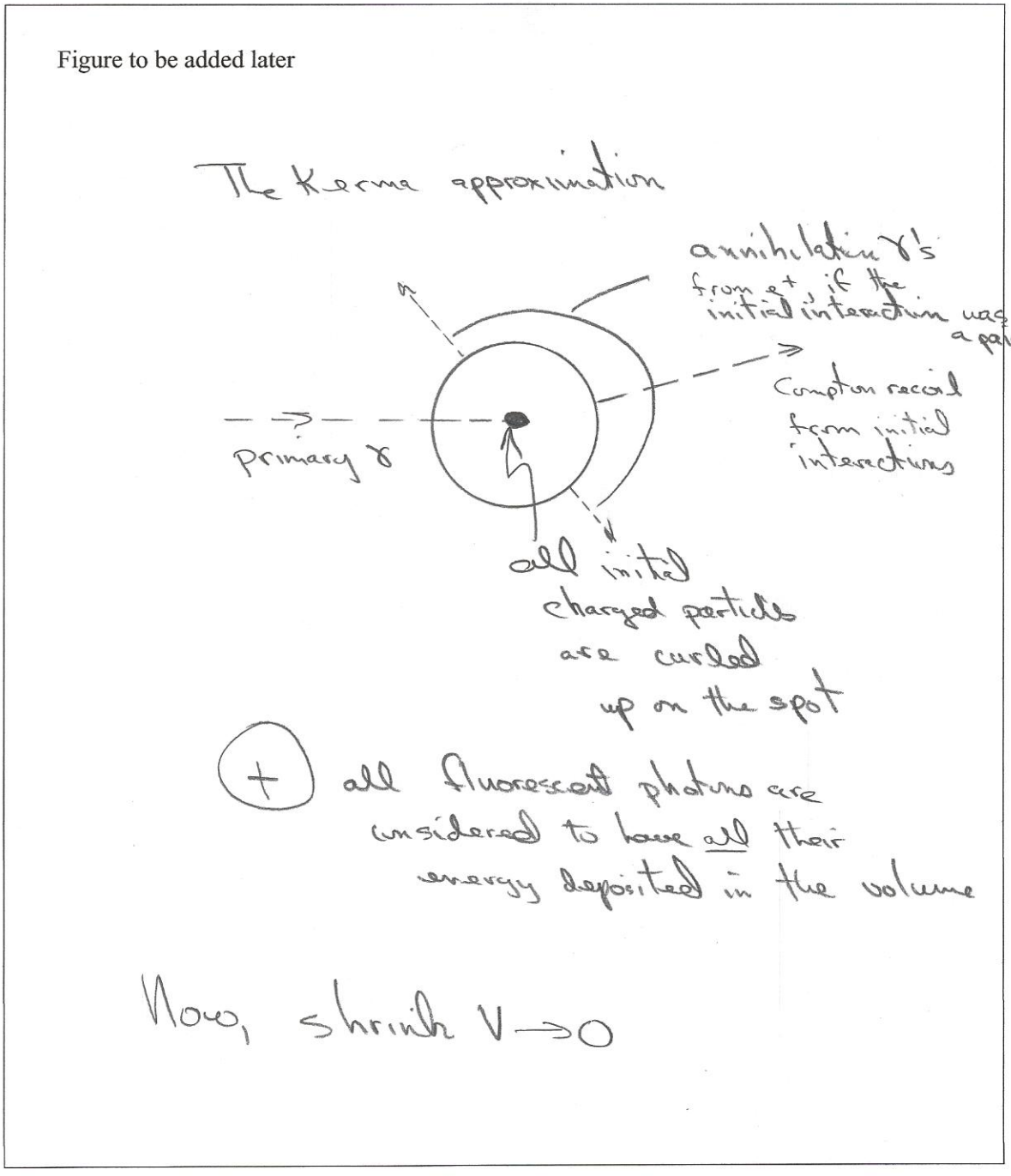


Figure 5.2: Trapping the primary charged particles within a small volume to illustrate Kerma.

On first encounter, Kerma seems like an odd thing

But, bear in mind, that it was invented when incident photon energies were low

90 keV → 1.25 MeV

↑ X-ray units ↑ ^{60}Co

there was not a lot of brem

It is calculated as follows: (no computers required!)

Consider a microscopic cross section normalized as follows

$$\tilde{\sigma}(E_\gamma, E_{e^-}^{kin}) = \frac{\sigma(E_\gamma, E_{e^-}^{kin})}{\int_0^\infty dE_{e^-}^{kin}\, \sigma(E_\gamma, E_{e^-}^{kin})} \qquad (5.2)$$

(E_γ: monoenergetic; $E_{e^-}^{kin}$: kinetic energy of charged particles)

Clearly $\int dE_{e^-}^{kin}\, \tilde{\sigma}(E_\gamma, E_{e^-}^{kin}) = 1$ by design

σ includes the pair, Compton & photoelectric processes.

Define a "mass energy transfer coefficient"

$$\mu_{tr}(E_\gamma) = \frac{\mu(E_\gamma)}{E_\gamma} \int_0^\infty dE_{e^-}^{kin} \; E_{e^-}^{kin} \; \Phi(E_\gamma, E_{e^-}^{kin})$$

(μ: attenuation coefficient; $E_{e^-}^{kin}$: note e)

which converts the attenuation coefficient into a factor that account for energy lost into charged particle kinetic energy from the initial interaction

Aside: You already did this, sort of!

Remember $\left(\frac{\bar{E}}{E}\right)$ from assignment 3?

$$\mu_{tr} = \frac{\mu_{KN}}{E_\gamma}\left(1 - \frac{\bar{E}_k}{E_k}\right)$$

if only Compton mattered!

Anyway,

with all this, we can state our mathematical expression for Kerma.

Kerma definition

(5.3) $$K(\vec{x}) = \int_0^{E_{\gamma,max}} dE_\gamma \, \Phi(\vec{x}, E_\gamma) E_\gamma \mu_{tr}(E_\gamma)$$

Φ: fluence

μ_{tr}: fraction of E_γ "trapped" in V

The above is more suitable for analytic calculation.

An alternative form, for Monte Carlo calculations, would be

(5.4) $$K(\vec{x}) = \lim_{V \to 0} \frac{\langle \Delta E^o_{kin} \rangle}{\rho(\vec{x}) \Delta V}$$

where $\langle \Delta E^o_{kin} \rangle$ is the expectation value of the initial kinetic energies of all charged particles, i.e. $e^\pm$ set in motion

What about the 2γ annihilation photons?

Recall that the pair creation process requires a $2m_e c^2$ energy threshold. It is assumed that the e^+ annihilated at rest, and that those photons left the volume.

If you are using an MC calculation to calculate K, you have to handle this correctly.

What about the bremsstrahlung γ's?

The K model works really well at low energies, where brem can be ignored.

At higher energies, or in high precision calculation, we can not ignore the brem.

We have to adapt K to account for this, bringing us to

o o c

5.1.2 Collision Kerma, K_c

First, we start with the figure on page (102)

and allow all bremsstrahlung, no matter what its orgin and allows us to define

$$K_c = K(1-G)$$

where G is the fraction of energy lost to bremsstrahlung.

Specifically, we defined a

"mass energy absorbtion coefficient"

$$\mu_{en}(E_\gamma) = \frac{\mu(E_\gamma)}{E_\gamma} \int_0^\infty dE_{e^-}^{kin} \left[\frac{E_{e^-}^{kin}}{E_{e^-}^{kin}} - g(E_{e^-}) \right] \tilde{\Phi}(E_\gamma, E_{e^-}^{kin})$$

$g(E_{e^-}^{kin})$ is the fraction of energy lost to bremsstrahlung

Suffice it to say, that there is a reliable albeit approximate way of calculating this, some things that we shall discuss later, when we discuss stopping powers.

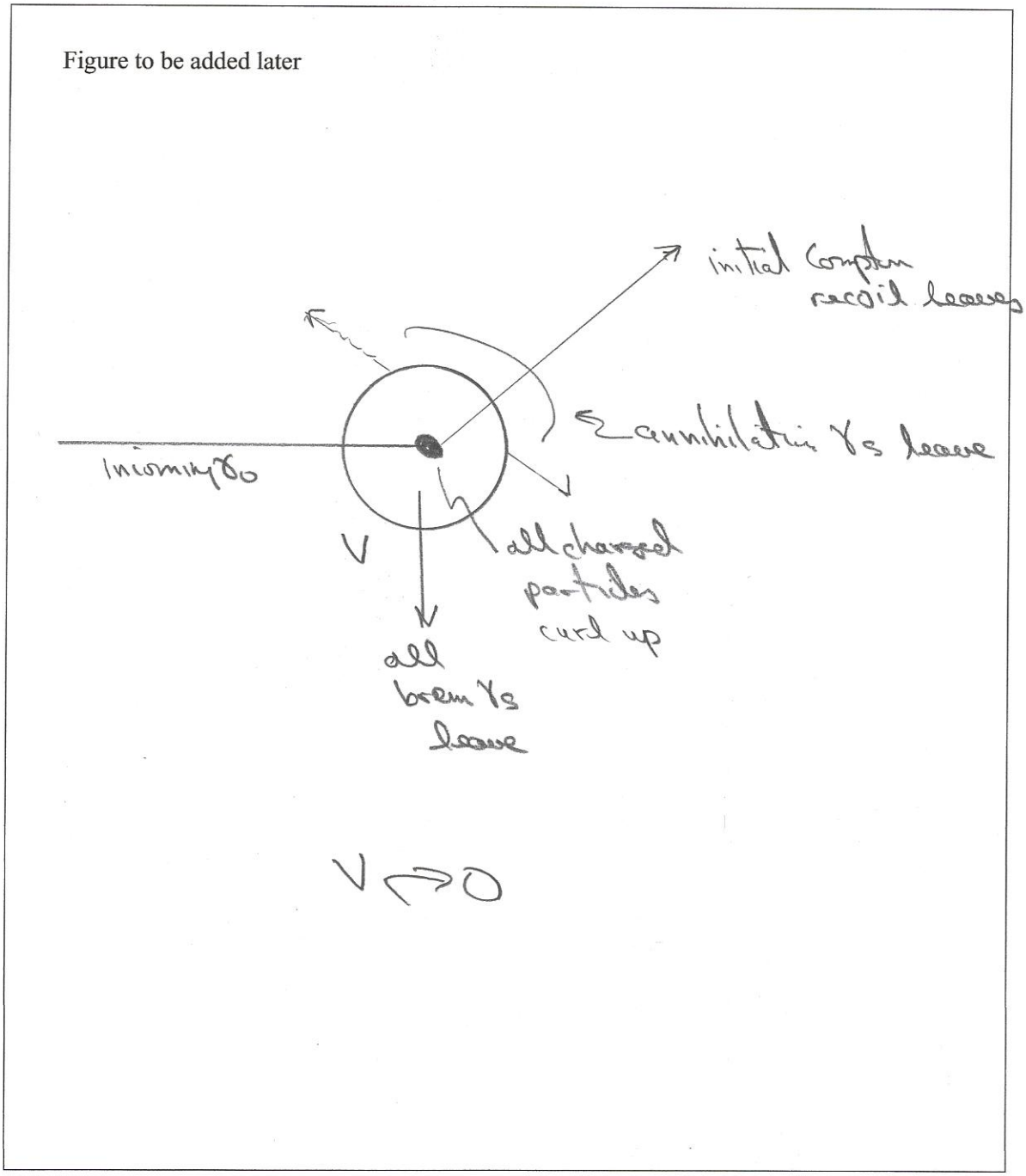


Figure 5.4: Trapping all the charged particles within a small volume to illustrate collision Kerma.

And finally -- Dose!

5.1.3

Dose is defined as follows:

$$D(\vec{x}) = \lim_{\Delta V \to 0} \left\langle \frac{\Delta \vec{\varepsilon}_{in} - \Delta \vec{\varepsilon}_{out}}{\rho(\vec{x})\,\Delta V} \right\rangle \qquad (5.7)$$

- $\Delta \vec{\varepsilon}_{in}$: radiant energy in, all particles
- $\Delta \vec{\varepsilon}_{out}$: radiant energy out, all particles
- $\Delta V \to 0$: small volume

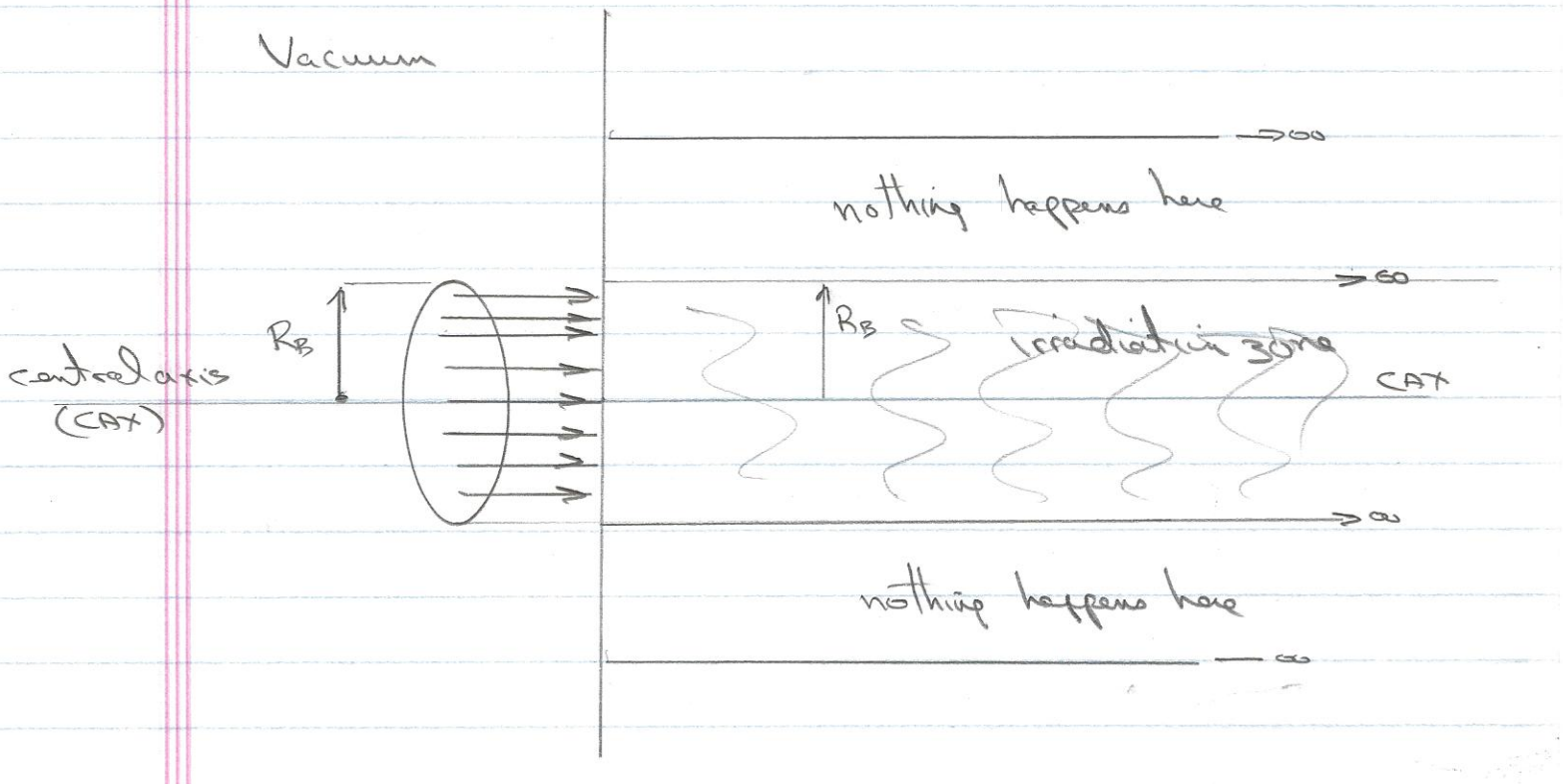
The radiant energies include charge particles, whose transport can only be done reliably, using Monte Carlo calculations.

We shall investigate approximate e^--transport models to build our intuition however.

5.1.4 Comparison of photon dose deposition models

Imagine that we have a monoenergetic beam of photons, radius R_B, incident normally, on a plane dividing the source (in vacuum) from the scattering medium (e.g. water phantom, patient).

Imagine, as well, that this photon interacts, but does not attenuate(!), nor does it generate any scattered photons (!) [Useful theoretical construct, for isolating the various parts of the physics]



What is the kerma dose? collision kerma dose?

kerma

$$K^0(\vec{\rho},z) = \Psi_0 \mu_{tr}(E_0)\,\Theta(R_B - |\vec{\rho}|)$$

K^0: kerma; $(\vec{\rho},z)$: cylindrical radius, depth; Ψ_0: energy fluence; μ_{tr}: energy mass transfer coefficient; Θ: fin.

$= \Phi_0 E_0$ in this case

Aside $\Theta(x) = 0$ for $x<0$

$= 1$ for $x>1$

or, if the source is polyenergetic

typical case

$$K^0(\vec{\rho},z) = \int_0^{E_0} dE\, \Psi(E)\,\mu_{tr}(E)\,\Theta(R_B - |\vec{\rho}|)$$

(E_0 ← max energy)

Similarly, the collision kerma is

mono

$$K_c^0(\vec{\rho},z) = \Psi_0 \mu_{en}(E_0)\,\Theta(R_B - |\vec{\rho}|)$$

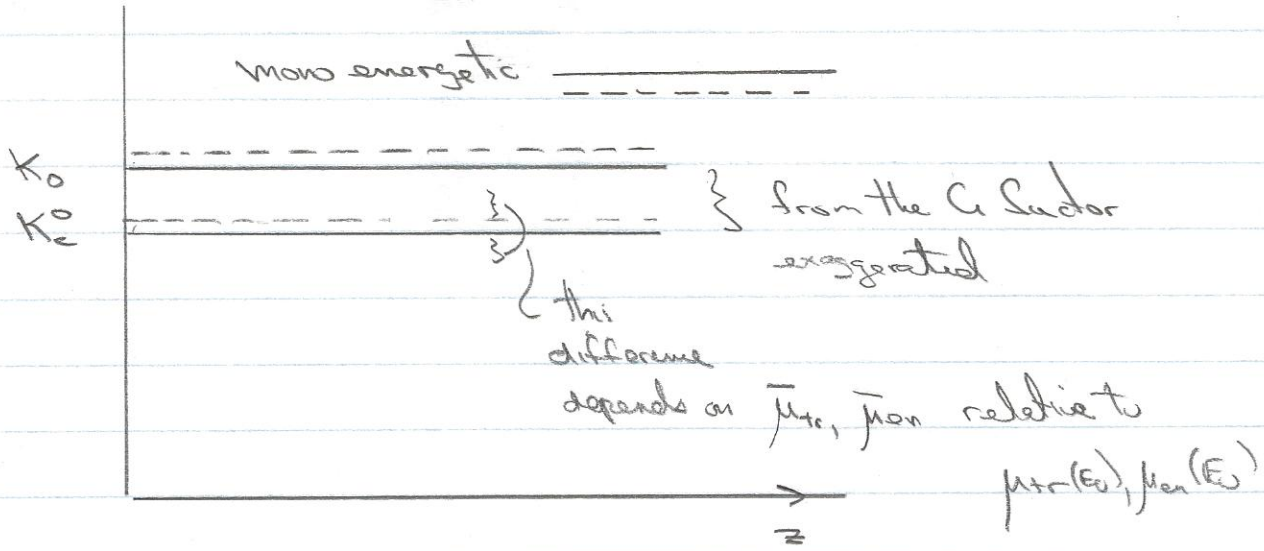
(K_c^0: collision)

note $K_c^0(\vec{\rho},z) = K^0(\vec{\rho},z)(1-G)$ for mono energetic beams

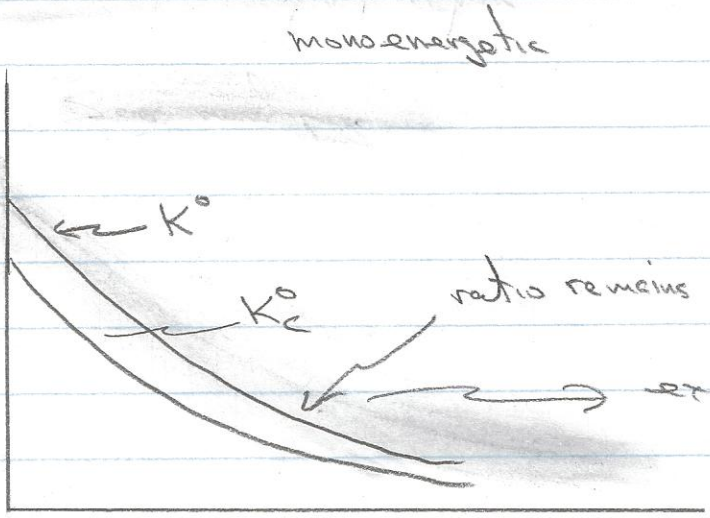
poly

$$K_c^0(\rho,z) = \int_0^{E_0} dE\, \Psi(E)\,\mu_{en}(E)\,\Theta(R_B - |\vec{\rho}|)$$

for poly beams, we'll have to construct a graph



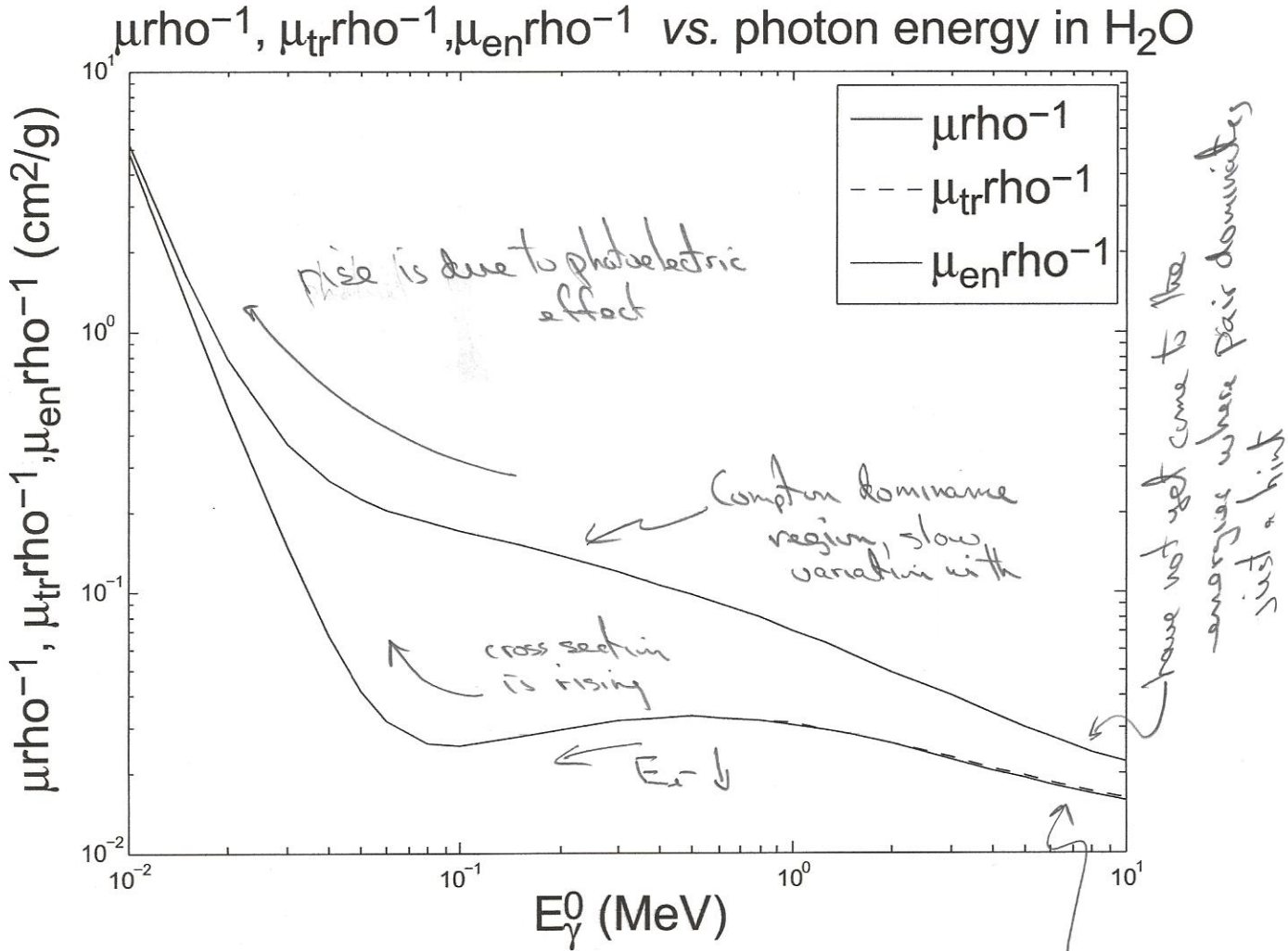
Now, turn on attenuation.
But, do not generate secondary photons



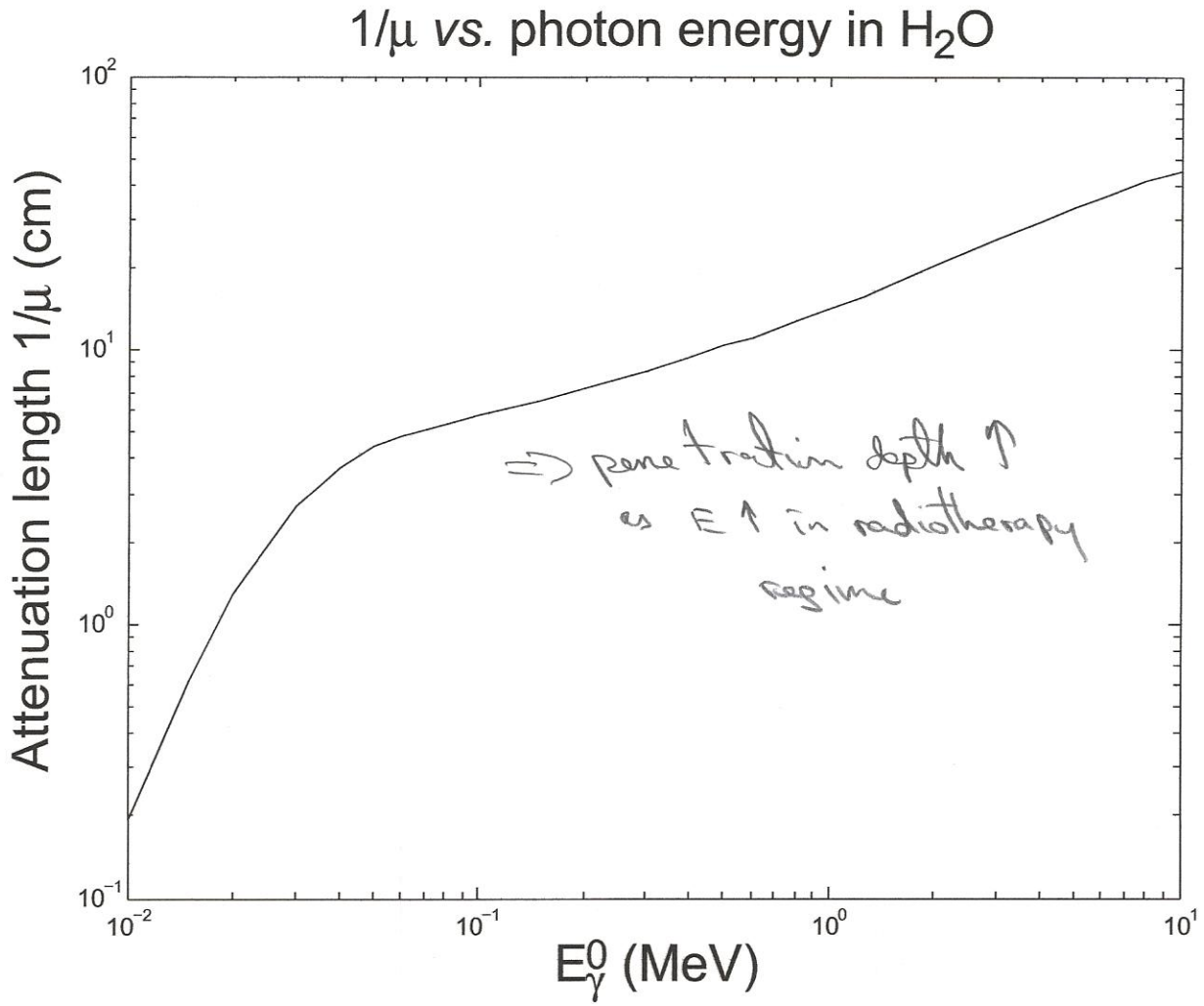
$$K^0(z) = K^0(0)e^{-\mu z}$$
$$K_c^0(z) = K_c^0(0)e^{-\mu z}$$
} same

$$\frac{K^0(z)}{K_c^0(z)} = \frac{K^0(0)}{K_c^0(0)}$$ the same

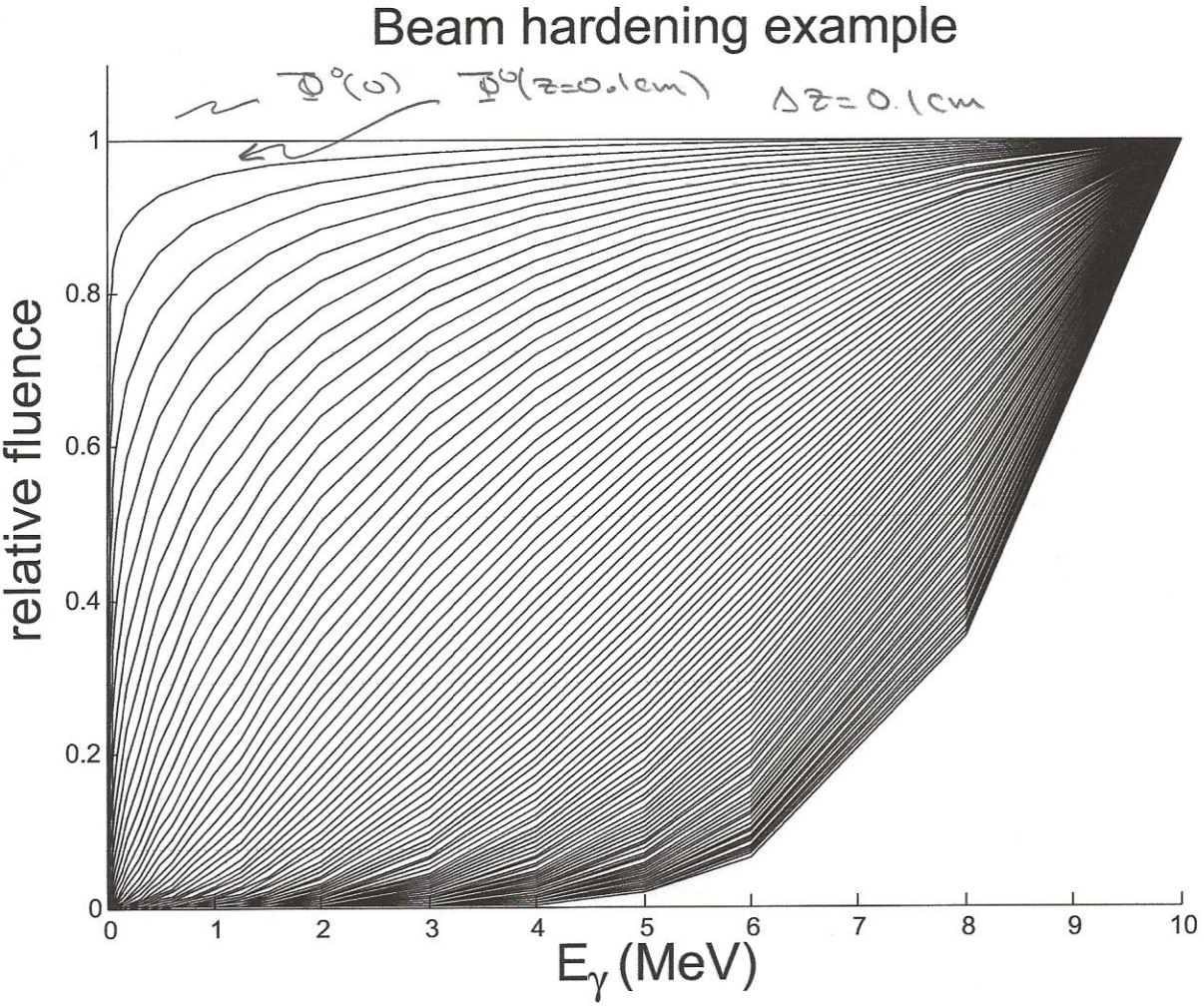
For polyenergetic beams, we need to understand "beam hardening"


μrho⁻¹, μtrrho⁻¹,μenrho⁻¹ vs. photon energy in H2O
μrho⁻¹
μtrrho⁻¹
μenrho⁻¹
μrho⁻¹, μtrrho⁻¹,μenrho⁻¹ (cm2/g)
E0γ (MeV)
Rise is due to photoelectric effect
Compton dominance region, slow variation with
cross section is rising
Eγ ↓
Pair production threshold
very small difference between
Mtr & Men

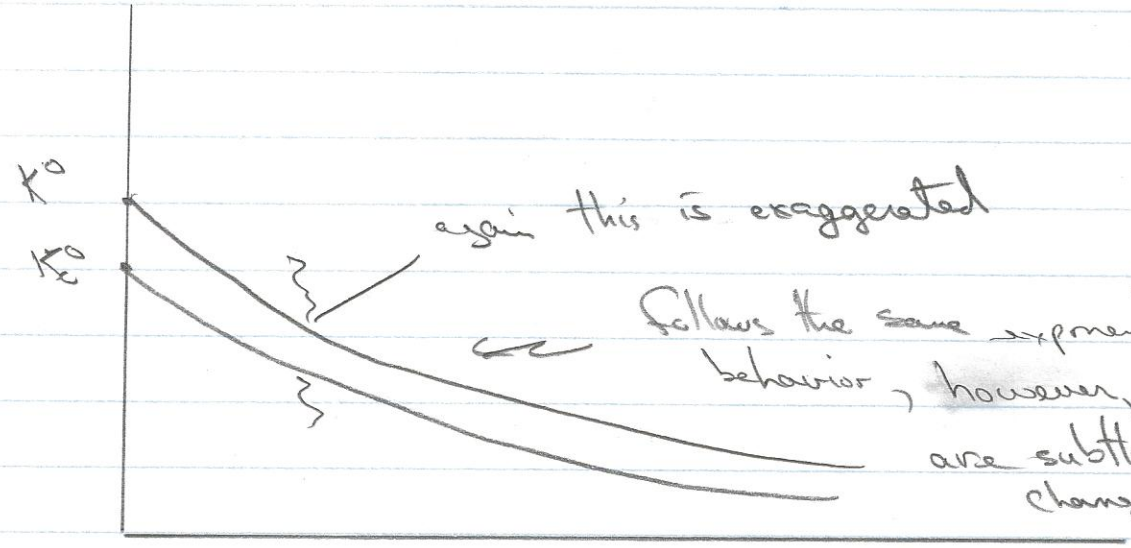
In general


1/μ vs. photon energy in H_2O
Attenuation length 1/μ (cm)
10^2
10^1
10^0
10^{-1}
10^{-2}
10^{-1}
10^0
10^1
E_γ^0 (MeV)
⇒ penetration depth ↑ as E ↑ in radiotherapy regime

How the beam hardens with depth

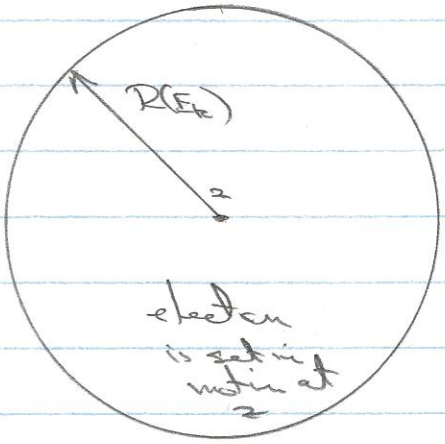


polyenergetic incident photons



What about electrons?

As discussed previously, when an electron is set in motion, with energy, E_k, (kinetic), the total length of its path, before it ranges out is $R(E_k)$.



Because of elastic scattering, it can end up, anywhere in the sphere.

On average, the distribution is more like the distribution function

$$f(\mu)\sin\theta\, d\theta = 1 + \varepsilon\cos\theta$$

or $$f(\mu)\, d\mu = 1 + \omega\mu$$

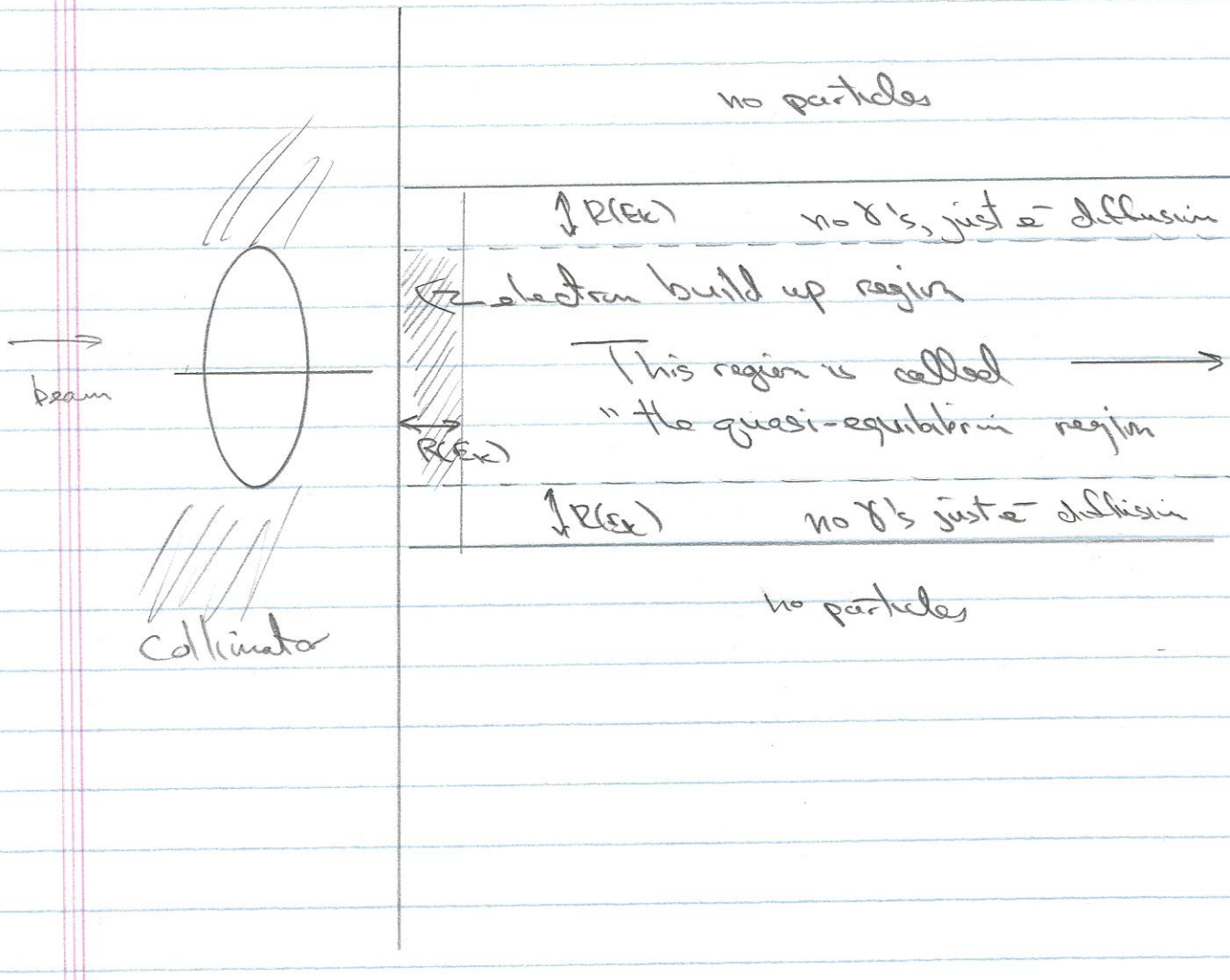
ω is determined by the energy

Low energy $\omega \downarrow$ high energy $\omega \uparrow$

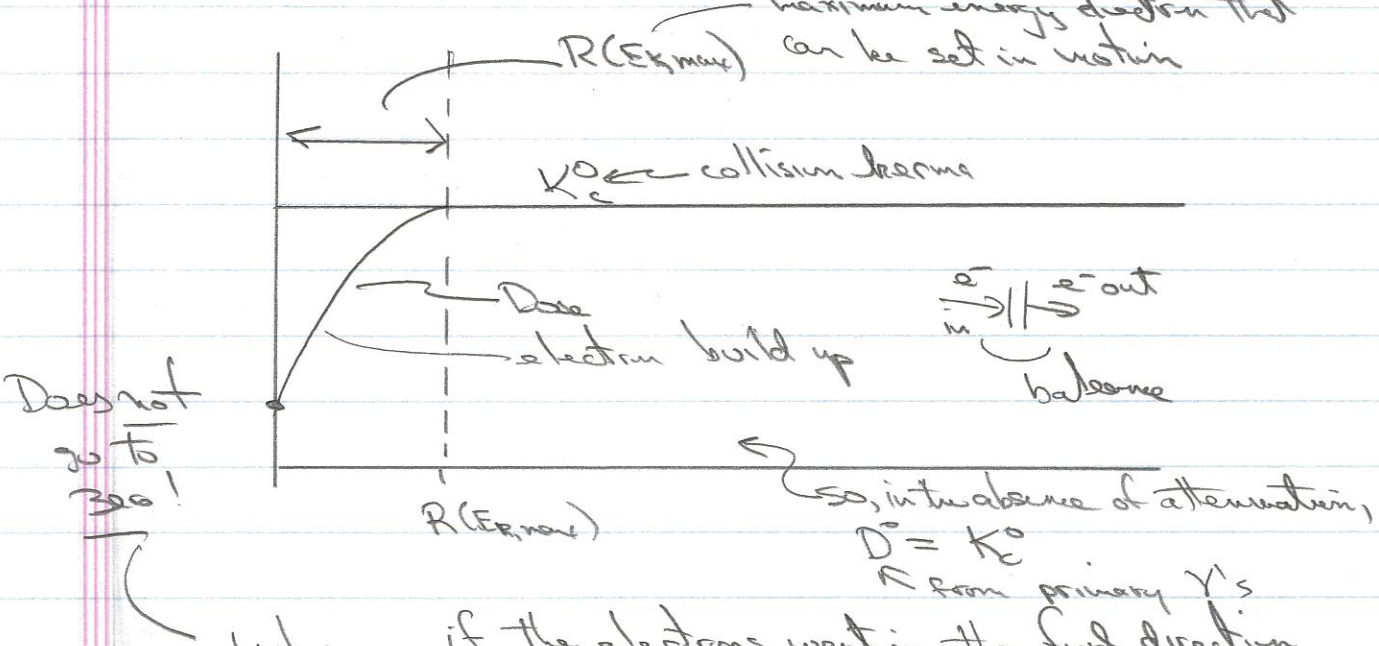
In Radiotherapy calculations:

$R(E_k) \ll 1/\mu$ ← attenuation length

Now, let's go back to the figure on p. 111, and adapt it for what we have just learned

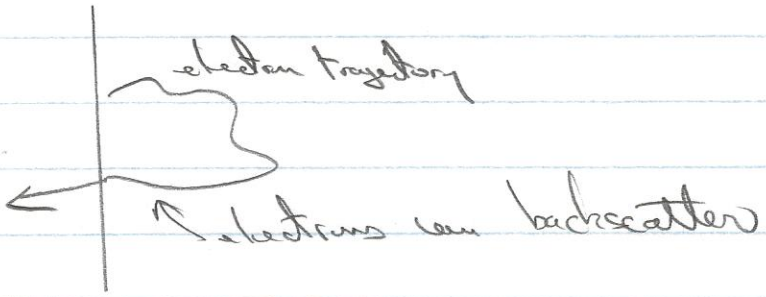


In the absence of γ scatter, (but allowing for e^- transport anywhere is the quasi-equilibrium region



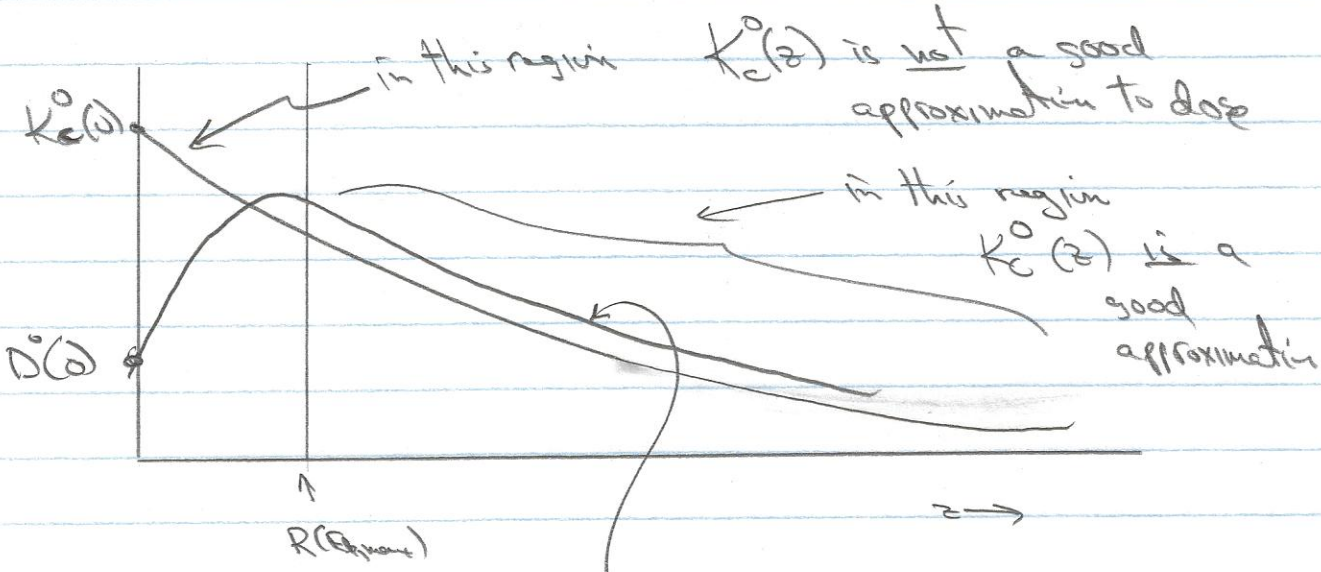
Why if the electrons went in the fwd direction only, the surface dose would be 0

But:



Fact: In the absence of e^- contaminants in the beam, the surface dose is due entirely to electrons that originate in the target, and backscatter out. (Proof at a later date. after we have done more e^- transport

What if we allow for attenuation of the primary photon beam?



One can model this region as

$$D_o(z) = K_c^o(z)\, e^{+\mu \bar{z}} \approx K_c^o(z)(1+\mu\bar{z}\ldots)$$

where $\bar{z}$ is called the "average electron drift"

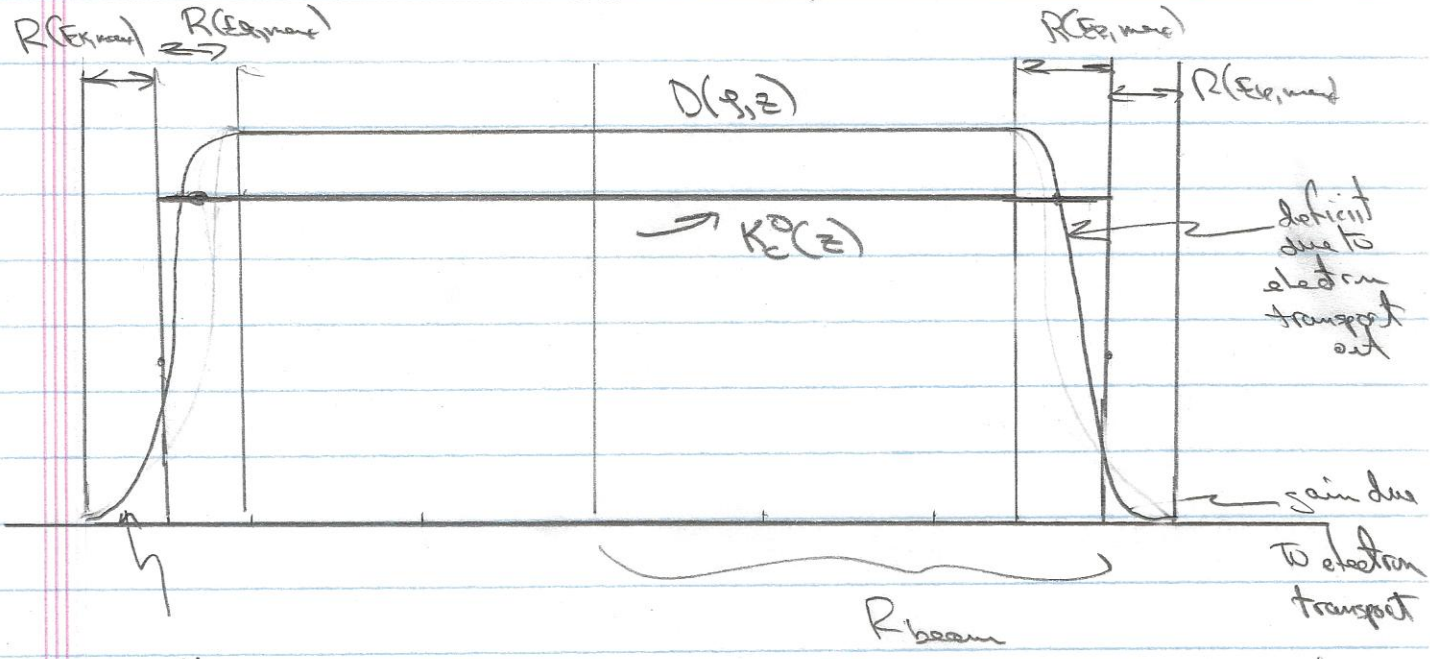
For now, we can only estimate $\bar{z}$ by MC calculations

However, we know that the beam hardens with depth, for polyenergetic beams

∴ For polyenergetic beams $\bar{E} \uparrow$ with depth!

What about the lateral profiles?

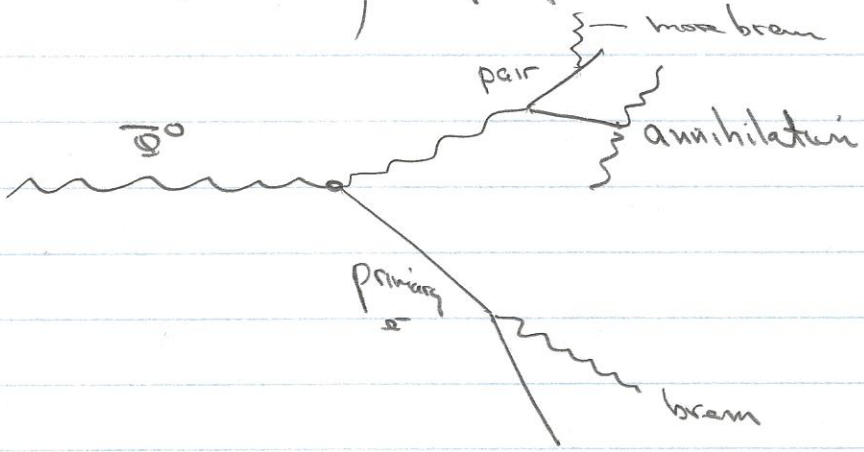
at some depth $z > R(E_{0,max})$



the technical name for this is "electron penumbra"

What about the scattered photons?
(primarily Compton scatter)

Returning to our μ-scopic picture



The primary γ interaction and the electron (or pair) set in motion, drives (is the source of) all other secondary particles in the target.

We can write the total fluence symbolically as

$$\Phi(E) = \Phi_0(E) + \Phi_s(E)$$

$\Phi_0(E)$: primary; $\Phi_s(E)$: the rest

If you have the strength, you can push this quite far, mathematically...

Let's consider the dominant contribution, the 1st compton scattered photon

We can write

$$K_c(\vec{x}) = K_c^0(\vec{x}) + K_c^1(\vec{x})$$ meaning 1st generation

$$K_c^1(\vec{x}) = \int_0^{E_{s,max}} dE_s \; \psi_s^1(\vec{x}, E_s)\, \mu_{en}(E_s)$$

(1st generation energy fluence)

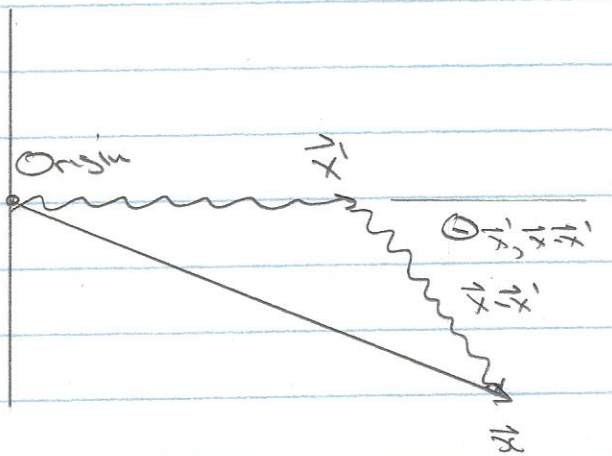
$$q_s(\vec{x}, E_s; \vec{x}', E_x)$$

($\vec{x}$: primary interaction; $\vec{x}'$: primary energy)

$$= E_s \frac{[d\mu_c(E_x, E_s, \cos\theta)/dE_s]}{\sigma_{c\text{-compton}}} \left(\frac{1}{4\pi|\vec{x}-\vec{x}'|^2}\right)$$ (fluence fall off from interaction point)

$$* \exp\left\{ - \int_0^{|\vec{x}-\vec{x}'|} dl\, \mu(\vec{l}, E_s) \right\}$$

(Radiological path)



Disclaimer: Any Rx calculation is reduced to multi-dimensional integrals and later loops. It can be shown that MC calcs are more efficient for 3-dimensionality ≥ 4

Complicated, but it is an accurate formulation of scatter kerma. This has been carried out to 4 generations. (John Wong et al 1984)

The effect of scatter dose, a heuristic model

Do a 1D calculation...

$$\frac{d\phi_n}{dz} = f\mu_{n-1}\phi_{n-1} - \mu_n\phi_n$$

f: survival fraction; n: scatter generation

Let

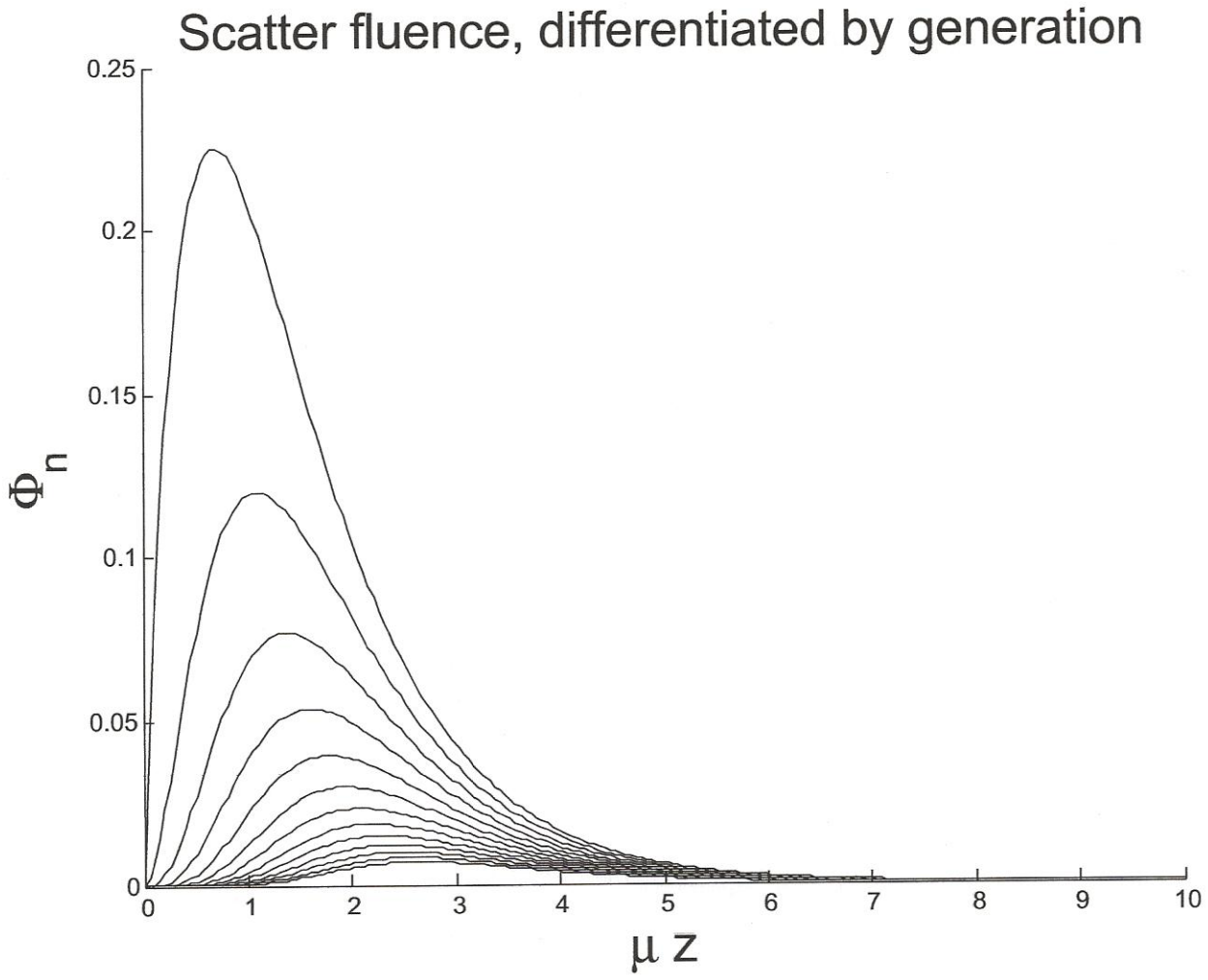
$$\mu_n = n\mu_{n-1}$$

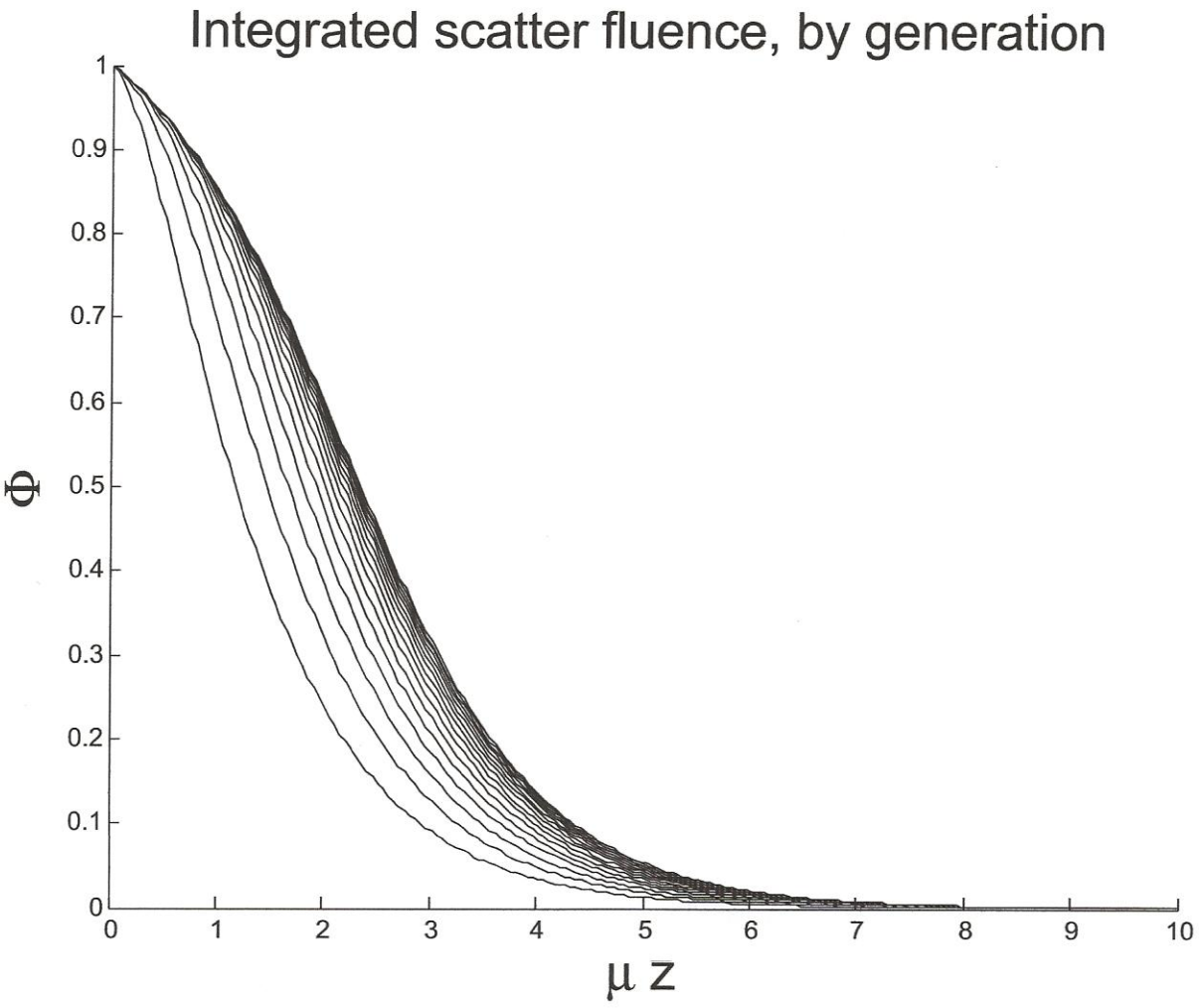
$$\mu_1 = \mu$$
$$\mu_2 = 2\mu_1 = 2\mu$$
$$\mu_3 = 3\mu_2 = 3\cdot 2\mu \ldots$$

This accounts for increase in attenuation as energy degrades

$$\phi_n = \phi_0 e^{-\mu z}\left[f(1-e^{-\mu z})\right]^{n-1}$$

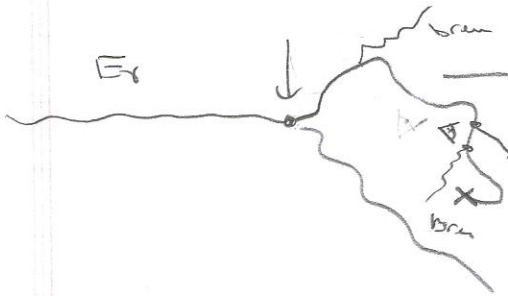
$$\Phi = \sum_{n=1}^{\infty}\phi_n = \frac{\phi_0 e^{-\mu z}}{\left[1 - f(1-e^{-\mu z})\right]}$$


Scatter fluence, differentiated by generation
0.25
0.2
0.15
0.1
0.05
0
Φ_n
0
1
2
3
4
5
6
7
8
9
10
μ z

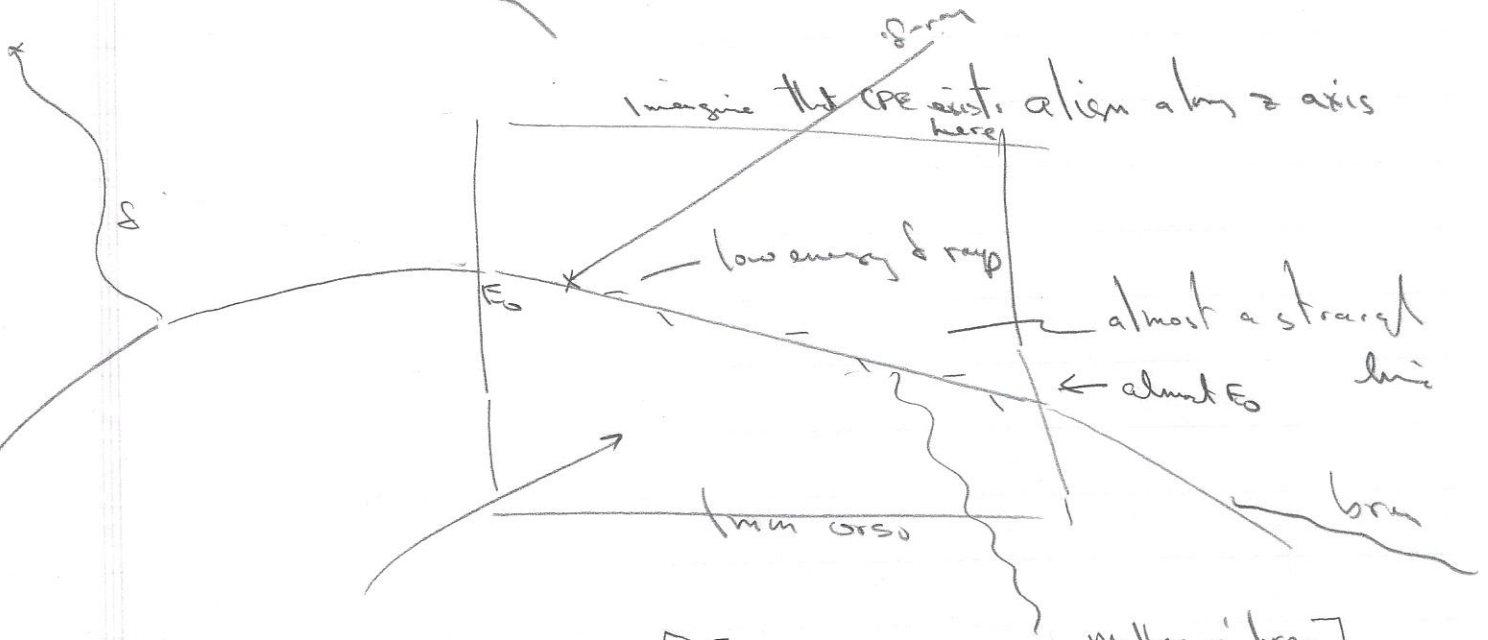

Integrated scatter fluence, by generation
Φ
μ z
0
0.1
0.2
0.3
0.4
0.5
0.6
0.7
0.8
0.9
1
0
1
2
3
4
5
6
7
8
9
10

Dose due to electrons

Compton interaction in water

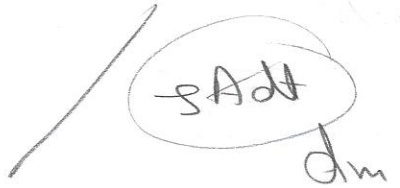


exercises a tortuous path



$$D^{e^-} = \underbrace{\Phi^e(E_0)\left[\int_0^{E_{tr,max}} dE_{tr}\, E_{tr}\, \frac{d\sigma}{dE_{tr}}(E_0, E_{tr})\right]}_{dE}\; n A dt$$

moller + brem



$$\frac{n}{\rho}\int_0^{E_{tr}} dE_{tr}\, E_{tr}\, \frac{d\sigma}{dE_{tr}}(E_0, E_{tr}) = \frac{S(E_0)}{\rho}$$

is called the "mass" stopping power

Recall the $\frac{\mu}{\rho}$ $\frac{\mu_{en}}{\rho}$ $\frac{\mu_{tr}}{\rho}$

are independent of density

$\frac{S(E_0)}{\rho}$ is almost independent of density.

Why?

Explain "density effect"

Note that this method of dose estimation assumes several things

1) over dm, CPE exists
2) a Mollers, brems considered "curled up"

2b) ↑ not so bad range very short ↑ dosimetry bad range very long Dose too high

3) extra bending of the primary e^- track is not accounted for

Dose a little too low

Better strategy, separate the Moller/Bhabha cross section into separate parts

$$D^{e^-} = \overline{\Phi}^e(E)\frac{S_c(E_0)}{\rho} + \overline{\Phi}^e(E)\frac{S_r(E_0)}{\rho}$$

mass collision stopping power

$$\frac{S_c}{\rho} = \frac{n}{\rho}\int_0^{E_{\max}} dE_s\, E_s \frac{d\sigma_{Moll}}{dE_s}$$

mass radiation stopping power

$$\frac{S_r}{\rho} = \frac{n}{\rho}\int_0^{E_{\max}} dE_\gamma\, E_\gamma \frac{d\sigma_{Brem}}{dE_\gamma}$$

if you know that you are only dealing with small regions, assume γ's carried away, deal with separately

usually quite successful.

[This is what we usually shall do]

See

If the δ-rays are not in CPE, split them off and handle separately. The dose due to small energy δ's, i.e.

$$D^e_\Delta = \overline{\Phi}(E_0)\frac{L(E_0,\Delta)}{\rho}$$

mass restricted stopping power

$$\frac{L(E_0,\Delta)}{\rho} = \frac{n}{\rho}\int_0^{\Delta} dE_s\, E_s \frac{d\sigma}{dE_s}(\delta, E_0)$$

Δ is a parameter

$\Delta \downarrow$ more accurate microscopic transport
more δ rays to consider
more computationally intensive

MCNP uses $\left(\frac{\Delta c}{\rho}\right)$, superimposes δ transport on top of primary track

EGS4,5 codes $\left(\frac{lc}{\rho}\right)$ $\Delta \downarrow$ 1 keV

Penelope codes $\left(\frac{lc}{\rho}\right)$ $\Delta \downarrow 0$! true event by event modelling

note: In the slowing down of a 1 MeV electron in water, it has ~

$\begin{cases} 10^5 & \text{elastic scatterings (Rutherford type)} \\ 10^4 & \text{inelastic " (E-loss events)} \end{cases}$

Radiotherapy calcs using MC require about 10^9 primary particle simulations

10^9 particles $\times \sim 10^6$ (interactions/primary) $\times \approx 10^4$ (flops/interaction)

$\sim 10^{19}$ floating point operations per application

$\Rightarrow$ 10^7 seconds, on a Teraflop machine

Modern MC techniques have reduced this to about 100 s

$\frac{EL^2}{M}$

Electron Ranges



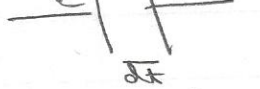
length of total curved path determined by E_0

units

$\frac{S_c(E_0)}{\rho}$ $\qquad$ $\frac{E}{(M/L^2)}$

$S_c(E_0)$ has units $\frac{E}{L}$ "energy loss / unit length"

energy deposited in thin slabs



$\Delta E \cong S(E)\,\Delta x$

$\Delta E = S(E)\,\Delta x$

So, $E_0 = \int_0^{R_e(E_0)} dx\, S_c(E)$ — collision stopping power is used

Note that E is really a function of x

$$E(t) = E_0 - \int_0^t dt' \, S(E(t'))$$

implicit equation relating E & t

given t, E found by integration
given $E(t)$, t found by iteration

When $E(t) = 0$, this t is called the electron range.

$$0 = E_0 - \int_0^{R_e(E_0)} dt' \, S(E(t'))$$

Rule of thumb
In water

$$R_e(E_0)^{[cm]} = \frac{E_0[MeV]}{2}$$

So $E_0 = 20\,MeV$ $R = 10\,cm$

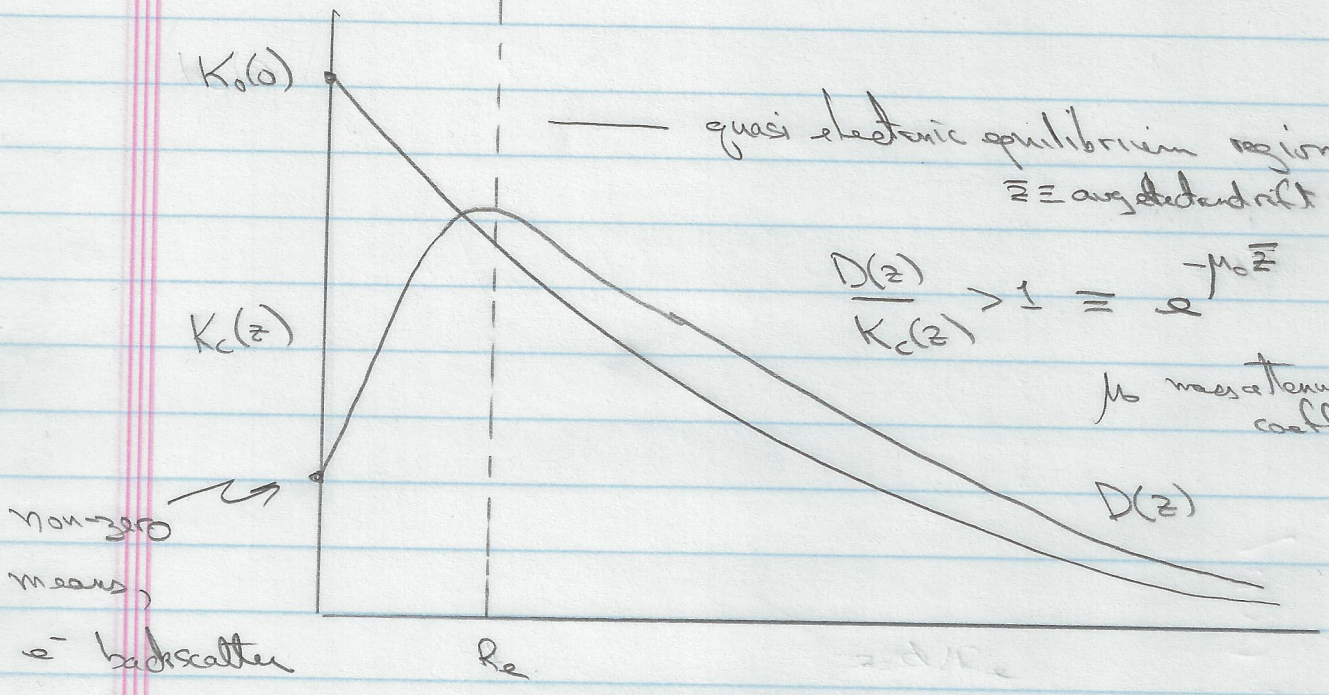
Electrons from first collisions in mono-energetic γ beams

- of course, we can always $\int dE_\gamma$!

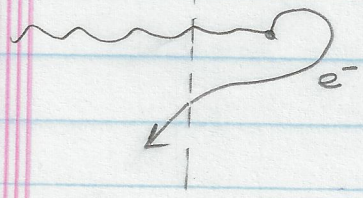
We'll also treat only, broad (meaning only wide), normally incident γ beams.

It's easy to make these adjustments

Recall our current level of understanding

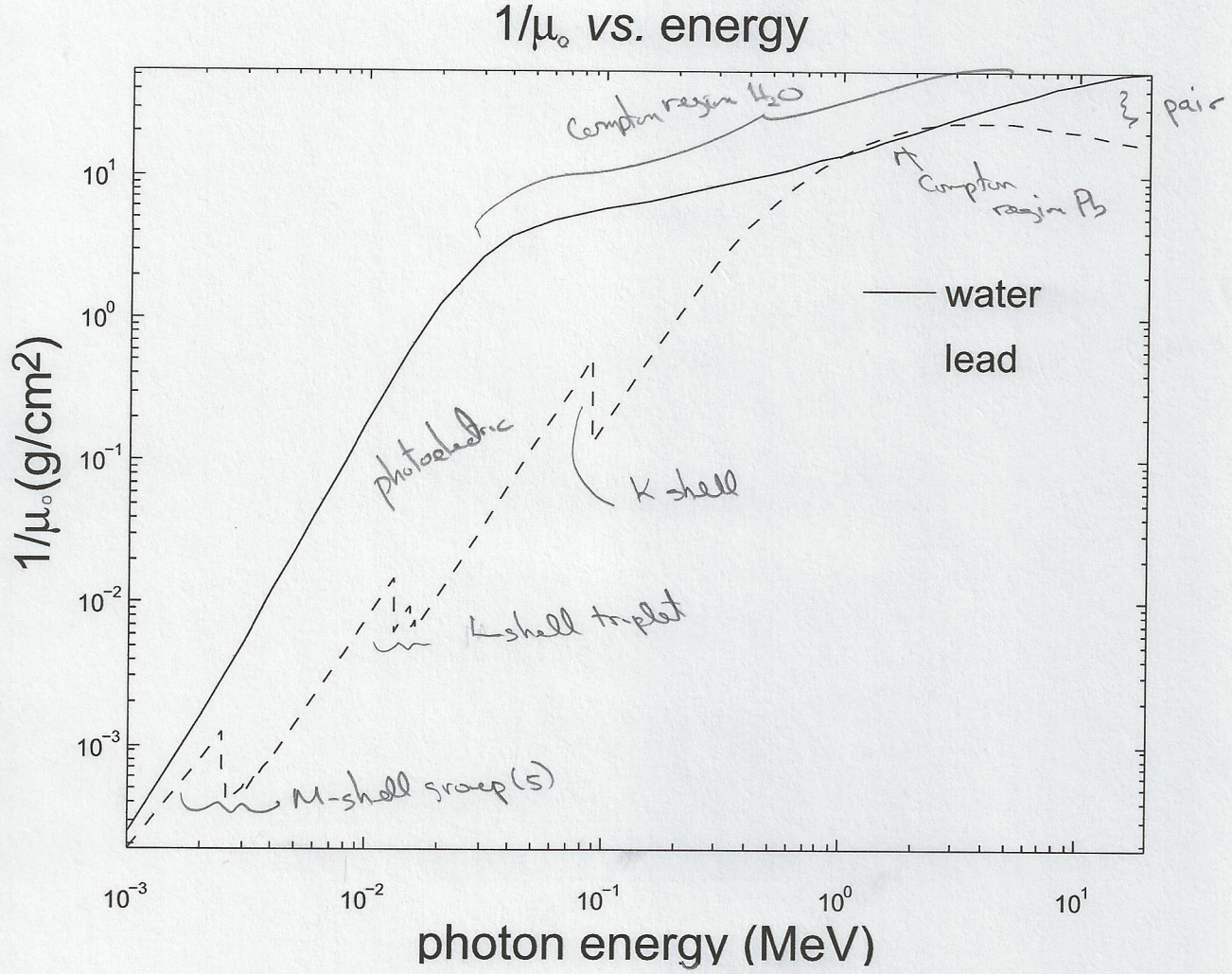


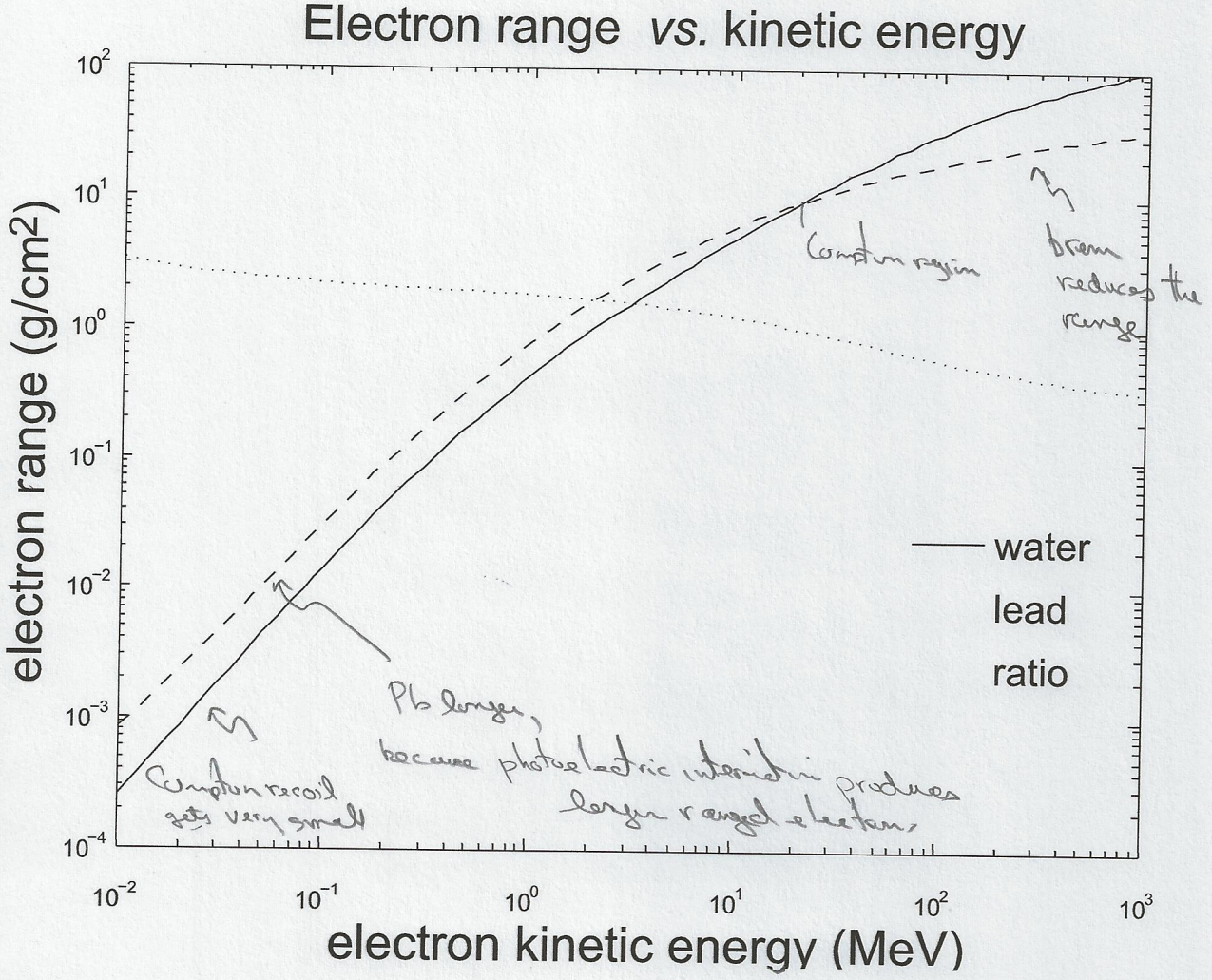
R_e ≡ electron range



We are going to model this analytically, but first some basic radiation physics

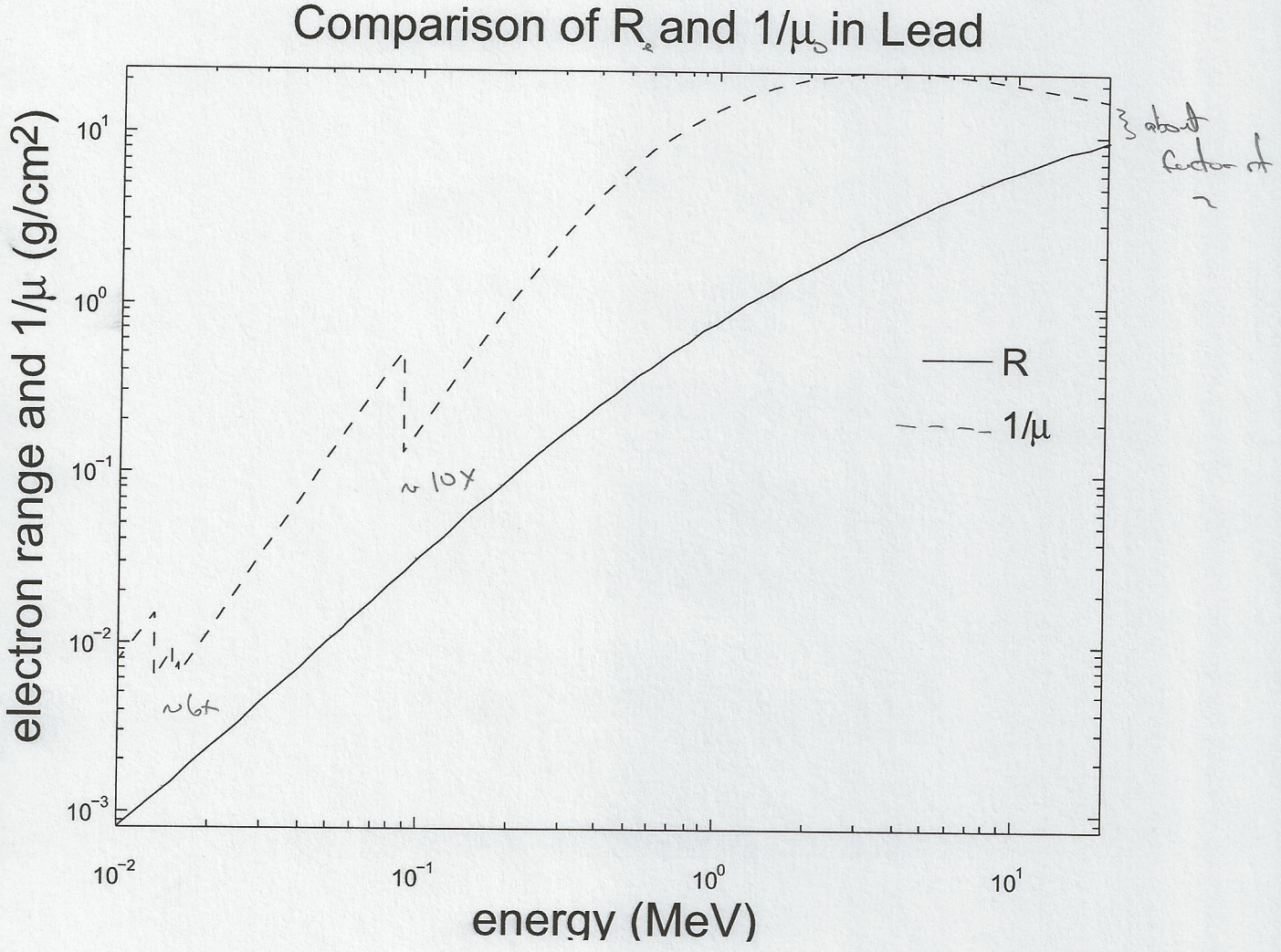
mean free path, as in $e^{-\mu_0 z}$




Electron range vs. kinetic energy
electron range (g/cm2)
electron kinetic energy (MeV)
water
lead
ratio
Compton region
Brem reduces the range
Pb longer, because photoelectric interaction produces longer ranged electrons
Compton recoil gets very small

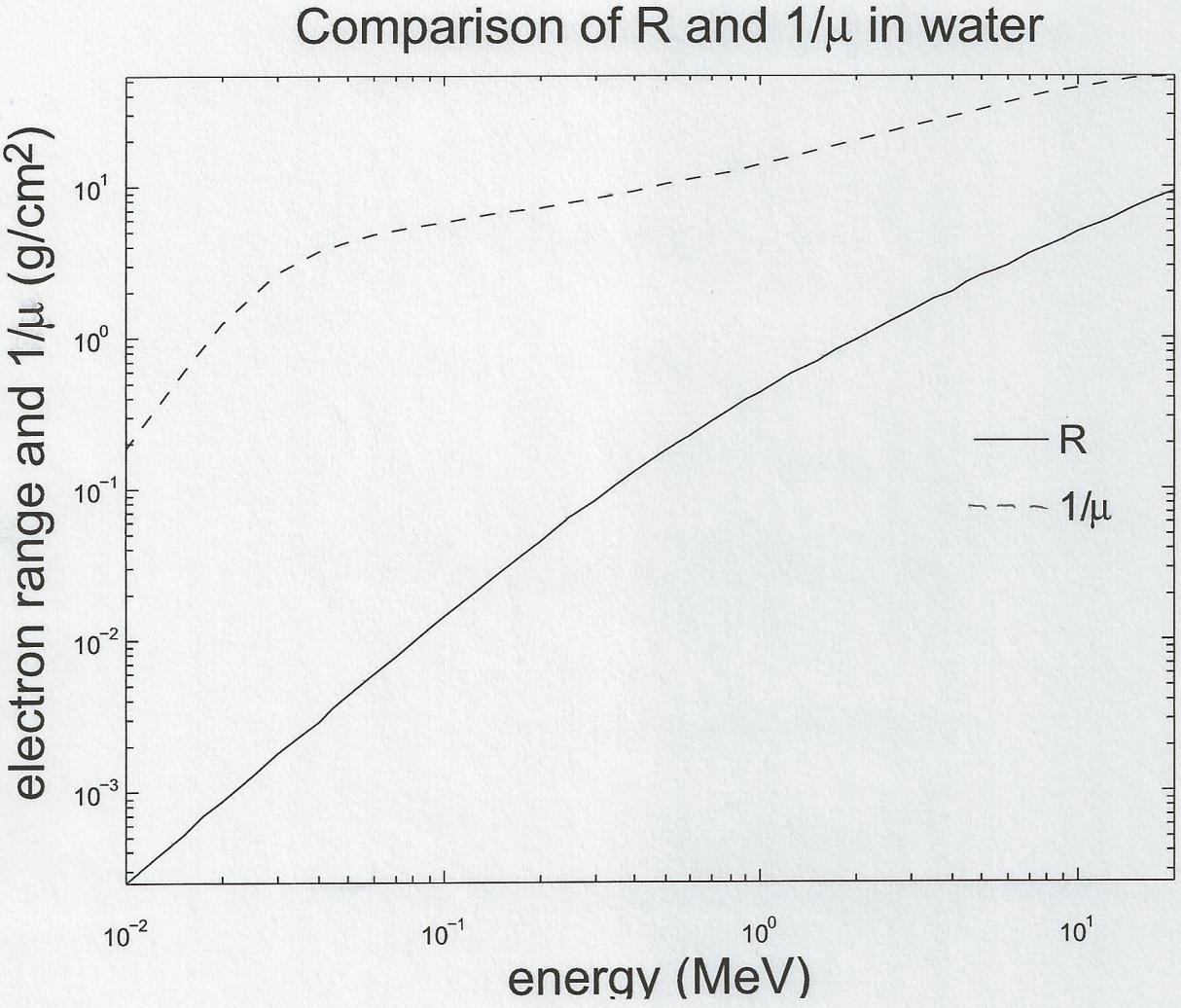
$R_e << \frac{1}{\mu_0}$ for most of the Rx range

$\Rightarrow \quad \mu_e R_e << 1$



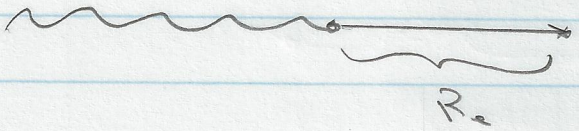
Again, $R_0/\mu_0 \ll 1$

This will facilitate the analysis



The electron transport models

Model Ia: The straight ahead model



Unrealistic, certainly, but it does lead to an estimate of the enhancement over the $K_c(z)$ line.

This gives $\frac{D(z)}{K_c(z)} = e^{+\mu_0 R_e/z}$

in the quasi equilibrium region

Note $\frac{D(z)}{K_c(z)} = e^{\mu_0 R_e/z} \doteq 1 + \mu_0\left(\frac{R_e}{z}\right)$

$z \equiv$ average electron drift in this model

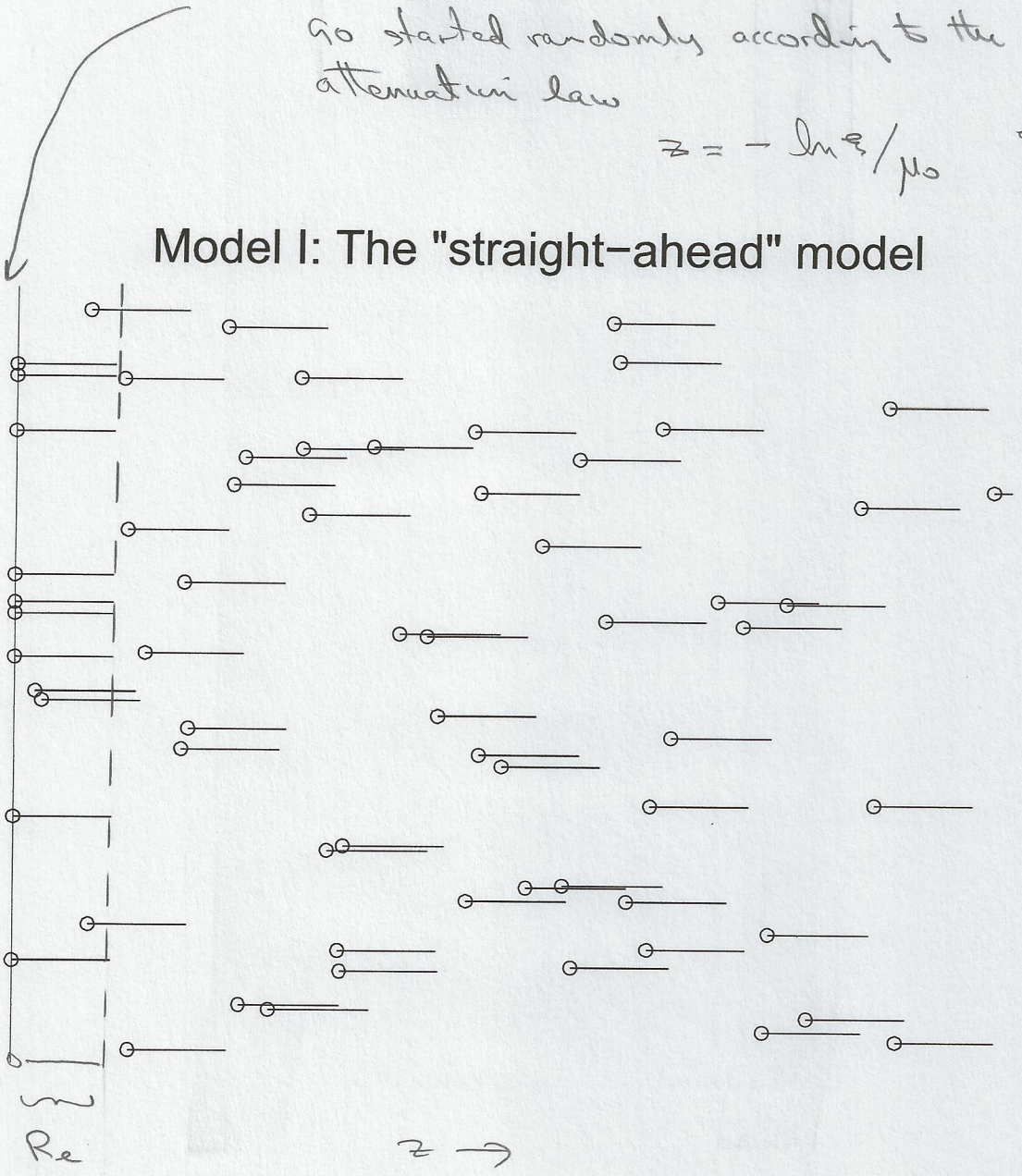
Graphs on next pages

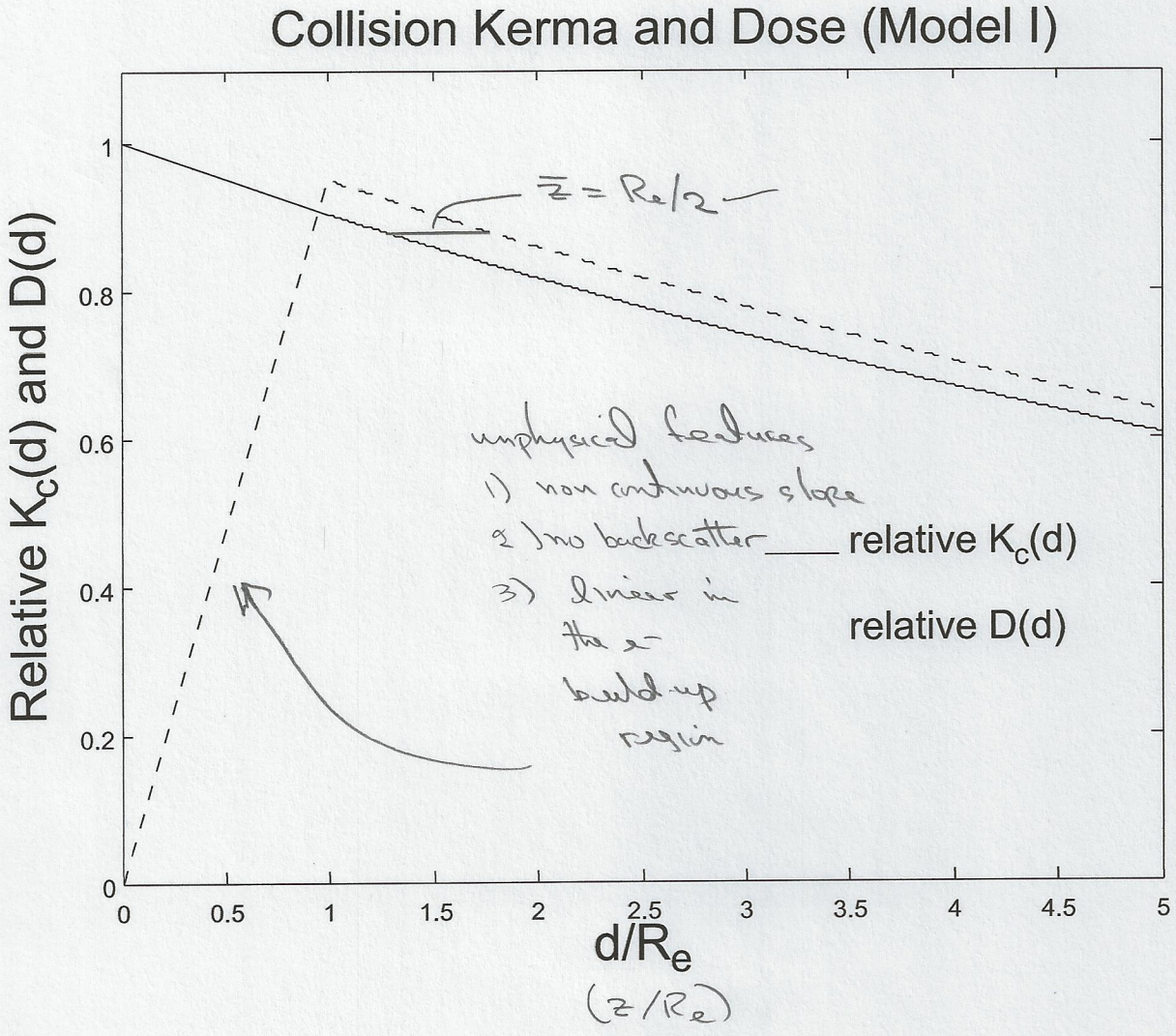
Monte Carlo Calculation

10 e^- started at the surface (for illustration)

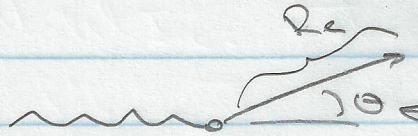
90 started randomly according to the attenuation law

$z = -\ln \xi / \mu_0$ ξ = random variable uniform on $0 \leq \xi \leq 1$




Collision Kerma and Dose (Model I)
Relative K_c(d) and D(d)
d/R_e
(z/R_e)
$\bar{z} = R_e/2$
unphysical features
1) non continuous slope
2) no backscatter
3) linear in the build-up region
relative K_c(d)
relative D(d)
0
0.2
0.4
0.6
0.8
1
0
0.5
1
1.5
2
2.5
3
3.5
4
4.5
5

Model Ib:



← use the Compton angular distribution

$$\bar{z} = \frac{R_\alpha}{2}\bar{\mu}_c$$ — average cosine from the Compton distribution

This will give some backscatter, undo the linearity, probably solve the discontinuity problem, but will still overestimate the z in the QER, because it ignores multiple scattering of the electrons.

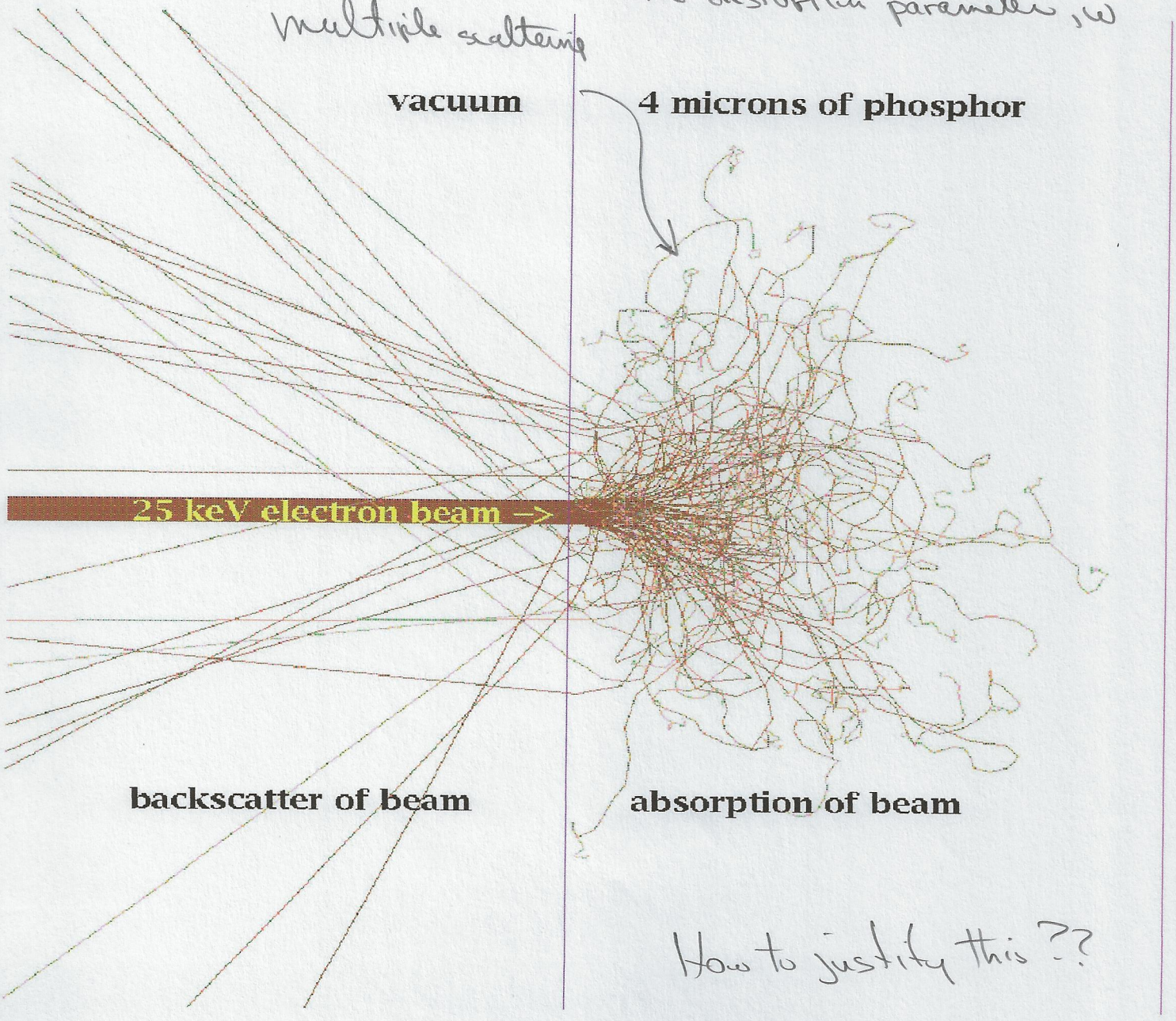
Anyone want to pursue this, for extra credit?

Instead, go to a "semi-isotropic" model

$$P_e(\theta, E)\, dE \sin\theta\, d\theta\, d\phi = \delta(E - f_c(F_0)E_0)\, \frac{1+w\cos\theta}{2} \sin\theta\, d\theta\, \frac{d\phi}{2\pi}$$

$f_c(F_0)$: $\frac{E}{E_0}$ as in K_c

All the multiple scattering info is buried in the distortion parameter, w



How to justify this??

(145)

Phys. Med. Biol., 1990, Vol. 35, No 4, 517–538. Printed in the UK

An analytic theory of the point-source non-uniformity correction factor for thick-walled ionisation chambers in photon beams

Alex F Bielajew

Division of Physics, Ionizing Radiation Standards, National Research Council of Canada, Ottawa, Canada K1A 0R6

Received 6 June 1989, in final form 26 September 1989

Abstract. In exposure and air kerma measurements, axial and radial non-uniformity perturbation correction factors are used to account for the non-uniformity of the incident photon field in the vicinity of the ionisation chamber cavity. An analytic theory for calculating the point source non-uniformity correction factor for thick-walled ionisation chambers is developed. The theory developed herein is compared with Monte Carlo calculations for chambers with pancake, cylindrical and spherical geometries similar in size to the instruments employed by Standards laboratories. The agreement between Monte Carlo calculations and the analytic theory is excellent and demonstrates the viability of the analytic theory at large and small source to chamber distances. The perturbations, which differ from those calculated or measured by some Standards laboratories, suggest that corrections of the order of 0.3% should be applied to typical pancake geometries, smaller corrections of the order of 0.05% or less for typical Farmer-type chambers, and no correction for spherical chambers. The analytic theory predicts chamber geometries which can either minimise or maximise the effect of point source non-uniformity. An experiment is described that would measure the correction with good accuracy.

1. Introduction

When a detector is placed in the field of a radiation source, the point at which the radiation field is being measured is uncertain, owing to the finite size of the detector. In the realm of exposure or air kerma measurement performed in Standards laboratories, one usually assumes that the 'point of measurement' is at the geometric centre of the chamber and the correction for the departure in ion chamber response from the inverse-square law is accounted for by the 'axial' and 'radial' non-uniformity correction factors, k_{an} and k_{rn}, respectively. The axial factor is a correction for the non-uniformity of the photon field along the line from the source through the cavity centre while the radial factor accounts for non-uniformity in the transverse direction. The radial correction also accounts for the transverse field non-uniformity due to finite-size source effects and scatter from the collimator and room.

There are divergent views as to how the correction for point source non-uniformity is to be applied (Gray 1937, Failla and Marinelli 1937, Mayneord and Roberts 1937, Spiers 1941, Burlin 1959, Kondo and Randolph 1960, Boutillon and Niatel 1973, Loftus and Weaver 1974, W H Henry as reported in Shortt and Ross 1986). For example, the BIPM (Bureau International des Poids et Mesures, France) ^{60}Co-exposure standard has a calculated correction of 0.9968 ± 0.0020 (Boutillon and Niatel 1973) for the axial

© 1990 NRCC, Government of Canada

from Nelms (1953) while the photoelectron distribution is from the theory of Sauter (1931). Sauter's theory was also employed to model the photoelectron angle in the Monte Carlo calculations (Bielajew and Rogers 1986).) Thus, the location of the peak is determined by the cutoff energy. At low incident energies approaching the cutoff energy, the use of the present theory is inappropriate since it neglects the electrons generated in the cavity gas. At higher energies, well above the cutoff, the values of ω are more realistic and only weakly dependent on the cutoff energy.

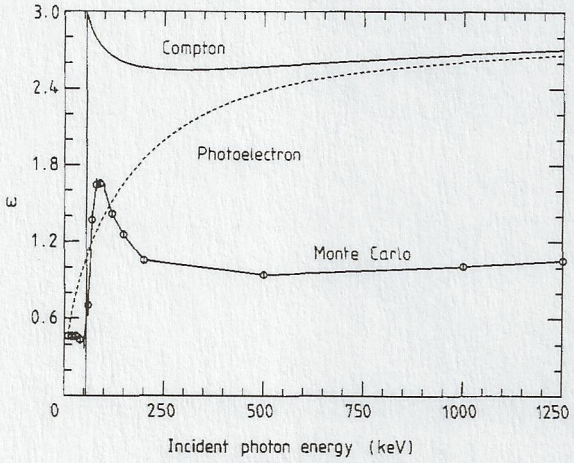


Figure 3. Values of ω against incident photon energy for the energy-deposition weighted electron distributions (δ-rays included) above 10 keV. ω-values for theoretical distributions Compton and photoelectron angular distributions are shown as well.

Therefore, the appropriate value of ω also depends indirectly on the size of the cavity through the parameter Δ of Spencer–Attix cavity theory (Spencer and Attix 1955). Electrons below this energy in a cavity should be considered to have been generated there through knock-on electron interactions. Recall that a basic assumption of the analytic theories was that electrons that deposit dose in the cavity are generated in the walls of the cavity. Therefore, only the electrons above Δ should be considered. Large cavities, where an appreciable part of the dose to the cavity comes from primary photon interactions within the cavity gas, are beyond the scope of the present theory. A plot of ω versus Δ in graphite is given in figure 4 for a monoenergetic incident energy of 1.25 MeV for a range of Δ covering almost any small chamber. The variation in ω is monotonic from about 0.88 to 1.15 for Δ ranging from 1 to 25 keV. Smaller values of ω are obtained for smaller values of Δ since more energy is deposited from more isotropically distributed δ-rays. For a typical ^{60}Co incident photon spectrum (Rogers *et al* 1988), ω was calculated to be 1.058 ± 0.0011, and for a typical ^{137}Cs spectrum (Costrell 1962) the value 0.975 ± 0.006 was obtained. Having determined the size of one's chamber in terms of Δ, one should use the ω-value from figure 4 in conjunction with the appropriate expressions from the previous section or the κ-factors depicted in figure 1.

3. Monte Carlo comparisons

In this section Monte Carlo calculations of ion chamber response and correction factors

The Kondo and Randolph isotropy assumption is represented by the constant line at unity. The anisotropy approximation, $1+\omega\cos\theta$, is a first order expansion in Legendre polynomials. Therefore, ω was obtained from the Monte Carlo data by the integral

$$\omega = \frac{3}{2}\int_{-1}^{1} \mathrm{d}(\cos\theta)\ \cos\theta[\mathrm{d}P/\mathrm{d}(\cos\theta)]_{\substack{\text{Monte}\\\text{Carlo}}}. \tag{22}$$

It is clear, at least for this example, that the Kondo and Randolph isotropy assumption is an over-simplification. The simple anisotropy assumption, $1+\omega\cos\theta$, fits the Monte Carlo better but a closer fit would require more terms in a Legendre series. Fortunately, the inclusion of just one term seems to work well for the calculation of A_{pn} for the cases studied. For 1.25 MeV photons, $\omega = 1.055 \pm 0.006(1\sigma)$. Although values of ω such that $|\omega| > 1$ are unphysical (the electron distributions can be negative!), one can accept this as part of the over-simplification of the first-order modelling of the electron distribution.

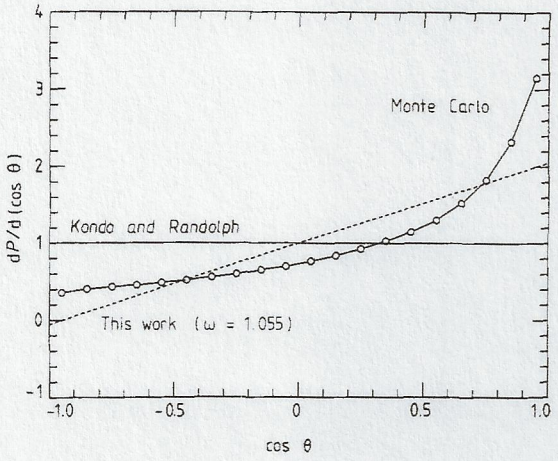
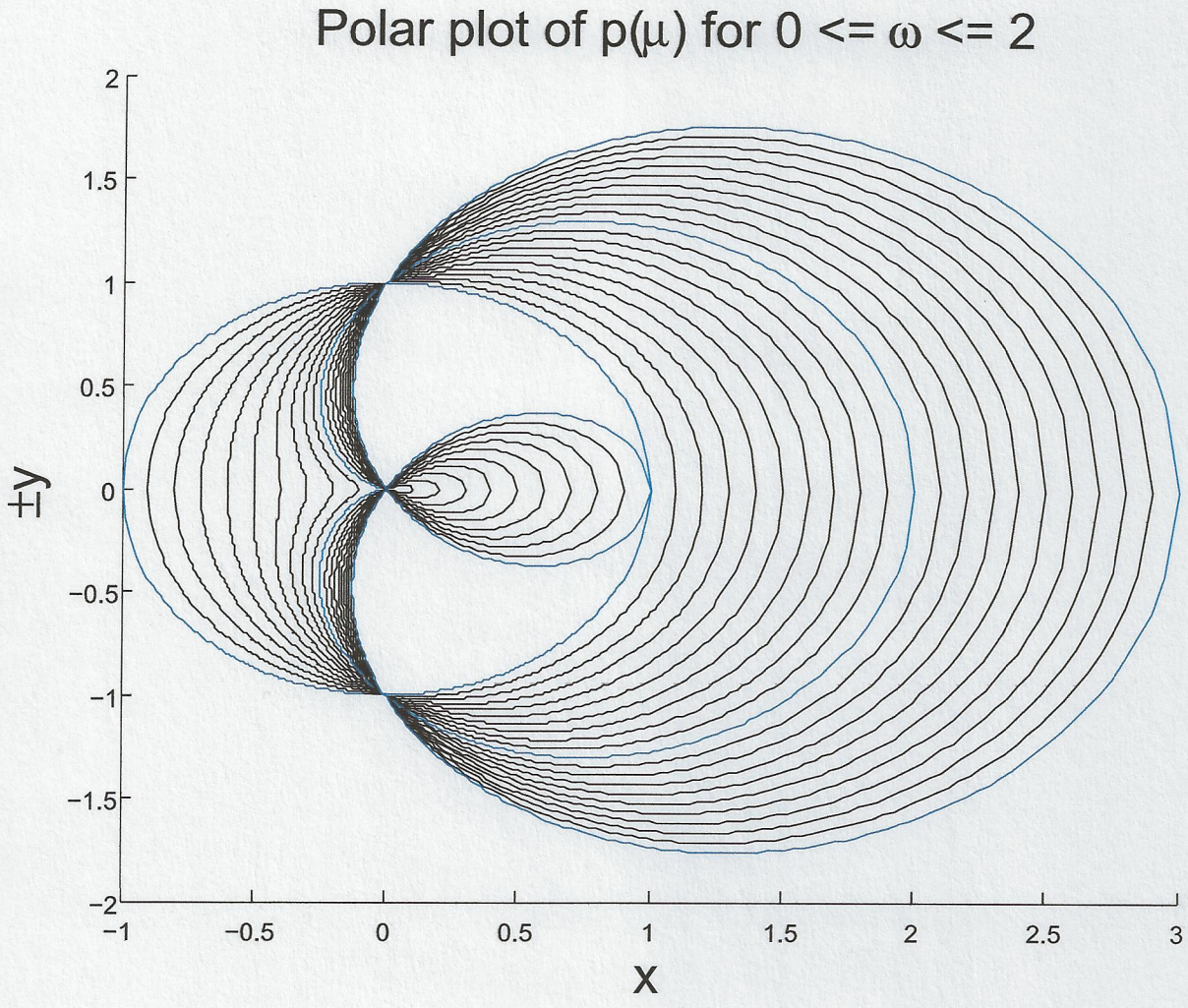


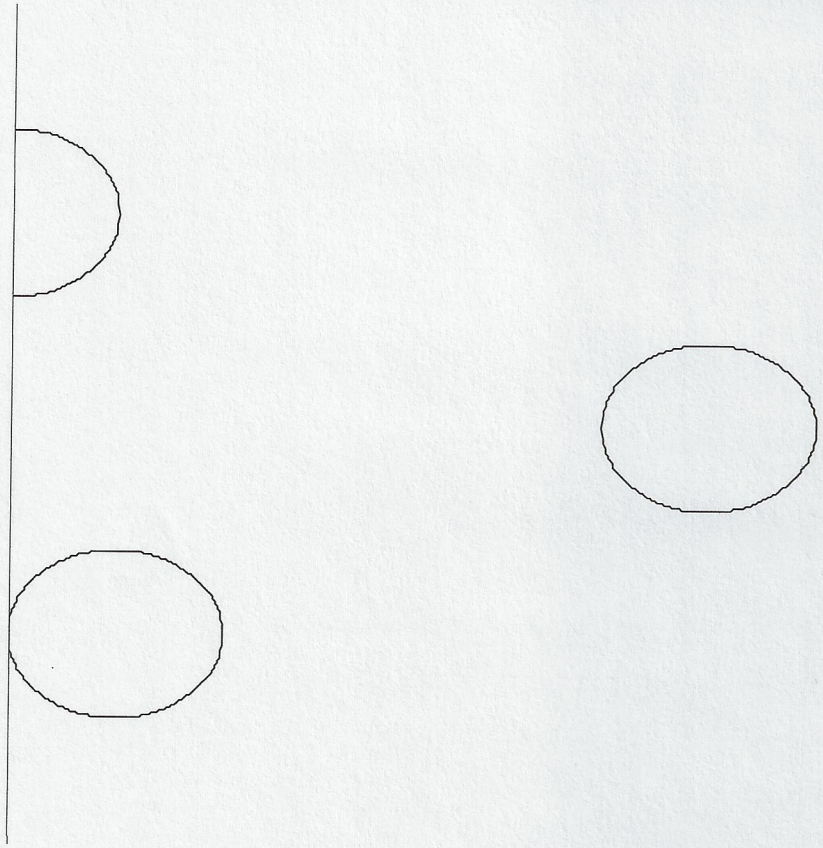
Figure 2. The energy-deposition weighted angular distribution of primary electrons (δ-rays included) above 10 keV for 1.25 MeV incident photons.

The dependence of ω with incident photon energy is given in figure 3 for the energy-deposition weighted primary electron distribution above a 10 keV cutoff in graphite. The maximum energy shown is for 1.25 MeV incident photons. As the incident energy is reduced, one sees a slow decrease in ω as increased multiple scattering causes the electron distribution to become more isotropic. However, a local minimum of about 0.95 occurs in the vicinity of 500 keV. Below this there is a sharp peak at around 85 keV. The explanation for this behaviour is that by employing energy weighting and restricting the contribution to electrons above the cutoff energy, the average Compton electron recoil angle for contributing electrons decreases as the incident photon energy is decreased. At a limit of about 55 keV incident photon energy, the only Compton electrons contributing are just above threshold and directed in the forward direction. Below this threshold, no Compton electrons contribute and the distribution is determined by the photoelectron distribution. The values for ω that would be obtained by using purely Compton or photoelectrons without multiple scattering are also shown in figure 3. (The unbound Compton distribution was taken

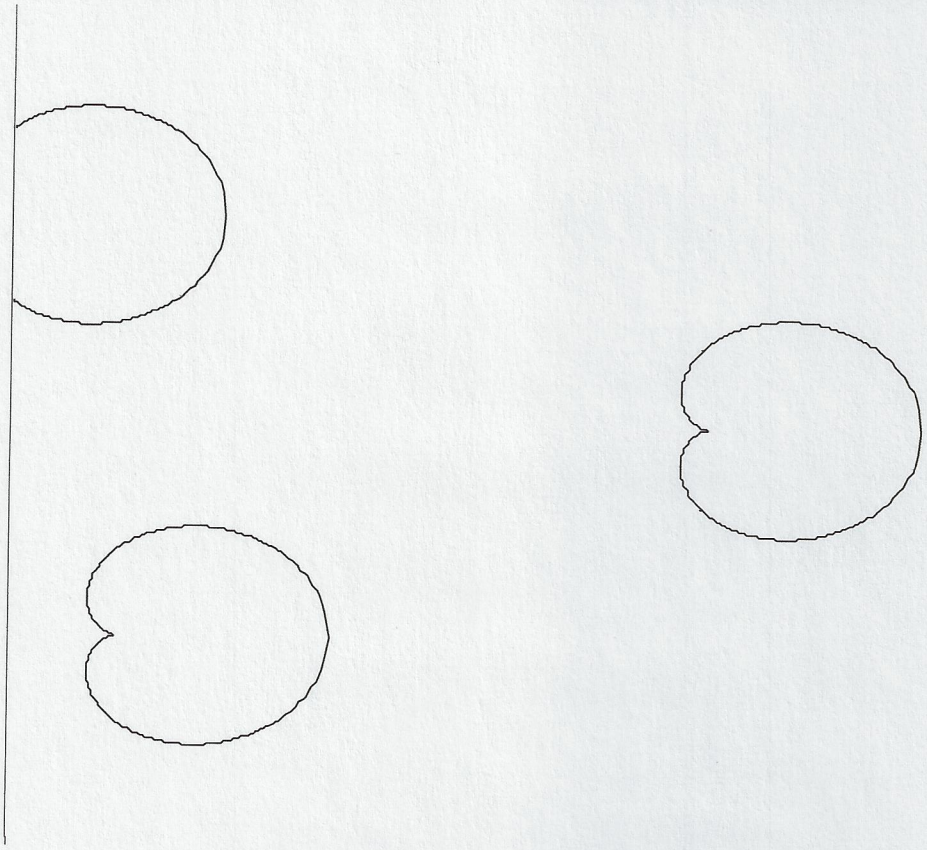
What do these electron distributions look like?



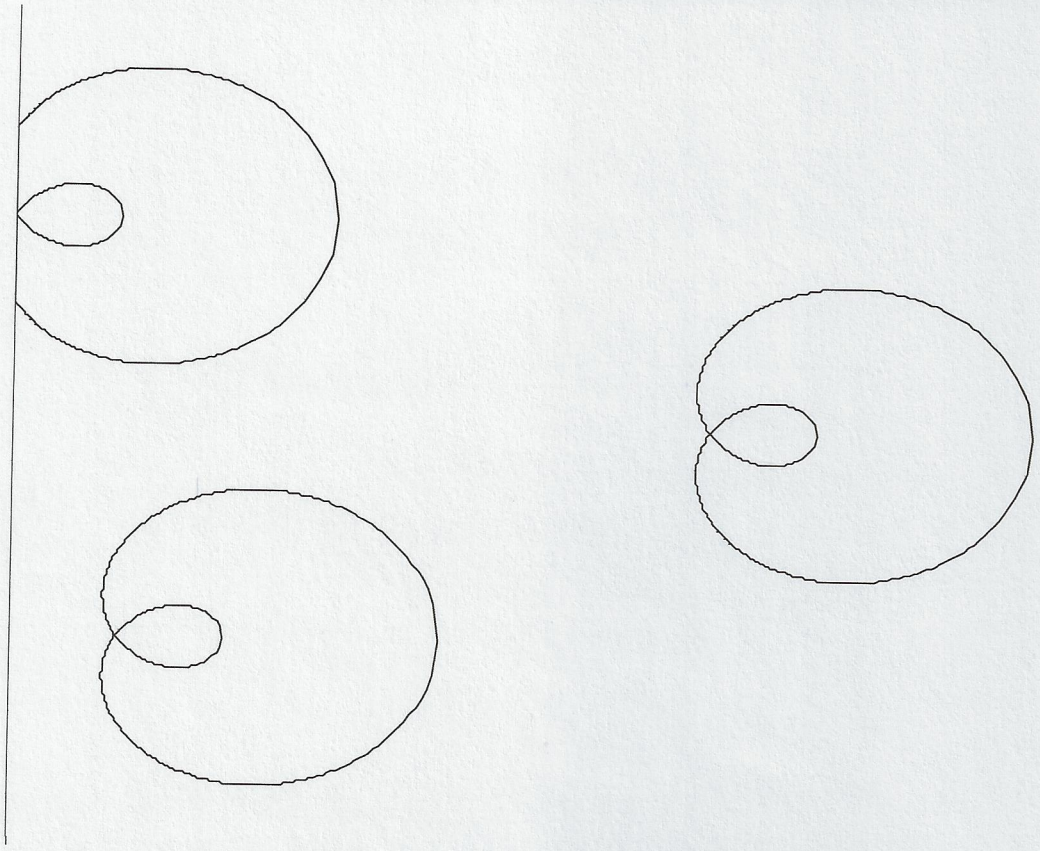
Model II: The isotropic model, $\omega = 0$



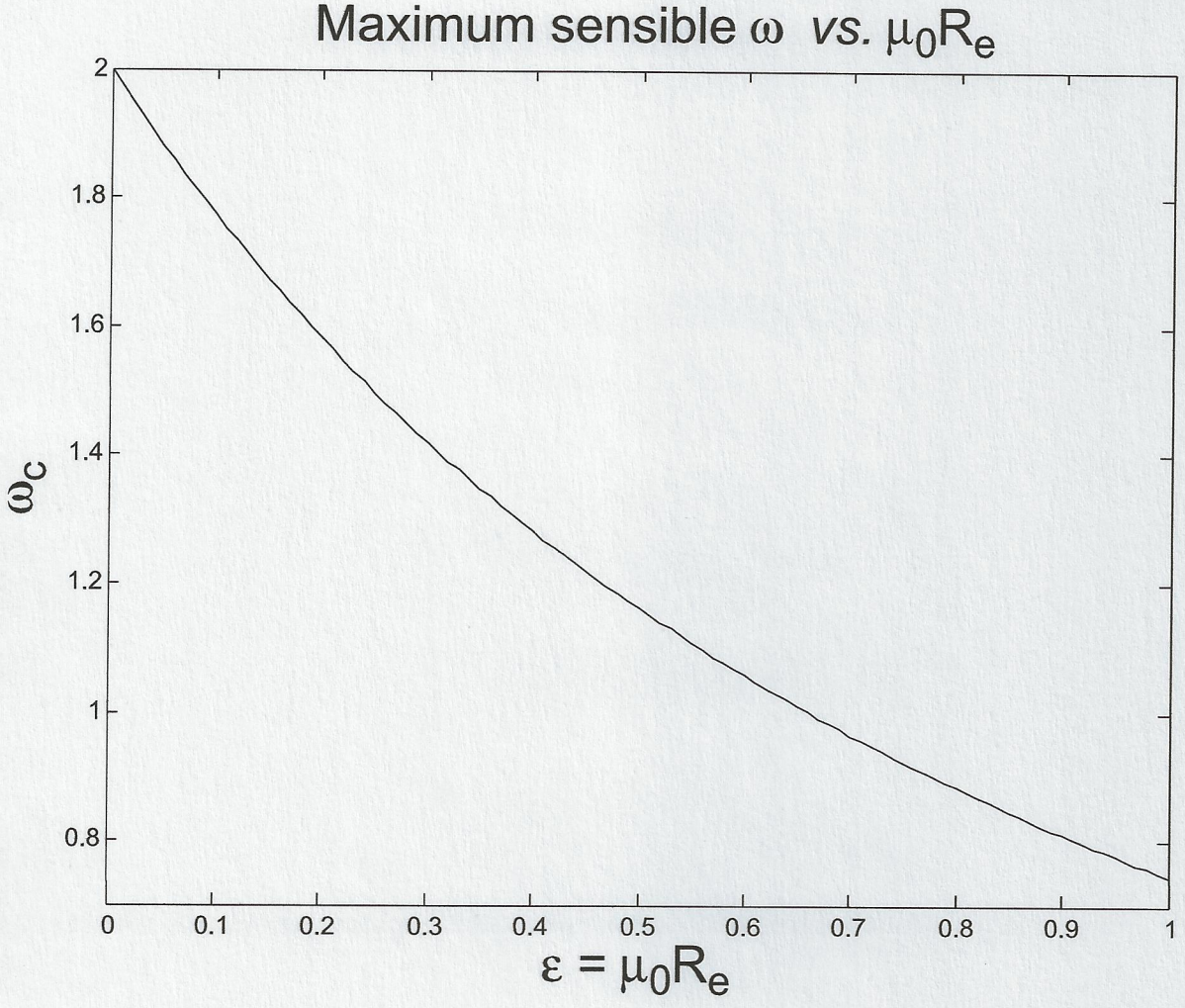
Model II: The semi−isotropic model, $\omega = 1$



Model II: The semi−isotropic model, $\omega = 2$

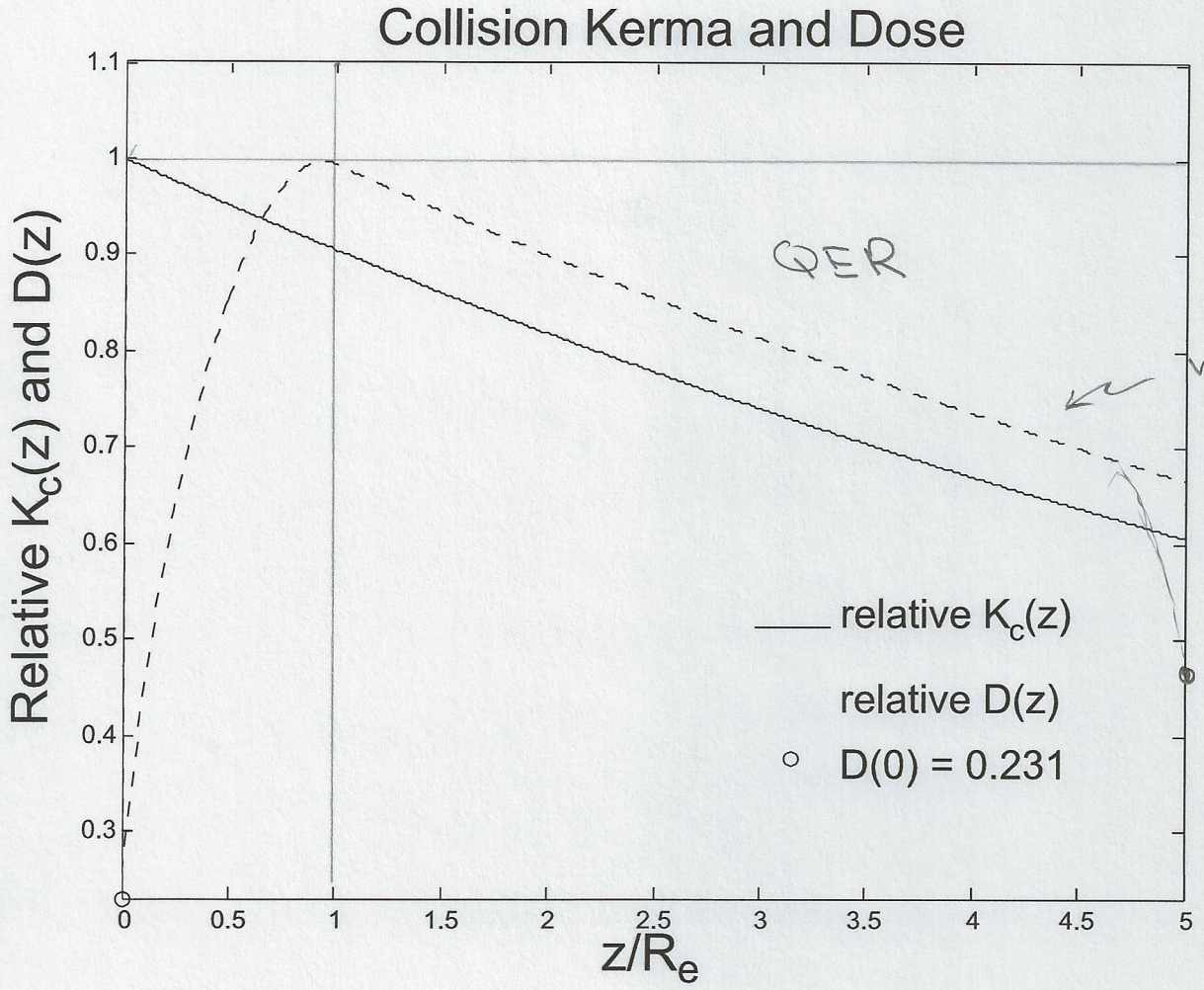


This the value of ω that forces the backscatter point D(ω) to 0



The results ...

This is for $\mu_0 R_e = 0.5$, $\mu_0 = \frac{1}{10}$ cm } a gross exaggeration for illustrative purpose



note: If there is a back boundary, there would be a build down

We'll talk about this more when we talk about "interfaces"

$\varepsilon \equiv \mu_0 R_e$

$$D(0) = \frac{K_c(0)}{2}\left[1 - \frac{\omega}{2} - \frac{\varepsilon}{4}\left(1 - \frac{2}{3}\omega\right) - \frac{\varepsilon^2}{18}\left(1 - \frac{3}{4}\omega\right) + O(\varepsilon^3)\right)$$

In the QER $\quad D(z) = K_c(z)\left(1 + \frac{\omega\varepsilon}{6} + \frac{\varepsilon^2}{18} + O(\varepsilon^3)\right)$

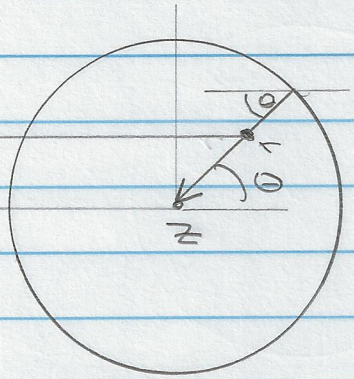
$\Rightarrow \bar{z} = \frac{\omega}{6} R_e$ — max value $\frac{1}{3} R_e$ of $\frac{1}{2} R_e$ for the simple model

How does one calculate this? [demo'd for $\omega = 0$]

Build up region (BUR)

Quasi-equilibrium region (QER)

attenuation is $e^{-\mu_0 z \cos\theta}$



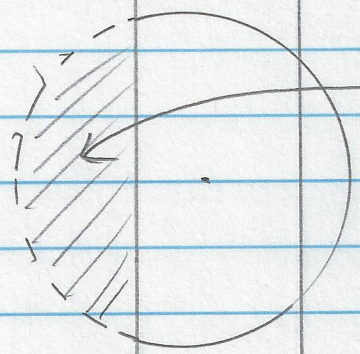
$0 \le r \le 1 + z\cos\theta$

$\varepsilon = \mu_0 R_e$

$$\frac{D(z)}{K_c(z)} = \frac{1}{2}\int_{-1}^{1} d\mu\,(1+\omega\mu)\left[\frac{e^{\varepsilon\mu}-1}{\varepsilon\mu}\right]$$

$$= I_>(z) = \frac{1}{\varepsilon^2}\left[\varepsilon\,Si(\varepsilon) + \omega(\sinh(\varepsilon) - \varepsilon)\right]$$

$$Si(\varepsilon) = \int_0^{\varepsilon} dx \frac{\sinh x}{x}$$



Call this part $I_<(z)$

$$I_<(z) = \frac{1}{2}\int_{z/R_e}^{1} d\mu\,(1+\omega\mu)\,\frac{\left[e^{\varepsilon\mu} - e^{\varepsilon y}\right]}{\varepsilon\mu}$$

= a very long and ugly expression

$$I_<(z) = I_>(z) - I_<(z)$$

Any new research results opens up more questions :)
than the answers provided (summer vacation, sabbatical)

Re w

Q. w, as calculated by MC calculations is very sensitive to δ, the lower bound of the electron transport used. How to nail this down? (See next page)

A.? Do MC calculations to lower and lower energies, to a threshold where ionization is no longer occuring.

Q. Real photon distributions are polyenergetic. How to adjust for this?

A1. QER. This is an easy one. $\int de$

A2. OK, this is complicated. Need to study (MC) w as a function of depth

Q. Are there any broader implications for electron transport theory?

Yes! ☺

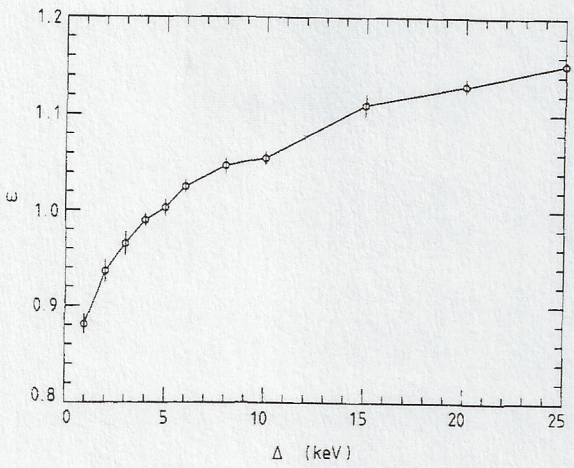


Figure 4. Values of ω for 1.25 MeV incident photons against Δ.

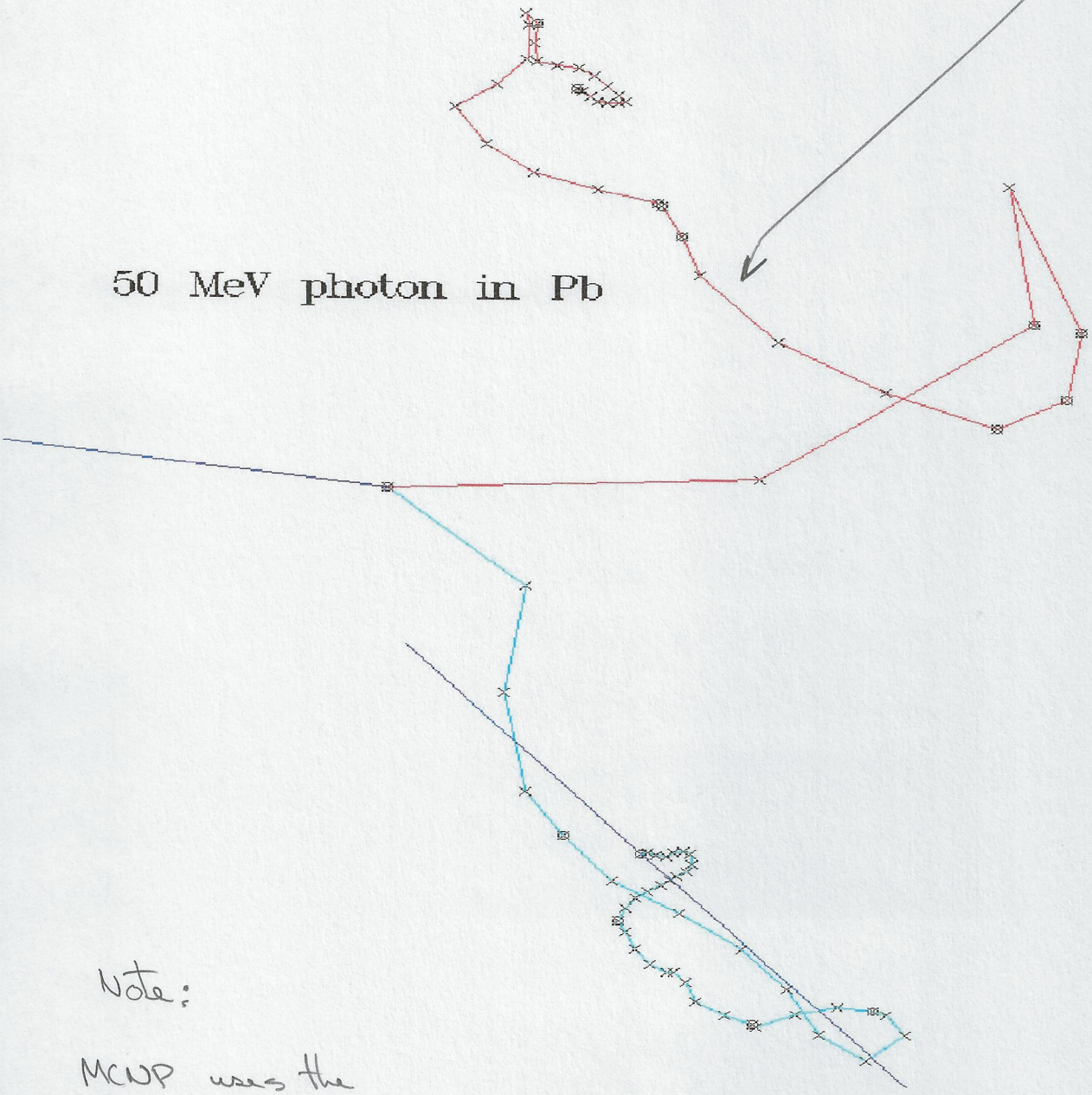
are described and the calculations to obtain the energy-deposition weighted primary electron distributions in § 2.1 are outlined. The EGS4 code system (Nelson *et al* 1985) is employed along with the PRESTA electron transport algorithm (Bielajew and Rogers 1987) that has been shown to calculate absolute ion chamber response reliably for carbon-walled chambers. For the ω anisotropy parameter, it was found necessary to employ an additional restriction on electron step-size whereby the maximum amount of energy lost to 'continuous' processes for each electron step was restricted to 2.0%. (ESTEPE was set to 0.02 (Rogers 1984).) Because PRESTA can take large electron steps, the additional restriction was found necessary to sample the angular distributions smoothly.

The EGS4 user codes employed in this report, DISTRZ (electron angular distributions, cylindrical-planar geometry) CAVRZ (cylindrical-planar geometry) and CAVSPH (spherical-conical geometry), are offspring of CAVITY, which has been used previously to calculate scatter and attenuation correction factors (Bielajew *et al* 1985, Rogers *et al* 1985). The reliability of the Monte Carlo calculations is considered to be within the stated uncertainties, which were estimated by dividing each calculation into 10 batches and calculating the estimated variance of the mean. For the angular distribution simulations, 10^4–10^5 primary photon interactions were used for each simulation which was performed on a μVAX 3600. Typical simulation times were 1–30 CPU minutes per incident photon energy. For the cavity chamber simulations, a minimum of about 8×10^5 primary photon interactions were employed for each simulation although as many as 9×10^6 were used for some cases. The cavity chamber simulations were performed on an IBM 3090 and typical simulation times were 1–7 h CPU per chamber for each distance. For both types of calculations, the primary photon was 'forced' to interact at least once in the chamber (a standard 'variance reduction' technique, see, for example, Rogers and Bielajew (1984)).

The angular distribution calculations were performed in a cylindrical-planar geometry. The medium was uniform 1.70 g cm^{-3} graphite, and the energy-deposition weighted angular distributions from electrons set in motion from the primary interactions as well as δ-rays set in motion by these electrons were scored. The electron transport threshold, below which no electron is transported, was set to Δ, the δ-ray creation threshold. (In

Monte Carlo breaks up the entire transport track into manageable, well understood segments.

The larger the segments, the larger the uncertainty!



Note:

MCNP uses the

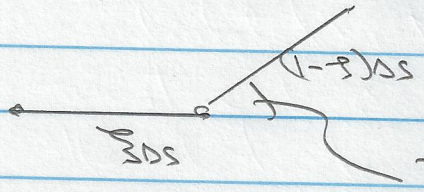
Model Ib method!

MCNP must use small steps to get the calculation stable.

Boundaries, interfaces, must be handled carefully.



The most sophisticated e- transport codes use the "random hinge"



ΔS = total step of the fragment

This angle is determined by multiple scattering distributions

Is there a connection?

Unknown

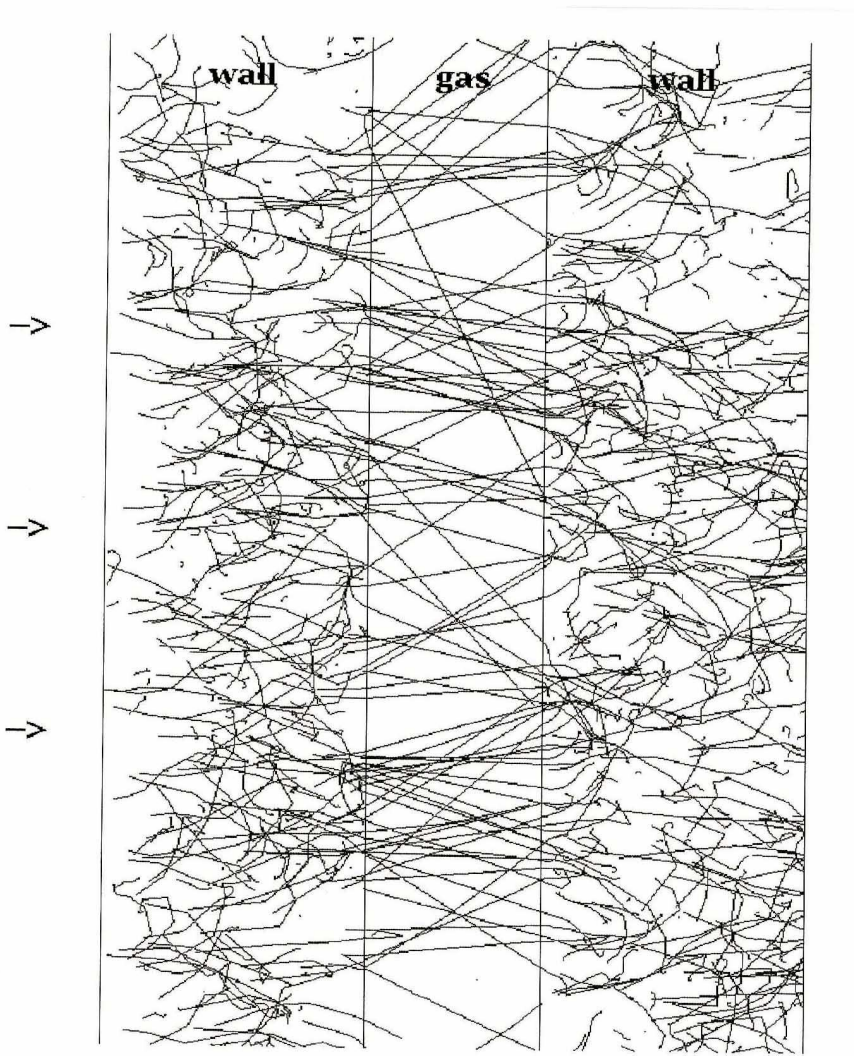
NERS590/Dosimetry/Lecture 7

- Cavity theory
- Review of electron transport applicable to the above
- The Convolution Method for photon dose deposition
- Prerequisite reading, Chapters 10 (Cavity Theory) in Attix.
- Read Attix, Chapter 12, for next time

Cavity theory and dosimetry

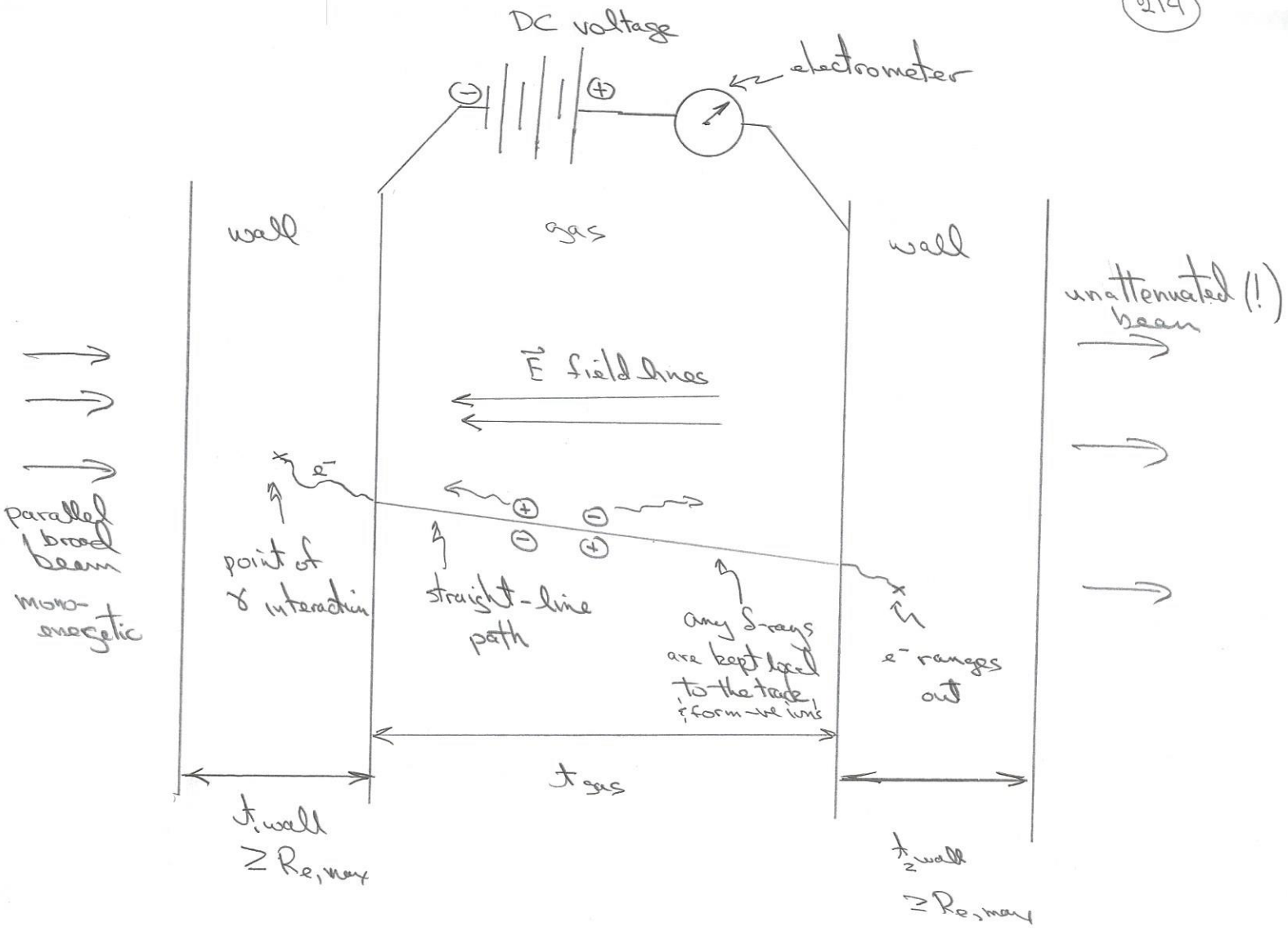
- Some of the most precise measurements in dosimetry involve instruments that can be characterized by "Cavity Theory".
- A cavity instrument is made up of walls, and a sensitive medium, from which a signal is extracted.
- There are 2 main types, depending on the material, and geometry of the sensitive medium
  - **Thin chambers** where the sensitive medium scatters very little, for example, gas or air-filled ionization chambers. The picture on the next page shows a Monte Carlo calculation that prodiced a graphical output of electron tracks in a thin chamber.
  - **Thick chambers** where the sensitive medium scatters very significantly, for example, lead-encased Thermoluminescence Detectors (TLDs).

Monte Carlo of an thin ion chamber subject to ^{60}Co γ



Thin chambers

- Thin chambers are the instruments upon which accurate transfer dosimetry is between Standards' Labs and hospitals are based.
- Standards'Labs can make measurements with these chambers to about a 0.01% relative precision, and an absolute uncertainty (for the dose to water) of less than 1%.
- In Hospital environments, relative precisions of 0.1% (or better) and absolute dose to water of about 2%.
- Thin chambers come in a variety of shapes, that are specific their application. We'll discuss that later.
- For now, we will focus on the reason why they work so well.

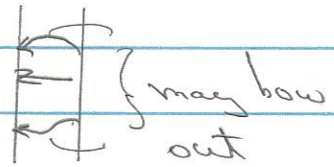


This is a theorist's idealization of a thin cavity

In reality, i) the gas is enclosed
ii) there is an electrode
iii) guards (to give the electric field lines a well-defined geometry)
iv) electric field (to sweep ions to the electrode)
v) insulators, to separate guards & the electrode
vi) a stem, to hold the ion chamber
vii) wires

In reality,

i) the beam is attenuated (less ionization collected)
ii) " " " scattered (more ionization collected)
iii) " " " other than a broad parallel beam
- $1/r^2$ effect
- finite source size
iv) the beam is mono-energetic
v) the electric field lines are not ideal
(⇒ volume then define is not purely geometric)



vi) δ rays transport from the originating e^- track
vii) primary e^- tracks are scattered
viii) ionization is not completely collected
ix) δ-rays may not attach to ions, and get collected

How can this possibly work?

Answer: a) Good chamber design
b) Good measurement practice
c) Fano's theorem & equilibrium to the rescue
d) Theoretical & Experimental corrections

Explanation...

a) b) c)

Good chamber design / good measurement practice / good luck!

1) Make the walls as thin as possible, but still such that $t_{wall} \geq R_{e,max} \Rightarrow e^-$ equilibrium is set up in the walls of the chamber
This is called a minimum, full build up
attenuation is minimized ✓ ~~i)~~ ~ −5%
scatter is " ✓ ~~ii)~~ ~ +3%
residual attenuation & scatter can be determined by experiments and/or MC-derived correction factors d) ✓

2) Electrode, guard design can be optimized ~~i)~~
Run with as high a voltage as possible b) ✓
(this straightens out $\vec{E}$-field lines) [don't fry the instrument]

Also $\vec{E} \uparrow \Rightarrow$ more of the ions produced are collected ~~iii)~~

There are theoretical corrections (saturation theory) (we'll cover this later) that come to the rescue d) ✓

3) ~~i)~~ S-cap to not attach ions are collected

Theoretical work has shown that this does not matter, except at very high voltages

4) Make the atomic composition of the walls and the gas as close as possible
e.g. C/Air, Air equivalent plastics ...

Fano & Equilibrium to the rescue! c) ✓

If the γ fluence is in equilibrium, so is the fluence of the δ-rays, and, so are the ions that are produced

This solves problems ~~vi)~~ ~~vii)~~

Finally

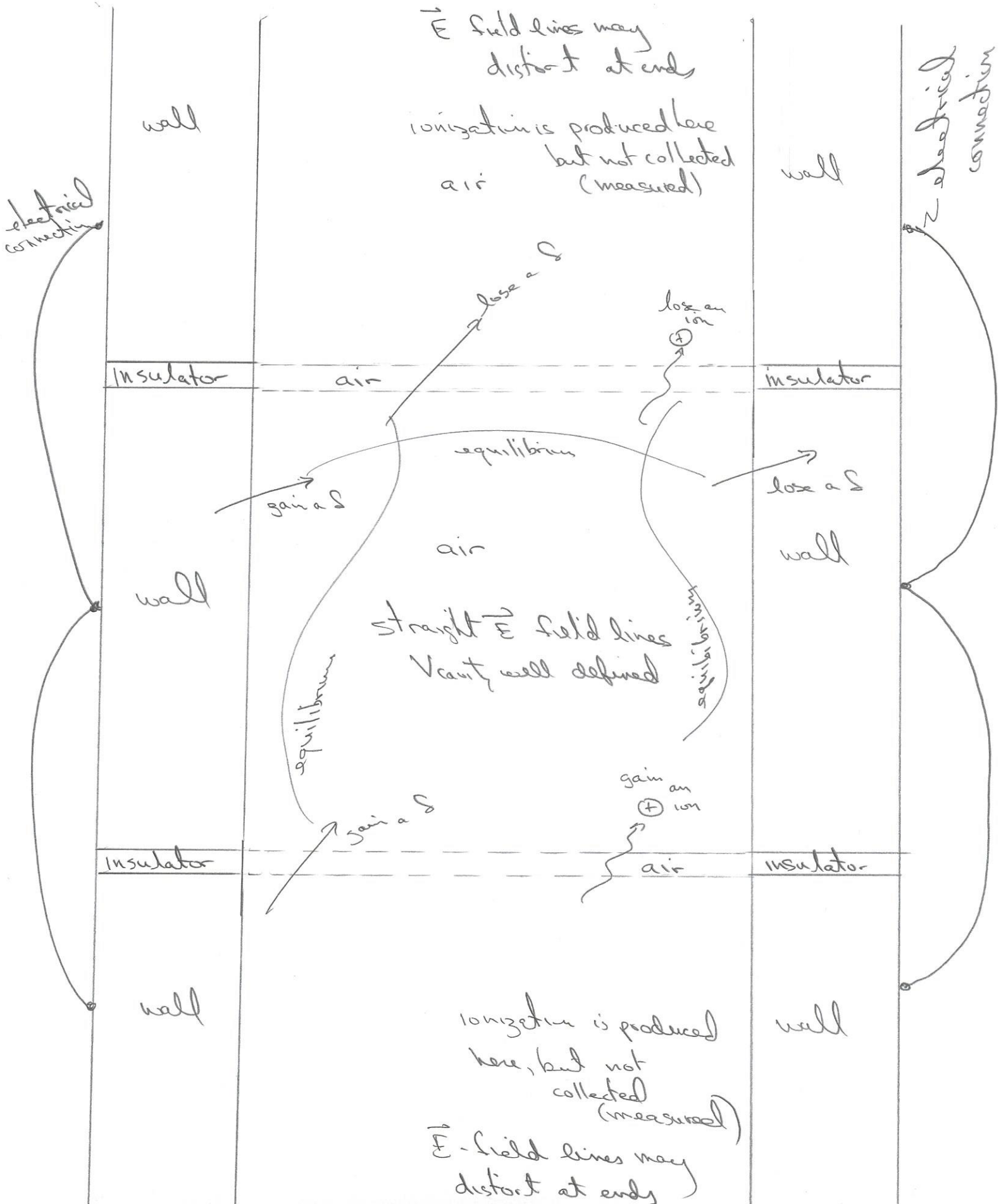
~~iv)~~ non-monoenergetic source

Theoretically, it's easy!

Just $\int dE_x \Phi_x(E_x)$ ...

Practically, it's difficult!

Must do a full MC of the source.


$\vec{E}$ field lines may distort at ends
wall
ionization is produced here but not collected (measured)
air
wall
electrical connection
electrical connection
lose a δ
lose an ion
insulator
air
insulator
equilibrium
gain a δ
lose a δ
air
wall
wall
straight $\vec{E}$ field lines
V cavity well defined
equilibrium
equilibrium
gain an ion
gain a δ
insulator
air
insulator
wall
wall
ionization is produced here, but not collected (measured)
$\vec{E}$-field lines may distort at ends

Dose to the air in the cavity

If you believe all the approximations...

Dose to wall

the dose to the wall material in the vicinity of the cavity is

(1) $D_w = K_c^w = \int dE_\gamma \Phi_\gamma(E_\gamma) E_\gamma \left(\frac{\mu_{en}^w(E_\gamma)}{\rho}\right)$

(D_w: dose to wall; K_c^w: collision kerma in the wall; Φ_γ: γ energy fluence; $\frac{\mu_{en}^w}{\rho}$: mass energy transfer coefficient)

where we presume to know what the photon fluence is. Note that we just relaxed the monoenergetic condition.

We can also write

(2) $D_w = \int dE_e \Phi_e^w(E_e) \left(\frac{S_c^w(E_e)}{\rho}\right)$

(Φ_e^w: electron fluence in the vicinity of the cavity; $\frac{S_c^w}{\rho}$: collision stopping power)

Recall, from L05 p130, for a monoenergetic e fluence

(3) $D = \Phi_e(E_e) \frac{S_c(E_e)}{\rho} + \Phi_e(E) \frac{S_r(E_e)}{\rho}$

(only this part is modelled by Collision Kerma)

Note: $E_{s,max} = E_e/2$ by definition

$\frac{S_c}{\rho} = \frac{n}{\rho} \int_0^{E_{s,max}} dE_s \, E_s \frac{d\sigma_{Miller}(E_e, E_s)}{dE_s}$ (collision; primary e⁻)

$\frac{S_r}{\rho} = \frac{n}{\rho} \int_0^{E_{\gamma,max}} dE_\gamma \, E_\gamma \frac{d\sigma_{brem}(E_e, E_\gamma)}{dE_\gamma}$ (radiative)

Dose to the cavity

Since there are no electrons generated in the gas cavity

$$(4)\quad D_g = \int dE_e \, \Phi_e^g(E_e) \, S_{\rho}^g(E_e)$$

Now, finally we make use of Fano's theorem, that, under equilibrium conditions, when the material in one region is compositionally the same, but the density different, that

$$(5)\quad \boxed{\Phi_e^w(E_e) \equiv \Phi_e^g(E_e)}$$

In that case, we can write (4) as

← note, this changed not this

$$(6)\quad D_g = \int dE_e \, \Phi_e^w(E_e) \, S_{\rho}^g(E_e)$$

Then, dividing (6) by (2), we get

(7) $$\frac{D_g}{D_w} = \frac{\int dE_\epsilon \; \Phi^w_\epsilon(E_\epsilon)\left(\frac{\bar{L}^g}{\rho}(E_\epsilon)\right)}{\int dE_\epsilon \; \Phi^w_\epsilon(E_\epsilon)\left(\frac{\bar{L}^w_c}{\rho}(E_\epsilon)\right)}$$

The right-hand side looks like a wall-fluence weighted stopping power ratio

It is conventially written $\left(\frac{\bar{L}}{\rho}\right)^g_w$

or $\bar{L}^g_w$, for short

It's real meaning is given by (7)

(7) can also be written using (1)

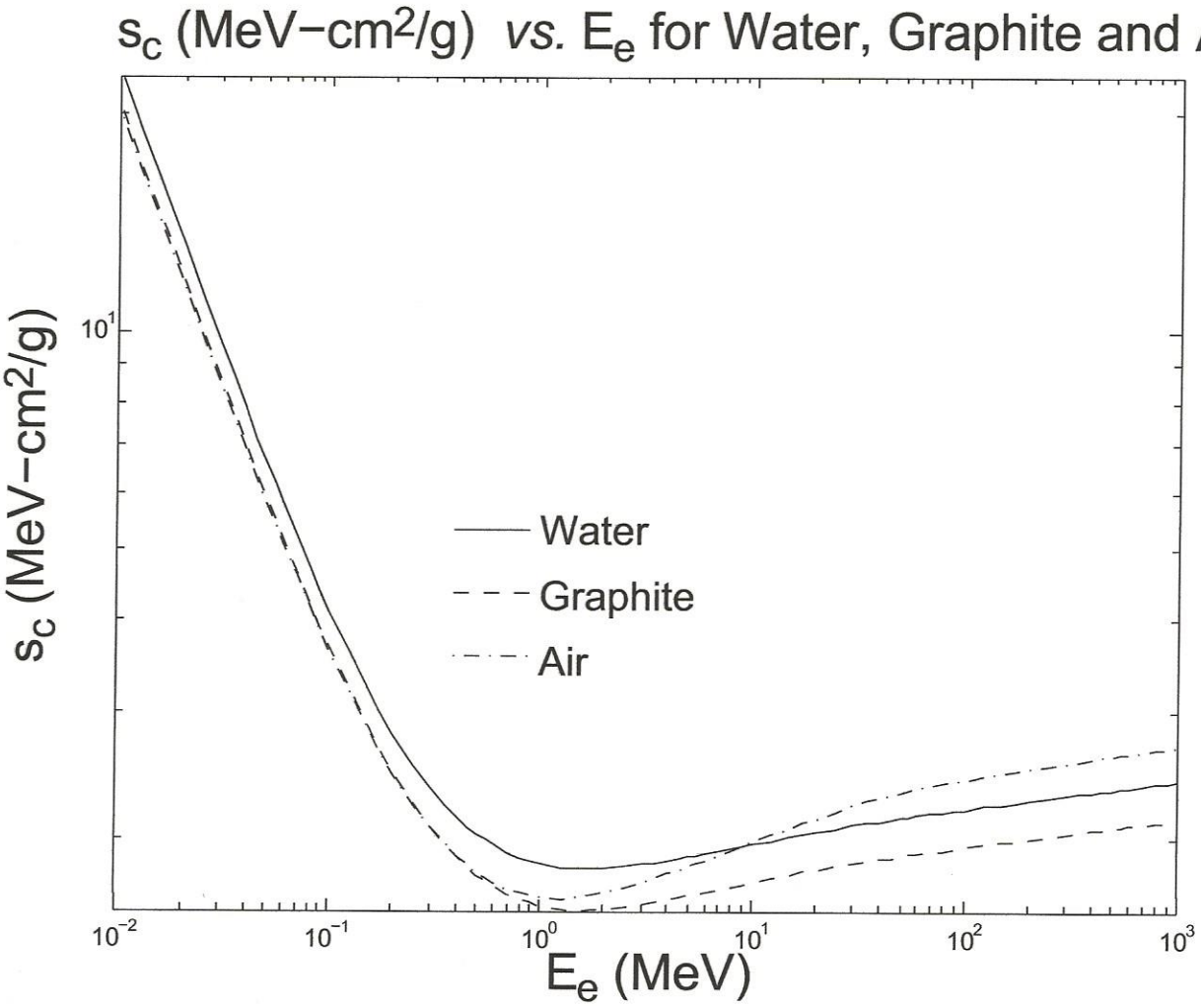
(8) $$\boxed{D_g = K^w_c \bar{L}^g_w}$$

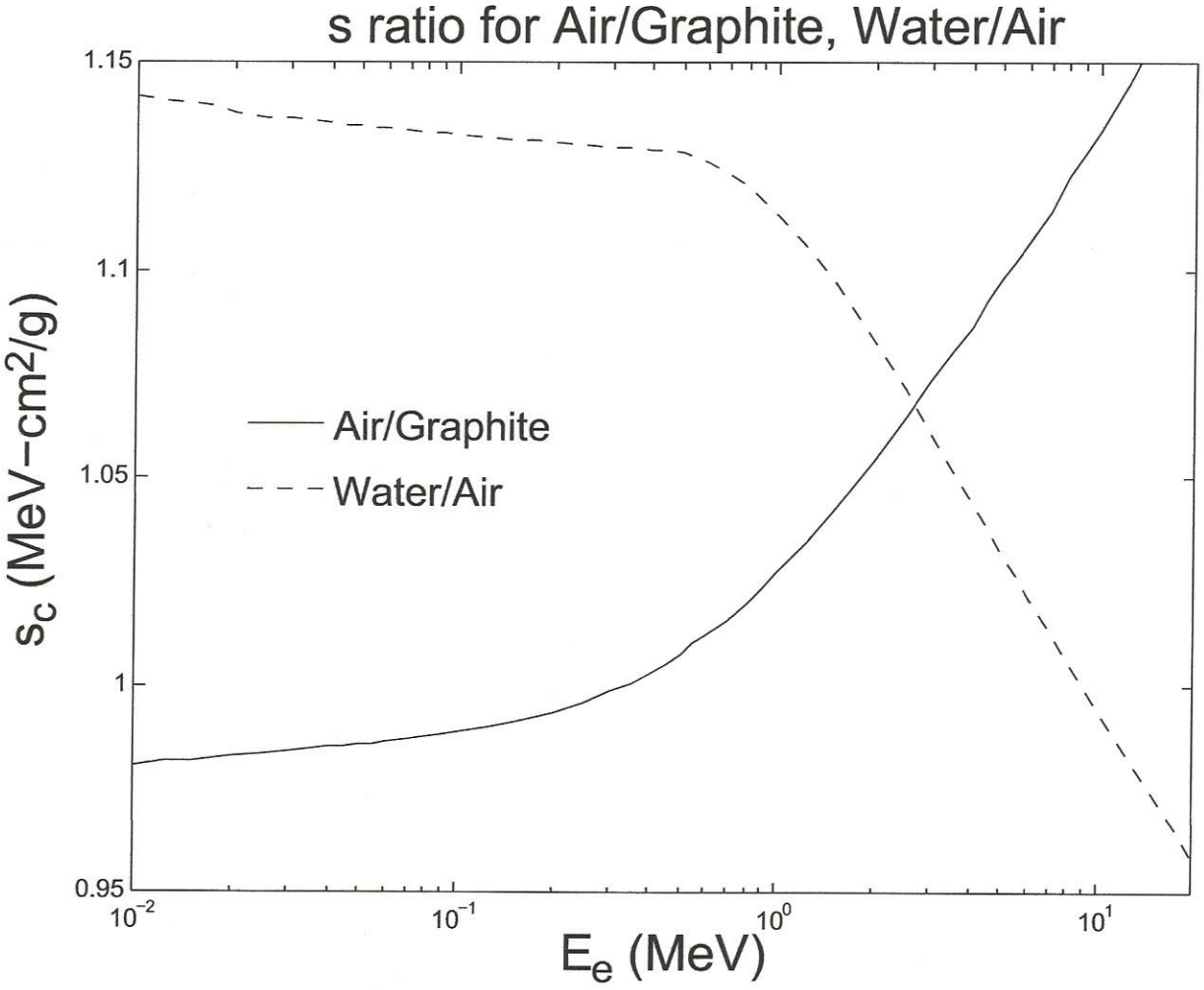
This is the most central equation in all of medical radiation dosimetry

The dose to the gas of an ion chamber under conditions of equilibrium is given by

K^w_c (wall)

times the stopping power ratio $\bar{L}^g_w$


s_c (MeV−cm²/g) *vs.* E_e for Water, Graphite and Air
s_c (MeV−cm²/g)
10^1
Water
Graphite
Air
10^{-2}
10^{-1}
10^0
10^1
10^2
10^3
E_e (MeV)


s ratio for Air/Graphite, Water/Air
1.15
1.1
1.05
1
0.95
s_c (MeV−cm2/g)
Air/Graphite
Water/Air
10^{-2}
10^{-1}
10^{0}
10^{1}
E_e (MeV)

Usually, it is dose to water, that is usually needed in the clinic

Assuming that you have D_g experimentally from a chamber inside a phantom irradiated by a treatment beam

(9) $$D_{H_2O} = (D_g)_{meas} \left(\overline{J}^{H_2O}_{Air}\right)$$

This equation is deceptively simple.

Recall, that accurate knowledge of the electron spectrum there is required.

Here is where MC calculations can be of enormous benefit

It would be a good idea to take a break for cavity theory for a while and discuss advanced dose calculation methods, namely, the convolution method and Monte Carlo.

The convolution method

The convolution method was proposed by

Dean RD U Kansas MP 7(429) 1980 abstract
Mackie TR Allan Blair Mem Clinic Regina 1983
MP 10(536)

Ahnesjo A 1984 Conf pp17-20
Bielajew A F, Rogers D W O and Nahum A E 1985 *Phys. Med. Biol.* **30** 419-27
Boyer A L 1984 *Med. Phys.* **11** 552-4
Boyer A L and Mok E C 1984 *Proc. 8th Int. Conf. on Computers in Radiotherapy* (*Toronto*) pp 14-16
—— 1985 *Med. Phys.* **12** 169-77
Brahme A 1977 *Report SSI: 1977-009* National Institute of Radiation Protection, Stockholm
Chui C and Mohan R 1986 private communication
Chui C, Mohan R and Lidofsky L 1984 *Med. Phys.* **11** 392 (abstract)
Dean R D 1980 *Med. Phys.* **7** 429 (abstract)
Ford R L and Nelson W R 1978 *The EGS Code System, Stanford Linear Accelerator Report 210* (Stanford, CA: Stanford Linear Accelerator)
Hubbell J H 1969 *Photon Cross Sections, Attenuation Coefficients, and Energy Absorption Coefficients from 10 keV to 100 GeV* NSRDS-NBS No 29 (Washington, DC: US Govt Printing Office)
—— 1977 *Radiat. Res.* **70** 58-81
—— 1982 *Int. J. Appl. Radiat. Isot.* **133** 1269-90
Johns H E and Cunningham J R 1983 *The Physics of Radiology* 4th edn (Springfield, IL: Thomas)
Loevinger R 1981 *Med. Phys.* **8** 1-12
Mackie T R 1983 *Med. Phys.* **10** 536 (abstract)
—— 1984 *PhD thesis* University of Alberta
Mackie T R, El-Khatib E, Scrimger J W, Battista J J, Van Dyk J and Cunningham J R 1985a *Med. Phys.* **12** 327-32
Mackie T R and Scrimger J W 1984 *Proc. 8th Int. Conf. on Computers in Radiotherapy* (*Toronto*) pp 36-40
Mackie T R, Scrimger J W and Battista J J 1985b *Med. Phys.* **12** 188-96
McEwan A C and Smyth V G 1984 *Med. Phys.* **11** 216-8
Mohan R and Chui C 1985 *Med. Phys.* **12** 726-30
Mohan R, Chui C and Lidofsky L 1985 *Med. Phys.* **12** 592-7
—— 1986 *Med. Phys.* **13** 64-73
NACP 1980 *Acta Radiol. Oncol.* **19** 55-79
—— 1981 *Acta Radiol. Oncol.* **20** 401-15
Nelson W R, Hirayama A and Rogers D W O 1985 *The EGS4 Code System, Stanford Linear Accelerator Report 265* (Stanford, CA: Stanford Linear Accelerator)
Roesch W C 1958 *Radiat. Res.* **9** 399-410
Rogers D W O 1982 *Nucl. Instrum. Meth. Phys. Res.* **199** 531-48
—— 1984 *Nucl. Instrum. Meth. Phys. Res.* **227** 535-48
Rogers D W O and Bielajew A F 1985 *Med. Phys.* **12** 738-44
Schulz R J and Loevinger R 1984 *Med. Phys.* **11** 218

1st publ abstract

1st conf proc

Communications (short)
Boyer 1984 MP 11 (552)

Abstracts 1980 Dean
1983 Mackie
1984 Chui Mohan Lidofsky

Papers
Mackie Scrimger Battista 12(188-196)
Boyer Mok 1985 12(169) 169-177
Mohan & Chui 1985 MP (726-730)
Mohan et al & Lidofsky

Proceedings Boyer & Mok 1984
Ahnesjo 1984
Mackie & Scrimger 1984

Thesis Mackie 1984 MP 13(64-73)

Earliest full refereed article
– used published MC data

(227)

A photon dose distribution model employing convolution calculations

Arthur Boyer and Ed Mok
Department of Radiology, The University of Texas Health Science Center at San Antonio, San Antonio, Texas 78284 and The Cancer Therapy and Research Center, San Antonio, Texas 78229

(Received 5 March 1984; accepted for publication 25 October 1984)

A three-dimensional photon beam calculation is described which models the primary, first-scatter, and multiple-scatter dose components from first principles. Three key features of the model are (1) a multiple-scatter calculation based on diffusion theory, (2) the demonstration of the modulation transfer function of the radiation dose transport process, and (3) the use of the finite fast Fourier transform to perform the required convolutions. The results of calculations for cobalt-60 in a homogeneous phantom are used to verify the accuracy of the model.

Key words: photon dose distribution, photon scatter, multiple-scatter dose, convolution, modulation transfer function

INTRODUCTION

A number of empirical and analytic models have been exploited to calculate the distribution of dose in radiation fields used for external beam radiation therapy.[1–5] The model described here is analytic and employs computed attenuation coefficients and scattering cross sections. The model convolves single-point interaction kernels with the primary beam fluence to build up the first-scatter and multiple-scatter components of the field. Use of convolution techniques to calculate scatter components has been described previously by Dean[6] and Mackie.[7] Convolutions can be carried out using Fourier transform methods which employ the Cooley–Tukey finite fast Fourier transform algorithm.[8]

The model described here is to be employed in the energy range 1–20 MeV. In a previous communication[9] it was pointed out that in principle considerable savings in computation time could be realized if the dose components could be calculated using convolutions of the form

$$D(\mathbf{r}) = \int_{V'} \Phi(\mathbf{r}') \cdot k(\mathbf{r} - \mathbf{r}') \cdot dV'. \tag{1}$$

The application here considers Φ to be a photon fluence distribution and k to be an interaction kernel which describes how radiation spreads out from the point $\mathbf{r}'$ after an interaction there. k can also be viewed as a Green's function for radiation dose transport. A formulation is given by which the dose components can be computed in this form assuming a homogeneous water phantom as the medium of propagation. It will be shown that $k(\mathbf{r})$ can be calculated for the entire radiation dose transport process. When this is done, $k(\mathbf{r})$ can be interpreted as the three-dimensional impulse response of the dose transport process. This is possible only when approximations are made which allow $k(\mathbf{r})$ to remain spatially invariant. Although all the physical processes involved are not strictly spatially invariant, the spatial variations are small enough to be ignored, at least in the lower end of the therapy energy range. In this case, the Fourier transform of $k(\mathbf{r})$ is the modulation transfer function for the physical processes which connect a photon fluence to the radiological dose produced by that fluence. We demonstrate these concepts and calculate an analytic form of the impulse response $k(\mathbf{r})$. We then present the results of our calculations of the dose components and total depth dose obtained by convolution employing the finite fast Fourier transform.

METHOD

Consider a flux of photons Φ_0 [photons/cm^2] of energy E_0 [MeV] moving in the $+z$ direction and incident upon a water surface at $z = 0$. The beam may in fact be multienergetic. In this more general case the calculations described below must be carried out for either an average energy or for several representative energies of the incident beam spectrum and added with appropriate weighting. In what follows we will not consider each energy explicitly, but will let it be understood that an energy spectrum may be involved for x-ray beams. Let the photons originate from a source a distance SSD[cm] from the surface. The primary fluence distribution in a homogeneous phantom can be calculated by essentially tracing rays originating from the radiation source and by applying inverse square and exponential attenuation to the fluence along a ray. A continuous phantom is replaced in this model by an array of calculation points. Each point is located in the center of a voxel and can be identified by indices corresponding to displacement in three dimensions. We will, however, continue to locate the calculation points by the vectors $\mathbf{r}$. The formulas required are

$$\Phi_p(\mathbf{r})\ [\text{photon/cm}^2] = \Phi_0\ [\text{photon/cm}^2] \left(\frac{\text{SSD}}{\text{SSD} + d}\right)^2 \prod_i e^{-\mu \Delta d_i}, \tag{2}$$

where Φ_0 is the photon fluence of the ray passing through the surface to $\mathbf{r}$, d is the depth into the phantom, and μ [cm^{-1}] is the total linear attenuation coefficient for energy E_0 at the voxel i along the ray trace path from the surface

$$d = s - s_{\text{air}} = \sum_i \Delta d_i, \tag{3}$$

where s is the distance from the source to the point of calculation, s_{air} is the distance traveled by the photons from the source to the phantom surface.

The kerma deposited by this primary fluence K_p is calculable[10] using the mass absorption coefficient μ_{en}/ρ and con-

 0094-2405/85/020169-09$01.20 © 1985 Am. Assoc. Phys. Med.

-did his own MC calculations

A convolution method of calculating dose for 15-MV x rays

T. R. Mackie,[a] J. W. Scrimger, and J. J. Battista
Department of Medical Physics, Cross Cancer Institute, Edmonton, Alberta, Canada T6G 1Z2

(Received 1 May 1984; accepted for publication 14 August 1984)

Arrays were generated using the Monte Carlo method representing the energy absorbed throughout waterlike phantoms from charged particles and scatter radiation set in motion by primary interactions at one location. The resulting "dose spread arrays" were normalized to the collision fraction of the kinetic energy released by the primary photons. These arrays are convolved with the relative primary fluence interacting in a phantom to obtain three-dimensional dose distributions. The method gives good agreement for the 15-MV x-ray dose in electronic disequilibrium situations, such as the buildup region, near beam boundaries, and near low-density heterogeneities.

this was the main motivator

Key words: photon dosimetry, convolution, charged particles, collision KERMA, Monte Carlo, 15-MV x rays, tissue-maximum ratios (TMR), lung corrections

I. INTRODUCTION

Present dose calculation methods are based on the assumption that all of the charged-particle energy liberated by photon radiation is deposited locally at the site of interaction. While this assumption is acceptable for cobalt-60 radiation, it weakens for higher energy x-rays for which the range of charged particles set in motion can be several centimeters. The need for considering this nonlocal energy deposition has been documented.[1–4] Some photon dose calculation methods have accounted for electronic "buildup" longitudinally along the central axis, but none have rigorously treated the lateral spread of charged particles set in motion.[5,6] Young and Kornelson[7] have taken into account the dose reduction caused by a lack of charged particles equilibrium using a semiempirical "loss factor."

For photon energies comparable to those of cobalt-60 radiation, existing methods rely on measured tissue–air ratio (TAR) data that assume that the primary dose is equal to the TAR extrapolated to a "zero-area field." This leads to a number of technical and fundamental problems for higher energy photon beams. Firstly, the TAR concept is usually replaced by a tissue–phantom ratio (TPR) which is based on measurements made in a phantom. It becomes more difficult to separate the contributions of primary and scattered radiation because the increase in TPR caused by scatter within the phantom must be isolated from increases caused by external factors[8] (e.g., collimators). Furthermore, extrapolation to a zero-area field to obtain the primary dose is not physically acceptable because lateral electronic equilibrium is lost and the dose is greatly reduced.

In this work, a physically sound and consistent method has been developed which allows calculation of three-dimensional dose distributions in homogeneous or heterogeneous phantoms irradiated with rectangular or irregularly shaped fields of high-energy photons. The use of measured data as a data base is abandoned and replaced with data generated from first principles by Monte Carlo techniques. The Monte Carlo method is used to map the spatial distribution of charged-particle energy away from a primary photon interaction site. This distribution, called a primary dose spread array, is convolved spatially, with the kinetic energy released at all the primary interaction sites to yield the primary dose distribution. In a heterogeneous phantom, the dose spread arrays need to be modified during convolution.

Any current method separating primary from scatter dose can be improved with the methodology proposed here. Since convolution is a well understood and documented technique, there are conceptual advantages for implementing a convolution framework for the spread of energy due to scattered photons, as well as charged particles set in motion. (Dean has used this approach to find where the scatter dose was being absorbed from cobalt-60 primary photons interacting in one location of a water phantom.[9])

The proposed method was based on concepts which will not become obsolete as improved computational power becomes available. The fundamental reason for this is the sound physical basis of the Monte Carlo and convolution procedures. Another reason is an inherent flexibility to compromise between speed and accuracy. Therefore, as computers become faster, greater accuracy can be achieved without modifying the algorithm substantially.

II. PRIMARY DOSE SPREAD ARRAYS

A primary dose spread array (analogous to the point spread array used in image processing) is the three-dimensional spatial distribution of energy deposited by electrons and positrons which spread from the site of the primary photon interactions. It is generated by tracking the motion of charged particles away from primary interaction sites occurring within a cubic volume element (voxel). These charged particles are followed, using the Monte Carlo method, in a homogeneous phantom consisting of voxels of the same size, atomic number, and density. The amount of energy deposited at, and in the neighborhood of, the interaction voxel is scored. Figure 1 illustrates the procedure schematically.

The incident photon fluence spectrum was not known and could not easily be measured. However, the spectrum was chosen by comparing measured depth dose values with the results of "electron gamma shower" (EGS) Monte Carlo sim-

 0094-2405/85/020188-09$01.20 © 1985 Am. Assoc. Phys. Med.

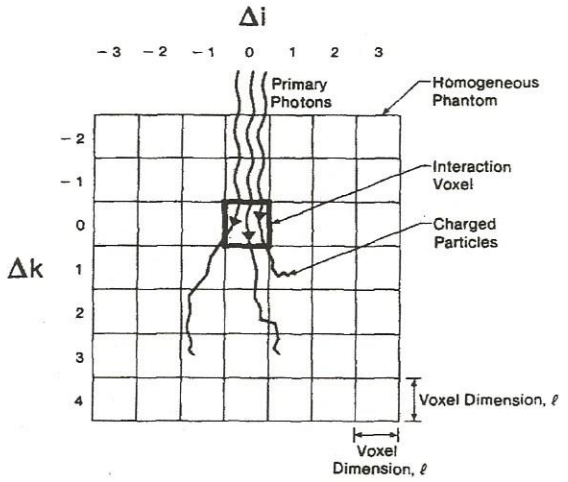


FIG. 1. Schematic representation of the generation of a primary dose spread array.

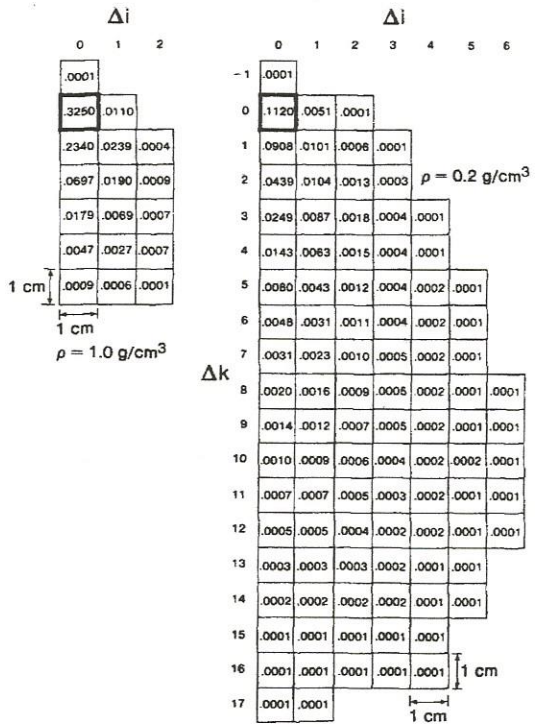


FIG. 2. Primary dose spread arrays. The numbers represent the dose deposited in the voxel normalized to the collision KERMA in the interaction voxel (bold borders).

ulations with various monoenergetic photon energies. (The 15-MV photon beam was obtained from a Siemens Mevatron-77. The measuring device was a Capintec PR-06C ion chamber with a Capintec 192A electrometer.) The EGS code was developed originally at Stanford University by Ford and Nelson,[10] and modified by Rogers at the National Research Council of Canada.[11,12] A monoenergetic 5.0-MeV beam duplicates the measured depth dose for a 15-MV x-ray beam to within 5% at depths up to 20 cm for a field size of 10×10 cm. (The EGS program employed cylindrical geometry so the equivalent circular field was used to model rectangular fields.[13]) A mixture of monoenergetic incident photon energies of 0.18, 0.67, 2.57, 6.61, 11.12, and 13.78 MeV with the photon fluence weighted in the proportions 0:11:11:11:5:0, respectively, improved the agreement to within 0.5%.

The dose spread arrays were actually generated by a homemade Monte Carlo code called MOCA, developed in our Institute. Both MOCA and EGS take into account the photoelectric effect, Compton effect, and pair production. EGS distinguishes positrons from electrons, whereas MOCA transports positrons as if they were electrons. Both programs produce photons when the positron annihilates. MOCA employs the approximations of continuous slowing down (without generation of secondary "knock-on" electrons) and Gaussian lateral scattering for charged particles. Bremsstrahlung was not included in MOCA.

Figure 2 shows voxel elements of two primary dose spread arrays for a pencil beam of 15-MV x rays interacting in a homogeneous phantom with cubic voxel dimensions of 1.0 cm. The density of the array on the left is 1.0 g/cm^3, and that on the right is 0.2 g/cm^3. The two media are assumed to be waterlike in chemical composition. The voxels shown in Fig. 2 are in the same plane as the interaction voxel. The beams have the same cross-sectional area as the voxels, and are made to interact only in the interaction voxel (bold borders). At least 10^6 charged particles/cm^2 were set in motion by primary photons to generate these arrays. The dose spread arrays are quadrilaterally symmetric about the primary photon direction, which is designated as the Δk axis. To speed up the convolution process for rectangular fields, the dose spread arrays are produced in a three-dimensional Cartesian geometry.

Figure 2 clearly illustrates that the assumption of local energy deposition at 15 MV is untenable. The value of the dose spread array at the interaction voxel (location 0, 0, 0) in a 1.0 g/cm^3 phantom with a voxel size of 1 cm is 0.325, which indicates that 32.5% of the energy released at the interaction site is deposited there. The value at the same location for a 0.2 g/cm^3 phantom with a voxel size of 1 cm is only 0.112. The maximum longitudinal range of charged particles set in motion in a 1.0 g/cm^3 phantom is about 4–6 cm, and in a 0.2 g/cm^3 phantom, the maximum longitudinal range is about 16–18 cm! In the lateral direction, charged particles can contribute to dose about 1–3 cm and 5–7 cm from the interaction site for 1.0 g/cm^3 and 0.2 g/cm^3 phantoms, respectively.

The primary dose spread array values indicate the primary energy deposited in each voxel normalized to the total energy released in the interaction voxel

$$Ap(\rho, l, \Delta i, \Delta j, \Delta k) = \frac{T(\rho, l, \Delta i, \Delta j, \Delta k)}{\mathrm{KER}_c(\rho, l, 0, 0, 0)}, \quad (1)$$

where $Ap(\rho, l, \Delta i, \Delta j, \Delta k)$ is the primary dose spread array at a distance $\Delta i, \Delta j, \Delta k$ from the interaction voxel, $T(\rho, l, \Delta i, \Delta j, \Delta k)$ is the energy deposited at the site, and $\mathrm{KER}_c(\rho, l, 0, 0, 0)$ is the total energy of charged particles set in motion at the interaction site that is lost to electron collisions (not bremsstrahlung) in the phantom.[14]

Since the phantom is homogeneous, the interaction and dose deposition voxels have the same density. Therefore, the

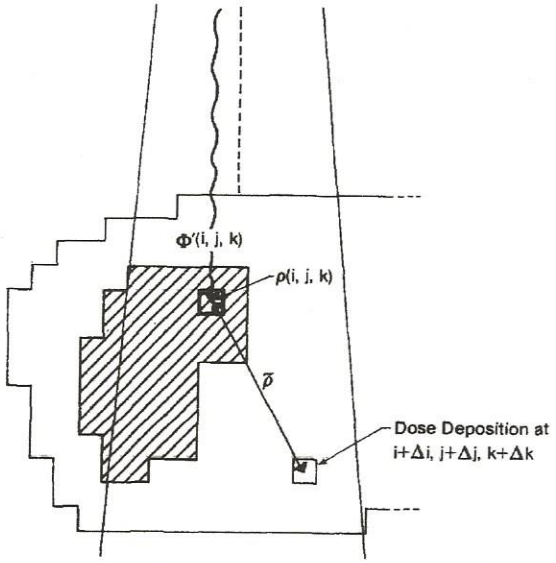


FIG. 11. Illustration of the extension of the algorithm to waterlike heterogeneous media. $\bar{\rho}$ is the average density between the interaction and dose deposition voxels.

$$\text{Dose contribution } (i+\Delta i, j+\Delta j, k+\Delta k) \propto \Phi'(i,j,k)\,\frac{\rho(i,j,k)}{\bar{\rho}}\,Ap(\bar{\rho}\cdot l, \Delta i, \Delta j, \Delta k). \quad (8)$$

(Note that the dose spread array value $Ap(\bar{\rho}\cdot l, \Delta i, \Delta j, \Delta k)$ is not invariant for the same value of $\Delta i, \Delta j, \Delta k$ at different values of i,j,k because $\bar{\rho}$ changes throughout the phantom. Convolution with a noninvariant kernel is called superposition.) The factor $\rho(i,j,k)/\bar{\rho}$ takes into account the difference in the amount of kinetic energy released in the heterogeneous interaction voxel compared to the amount set in motion in the interpolated homogeneous voxel of density $\bar{\rho}$. Otherwise, the calculation is carried out in the same manner as in a homogeneous phantom. Therefore, this procedure avoids the need to first compute the dose in water and then calculate a correction for inhomogeneity, separately.

The TFS dose spread array is scaled using the same algorithm. In fact, using this algorithm, the TFS dose spread array gives the exact correction. This is because a first-scatter photon interacting at the dose deposition voxel could not have interacted anywhere other than along the path between the primary interaction and dose deposition voxels. Since the same algorithm is used for the primary and TFS dose spread arrays, and they are stored for the same values of $\rho\cdot l$, these arrays may be combined where they coincide spatially. The TFS dose spread array need only be dealt with separately where it extends beyond the border of the primary dose spread array.

Multiple-scatter photons may have interacted anywhere within the phantom, not just between the primary interaction and dose deposition voxels.[22] Therefore, the average density of the *phantom* is used in Eq. (8) instead of the mean density along the path between the interaction and dose deposition voxels. This approximation is further justified because multiple scattering is a minority contribution to the total dose.[17] This approximation avoids calculating the mean density between the interaction and dose deposition voxels of the RFMS dose spread array, resulting in a saving of computation time.

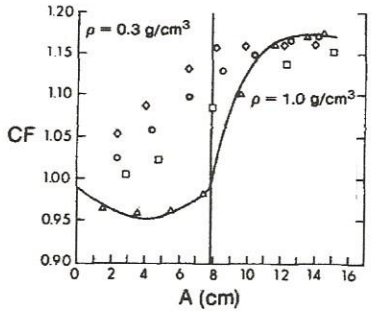


FIG. 12. Comparison of measured and various calculated correction factors (TMR in a heterogeneous medium normalized to the TMR in a unit-density medium) along the central axis. The measuring probe was kept at a constant 100 cm from the source. The thickness of overlying material was a constant 15.5 cm. The parameter A is the distance from the first interface to the probe. The field size is 5×5 cm. ◇ = TAR ratio; □ = Batho; ○ = equivalent TAR; △ = convolution; and — = measured.

Figures 12 and 13 illustrate the TMR correction factor along the central axis for a heterogeneous phantom consisting of horizontal slabs of low- and unit-density materials for field sizes of 5×5 and 10×10 cm. The experimental measurements were obtained using cork and polystyrene slabs. No buildup cap was used on the ion chamber when measuring the dose in cork. The cork density was measured gravimetrically to be 0.30 ± 0.02 g/cm³. The ion chamber was kept at a constant distance of 100 cm from the source, and the position of the cork region, with respect to the chamber, was varied. The parameter A is the distance from the first cork interface to the ion chamber. The cork thickness was 7.90 ± 0.2 cm. The correction factor (CF) is the dose in the heterogeneous phantom normalized to the dose in a unit-density homogeneous phantom. The correction factor is less than 1.0 in cork at 5×5 cm, which indicates that the dose to cork is less than the dose in the homogeneous phantom, even though the primary photon fluence is greater. This is due to a loss of lateral electronic equilibrium, because the distance from the central axis to the field boundary is smaller than the lateral range of charged particles. The doses calculated by some existing methods are shown for comparison in Figs. 12 and 13. The existing methods assume electronic equilibrium, and poorly predict the dose in this situation. The convolu-

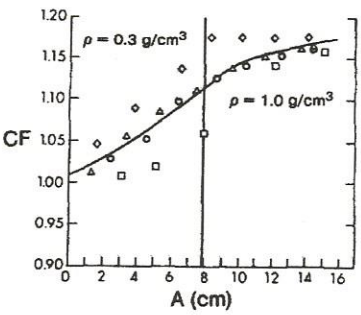


FIG. 13. Same as Fig. 12, except the field size is 10×10 cm.

This paper described the generation of the database.

(231)

Phys. Med. Biol., 1988, Vol. 33, No 1, 1–20. Printed in the UK

Generation of photon energy deposition kernels using the EGS Monte Carlo code

T R Mackie†‖, A F Bielajew‡, D W O Rogers‡ and J J Battista§

† Physics Services, Allan Blair Memorial Clinic, Regina, Canada, S4T 7T1
‡ Physics Division, National Research Council of Canada, Ottawa, Canada, K1A 0R6
§ Department of Medical Physics, Cross Cancer Institute, Edmonton, Canada, T6G 1Z2

Received 8 September 1986, in final form 29 April 1987

Abstract. The EGS Monte Carlo code was used to generate photon energy deposition kernels which describe the energy deposited by charged particles set in motion by primary, first scattered, second scattered, multiple scattered and bremsstrahlung plus annihilation photons. These were calculated for a water medium irradiated with monoenergetic photons with energies in the range 0.1–50 MeV. In addition to the primary energy deposition kernels, primary charged particle transport was further characterised by computing the effective centre of the voxels, and the effective penetration depth, effective radius and effective lateral distance travelled by these particles. The dose per unit collision kerma for parallel monoenergetic primary photons β' was calculated. Additional applications of the energy deposition kernels are discussed.

1. Introduction

A number of authors have proposed that photon dose be calculated using convolution mathematics (Dean 1980, Mackie 1983, 1984, Mackie and Scrimger 1984, Boyer and Mok 1984, 1985, Ahnesjo 1984, Boyer 1984, Chui *et al* 1984, Mackie *et al* 1985b, Mohan *et al* 1986). The technique involves convolving the primary photon fluence with a kernel that describes the transport and deposition of energy by secondary particles. The convolution kernel has been termed a dose spread array because it describes the spread of dose from a primary photon interaction site (Mackie *et al* 1985b). Mohan *et al* (1986) have called the convolution kernel a 'differential pencil beam'.

In principle, the energy deposition kernels can be obtained by deconvolving measured narrow beam dose distributions (Ahnesjo 1984). Alternatively, one can calculate monoenergetic energy deposition kernels using Monte Carlo simulation. In this approach, the contributions from each photon scattering order (e.g. primary, first scatter, etc) may be obtained separately (Mackie *et al* 1985b). The transport of several orders of photon scattering may be modelled analytically, but higher-order scattering is more effectively modelled with the Monte Carlo method.

Roesch (1958) defined a distribution called an 'influence function' which is equivalent to a primary energy deposition kernel and showed how it could be used to obtain the amount of dose deposited in situations of electronic disequilibrium. The influence function was not calculated but its first moments, called $\bar{x}$ in the incident photon direction and $\bar{y}$ in the perpendicular direction, were estimated. The first moment $\bar{x}$ was used to approximate the ratio of dose to collision kerma β (Loevinger 1981). Brahme (1977) analytically estimated a distribution equivalent to the primary energy deposition kernel and the influence function.

‖ Currently at: Department of Medical Physics, 1300 University Avenue, University of Wisconsin, Madison, WI 53706, USA.

0031-9155/88/010001+20$02.50 © 1988 IOP Publishing Ltd

The EGS (electron gamma shower) Monte Carlo code is a general purpose photon–charged-particle transport simulation system which can be used for medical physics problems (Ford and Nelson 1978, Rogers 1982, 1984, Mackie *et al* 1985a, Rogers and Bielajew 1985, Mohan and Chui 1985, Mohan *et al* 1986). It was originally written at Stanford Linear Accelerator Center (SLAC) to describe the transport through matter of photons and charged particles (electrons and positrons) from very high-energy linear accelerators and cosmic rays. It has recently been modified (Rogers 1984, Nelson *et al* 1985) for improved simulation of the transport of particles with energies relevant to those encountered in medical physics.

This paper reports the use of EGS to produce energy deposition kernels in water for several scattering orders at a wide range of incident photon energies. Although the original motivation for this work was to produce a data base for the convolution method of calculating dose distributions in radiotherapy, we have also computed fundamental information that can be of use to predict the energy deposition behaviour of secondary particles following photon interactions.

2. Generation of energy deposition kernels

2.1. Geometry of the simulated phantom

An EGS user code called SCASPH (scatter spherical) modelled the passage of photons and charged particles in a homogeneous sphere of water with a radius of 60 g cm^{-2}. Incident photons were forced to interact at the centre of the sphere and secondary particles generated. The history of any particle which escaped the phantom was terminated.

There was rotational symmetry about an axis defined by the incident photon direction. The polar angle with respect to this axis and the radius from the origin completely specified the voxel boundaries. Figure 1 illustrates a volume element (voxel) defined in spherical coordinates. The voxel boundaries were defined at the intersection of 48 cones (each separated by a polar angle of 3.75°) and 24 radial shells. The distance between the shells was smaller nearer the origin. The smallest radial spacing was

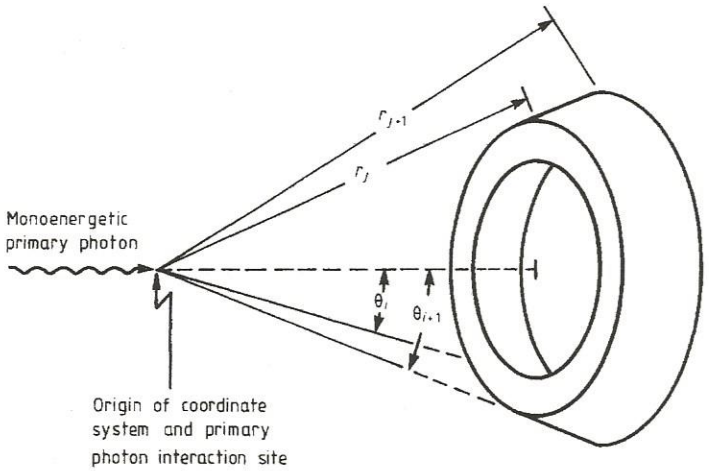


Figure 1. Illustration of a volume element (voxel) in a spherical water phantom with a radius of 60 g cm^{-2}. Monoenergetic primary photons interact at the centre of the sphere.



Figure 2. The partitioning of energy into the scoring categories.

only part way. Therefore, the effective centre for these voxels is uncertain. SCASPH was used to monitor the primary energy deposited within voxels and to calculate a weighted average position of the voxels. Two additional categories were scored for each voxel: the effective radius $\hat{r}_p(i,j)$ and the effective cosine, $\cos[\hat{\theta}_p(i,j)]$,

$$\hat{r}_p(i,j) = \sum_n r_n[\Delta E_p(i,j)]_n \left(\sum_n [\Delta E_p(i,j)]_n \right)^{-1} \tag{3}$$

$$\cos[\hat{\theta}_p(i,j)] = \sum_n \cos(\theta_n)[\Delta E_p(i,j)]_n \left(\sum_n [\Delta E_p(i,j)]_n \right)^{-1} \tag{4}$$

where r_n is the radius corresponding to the middle of step n, $\cos(\theta_n)$ is the cosine of the polar angle at the middle of the step and $[\Delta E_p(i,j)]_n$ is the amount of primary generated energy deposited in the nth step within voxel i,j.

These primary energy-weighted mean quantities represent the effective centre of the voxels for the primary energy deposition kernel. Multiplied together these quantities

Table 2. The relative amount of energy deposited in a spherical phantom of radius 60 g cm^{-2} as a function of the incident photon energy. Column 2 is the fraction of incident energy deposited in the phantom from all components. Column 3 is the percentage of the total energy fraction that is backscattered. Column 4 is the fraction of incident energy deposited in the phantom from the primary component only. The ratio of energy absorption coefficient to the total attenuation coefficient in column 5 should equal the primary energy fraction. Column 6 is the percentage of the primary energy fraction that is backscattered. One standard deviation uncertainty is shown in brackets.

Incident energy (MeV)	Total energy fraction, F_{tot} (0.0004)	Percentage of total energy backscattered	Primary energy fraction, F_p (0.0002)	μ_{en}/μ[a] (0.001)	Percentage of primary energy backscattered
0.10	0.9981	37.27 (0.04)	0.1520	0.152[b]	2.71 (0.01)
0.15	0.9953	33.43 (0.03)	0.1853	0.186[b]	4.08 (0.01)
0.20	0.9928	30.08 (0.03)	0.2179	0.219[b]	4.56 (0.01)
0.30	0.9890	24.92 (0.02)	0.2701	0.271[b]	4.76 (0.01)
0.40	0.9859	21.28 (0.02)	0.3097	0.309	4.60 (0.01)
0.50	0.9832	18.53 (0.01)	0.3411	0.341	4.401 (0.009)
0.60	0.9808	16.41 (0.01)	0.3672	0.367	4.113 (0.009)
0.80	0.9764	13.34 (0.01)	0.4079	0.407	3.642 (0.007)
1.00	0.9726	11.22 (0.01)	0.4388	0.439	3.216 (0.007)
1.25	0.9686	9.352 (0.008)	0.4690	0.469[c]	2.725 (0.006)
1.50	0.9646	8.034 (0.007)	0.4923	0.492	2.413 (0.006)
2.00	0.9578	6.320 (0.006)	0.5276	0.527	1.869 (0.005)
3.00	0.9476	4.569 (0.004)	0.5745	0.574	1.216 (0.003)
4.00	0.9405	3.687 (0.004)	0.6056	0.606	0.857 (0.002)
5.00	0.9362	3.157 (0.003)	0.6308	0.631	0.631 (0.002)
6.00	0.9333	2.806 (0.003)	0.6508	0.651	0.500 (0.002)
8.00	0.9304	2.352 (0.002)	0.6812	0.682	0.337 (0.001)
10.0	0.9296	2.055 (0.002)	0.7042	0.706	0.255 (0.001)
15.0	0.9306	1.583 (0.002)	0.7405	0.743	0.1560 (0.0009)
20.0	0.9316	1.282 (0.001)	0.7600	0.764	0.1088 (0.0007)
30.0	0.9300	0.9116 (0.0009)	0.7728	0.784[d]	0.0672 (0.0005)
40.0	0.9249	0.6962 (0.0007)	0.7705	0.784[d]	0.0506 (0.0005)
50.0	0.9177	0.5612 (0.0006)	0.7618	0.778[d]	0.0408 (0.0004)

[a] From Hubbell (1982) except where otherwise indicated.
[b] From Hubbell (1969). Corrected to exclude coherent (Rayleigh) scattering. This affects values below 300 keV only.
[c] From Hubbell (1977).
[d] From Johns and Cunningham (1983).

decreases with increasing energy. Similarly, the primary backscatter is listed in column 6 of table 2 as a percentage of the fraction of primary generated energy deposited. The amount of primary energy backscattered also decreases with increasing energy at incident photon energies above 300 keV. The decrease in the total and primary backscatter at higher energies is because more Compton recoil electrons and scattered photons are projected forward.

In general, there is very little primary energy backscattered from the primary interaction site. This suggests that the primary component represents about 1–2% of the incident primary energy (product of the primary energy fraction and the fraction of primary energy backscattered) at the entrance surface of a megavoltage photon beam. This agrees with the estimate of Rogers and Bielajew (1985) for a ^{60}Co beam.

235

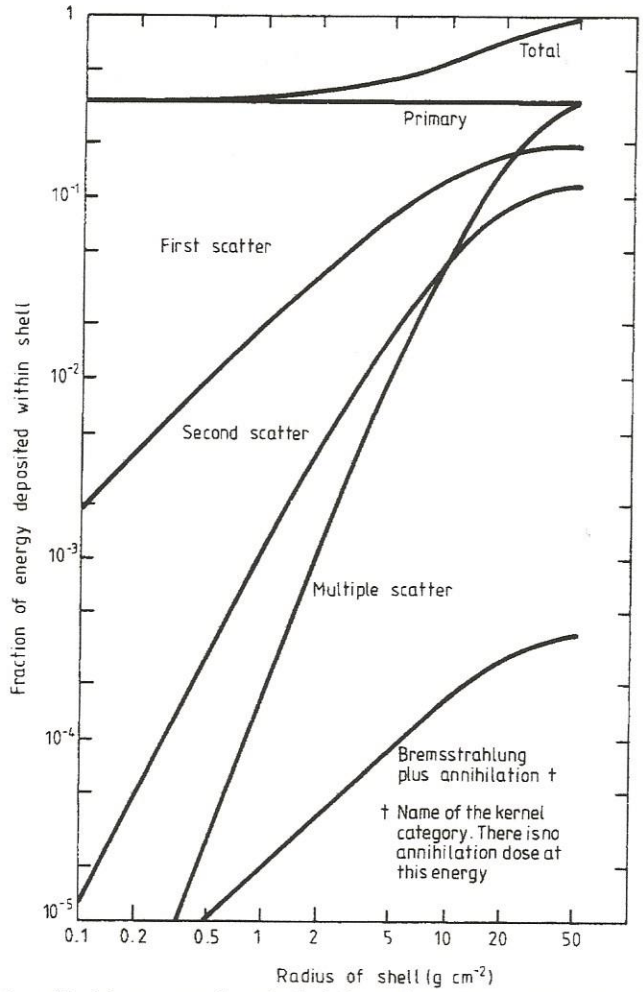


Figure 11. The fraction of incident energy deposited within radial shells as a function of radius for 500 keV photons interacting at the centre of a 60 g cm^{-2} sphere.

A convolution calculation may be done separately for different scattering components of dose. This allows correction for tissue heterogeneity which affects the different scattering components in differing ways (Mackie *et al* 1985b). On the other hand, if the same heterogeneity correction is being employed for all scattering orders the total energy deposition kernel can be used (Mohan *et al* 1986).

The primary energy deposition kernel is difficult to obtain analytically. It can be used in convolution calculations that obtain the scatter convolution kernels analytically (Boyer 1984). In addition, it can also be used to generate the effect of charged particles set in motion from any order of scattering. The photon fluence distribution for the scattering order would be first determined analytically for each scattered photon energy and angle. At each of these energies and angles the primary kernel corresponding to the scattered photon energy would then be weighted with respect to the scattered photon fluence and oriented in the same direction as the scattered photon.

The primary energy deposition kernels can also be used to estimate the transport of charged particles in photon Monte Carlo codes instead of assuming that the energy

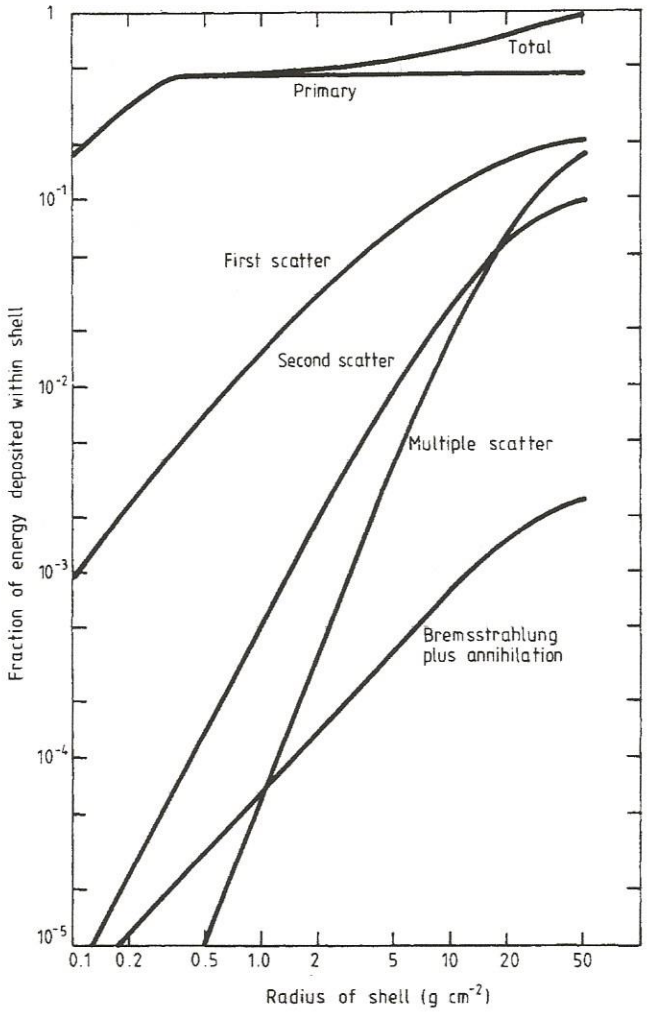


Figure 12. The fraction of incident energy deposited within radial shells as a function of radius for 1.25 MeV photons interacting at the centre of a 60 g cm^{-2} sphere.

is deposited 'on the spot'. Such a hybrid code would not be as accurate as a complete coupled charged-particle–photon Monte Carlo simulation in heterogeneous media and it could not be used to model an electron beam. However, it would have some advantages. It would be more accurate than a Monte Carlo code which models photon transport only. It would be much shorter and easier to write than a traditional Monte Carlo code. Most importantly, it would avoid the calculation time spent in simulating the charged particle path step by step.

5. Conclusions

The energy deposition kernels for all categories were forward peaked at the highest incident photon energies and more isotropically distributed at lower energies. This is compatible with the finding that the amount of energy backscattered from all categories decreases as a function of incident photon energy. The relative amount of energy

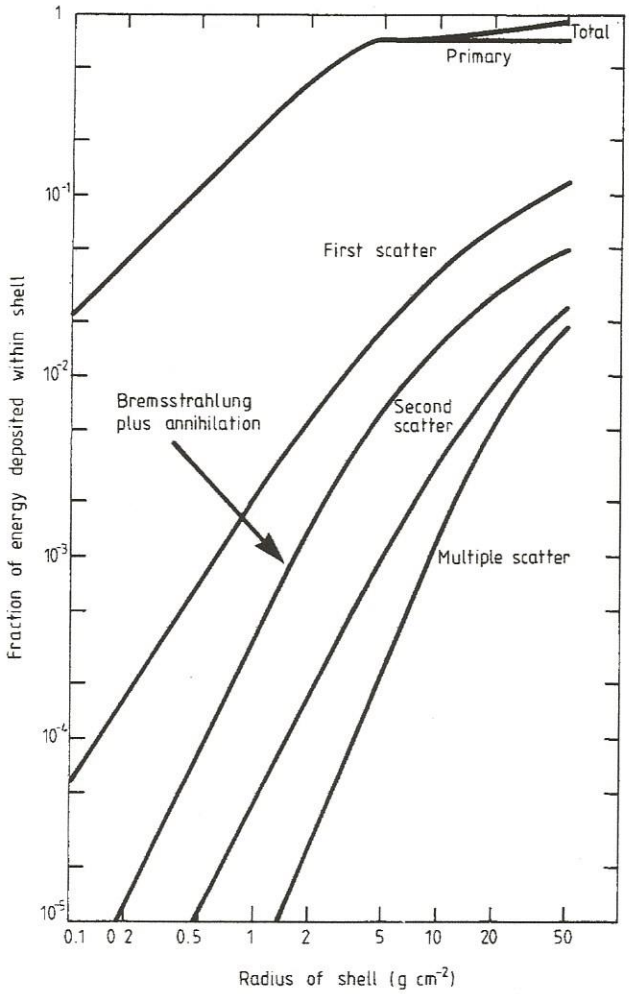


Figure 13. The fraction of incident energy deposited within radial shells as a function of radius for 10 MeV photons interacting at the centre of a 60 g cm^{-2} sphere.

backscattered from the primary component is very small at all incident photon energies. Qualitatively, this indicates that the kernels behave as expected.

Quantitatively, the energy deposition kernels are in good agreement with recent differential pencil beams of Chui and Mohan (1986). Except at the highest photon energies, there is good agreement between the ratio of the total primary energy to the total incident photon energy and the ratio of the energy absorption to the attenuation coefficients. It is likely that our determination of this ratio is superior at high energies because of the inclusion in EGS of positron annihilation in flight.

The mean radii and polar angles weighted with respect to the primary energy deposited in a voxel were calculated for all voxels in which there was primary energy deposited. Together these defined the effective centre of the voxels with respect to the primary component. Except at voxels near the end of the range of the charged particles set in motion, the effective centre of the voxel corresponds to the geometrical centre of the voxel. This indicates that the geometrical centre of the voxel may be used to define the location of the voxel in interpolation routines.

The convolution method

At the surface of a phantom $\vec{x} = \vec{x}_s$
the primary fluence is

$$\Phi^0(\vec{x}_s, E_x)$$

At some depth

$$\Phi^0(\vec{x}, E_x) = \Phi^0(\vec{x}_s, E_x)\, e^{-\mu|\vec{x}-\vec{x}_s|}$$

The dose at $\vec{x}$ is

Call this "Bat convolution"

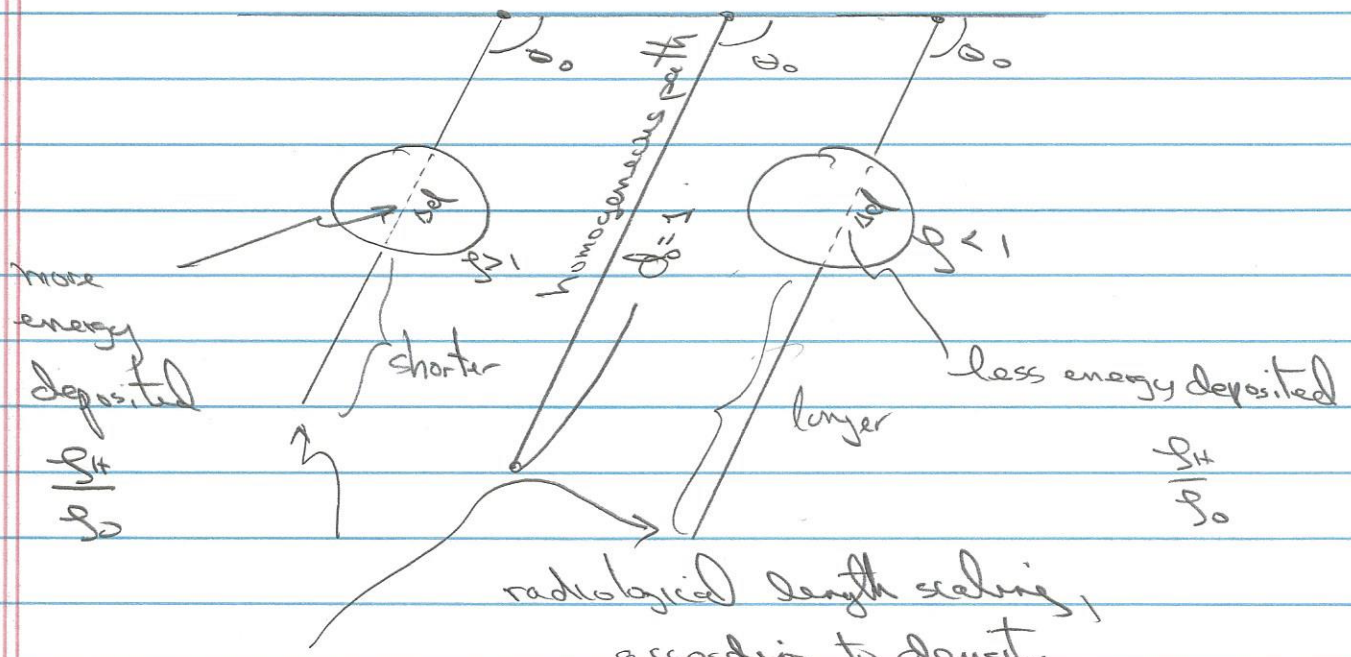
convolution kernel

$$D(\vec{x}) = \int dE_x^0 \int d\vec{x}_s \int d\vec{x}_a \; \Phi^0(\vec{x}_s, E_x^0)\, e^{-\mu|\vec{x}-\vec{x}_a|} \frac{k(\vec{x}-\vec{x}_a)}{4\pi|\vec{x}-\vec{x}_a|^2}$$

- $\int dE_x^0$: integral over initial fluence energy spectrum — 1D
- $\int d\vec{x}_s$: integral over the surface — 3D — a patient surface is a 3D object
- $\int d\vec{x}_a$: integral over the kernel — 3D — the kernel area is 3D

In general, this is a 7D calculation

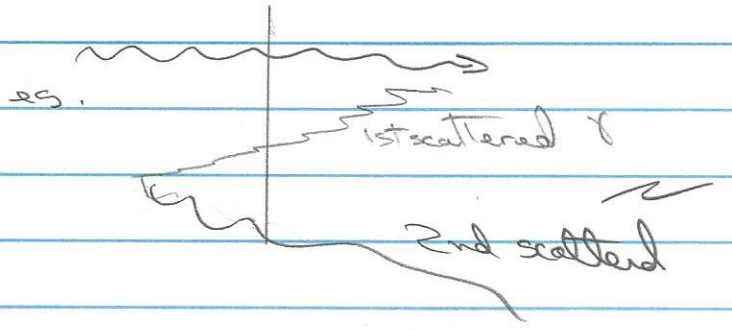
To account for heterogeneities



---

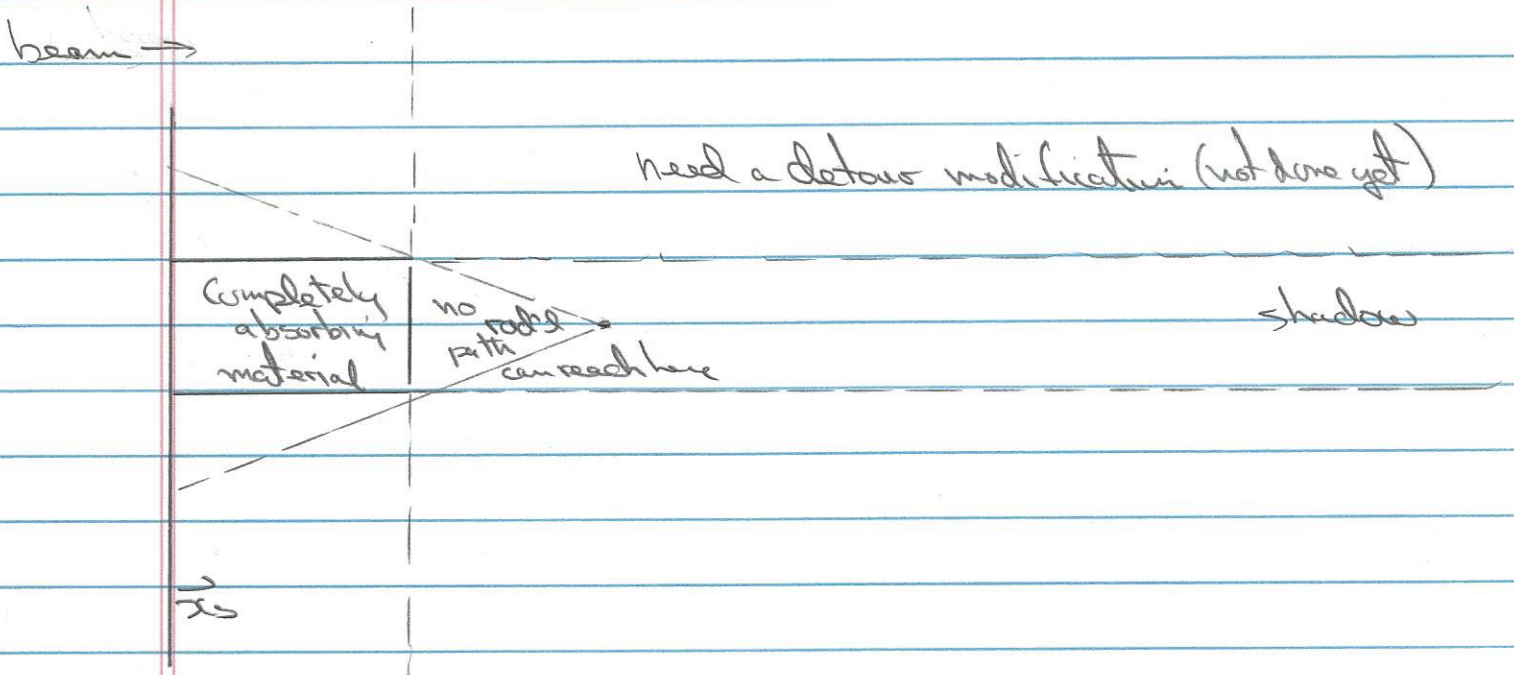
1) "Best Convolution" gets the surface wrong.

Why? It assume that transport of e^-, γ_{scat} is always directed away from the point of interaction



So, the surface dose is too high (worse for small E_γ^0)

2) Wrong near interfaces



3) It's 7 dimensional

Reduce dimensionality of E_γ^0

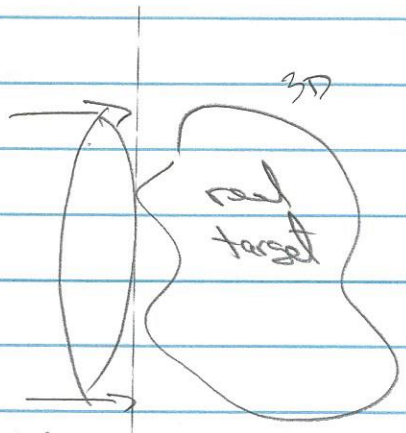
strategies

a) $\int dE_\gamma\, f(E_\gamma) \rightarrow f(E_{\gamma,1}) + f(E_{\gamma,2}) + f(E_{\gamma,3})$

discrete polyenergetic kernels.

only approximates beam hardening

b) Reduce dimensionality of $\vec{x}_s$



start convolution on the plane 3D - 2D ↙

c) Make integration less refined, i.e. coarser voxels for higher order of scatter. ↙

These strategies can make convolution competitive with MC.

} onto better things

Remember the 4π rule.

AAPM REPORT NO. 85

TISSUE INHOMOGENEITY CORRECTIONS FOR MEGAVOLTAGE PHOTON BEAMS

Report of Task Group No. 65 of the Radiation Therapy Committee of the American Association of Physicists in Medicine

Members

Nikos Papanikolaou (Chair) University of Arkansas, Little Rock, Arkansas
Jerry J. Battista London Regional Cancer Centre, London, Ontario, Canada
Arthur L. Boyer Stanford University, Stanford, California
Constantin Kappas University of Thessaly, Medical School, Larissa, Hellas
Eric Klein Mallinckrodt Institute of Radiology, St. Louis, Missouri
T. Rock Mackie University of Wisconsin, Madison, Wisconsin
Michael Sharpe Princess Margaret Hospital, Toronto, Ontario, Canada
Jake Van Dyk London Regional Cancer Centre, London, Ontario, Canada

August 2004

Published for the
American Association of Physicists in Medicine
by Medical Physics Publishing

A photon dose distribution model employing convolution calculations

Arthur Boyer and Ed Mok
Department of Radiology, The University of Texas Health Science Center at San Antonio, San Antonio, Texas 78284 and The Cancer Therapy and Research Center, San Antonio, Texas 78229

(Received 5 March 1984; accepted for publication 25 October 1984)

A three-dimensional photon beam calculation is described which models the primary, first-scatter, and multiple-scatter dose components from first principles. Three key features of the model are (1) a multiple-scatter calculation based on diffusion theory, (2) the demonstration of the modulation transfer function of the radiation dose transport process, and (3) the use of the finite fast Fourier transform to perform the required convolutions. The results of calculations for cobalt-60 in a homogeneous phantom are used to verify the accuracy of the model.

Key words: photon dose distribution, photon scatter, multiple-scatter dose, convolution, modulation transfer function

INTRODUCTION

A number of empirical and analytic models have been exploited to calculate the distribution of dose in radiation fields used for external beam radiation therapy.[1–5] The model described here is analytic and employs computed attenuation coefficients and scattering cross sections. The model convolves single-point interaction kernels with the primary beam fluence to build up the first-scatter and multiple-scatter components of the field. Use of convolution techniques to calculate scatter components has been described previously by Dean[6] and Mackie.[7] Convolutions can be carried out using Fourier transform methods which employ the Cooley–Tukey finite fast Fourier transform algorithm.[8]

The model described here is to be employed in the energy range 1–20 MeV. In a previous communication[9] it was pointed out that in principle considerable savings in computation time could be realized if the dose components could be calculated using convolutions of the form

$$D(\mathbf{r}) = \int_{V'} \Phi(\mathbf{r}') \cdot k(\mathbf{r} - \mathbf{r}') \cdot dV'. \tag{1}$$

The application here considers Φ to be a photon fluence distribution and k to be an interaction kernel which describes how radiation spreads out from the point $\mathbf{r}'$ after an interaction there. k can also be viewed as a Green's function for radiation dose transport. A formulation is given by which the dose components can be computed in this form assuming a homogeneous water phantom as the medium of propagation. It will be shown that $k(\mathbf{r})$ can be calculated for the entire radiation dose transport process. When this is done, $k(\mathbf{r})$ can be interpreted as the three-dimensional impulse response of the dose transport process. This is possible only when approximations are made which allow $k(\mathbf{r})$ to remain spatially invariant. Although all the physical processes involved are not strictly spatially invariant, the spatial variations are small enough to be ignored, at least in the lower end of the therapy energy range. In this case, the Fourier transform of $k(\mathbf{r})$ is the modulation transfer function for the physical processes which connect a photon fluence to the radiological dose produced by that fluence. We demonstrate these concepts and calculate an analytic form of the impulse response $k(\mathbf{r})$. We then present the results of our calculations of the dose components and total depth dose obtained by convolution employing the finite fast Fourier transform.

METHOD

Consider a flux of photons Φ_0 [photons/cm^2] of energy E_0 [MeV] moving in the $+z$ direction and incident upon a water surface at $z = 0$. The beam may in fact be multienergetic. In this more general case the calculations described below must be carried out for either an average energy or for several representative energies of the incident beam spectrum and added with appropriate weighting. In what follows we will not consider each energy explicitly, but will let it be understood that an energy spectrum may be involved for x-ray beams. Let the photons originate from a source a distance SSD[cm] from the surface. The primary fluence distribution in a homogeneous phantom can be calculated by essentially tracing rays originating from the radiation source and by applying inverse square and exponential attenuation to the fluence along a ray. A continuous phantom is replaced in this model by an array of calculation points. Each point is located in the center of a voxel and can be identified by indices corresponding to displacement in three dimensions. We will, however, continue to locate the calculation points by the vectors $\mathbf{r}$. The formulas required are

$$\Phi_p(\mathbf{r})\ [\text{photon/cm}^2] = \Phi_0\ [\text{photon/cm}^2] \left(\frac{\text{SSD}}{\text{SSD} + d}\right)^2 \prod_i e^{-\mu \Delta d_i}, \tag{2}$$

where Φ_0 is the photon fluence of the ray passing through the surface to $\mathbf{r}$, d is the depth into the phantom, and μ [cm^{-1}] is the total linear attenuation coefficient for energy E_0 at the voxel i along the ray trace path from the surface

$$d = s - s_{\text{air}} = \sum_i \Delta d_i, \tag{3}$$

where s is the distance from the source to the point of calculation, s_{air} is the distance traveled by the photons from the source to the phantom surface.

The kerma deposited by this primary fluence K_p is calculable[10] using the mass absorption coefficient μ_{en}/ρ and con-

 0094-2405/85/020169-09$01.20 © 1985 Am. Assoc. Phys. Med.

A convolution method of calculating dose for 15-MV x rays

T. R. Mackie,[a] J. W. Scrimger, and J. J. Battista
Department of Medical Physics, Cross Cancer Institute, Edmonton, Alberta, Canada T6G 1Z2

(Received 1 May 1984; accepted for publication 14 August 1984)

Arrays were generated using the Monte Carlo method representing the energy absorbed throughout waterlike phantoms from charged particles and scatter radiation set in motion by primary interactions at one location. The resulting "dose spread arrays" were normalized to the collision fraction of the kinetic energy released by the primary photons. These arrays are convolved with the relative primary fluence interacting in a phantom to obtain three-dimensional dose distributions. The method gives good agreement for the 15-MV x-ray dose in electronic disequilibrium situations, such as the buildup region, near beam boundaries, and near low-density heterogeneities.

Key words: photon dosimetry, convolution, charged particles, collision KERMA, Monte Carlo, 15-MV x rays, tissue-maximum ratios (TMR), lung corrections

I. INTRODUCTION

Present dose calculation methods are based on the assumption that all of the charged-particle energy liberated by photon radiation is deposited locally at the site of interaction. While this assumption is acceptable for cobalt-60 radiation, it weakens for higher energy x-rays for which the range of charged particles set in motion can be several centimeters. The need for considering this nonlocal energy deposition has been documented.[1–4] Some photon dose calculation methods have accounted for electronic "buildup" longitudinally along the central axis, but none have rigorously treated the lateral spread of charged particles set in motion.[5,6] Young and Kornelson[7] have taken into account the dose reduction caused by a lack of charged particles equilibrium using a semiempirical "loss factor."

For photon energies comparable to those of cobalt-60 radiation, existing methods rely on measured tissue–air ratio (TAR) data that assume that the primary dose is equal to the TAR extrapolated to a "zero-area field." This leads to a number of technical and fundamental problems for higher energy photon beams. Firstly, the TAR concept is usually replaced by a tissue–phantom ratio (TPR) which is based on measurements made in a phantom. It becomes more difficult to separate the contributions of primary and scattered radiation because the increase in TPR caused by scatter within the phantom must be isolated from increases caused by external factors[8] (e.g., collimators). Furthermore, extrapolation to a zero-area field to obtain the primary dose is not physically acceptable because lateral electronic equilibrium is lost and the dose is greatly reduced.

In this work, a physically sound and consistent method has been developed which allows calculation of three-dimensional dose distributions in homogeneous or heterogeneous phantoms irradiated with rectangular or irregularly shaped fields of high-energy photons. The use of measured data as a data base is abandoned and replaced with data generated from first principles by Monte Carlo techniques. The Monte Carlo method is used to map the spatial distribution of charged-particle energy away from a primary photon interaction site. This distribution, called a primary dose spread array, is convolved spatially, with the kinetic energy released at all the primary interaction sites to yield the primary dose distribution. In a heterogeneous phantom, the dose spread arrays need to be modified during convolution.

Any current method separating primary from scatter dose can be improved with the methodology proposed here. Since convolution is a well understood and documented technique, there are conceptual advantages for implementing a convolution framework for the spread of energy due to scattered photons, as well as charged particles set in motion. (Dean has used this approach to find where the scatter dose was being absorbed from cobalt-60 primary photons interacting in one location of a water phantom.[9])

The proposed method was based on concepts which will not become obsolete as improved computational power becomes available. The fundamental reason for this is the sound physical basis of the Monte Carlo and convolution procedures. Another reason is an inherent flexibility to compromise between speed and accuracy. Therefore, as computers become faster, greater accuracy can be achieved without modifying the algorithm substantially.

II. PRIMARY DOSE SPREAD ARRAYS

A primary dose spread array (analogous to the point spread array used in image processing) is the three-dimensional spatial distribution of energy deposited by electrons and positrons which spread from the site of the primary photon interactions. It is generated by tracking the motion of charged particles away from primary interaction sites occurring within a cubic volume element (voxel). These charged particles are followed, using the Monte Carlo method, in a homogeneous phantom consisting of voxels of the same size, atomic number, and density. The amount of energy deposited at, and in the neighborhood of, the interaction voxel is scored. Figure 1 illustrates the procedure schematically.

The incident photon fluence spectrum was not known and could not easily be measured. However, the spectrum was chosen by comparing measured depth dose values with the results of "electron gamma shower" (EGS) Monte Carlo sim-

 0094-2405/85/020188-09$01.20 © 1985 Am. Assoc. Phys. Med.

Phys. Med. Biol., 1988, Vol. 33, No 1, 1-20. Printed in the UK

Generation of photon energy deposition kernels using the EGS Monte Carlo code

T R Mackie†‖, A F Bielajew‡, D W O Rogers‡ and J J Battista§

† Physics Services, Allan Blair Memorial Clinic, Regina, Canada, S4T 7T1
‡ Physics Division, National Research Council of Canada, Ottawa, Canada, K1A 0R6
§ Department of Medical Physics, Cross Cancer Institute, Edmonton, Canada, T6G 1Z2

Received 8 September 1986, in final form 29 April 1987

Abstract. The EGS Monte Carlo code was used to generate photon energy deposition kernels which describe the energy deposited by charged particles set in motion by primary, first scattered, second scattered, multiple scattered and bremsstrahlung plus annihilation photons. These were calculated for a water medium irradiated with monoenergetic photons with energies in the range 0.1-50 MeV. In addition to the primary energy deposition kernels, primary charged particle transport was further characterised by computing the effective centre of the voxels, and the effective penetration depth, effective radius and effective lateral distance travelled by these particles. The dose per unit collision kerma for parallel monoenergetic primary photons β' was calculated. Additional applications of the energy deposition kernels are discussed.

1. Introduction

A number of authors have proposed that photon dose be calculated using convolution mathematics (Dean 1980, Mackie 1983, 1984, Mackie and Scrimger 1984, Boyer and Mok 1984, 1985, Ahnesjo 1984, Boyer 1984, Chui *et al* 1984, Mackie *et al* 1985b, Mohan *et al* 1986). The technique involves convolving the primary photon fluence with a kernel that describes the transport and deposition of energy by secondary particles. The convolution kernel has been termed a dose spread array because it describes the spread of dose from a primary photon interaction site (Mackie *et al* 1985b). Mohan *et al* (1986) have called the convolution kernel a 'differential pencil beam'.

In principle, the energy deposition kernels can be obtained by deconvolving measured narrow beam dose distributions (Ahnesjo 1984). Alternatively, one can calculate monoenergetic energy deposition kernels using Monte Carlo simulation. In this approach, the contributions from each photon scattering order (e.g. primary, first scatter, etc) may be obtained separately (Mackie *et al* 1985b). The transport of several orders of photon scattering may be modelled analytically, but higher-order scattering is more effectively modelled with the Monte Carlo method.

Roesch (1958) defined a distribution called an 'influence function' which is equivalent to a primary energy deposition kernel and showed how it could be used to obtain the amount of dose deposited in situations of electronic disequilibrium. The influence function was not calculated but its first moments, called $\bar{x}$ in the incident photon direction and $\bar{y}$ in the perpendicular direction, were estimated. The first moment $\bar{x}$ was used to approximate the ratio of dose to collision kerma β (Loevinger 1981). Brahme (1977) analytically estimated a distribution equivalent to the primary energy deposition kernel and the influence function.

‖ Currently at: Department of Medical Physics, 1300 University Avenue, University of Wisconsin, Madison, WI 53706, USA.

0031-9155/88/010001+20$02.50 © 1988 IOP Publishing Ltd

Accuracy of patient dose calculation for lung IMRT: A comparison of Monte Carlo, convolution/superposition, and pencil beam computations

Barbara Vanderstraeten[a)]
Department of Medical Physics, Ghent University, Proeftuinstraat 86, 9000 Ghent, Belgium and Department of Radiotherapy, Ghent University Hospital, De Pintelaan 185, 9000 Ghent, Belgium

Nick Reynaert
Department of Medical Physics, Ghent University, Proeftuinstraat 86, 9000 Ghent, Belgium

Leen Paelinck, Indira Madani, Carlos De Wagter, Werner De Gersem, and Wilfried De Neve
Department of Radiotherapy, Ghent University Hospital, De Pintelaan 185, 9000 Ghent, Belgium

Hubert Thierens
Department of Medical Physics, Ghent University, Proeftuinstraat 86, 9000 Ghent, Belgium

(Received 5 December 2005; revised 19 May 2006; accepted for publication 6 July 2006; published 17 August 2006)

The accuracy of dose computation within the lungs depends strongly on the performance of the calculation algorithm in regions of electronic disequilibrium that arise near tissue inhomogeneities with large density variations. There is a lack of data evaluating the performance of highly developed analytical dose calculation algorithms compared to Monte Carlo computations in a clinical setting. We compared full Monte Carlo calculations (performed by our Monte Carlo dose engine MCDE) with two different commercial convolution/superposition (CS) implementations (Pinnacle-CS and Helax-TMS's collapsed cone model Helax-CC) and one pencil beam algorithm (Helax-TMS's pencil beam model Helax-PB) for 10 intensity modulated radiation therapy (IMRT) lung cancer patients. Treatment plans were created for two photon beam qualities (6 and 18 MV). For each dose calculation algorithm, patient, and beam quality, the following set of clinically relevant dose-volume values was reported: (i) minimal, median, and maximal dose (D_{min}, D_{50}, and D_{max}) for the gross tumor and planning target volumes (GTV and PTV); (ii) the volume of the lungs (excluding the GTV) receiving at least 20 and 30 Gy (V_{20} and V_{30}) and the mean lung dose; (iii) the 33rd percentile dose (D_{33}) and D_{max} delivered to the heart and the expanded esophagus; and (iv) D_{max} for the expanded spinal cord. Statistical analysis was performed by means of one-way analysis of variance for repeated measurements and Tukey pairwise comparison of means. Pinnacle-CS showed an excellent agreement with MCDE within the target structures, whereas the best correspondence for the organs at risk (OARs) was found between Helax-CC and MCDE. Results from Helax-PB were unsatisfying for both targets and OARs. Additionally, individual patient results were analyzed. Within the target structures, deviations above 5% were found in one patient for the comparison of MCDE and Helax-CC, while all differences between MCDE and Pinnacle-CS were below 5%. For both Pinnacle-CS and Helax-CC, deviations from MCDE above 5% were found within the OARs: within the lungs for two (6 MV) and six (18 MV) patients for Pinnacle-CS, and within other OARs for two patients for Helax-CC (for D_{max} of the heart and D_{33} of the expanded esophagus) but only for 6 MV. For one patient, all four algorithms were used to recompute the dose after replacing all computed tomography voxels within the patient's skin contour by water. This made all differences above 5% between MCDE and the other dose calculation algorithms disappear. Thus, the observed deviations mainly arose from differences in particle transport modeling within the lungs, and the commissioning of the algorithms was adequately performed (or the commissioning was less important for this type of treatment). In conclusion, not one pair of the dose calculation algorithms we investigated could provide results that were consistent within 5% for all 10 patients for the set of clinically relevant dose-volume indices studied. As the results from both CS algorithms differed significantly, care should be taken when evaluating treatment plans as the choice of dose calculation algorithm may influence clinical results. Full Monte Carlo provides a great benchmarking tool for evaluating the performance of other algorithms for patient dose computations. © *2006 American Association of Physicists in Medicine*.
[DOI: 10.1118/1.2241992]

Key words: Monte Carlo, convolution/superposition, pencil beam, lung cancer, intensity modulated radiation therapy (IMRT)

NERS 590

Introduction to Radiological Physics and Radiation Dosimetry

aka Dosimetry

Lecture Notes for Chapter 7: Ionization chamber-based air kerma standards

The lecture number corresponds directly to the chapter number in the online book.
The section numbers, and equation numbers correspond directly to those in the online book.

©Alex F Bielajew 2013, Nuclear Engineering and Radiological Sciences, The University of Michigan

Ionization chamber-based air kerma standards

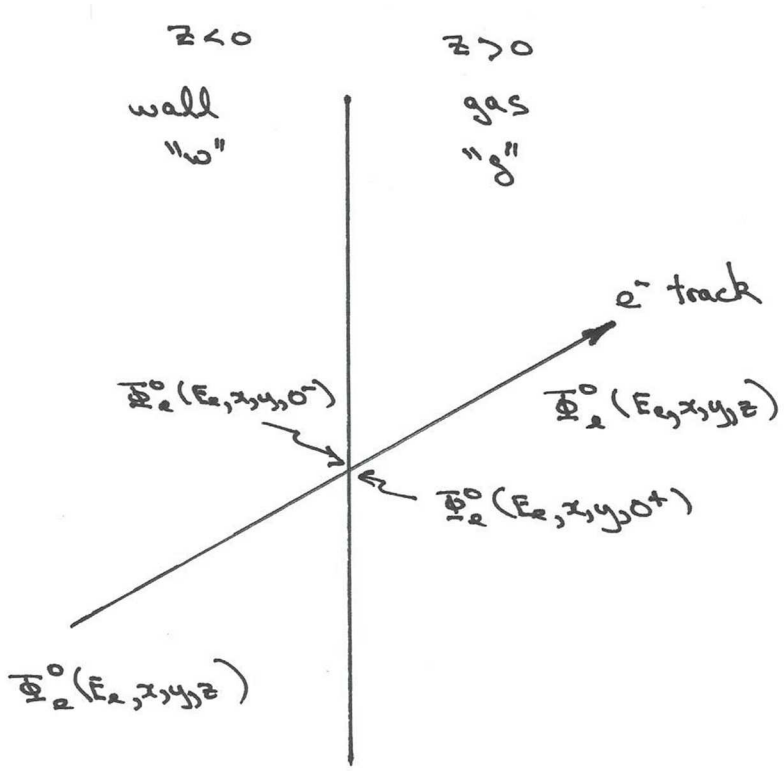
1. Bragg-Gray cavity theory
   (a) Exposure measurements
2. Spencer-Attix cavity theory
3. Modern cavity theory
4. Interface effects
5. Saturation corrections
6. Burlin cavity theory
7. The dosimetry chain

Chapter 7.1: Bragg-Gray cavity theory

Imagine a planar interface formed by two materials.

- To the left, $z < 0$, is material "w", or "wall"

- To the right, $z > 0$, is material "g", or "gas"



Consider an electron transport model in the vicinity of the interface where energy losses are computed using the total mass collision stopping power.

That is, δ-rays are not transported explicitly, but their energies are "rolled up" in the stopping powers.

Imagine than an electron fluence, represented by $\Phi_e^0(E_e, x, y, z)$ crosses that interface.

Since electron fluence is conserved at the interface
(an interface can not cause a deflection),
we can say that,

$$\Phi_e^0(E_e, x, y, 0-) = \Phi_e^0(E_e, x, y, 0+) = \Phi_e^0(E_e, x, y, 0) \ . \tag{1}$$

The doses on either side of the interface are, however, discontinuous:

$$D_{\rm w}(x,y,0-) = \int_0^\infty {\rm d}E_e\, \Phi_e^0(x,y,0) s_{\rm w}(E_e) \ , \tag{2}$$

and,

$$D_{\rm g}(x,y,0+) = \int_0^\infty {\rm d}\, \Phi_e^0(x,y,0) s_{\rm g}(E_e) \ , \tag{3}$$

from which we can infer that,

$$\frac{D_{\rm g}(x,y,0+)}{D_{\rm w}(x,y,0-)} = (\overline{s})^{\rm g}_{\rm w} \tag{4}$$

where,

$$(\overline{s})^{\rm g}_{\rm w} \equiv \frac{\int_0^\infty {\rm d}E_e\, \Phi_e^0(x,y,0) s_{\rm g}(E_e)}{\int_0^\infty {\rm d}E_e\, \Phi_e^0(x,y,0) s_{\rm w}(E_e)} \ . \tag{5}$$

Now consider a volume of material "w" (wall material). We wish to measure the dose at some point $\vec{x}$ in "w" by placing within it, a gas cavity "g" that has $\vec{x}$ within its domain. Thus, under the following assumptions:

BG-1 the size of the gas layer is so small that in any dimension it is smaller than R_e^{w}, the electron range in the "w" material,

BG-2 the dose in the cavity is assumed to be deposited entirely by electrons crossing it,

photon interactions in the cavity may be ignored,

then,

$$D_{\mathrm{w}}(\vec{x}) = D_{\mathrm{g}}(\vec{x})(\overline{s})^{\mathrm{w}}_{\mathrm{g}} \ . \tag{6}$$

That is, we can determine the dose to the wall material from a measurement of the dose to the gas.

Note that under conditions of charged particle equilibrium, but with the proviso that the atomic composition of the gas and wall material are the same, **BG-1** may be relaxed, and the cavity allowed to assume any shape and size.

Under these conditions, we may also write,

$$K_c^{\mathrm{w}}(\vec{x}) = K_c^{\mathrm{g}}(\vec{x})(\overline{s})_{\mathrm{g}}^{\mathrm{w}} \ . \tag{7}$$

Exposure measurements

Ionization chamber measurements are made in terms of exposure. Dose and "exposure" are related by the following relation,

$$D_{\mathrm{g}} = \left(\frac{\Delta Q}{\Delta m}\right)\left(\frac{\overline{W}}{e}\right)_{\mathrm{g}} , \tag{8}$$

where, ΔQ is the charge of the ions of one sign collected (assuming complete collection) from the "active volume" of the gas during irradiation, Δm is the mass of the "active volume" of the gas, and $\left(\frac{\overline{W}}{e}\right)_{\mathrm{g}}$ is the average energy deposited in the gas divided by the charge of one of the ion pairs, per ion pair created.

The concept of "active volume" just means that volume of the gas for which electric field lines can sweep ions toward the electrodes. There may be "guard" volumes or inactive volumes that still logically comprise the cavity volume, but do not participate in sweeping the ions toward the electrodes.

Therefore, assuming an exposure measurement has been made, we may write,

$$D_{\mathrm{w}} = \left(\frac{\Delta Q}{\Delta m}\right) \left(\frac{\overline{\overline{W}}}{e}\right)_{\mathrm{g}} (\overline{s})^{\mathrm{w}}_{\mathrm{g}} \ . \tag{9}$$

Corollary 1: Same wall, different gases

Consider two exposure measurements involving the same instrument involving the same source of radiation, but one in which the gas may be substituted. It can be shown, from (9), that,

$$\frac{\Delta Q_2}{\Delta Q_1} = \left(\frac{\rho_2}{\rho_1}\right) \frac{\left(\overline{W}/e\right)_1}{\left(\overline{W}/e\right)_2} \left(\overline{s}\right)_{\mathrm{g_1}}^{\mathrm{g_2}} \ . \tag{10}$$

It appears that the wall material has vanished from the above equation! However, it is still there, represented by the electron fluence within it, in the stopping power ratio

That the fluence is not perturbed by the gas cavity deserves the same emphasis here.

Corollary 2: Different walls, same gases

Consider two exposure measurements involving two similar instruments involving the same source of radiation, but one in which the wall material may be different, and the gas, while remaining the same, may occupy a different volume.

To start, imagine that the cavity region is filled with wall material. Under conditions of charged particle equilibrium, we note that the dose to any point in this location is,

$$D_{\rm w}^{\rm CPE} = K_{\rm c} = \int_0^\infty {\rm d}E_\gamma \, \Psi(E_\gamma)\mu_{\rm en}(E_\gamma) \ , \tag{11}$$

or,

$$D_{\rm w}^{\rm CPE} = \Psi\overline{\mu}_{\rm en} \ . \tag{12}$$

Here,

$$\Psi = \int_0^\infty \mathrm{d}E_\gamma \, \Psi(E_\gamma) \ , \tag{13}$$

and,

$$\overline{\mu}_{\mathrm{en}} = \frac{1}{\Psi} \int_0^\infty \mathrm{d}E_\gamma \, \Psi(E_\gamma) \mu_{\mathrm{en}}(E_\gamma) \ . \ , \tag{14}$$

Therefore,

$$\frac{D_{\mathrm{w}2}}{D_{\mathrm{w}1}} = (\overline{\mu}_{\mathrm{en}})_{\mathrm{w}1}^{\mathrm{w}2} \ , \tag{15}$$

where,

$$(\overline{\mu}_{\mathrm{en}})_{\mathrm{w}1}^{\mathrm{w}2} = \frac{\int_0^\infty \mathrm{d}E_\gamma \, \Psi(E_\gamma) \mu_{\mathrm{en}}^{\mathrm{w}2}(E_\gamma)}{\int_0^\infty \mathrm{d}E_\gamma \, \Psi(E_\gamma) \mu_{\mathrm{en}}^{\mathrm{w}1}(E_\gamma)} \ , \tag{16}$$

from which it can be shown, from (9), that,

$$\frac{\Delta Q_2}{\Delta Q_1} = \left(\frac{\Delta V_2}{\Delta V_1} \right) (\overline{\mu}_{\mathrm{en}})_{\mathrm{w}1}^{\mathrm{w}2} \, (\overline{s})_{\mathrm{w}2}^{\mathrm{w}1} \ . \tag{17}$$

It appears that the gas material has vanished from the above equation, except for the volume they occupy. This is an interesting consequence of radiation equilibrium.

Spencer-Attix cavity theory

Spencer and Attix improved on Bragg-Gray cavity theory by using restricted stopping powers, assuming that the high-energy δ-ray fluence spectrum might be insensitive to atomic differences as the interface.

Therefore, the foregoing discussion may be modified straightforwardly by employing restricted stopping powers.

Ignoring the contribution of bremsstrahlung to the stopping power, the dose may be calculated from

$$D = \int_0^\infty \mathrm{d}E\, \Phi_e(E) \ell_{\mathrm{c}}(E, \Delta) \ , \tag{18}$$

where Δ is the energy above which electrons can be set in motion and contribute to the electron fluence spectrum, $\Phi_{e^-}(E)$.

The choice of Δ is an interesting one. General practice is to set Δ to an energy that corresponds to a an electron range, $R_e(\Delta)$, in the gas material that is characteristic of the size of the cavity, or less.

To my knowledge, this parameter has not been effectively tested over a range of materials and parameter-size selections.

Direct analytic calculations of (18) are problematic, as there is no sufficiently accurate theory to predict $\Phi_e(E)$.

However, as we shall soon see in "Modern Cavity Theory" that analytic calculations still have an important role to play.

Modern cavity theory

The existence of radiation equilibrium is a mathematical fiction, yet, it is closely approximated by thick-walled ionization chambers.

In this section we develop modern cavity theory and demonstrate the important role of radiation equilibrium conditions and the role of Fano's theorem.

Consider a volume of gas material in which there exists an electron fluence of any character.

The dose to that gas, obtained by integrating over the energy deposited in the gas, and dividing by it's mass, may be written as:

$$D_{\rm g} = \frac{1}{V_{\rm g}} \int {\rm d}E_e \int {\rm d}\vec{x}\, \varphi_{\rm g}(E_e, \vec{x}) R_{\rm g}(E_e, \vec{x}) \ , \tag{19}$$

where $V_{\rm g}$ is the volume of the gas, $\varphi_{\rm g}(E_e, \vec{x})$ is the electron fluence arising from all sources, and $R_{\rm g}(E_e, \vec{x})$ is a response function of the gas, that has units EL^2/M.

We keep the discussion general for now, but have in mind to use restricted stopping powers later on. Henceforth, we will employ a a compact notation for the above,

$$D_{\mathrm{g}} = \int \varphi_{\mathrm{g}} R_{\mathrm{g}} \ . \tag{20}$$

We would like to transform (19) into a form that exhibits radiation equilibrium explicitly.

It will take many steps to get there.

First, split the electron fluence into that which arises from the primary interaction of a photon, including all δ-rays.

Bremsstrahlung and annihilation photons are considered, but if they produce an electron fluence in the cavity, that fluence goes into the "scattered" part.

Therefore, we write, $\varphi_{\rm g} = \varphi_{\rm g}^0 + \varphi_{\rm g}^{\rm s}$, and we rewrite the dose as,

$$D_{\rm g} = \left(\int \varphi_{\rm g}^0 R_{\rm g} \right) A_{\rm scat} \ , \tag{21}$$

where

$$A_{\rm scat} = \frac{1 + \left(\int \varphi_{\rm g}^{\rm s} R_{\rm g} \right)}{\int \varphi_{\rm g}^0 R_{\rm g}} \ . \tag{22}$$

$Ascat$ is usually close to unity, for most ionization chambers, since the scattered radiation that results in ionization in the chamber is usually overwhelmed by the primary ionization.

Now the strategy is revealed.

We will keep simplifying the electron fluence until we get it into equilibrium, and produce correction factors that are close to unity (we hope) and amenable to analytic or Monte Carlo calculations.

The primary photon fluence is not yet in equilibrium, since it is attenuating across the chamber.

Therefore, assume that we can undo this this contribution to disequilibrium, thereby producing a primary electron fluence that arises from unattenuated primary photons. We call this fluence, $\tilde{\varphi}^0_{\rm g}$ and rewrite (21) as,

$$D_{\rm g} = \left(\int \tilde{\varphi}^0_{\rm g} R_{\rm g} \right) A_{\rm scat} A_{\rm att} \ , \tag{23}$$

where

$$A_{\rm att} = \frac{\int \varphi^0_{\rm g} R_{\rm g}}{\int \tilde{\varphi}^0_{\rm g} R_{\rm g}} \ . \tag{24}$$

As $A_{\rm scat}$ is close to, but greater than unity, $A_{\rm att}$ is close to, but less than unity.

To some extent they undo each other, as the action of attenuation usually leads to scattered radiation.

We still have not completely undone primary photon disequilibrium, because the photon fluence arises from a geometric source, usually a near-point source, at some distance from the chamber, yet close enough that the fluence is in some small disequilibrium.

Nonetheless, $1/r^2$-effects and other geometric effects must be undone.

We determine the photon fluence at the center of the chamber (one may use the center-of-mass to define this) and call this the *point of measurement*.

The source can then be converted into a broad parallel beam with the same energy spectrum. Now we rename the electron fluence obtained in this way, $\tilde{\varphi}_{\rm g}^{0,||}$, and rewrite as,

$$D_{\rm g} = \left(\int \tilde{\varphi}_{\rm g}^{0,||} R_{\rm g} \right) A_{\rm scat} A_{\rm att} A_{\rm pn} \ , \tag{25}$$

where

$$A_{\rm pn} = \frac{\int \varphi_{\rm g}^{0} R_{\rm g}}{\int \tilde{\varphi}_{\rm g}^{0,||} R_{\rm g}} \ . \tag{26}$$

A typical source configuration for a standards measurement is a small radioactive source about 1 cm across at a distance of 100 cm. So, this correction is near unity as well, but is can be less than, or greater than unity, depending on the design of the instrument.

Now, the primary photon fluence that set the electrons in motion is now in equilibrium, however, the electron fluence is not. Imagine that we have wall material in the place of the cavity, and we employ that fluence, but with the gas response function. That permits a rewrite of (25) as,

$$D_{\rm g} = \left(\int \tilde{\varphi}^{0,||}_{\rm w} R_{\rm g} \right) A_{\rm scat} A_{\rm att} A_{\rm pn} A_{\rm fl} \ , \tag{27}$$

where

$$A_{\rm fl} = \frac{\int \tilde{\varphi}^{0}_{\rm g} R_{\rm g}}{\int \tilde{\varphi}^{0,||}_{\rm w} R_{\rm g}} \ . \tag{28}$$

$A_{\rm fl}$ is a correction that accounts for the perturbation of the electron fluence by the difference in atomic composition of the gas cavity. If the atomic composition of the gas and the wall is not too dissimilar, this is expected to be a small effect.

We may also rewrite (27) to be,

$$D_{\rm g} = \left(\int \tilde{\varphi}_{\rm w}^{0,||} R_{\rm w} \right) A_{\rm scat} A_{\rm att} A_{\rm pn} A_{\rm fl} \left(\overline{s}\right)_{\rm w}^{\rm g} \ , \tag{29}$$

where

$$\left(\overline{s}\right)_{\rm w}^{\rm g} = \frac{\int \tilde{\varphi}_{\rm g}^{0} R_{\rm g}}{\int \tilde{\varphi}_{\rm w}^{0,||} R_{\rm w}} \ . \tag{30}$$

Here we identify $\left(\overline{s}\right)_{\rm w}^{\rm g}$ as a generalized "stopping power" ratio. We can also identify the first term in (29) as the dose to the wall material due to primary photons in a state of complete radiation equilibrium.

Thus, (29) can also be expressed as,

$$D_{\rm g} = \Psi^{0,||}(\overline{\mu}_{en})_{\rm w}\,(\overline{s})^{\rm g}_{\rm w}\,A_{\rm scat}A_{\rm att}A_{\rm pn}A_{\rm fl}\ , \tag{31}$$

where,

$$(\overline{\mu}_{en})_{\rm w} = \frac{1}{\Psi^{0,||}}\int_0^\infty {\rm d}E_\gamma\,\Psi^{0,||}(E_\gamma)\mu_{en}(E_\gamma)\ . \tag{32}$$

Finally, we may rewrite (32) as, or equivalently,

$$D_{\rm g} = K^{0,||}_{\rm c,g}(\overline{\mu}_{en})^{\rm w}_{\rm g}\,(\overline{s})^{\rm g}_{\rm w}\,A_{\rm scat}A_{\rm att}A_{\rm pn}A_{\rm fl}\ , \tag{33}$$

or

$$\frac{D_{\rm g}}{K^{0,||}_{\rm c,g}} = (\overline{\mu}_{en})^{\rm w}_{\rm g}\,(\overline{s})^{\rm g}_{\rm w}\,A_{\rm scat}A_{\rm att}A_{\rm pn}A_{\rm fl}$$

which relates a real measurement of dose to the gas to its collision Kerma, $K^{0,||}_{\rm c,g}$, under conditions of radiation equilibrium. The connection between the two is really a ratio of factors quite close to unity.

Chapter 7.4: Interface effects

This topic has to be researched further, before it can be presented, in a coherent fashion, to students. Remember to tune in, in a year or two.

Chapter 7.5: Saturation corrections

In all the previous discussion, it was assumed that the radiation produced ions of both signs in the gas of an ion chamber, and that these ions were completely collected at the electrodes. However, many physical phenomena can interfere with complete collection.

- Ions can recombine in the ionization column of the charged particle track. This "initial" or "columnar" recombination has been discussed by G. Jaffe [Ann Physik, 42, 303–344 (1913)] and H. Zanstra [Physica, 2, 817–824 (1935)]. For medical applications, this effect is thought to be negligible. However, the effect is more prominent for intense beams, and it is unclear whether the pulsed beams of modern linacs may be effected. More work is needed on this topic.
- Ions that have drifted away from the ionization column can recombine, reducing the collection efficiency. This effect must be corrected for, and forms the bulk of the following discussion.
- The shape of the saturation curve (collection efficiency *vs.* applied voltage) can be different if free electrons are collected. This has been discussed by Bielajew [Med. Phys. 12, 197 (1985)], and found to be inconsequential for medical physics applications.

- Poor chamber design can lead to dead areas where ions can collect and reduce the efficiency, or sharp points can generate spurious ions. Poor chamber design can also allow ions to diffuse out from the collection zone.

The atomic/molecular composition of the gases in ion chambers have different behaviors, when exposed to radiation. Most ion chambers employed in medical physics applications have their gas cavities exposed to air. Dry air is comprised of N_2:0.78084, O_2:0.20946, Ar:0.00934, CO_2:0.00035, and traces of Ne:0.00001818, He:0.00000524, CH_4:0.000001745, Kr:0.00000114, and O_2:0.00000055. Thus, air has about a 21% electronegative (scavenges and attaches free electrons to form negative ions) component (mostly O_2), and a 79% non-electronegative component.

Under normal conditions, all of the free electrons in air attach to its electronegative component. The radicals in air have a drift velocity of ≈ 1 cm/s/(V/cm), while free a free electron's drift velocity can be ≈ 1000 cm/s/(V/cm).

Humidity plays an important role as well, since water vapor is electronegative, and can be up to a few percent of the total mass of air.

Saturation theory, or *ion-collection efficiency theory*, for ion chambers exposed to continuous beams, such as radiative sources, is the most developed. Pulsed beams, or scanned beams must be treated treated differently, and are discussed in the next section. The theory for pulsed beams is discussed in the next section.

Continuous beams

The investigation of volume recombination in parallel-plate ionization chambers exposed to continuous beams (from radiative sources) has a long history in physics. E. Rutherford and J. J. Thomson [Philos. Mag. 42, 392 (1896)] reported the first measurements of the saturation curve, and Thomson [Philos. Mag. 47, 253 (1899)] later proposed a theory that may be used to study the details of the saturation curve in terms of the applied voltage, ionic mobilities, volume recombination, and self fields (space-charge effect) of single positive and negative charge carriers.

The Thomson differential equations are mathematically complex, and analytic solutions which are valid for the entire saturation curve have not been found. An exhaustive mathematical treatment has been given by G. Mie [Ann. Phys. (Leipzig) 13, 857 (1904)], based on an iterative approach to the Thomson equations, and he gives simple analytic forms at both low and high collection efficiencies.

The near-saturation (high collection efficiency) region has had the most relevance for medical physics. J. W. Boag and T. Wilson [Br. J. Appl. Phys. 3, 222 (1952)], and Boag [5J. W. Boag, "Ionization Chambers," in Radiation Dosimetry, 2nd ed., edited by F. H. Attix and W. C. Roesch (Academic, New York, 1966), Vol. 2] have developed simpler theories that adequately describe the saturation curve near full collection efficiency for most practical applications. They all agree with Mie's expression near saturation. The region of low collection efficiency has been studied less thoroughly.

J. S. Townsend [J. S. Townsend, Electricity in Gases (Clarendon, Oxford, 1915)] has derived an analytic solution to the Thomson theory which is valid for the entire saturation curve in the approximation that the space-charge effect can be neglected. This solution agrees with the near-saturation expressions of Mie, Boag and Wilson, and Boag, and also with Mie's expression at low collection efficiency, if the ion mobilities are equal. This is nearly true for air, a common ion chamber gas.

Bielajew [Med. Phys. 12, 197 (1985)] showed that the Townsend solution provide a good fit to the entire saturation curve and it serves as a good basis for improved approximations.

Correcting for incomplete ion collection: the two-voltage technique

For ion chamber in continuous beams, in the near saturation region, where ion collection efficiencies are greater than about 0.9, it can be shown that the charge collected, Q, and the charge produced, Q_0, are related by:

$$\frac{1}{Q} = \frac{1}{Q_0} + \frac{c}{V^2} \ ,$$

where c is a constant that depends on chamber design, as well as temperature, humidity and pressure.

Charge collection measurements are precise enough, so that it is sufficient to measure the charge collected at two voltage, V_1, the normal operating voltage, as specified by the manufacturer of the chamber, and a second voltage, V_2, usually half that of V_1.

The constant c can be determined from the measurements to be:

$$c = \left(\frac{1}{Q_2} - \frac{1}{Q_1}\right) \Big/ \left(\frac{1}{V_2^2} - \frac{1}{V_1^2}\right) \ .$$

Once having done this, the multiplicative correction to the charge collected at the normal operating voltage is:

$$\frac{Q_0}{Q_1} = \left(1 - \frac{cQ_1}{V^2}\right)^{-1} \ .$$

Pulsed and scanned beams

For pulsed and scanned beam, the two-voltage technique, can be applied, although the relationship is different:

$$\frac{1}{Q} = \frac{1}{Q_0} + \frac{c}{V} \ ,$$

Replacing V^2 with V works, although once must be close to saturation, with collection efficiencies needing to be greater than 0.96.

Corrections for diffusive losses, usually not a factor in these applications, also falls under the $1/V$ behavior.

It is necessary to completely characterize the saturation characteristics of one's chamber, by mapping out its response over a range of voltages, before using it in practice.

In cases where neither law applies, a more complicated expression may be used, where a combination of the two:

$$\frac{1}{Q} = \frac{1}{Q_0} + \frac{c_1}{V} + \frac{c_2}{V^2} \ ,$$

necessitating 3 measurements per calibration, and a slightly more complicated, but obvious, arithmetic procedure.

Chapter 7.6: Burlin cavity theory

This is an application of the interface effect. The same comment applies here, as it did to that section.

Chapter 7.7: The dosimetry chain

We start with (33), but expressed as a charge measurement of the primary standard instrument in a Standards Laboratory. That is,

$$\left(\frac{\Delta Q}{\Delta m}\right)\left(\frac{\overline{W}}{e}\right)_{\rm g} = D_{\rm g} = K^{0,||}_{\rm c,g}(\overline{\mu}_{en})^{\rm w}_{\rm g}\,(\overline{s})^{\rm g}_{\rm w}\,(\prod A)_{\rm S}\ , \tag{34}$$

where $(\prod A)$ is the product of all the "A" correction factors.

We can can rewrite the above as,

$$K^{0,||}_{\rm c,g} = \frac{\left(\frac{\Delta Q_{\rm S}}{\Delta m_{\rm S}}\right)\left(\frac{\overline{W}}{e}\right)_{\rm g}}{(\overline{\mu}_{en})^{\rm w}_{\rm g}\,(\overline{s})^{\rm g}_{\rm w}\,(\prod A)_{\rm S}}\ . \tag{35}$$

All the factors on the right hand side are known accurately by the Standards Laboratory, and thus, an internal calibration of the primary chamber provides a measurement of the primary Kerma at the Standard Laboratory.

Now, consider a client's chamber, subject to a charge measurement in the standard field of the Standards Laboratory, namely,

$$\left(\frac{\Delta Q}{\Delta m}\right)_{\rm C}\left(\frac{\overline{W}}{e}\right)_{\rm g} = K^{0,||}_{\rm c,g}(\overline{\mu}_{en})^{\rm w}_{\rm g}\,(\overline{s})^{\rm g}_{\rm w}\,(\prod A)_{\rm C}\ , \tag{36}$$

This, taken in ratio with a similar measurement of the standard chamber yields,

$$\Delta m_{\rm C} = \Delta m_{\rm S}(\Delta Q)^{\rm C}_{\rm S}(\overline{\mu}_{en})^{\rm wS}_{\rm wC}\,(\overline{s})^{\rm wC}_{\rm wS}\,(\prod A)^{\rm S}_{\rm C}\ . \tag{37}$$

All quantities on the right hand side are measured or calculable. Therefore, the measurement in the Standards Laboratory is tantamount to measuring the active mass of gas in the client's chamber.

Once the client receives their chamber, they wish to determine the dose to the air cavity of an ion chamber in their beam. Thus, they measure,

$$D^{\rm H}_{\rm g} = \left(\frac{\Delta Q}{\Delta m}\right)_{\rm H}\left(\frac{\overline{W}}{e}\right)_{\rm g}\ , \tag{38}$$

back in, for example, their hospital setting.

The only unknown in (38) is the mass of the gas in their standard chamber, and this is provided by the calibration from the Standards Laboratory.

How one goes from dose in the gas to the dose to the medium in the client's laboratory is the subject of various dosimetry protocols which will not be compared here.

However, before concluding, it it worthy to note how robust the calibration is.

All the factors on the right hand side of (37) are very well known, typically to less then several 10'ths of a percent.